Understanding CO_2 at aqueous interfaces using atomistic machine-learned potentials

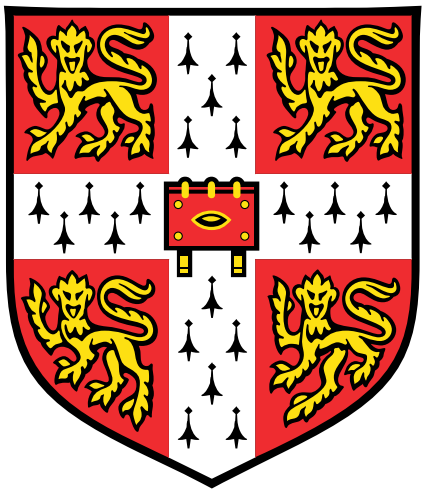

Samuel George Hamer Brookes

Yusuf Hamied Department of Chemistry

Cavendish Laboratory, Department of Physics

This thesis is submitted for the degree of

Doctor of Philosophy

Prof. Angelos Michaelides, Jesus College

Dr. Christoph Schran

September 2025

This thesis is the result of my own work and includes nothing which is the outcome of work done in collaboration except as declared in the preface and specified in the text. It is not substantially the same as any work that has already been submitted, or is being concurrently submitted, for any degree, diploma or other qualification at the University of Cambridge or any other University or similar institution except as declared in the preface and specified in the text. It does not exceed the prescribed word limit for the relevant Degree Committee.

Abstract

In today's scientific landscape, no molecule is more synonymous with risk and catastrophe than carbon dioxide (CO_2). Over the past several decades, billions of tons of CO_2 have been pumped into the atmosphere, giving rise to drastic increases in global temperatures alongside a myriad of other detrimental effects. Understanding the way in which CO_2 interacts with its environment is crucial for being able to mitigate rising CO_2 levels and some of its more harmful effects. Many of these environments are aqueous in nature; accordingly, it is vital that we can describe the way in which CO_2 and H_2O interact under various conditions. This PhD constitutes new insights into the way these two molecules interact with one another. Utilising machine-learned interatomic potentials (MLIPs), we provide a new understanding of how CO_2 behaves at the air-water, liquid-water, and solid-water interfaces. First, we demonstrate the existence of a new type of reaction mechanism affecting gaseous CO_2 molecules adsorbed at the air-water interface. This surface-mediated mechanism involves the partial dissolution of the reaction site at the topmost water layer, imparting bulk-like thermodynamic properties on an inherently interfacial process. Second, we show the efficacy of MLIPs for estimating interfacial tensions and identify the build-up of a liquid-like CO_2 monolayer at the water interface. Finally, we show that CO_2 uptake in solvent-saturated nanoporous carbon environments occurs due to favourable solute-wall interactions which out-compete those between the solvent and the pore wall. This thesis represents a step forward in understanding the behaviour of CO_2 at aqueous interfaces, leading to the uncovering of new fundamental physicochemical insights as well as providing clarity on experimental measurements and observations.

Rwy'n cyflwyno'r gwaith hwn i'm rhieni, Melanie a Daryl,

i'm chwaer, Kate,

ac i'm cariad, Georgia.

Preface

This thesis describes research undertaken in the Yusuf Hamied Department of Chemistry and the Cavendish Laboratory, University of Cambridge between October 2021 and September 2025 under the dual supervision of Prof. Angelos Michaelides and Dr. Christoph Schran. This thesis is the result of my own work and includes nothing which is the outcome of work done in collaboration except as declared in the preface and specified in the text. It is not substantially the same as any work that has already been submitted, or, is being concurrently submitted, for any degree, diploma or other qualification at the University of Cambridge or any other University or similar institution except as declared in the preface and specified in the text. It does not exceed the prescribed word limit for the relevant Degree Committee.

Chapters 1 and 2 will set out and contextualise the topics to be studied in this thesis. The remaining chapters will contribute the results of the following publications:

- **Chapter 3**: Samuel G. H. Brookes, Venkat Kapil, Angelos Michaelides, Christoph Schran, "CO_2 hydration at the air–water interface: A surface-mediated "in-and-out" mechanism", *Proc. Natl. Acad. Sci.* U.S.A. **122**, e2502684122 (2025) [187].

- **Chapter 4**: Samuel G. H. Brookes, Venkat Kapil, Christoph Schran, Angelos Michaelides, "The wetting of H_2O by CO_2", *J. Chem. Phys.* **161**, 84711 (2024) [223].

- **Chapter 5**: Zeke Coady, Samuel G. H. Brookes, Zhaohan Shen, Benjamin Rhodes, Grace Mapstone, Zhen Xu, Wei Yu, Hirotomo Nishihara, Christoph Schran, Angelos Michaelides, Alexander Forse, "Unexpected oversolubility of CO_2 measured at electrode-electrolyte interfaces", *J. Am. Chem. Soc.* **147**, 36310-36319 (2025) [302].

- **Chapter 6**: Work in progress - Samuel G. H. Brookes, Fabian Berger, Kara Fong, Angelos Michaelides, and Christoph Schran.

The vast majority of results were generated by myself, along with the analysis of all the data and graphs. A minor set of results and calculations were contributed by others and are declared as follows:

- Chapter 5: Experimental results pertaining to oversolubilities measured for nanoporous carbon environments (Fig. 5.1). These experimental results were obtained by Zeke Coady, with whom I collaborated for this paper. Mole fractions obtained for experimental and computational setups (shown in Table C.2) were also computed by Zeke. Results are reproduced with permission.

- Chapter 5: Interaction energies obtained for gaseous CO_2 and H_2O interacting with isolated graphene sheets (Fig. 5.3). These measurements were obtained from Flaviano della Pia and contributed as part of this work.

The calculations generated by myself were made possible thanks to computational resources provided by: the Cambridge Service for Data Driven Discovery (CSD3) operated by the University of Cambridge Research Computing Service, provided by Dell EMC and Intel using Tier-2 funding from the Engineering and Physical Sciences Research Council (capital grant EP/T022159/1), and DiRAC funding from the Science and Technology Facilities Council; and computational support from the UK national high performance computing service, ARCHER2, for which access was obtained via the UKCP consortium and funded by EPSRC grant EP/P022561/1.

This PhD additionally contributed to the following publications which are not included in this thesis:

- Gareth A. Tribello, Massimiliano Bonomi, Giovanni Bussi, Carlo Camilloni, Blake I. Armstrong, Andrea Arsiccio, Simone Aureli, Federico Ballabio, Mattia Bernetti, Luigi Bonati, Samuel G. H. Brookes, Z. Faidon Brotzakis, Riccardo Capelli, Michele Ceriotti, Kam-Tung Chan, Pilar Cossio, Siva Dasetty, Davide Donadio, Bernd Ensing, Andrew L. Ferguson, Guillaume Fraux, Julian D. Gale, Francesco Luigi Gervasio,

Toni Giorgino, Nicholas S. M. Herringer, Glen M. Hocky, Samuel E. Hoff, Michele Invernizzi, Olivier Languin-Cattoën, Vanessa Leone, Vittorio Limongelli, Olga Lopez-Acevedo, Fabrizio Marinelli, Pedro Febrer Martinez, Matteo Masetti, Shams Mehdi, Angelos Michaelides, Mhd Hussein Murtada, Michele Parrinello, Pablo M. Piaggi, Adriana Pietropaolo, Fabio Pietrucci, Silvio Pipolo, Claire Pritchard, Paolo Raiteri, Stefano Raniolo, Daniele Rapetti, Valerio Rizzi, Jakub Rydzewski, Matteo Salvalaglio, Christoph Schran, Aniruddha Seal, Armin Shayesteh Zadeh, Tomás F. D. Silva, Vojtěch Spiwok, Guillaume Stirnemann, Daniel Sucerquia, Pratyush Tiwary, Omar Valsson, Michele Vendruscolo, Gregory A. Voth, Andrew D. White, Jiangbo Wu, "PLUMED Tutorials: A collaborative, community-driven learning ecosystem", J. Chem. Phys. 7 March 2025; 162 (9): 092501 [233].

Samuel George Hamer Brookes

Jesus College

September 2025

Acknowledgements

Doing a PhD is by no means an easy task; indeed, these past four years have felt more like ten. The work accomplished during this period would not have been possible but for the guidance, support, and friendships of those around me. Everyone, from colleagues in the department to friends from college and from home, has greatly enriched these past few years.

I'd like to thank two people in particular. First, I'd like to thank my supervisor, Angelos. I will forever be grateful for the lessons and insights offered by Angelos, which I believe have been instrumental in my transition from a student to a researcher and a professional. Under Angelos' guidance, I have learnt the importance of collaboration, of the sharing and communication of ideas, and that science - at its core - can be both a fun and meaningful pursuit. I would also like to thank my supervisor, Christoph. During my time as a PhD student, there was no problem too big or too small that Christoph would not want to help with - and for that I am truly grateful. I cherish the regular chats and scientific discussions shared between us, and will be forever grateful for all the words of encouragement that kept me going - even when nothing seemed to be going right. The work detailed in this thesis has only been made possible as a result of these two great supervisors.

I would also like to thank my colleagues in both the Chemistry and Physics departments for providing such a welcoming and stimulating scientific environment. In no particular order, I'd like to thank Lisa, Domantas, Ini, Hugo, Giaan, Mandy, Alex E, Fiona, Connie, Fabian T, Michael, Kara, Kaifeng, Julia, Pavan, Isaac, Eszter, Ioannis, Oxana, Paramvir, Yair, Anna, John, Romain, Thomas, Asmita, Ioachim, Darren, and Lars. A special mention should go to Venkat, whose involvement in my projects helped shape much of this work, and with whom I have shared many an interesting conversation (and chess match). I

would also like to thank Xavi, Flaviano, Niamh, Fabian B, and Sam C - whose friendships I hold dear and with whom a laugh is only ever a sentence away.

Outside the department, my life has been immeasurably enriched by my friends and those around me. During the course of my PhD, I have had the privilege of meeting and coming to know so many interesting and amusing characters. This includes Sam F, Hol, Julia, Harry, Soo, Su, Chris, Matthew M, Pawel, Julien, Artik, James B, Charles K, Tim A, David, and all the boys at CURUFC - thank you for making life a wonderful and happy affair. To my friends outside of Cambridge - Nadine, Dan T, Jack, Emily, Dan C, Rory, Henry, Angus, Emma, Sophie, Jamie, Archie, Charles, Mikey, Dan M - you have made my life meaningful in so many ways. I'd like to also thank the lads at Cantabrigians RUFC, with whom I have shared so many valuable memories both on and off the field. In particular, I'd like to thank Glen, who always reminds me that, no matter what, things are never truly as bad as they seem.

Finally, I must highlight the continued support of my family. To my parents, Mel and Daryl, I will forever be grateful for all the guidance, encouragement, and love you have provided me these past 26 years. Your unending belief in me forms the cornerstone of my motivation, and everything that I have achieved or will achieve in life is down to you. You are my biggest role models, always. To Kate, thank you for all the cherished memories of our childhood and of home. I am in constant admiration of your caring and empathetic nature, and I am so proud to see the woman you have grown up to be.

And to Georgia, as ever, *diolch am fod yno i mi, fy nghariad.*

Table of contents

List of figures

Chapter 1

Introduction

> In the beginning the Universe was created. This has made a lot of people very angry and been widely regarded as a bad move.
>
> *Douglas Adams*
> *The Restaurant at the End of the Universe*

Over recent decades, atmospheric CO_2 levels have increased by over 100 ppm as a result of carbon-intensive anthropogenic activity [1]. The effects of this increase have been pronounced: rising global temperatures, irregular weather patterns, the destruction of wildlife, and the poisoning of our oceans [2–5], to name a few. The harmful nature of CO_2 arises from its role as a greenhouse gas [6]; CO_2 absorbs and re-emits long-wave IR radiation, thus heating Earth's lower atmosphere. With global CO_2 levels poised to rise even further, the need for new green policies, technologies, and mitigation strategies has become ever more pressing [7].

The substantial increases in atmospheric CO_2 demand a detailed understanding of the way this molecule interacts with its surroundings. Specifically, it is crucial that we understand the way in which CO_2 interacts with water - the molecule of life and the most abundant substance on Earth's surface. CO_2-H_2O systems are central to several technological applications and natural phenomena. Ocean acidification, for example,

results from the hydration reaction between CO_2 and water to form carbonic acid [8, 9], which can then deprotonate to form bicarbonate and hydronium ions. In carbon sequestration schemes, CO_2 is captured at source and injected underground where it is trapped in porous rock material through either physical or chemical means (e.g., capillary trapping or mineralisation) [10, 11]. Additionally, CO_2 can be electrochemically captured using various electrode-electrolyte setups [12, 13]. These various settings are intrinsically *interfacial* in nature and characterised by sharp changes in structuring, solvation, and reactivity over several angstroms.

We can gain much insight on CO_2-H_2O systems through the use of computational atomistic modelling. Methods such as molecular dynamics (MD) and Monte Carlo (MC) have provided an invaluable lens into the sub-microscopic world, allowing us to extract insights at the level of atoms and molecules and then apply them for macroscopic-level understanding [14, 15]. Undoubtedly, the field of atomistic simulations has developed significantly since their first implementation in the mid-20th century [16–18]. Over the last several decades, classical force field (FF) MD has led the way in understanding extended molecular systems and processes, e.g., condensed-phase systems [19], protein folding dynamics [20], and other biological functionalities [21]. The development of density functional theory (DFT) in 1964 and its extension to *ab initio* MD simulations in 1985 [22] have proved pivotal in providing quantum-level descriptions of complex chemical systems, such as those involving proton transfer mechanisms [23] or under extreme temperature and pressure conditions [24]. Indeed, much of our current insight on CO_2-H_2O systems has come from these two flavours of atomistic modelling. For example, from classical FF simulations, we know that the bulk solvation of CO_2 is generally a weak phenomenon, suggesting CO_2 to be a large and mostly hydrophobic species [25]. Testament to the immiscibility of these two molecules are the large interfacial tensions (IFTs) reported for biphasic CO_2-H_2O systems from large-scale MD simulations [26]. From an *ab initio* perspective, previous studies have worked to identify elementary CO_2-water reactions in solution [27] as well as characterise hydration structures and small cluster binding

effects [28, 29], among other pursuits. We delve more deeply into these studies later on in Chapters 3–6.

Despite these various insights, there is still a lot that we don't know about CO_2-H_2O systems. This is particularly true for CO_2 molecules residing at aqueous interfaces, for example, at the air-water interface or at the pressurised CO_2-H_2O liquid-liquid boundary. These interfacial regimes - central to a number of natural phenomena and technological applications - are fascinating yet difficult to probe [30, 31], both experimentally and computationally. Despite recent developments in the form of sum frequency generation and second harmonic generation [32], spectroscopic measurements are often hampered by low effective surface populations and contamination from organic impurities [33]. On the theory side, the modelling of aqueous interfaces is impeded by large, correlated fluctuations in the molecular positions. These fluctuations impede the exploration of phase space and the realisation of ergodicity (that is, the equivalence of time and ensemble averages (see Chapter 2)), requiring prohibitively long simulations over extended molecular systems to obtain converged thermodynamic estimates. The choice of underlying force-generation method introduces further caveats; classical FFs enable fully atomistic simulations over both large length and timescales but cannot capture bond making and breaking, whereas *ab initio* methods allow for a fully reactive treatment but are limited in terms of the accessible system sizes and complexities. Insights from these approaches may therefore be limited in their robustness and generalisability [34].

We are therefore left with several open questions concerning the nature of interfacial CO_2-H_2O systems. *Ab initio* studies are relatively limited in the context of interfacial CO_2, meaning that a first-principles description of these species is primitive. We duly identify four outstanding questions from literature:

(i) What happens to CO_2 at aqueous interfaces?

(ii) How does the physicochemical nature of CO_2 change with the type of interface, for example, in terms of the adsorption propensity, molecular orientation, and inherent molecule reactivity?

(iii) In turn, how does CO_2 influence the physicochemical properties of the interfacial media, for example, the structuring and bonding of nearby solvent media?

(iv) And how does the behaviour of CO_2 at interfaces compare with CO_2 in bulk? How do the relative stabilities of these species compare?

Acknowledging the gaps in our understanding of aqueous interfaces, we note that the field of atomistic simulations, like many other scientific fields, is currently undergoing drastic methodological change. Advances in artificial intelligence - specifically, in machine learning (ML) - have significantly improved the way we perform atomistic simulations. The advent of machine-learned interatomic potentials (MLIPs), which constitute a flexible, many-body mapping between a local chemical environment and an underlying first-principles-level potential energy surface (PES), now allows us to treat complex systems with an accuracy approaching that of quantum methods but with a computational efficiency approaching that of classical FF models [35]. Indeed, over the past two decades, this field has exploded with a diverse array of architectures and approaches, from high-dimensional neural networks and kernel methods to message-passing and graph networks [36–38].

Already, a number of MLIP studies looking at aqueous interfaces have been published [36]. Several studies have identified novel reaction phenomena occurring at water surfaces. For example, work by Galib et al. showed how atmospheric N_2O_5 undergoes surface-mediated decomposition in aerosols as a result of competitive hydrolytic and evaporative processes [39]. More recent work by de la Puente et al. demonstrated that the acidity of certain acid species can change depending on where they sit relative to the water surface [40]. A number of MLIP studies have also looked at characterising the structural properties of water, both under ambient conditions [41, 42] and under extreme pressures and spatial confinement [43–45]. This has included attempts to generate a first-principles phase diagram of confined monolayer water [43] as well as determine ionic behaviour in confined electrolytic media [44, 45]. Work by Fong et al. reported reduced contact-ion-pair formation for NaCl electrolytes placed under graphene confinement [44], whilst work by Advincula et al. determined that hydronium ions tend to accumulate at graphene-water

interfaces [45]. Most recently, we have seen attempts to incorporate electrochemical potentials into the description of electrode-electrolyte systems [46].

Building on the latest success and developments in this field, this PhD attempts to extend the described methods towards understanding complex CO_2-H_2O interfaces. We combine MLIP-accelerated simulations with enhanced sampling methods to interrogate three CO_2-water interfaces of practical importance: the air-water interface, the liquid CO_2-water interface, and the solid (carbon)-water interface.

The air-water interface forms under ambient conditions and hosts a small excess of atmospheric molecules adsorbing at the water surface. Under these conditions, CO_2 exists as a gaseous compound interacting through weak dispersion and quadrupolar interactions, and so relative CO_2 surface concentrations are low. Nevertheless, the air-water interface forms a key part of CO_2 exchange and acidification processes near the ocean surface [9]. Currently unclear is how surface-adsorbed CO_2 reacts with interfacial water and whether we observe any novel reaction phenomena for this process (as seen in Refs. [39, 40]). Further, it is unclear how the relative adsorption propensities of the reaction species (i.e., CO_2, HCO_3^- and H_2CO_3) influence the overall chemical and exchange processes - the adsorption of ions at the air-water interface remains a large and unresolved topic [47].

At elevated pressures, CO_2 can condense to a liquid (or become supercritical), thus leading to the formation of a biphasic liquid CO_2-H_2O interface. This interface underpins a number of carbon storage techniques, including injection into saline aquifers and deep-sea storage through CO_2 lake formation [48, 49]. Central to the efficacy and duration of this storage are the interactions between the bulk CO_2 and bulk water phases. Whilst previous MLIP work has investigated the properties of interfacial water [41] and interfacial CO_2 [50] in isolation, no study has looked at these phases in contact with one another. Accordingly, it is uncertain how CO_2-H_2O interactions manifest under high-pressure conditions, and questions remain concerning collective phase behaviour and CO_2 build-up at the phase boundary.

And finally for the solid-water interface, owing to the rarity and practical difficulty of forming solid CO_2, we instead direct our attention to interfaces between graphene-like,

porous carbon and (CO_2-containing) aqueous solutions. These interfaces, on account of their inherently large surface areas, find application across a range of fields and technologies, such as catalysis, energy generation and storage, and climate science [12, 51–53]. Recent experimental work has also highlighted the potential of nanoporous carbons for electrochemical CO_2 capture [12]. Whilst several MLIP studies have characterised the behaviour of electrolytes under confined conditions [44, 45, 54], a first-principles description of in-pore CO_2 is currently missing. Therefore it is currently unclear how nanoporous environments facilitate CO_2 uptake and capture under solvent-saturated conditions. Further, it is unclear how defects and structural heterogeneities modulate molecule uptake and reaction. This is particularly true for atom vacancies and point defects, meaning that a microscopic description of realistic nanoporous carbon has remained elusive.

In this PhD, we uncover new chemical insights into these three distinct interfaces. Methodologically, we combine state-of-the-art MLIPs with established enhanced sampling techniques such as metadynamics, umbrella sampling, and replica exchange to obtain thermodynamic and free energy properties at DFT and beyond-DFT levels. In Chapter 3, we describe our investigation into the nature of CO_2 reactivity at the air-water interface. We uncover a new style of reaction mechanism - a so-called 'in-and-out' mechanism - that exploits the dynamic nature of the reaction site to impart bulk-like properties and energies on interfacial processes. In this way, reactions at the air-water interface can proceed in a similar manner to their bulk counterparts. In Chapter 4, we describe an approach for modelling liquid-liquid interfaces and obtaining accurate IFT predictions. With increasing pressure, initial reductions in the IFT coincide with the build-up of an adsorbed, saturated CO_2 film forming at a low pressure (20 bar) and with properties similar to those of the bulk liquid. In Chapter 5, we describe a collaborative project in which a heightened solubility of CO_2 in solvent-saturated nanoporous carbon environments is reported. This solubility is facilitated by CO_2-graphene interactions, which outcompete similar interactions between H_2O and the pore wall. And finally, in Chapter 6, we then move beyond the standard

of nanoporous carbon modelling to explore spin-polarised vacancy defects in extended graphene systems.

We start with an introduction to the theoretical and computational frameworks employed in this thesis. Then, for each subsequent chapter, we provide some context to the work, followed by the methods, the results, and a brief summary and outlook for that section. Links to the relevant simulation data are provided at the start of each chapter.

Chapter 2

Theoretical and computational framework

> You don't know much and that's a fact.
>
> *Lewis Carroll*
> *Alice's Adventures in Wonderland*

This thesis has utilised a range of methods and techniques for modelling atomistic CO_2-H_2O systems. This includes (but is not limited to) molecular dynamics simulations, density functional theory, *ab initio* MD, machine-learned interatomic potentials, and enhanced sampling methods. The more salient features of these methodologies are described below, with full details provided in the supplied references.

2.1 Statistical mechanics

Statistical mechanics provides the means of relating microscopic behaviour to macroscopic observables. It forms the basis upon which molecular simulations are performed, showing how conventional experimental observations are born out of an averaging of properties at the molecular level. Statistical mechanics can be derived through both quantum and classical routes, though the former is more straightforward. There exist a number of

excellent texts that meticulously explore these derivations [55–57]. For the purposes of this chapter, we shall leave much of the derivations to them, detailing only the most important concepts from this framework.

A quantum formalism

The theory of statistical mechanics can be built upon two main assumptions: first, that we can express a particular system as occupying a finite number of quantised states; second, that all states of a fixed composition (volume V and number of particles N) and fixed energy E are visited with equal probability - this is known as the *equal a priori* postulate. In statistical mechanics, we are often interested in the way in which energy can be distributed among a number of subsystems. For example, for the case where we have two subsystems, the total energy E can be found by $E = E_1 + E_2$. The total number of states corresponding to energy E is given by $\Omega = \Omega_1 \times \Omega_2$, where Ω gives the degeneracy (i.e., the number of states) corresponding to the labelled energy. To find the most likely distribution of energy across the two subsystems, we can look for the instance where $\Omega(E)$ is maximised,

$$\left(\frac{\partial \ln \Omega(E_1, E - E_1)}{\partial E_1}\right)_{N,V,E} = 0. \tag{2.1}$$

Using the fact that $dE_1 = -dE_2$, we can set

$$\left(\frac{\partial \ln \Omega_1(E_1)}{\partial E_1}\right)_{N_1,V_1} = \left(\frac{\partial \ln \Omega_2(E_2)}{\partial E_2}\right)_{N_2,V_2} \tag{2.2}$$

for the two systems at thermal equilibrium. Under these conditions, we know that the temperature T will be equivalent for systems 1 and 2. Using this knowledge, we can define an inverse temperature,

$$\beta(E, V, N) = \frac{1}{k_\mathrm{B} T} = \left(\frac{\partial \ln \Omega(E, V, N)}{\partial E}\right)_{N,V}, \tag{2.3}$$

where T is the temperature, and k_B is the Boltzmann constant. For two weakly coupled subsystems, we say that thermal equilibrium is established when $\beta_1 = \beta_2$ and $\ln \Omega$ is at a

maximum. We know from basic thermodynamics that the entropy of the system will also be at a maximum at thermal equilibrium. Accordingly, we can equate the two quantities and write down Boltzmann's formulation of the system entropy as

$$S(N, V, E) \equiv k_{\mathrm{B}} \ln \Omega(N, V, E) \tag{2.4}$$

This formula,[1] famously engraved on Boltzmann's tomb, is a cornerstone of modern statistical mechanics and provides some clarity on the second law of thermodynamics - an isolated system is most likely to be found in a state that possesses the largest number of microstates.

Now suppose we have a system where a particular subsystem A is coupled to a large thermal bath B. The probability of finding the subsystem A in state i is given by

$$P_i = \frac{\Omega_{\mathrm{B}}(E - E_i)}{\sum_j \Omega_{\mathrm{B}}(E - E_j)} \tag{2.5}$$

By expanding $\ln \Omega_{\mathrm{B}}(E - E_i) \approx \ln \Omega_{\mathrm{B}}(E) - \beta E_i$, we can arrive at

$$P_i = \frac{\exp(-E_i / k_{\mathrm{B}} T)}{\sum_j \exp(-E_j / k_{\mathrm{B}} T)}, \tag{2.6}$$

which is the well-known Boltzmann distribution of states for a system at temperature T. Under the canonical ensemble (fixed N, V, T), we can use eqn. 2.6 to determine the probability of finding the system in a particular state. We can also use it to calculate the averaged energy of the system according to

$$\langle E \rangle = \sum_i E_i P_i = -\left(\frac{\partial \ln(Q)}{\partial \beta} \right)_{N,V} \tag{2.7}$$

[1] Using the thermodynamic definition of temperature, $1/T = \left(\frac{\partial S}{\partial E}\right)_{V,N}$, one may use Boltzmann's entropy formula to derive the inverse temperature β given in Eq. 2.3.

where $Q = \sum_j \exp(-E_j/k_\mathrm{B}T)$ is known as the *partition function* of the system and represents a weighted sum of the allowed microstates. Through comparison with the Helmholtz energy analogue of the Gibbs-Helmholtz relation, we extract the following important equation for determining the Helmholtz energy, A, of a system,

$$A = -k_\mathrm{B}T \ln Q \tag{2.8}$$

This 'bridge relation' constitutes an important relationship in statistical mechanics; it allows us to obtain macroscopic information (i.e., the Helmholtz energy) from an aggregated knowledge of the microstates of a system. Whilst Q is generally intractable for realistic systems (a product of the vast number of states and the difficulty associated with obtaining all relevant state energies, E_j), Eq. 2.8 is significant in providing a direct connection between the microscopic and macroscopic worlds.

Classical formalism

As stated at the start of this chapter, it is also possible to formulate statistical mechanics in a classical sense, substituting discrete levels for continua and summations for integrals. Whilst we will not delve too much into its derivation, we do quote the classical canonical partition function here for a system of N particles of mass m_i, momenta p_i, and position r_i:

$$Q_\mathrm{classical} = \frac{1}{h^{dN}N!}\int d\boldsymbol{p}^N d\boldsymbol{r}^N \exp\left(-\beta\left[\sum_i \frac{p_i^2}{2m_i} + U(\boldsymbol{r}^N)\right]\right), \tag{2.9}$$

where $\boldsymbol{r}^N \equiv (r_1, r_2, ..., r_N)$ and $\boldsymbol{p}^N \equiv (p_1, p_2, ..., p_N)$. Eq. 2.9 amounts to integrating the kinetic and potential components of the Hamiltonian - given by the argument of the exponential, $H = \sum_i \frac{p_i^2}{2m_i} + U(\boldsymbol{r}^N)$ - over the phase space $(\mathbb{R}, \mathbb{P})$ of a system. The h^{dN} term accounts for the dimensionality of the system, where d is the number of spatial dimensions, N is the number of atoms, and h is Planck's constant. The $N!$ term corrects for the indistinguishability of identical particles and prevents overcounting states.[2] Practically, Eq. 2.9 is easier to compute than its quantum counterpart, which requires a knowledge of all

[2] In the case of distinguishable particle, $N! \to \prod_\alpha N_\alpha!$, where α runs over the distinct species.

eigenstates of a particular system - this is an impossibly large task! Therefore, we generally use $Q_{\text{classical}}$ for obtaining the ensemble-averaged properties from MD simulations.

Ensembles

In this chapter, we started our discussion with the assumption that we were dealing with a system of fixed energy E, volume V, and composition N. In practice, we can choose to fix different sets of macroscopic control variables. The collection of microstates or 'realisations' that adhere to these specified macroscopic control parameters are referred to as an ensemble. In the case of fixed NVE, this is known as the *microcanonical* ensemble. For ensembles employing fixed N, V, and temperature T, we refer to them as the *canonical ensemble*; we have already covered this ensemble in Eq. 2.5-2.7 (with the partition function Q corresponding to the canonical partition function). The *isothermal-isobaric* ensemble has fixed N, T, and pressure P, whilst the *grand canonical* ensemble fixes V, T, and the chemical potential μ. Our choice of ensemble ultimately determines which 'lens' we wish to view our microscopic system with (though it can be shown that these ensembles are equivalent in the thermodynamic limit, $N \to \infty$ [57]).

Molecular dynamics

Using statistical mechanics, we can obtain macroscopic properties from a knowledge of microscopic, many-particle systems. We obtain such estimates either by averaging over a series of time-evolved phase space ($\{\mathbb{R},\mathbb{P}\}$) coordinates or by averaging over all initial phase space coordinates (this equivalence is known as the *ergodic hypothesis*). Our choice of averaging ultimately determines which molecular modelling scheme we use: time averaging through molecular dynamics or ensemble averaging through Monte Carlo methods.

In molecular dynamics, we can explore the phase space of a system by explicitly solving Newton's equations of motion. Starting from the second law, we know that

$$\mathbf{F} = m\frac{d^2\mathbf{R}}{dt^2} = -\nabla U(\mathbf{R}), \tag{2.10}$$

where $\mathbf{R}$ are the atomic coordinates, m is the mass, U the potential energy, and $\mathbf{F}$ is the resulting force vector. Following the determination of $\mathbf{F}$, specialised integrators can be used to understand how molecules at time t will behave at future time $t + \delta t$,

$$\mathbf{R}(t + \delta t) = \mathbf{R}(t) + \delta t \mathbf{v}(t) + \frac{1}{2}\delta t^2 \mathbf{a}(t), \tag{2.11}$$

$$\mathbf{v}(t + \delta t) = \mathbf{v}(t) + \frac{1}{2}\delta t \left[\mathbf{a}(t) + \mathbf{a}(t + \delta t)\right], \tag{2.12}$$

where $\mathbf{v}$ and $\mathbf{a}$ are the velocity and acceleration vectors, respectively. The equations presented above belong to the velocity Verlet algorithm [58], which is both symplectic (that is, it conserves phase-space volume and helps improve the long-term stability of the integration algorithm) and time-reversible. Other integrators, such as the classic Verlet or Gear algorithms, could also be used [59, 60]; however, the forms presented in (2.11) and (2.12) are some of the simplest and most numerically stable, making the velocity Verlet algorithm one of the more popular methods for conventional MD. More information on numerical integrators can be found in Ref. [57].

An important decision for performing MD simulations comes with the choice of which ensemble to use. The equations presented in Eqs. 2.10-2.12 above, provided no external perturbation and a reasonable choice of δt, roughly adhere to the conservation of energy and thus sample the microcanonical ensemble. However, for the purposes of many of our simulations, we would like to sample other ensembles, such as the canonical or the isothermal-isobaric ensembles. Constant temperature simulations can be performed through the introduction of 'thermostats', which serve to alter either the local or global velocity distributions to ensure a correct sampling of the NVT ensemble. Examples of these thermostats include the stochastic Andersen thermostat [61], the canonical sampling through velocity rescaling (CSVR) [62], and the global Nosé-Hoover (NH) thermostat [63]. Citing the mild influence of the NH approach on particle dynamics (such that they approach Newtonian dynamics in the limit of large system sizes), this thermostat was selected for most of this thesis' work. For constant pressure simulations, 'barostats' may be employed to couple systems to a fictitious pressure bath. In the case of the Andersen

barostat, a 'piston-like' degree of freedom (DOF) is added to equations of motion, enabling the isotropic scaling of cell dimensions so as to sample a desired pressure P [61]. An extension to this barostat is seen in the Parrinello-Rahman barostat, which supports an anisotropic scaling of the cell dimensions through additional DOFs [64]. Related extended-system formulations, such as the Martyna–Tuckerman–Tobias–Klein, introduce new equations of motions to ensure a correct isothermal-isobaric sampling [65, 66].

Beyond thermostats and barostats, another crucial aspect of MD simulations lies in how one obtains $\mathbf{F}$ for equation (2.10). Traditional FF methods use empirical potentials based on simple mathematical forms to determine a system's potential energy surface, $U(\mathbf{R})$. These include potentials such as the renowned Lennard-Jones potential for describing van der Waals interactions [67], the extended single point charge (SPC/E) potential for modelling rigid water molecules [68], the all-atom AMBER FF for modelling proteins [69], and the coarse-grained MARTINI FF for modelling large biomolecular systems [21]. Whilst computationally efficient, these potentials are formulated with pre-specified connectivities such that bond-making and -breaking events cannot be described.[3] For this, one must turn to *ab initio* MD, which combines finite-temperature trajectories with *ab initio*-level forces computed 'on-the-fly' from electronic structure theory. By explicitly considering the underlying electronic structure, we can describe many-body forces, electronic polarisation, and bond-making and -breaking events at the level of first-principles calculations [71]. In this way, quantum-mechanical forces can be used to propagate a system of classical particles. Providing that nuclear quantum effects (NQEs) are sufficiently negligible, this approach to molecular dynamics is usually well-grounded [72] (citing the Born-Oppenheimer approximation), though we can extend our description to include NQEs if needed (e.g., low temperatures and light nuclei) [73, 74]. In the next section, we cover the topic of *ab initio* MD more closely, showing how exactly electronic structure theory can be integrated with finite temperature dynamics.

[3] Notable exceptions such as ReaxFF do exist [70].

2.2 *Ab initio* molecular dynamics

Ab initio molecular dynamics represents the coming together of two separate communities: the electronic structure community and the statistical mechanics community. Since the first AIMD simulation of crystalline silicon in 1985 [22], this field has provided a number of insights into the thermodynamic and dynamical properties of complex systems, from understanding the nature of silicates and glasses to modelling proton transfer and complex surface reactions [75–78]. To begin this section, we look back at the fundamental problem of electronic structure theory and try to understand what happens at the sub-nanometre level.

The physics of small things

When approaching this theory, one usually starts with the full time-independent Schrödinger equation,

$$\hat{H}\Psi(\mathbf{r},\mathbf{R}) = E\Psi(\mathbf{r},\mathbf{R}), \tag{2.13}$$

where E is the energy, $\hat{H}$ is the Hamiltonian operator, and Ψ is the wavefunction of the system, dependent upon both the electronic ($\mathbf{r}$) and nuclear ($\mathbf{R}$) coordinates. For a system of N electrons and M nuclei, $\hat{H}$ is defined according to

$$\hat{H} = -\frac{1}{2}\sum_{i=1}^{N}\nabla_i^2 - \frac{1}{2}\sum_{I=1}^{M}\frac{\nabla_I^2}{M_I} - \sum_{i,I}^{N,M}\frac{Z_I}{R_{iI}} + \sum_{i,j>i}^{N}\frac{1}{r_{ij}} + \sum_{I,J>I}^{M}\frac{Z_I Z_J}{R_{IJ}}, \tag{2.14}$$

where I and J run over the nuclei, and i and j run over the electrons. ∇_I^2 and ∇_i^2 are the corresponding nuclear and electronic gradient operators, whilst M_I and Z_I represent the nuclear mass and charge, respectively. We define r_{ij}, R_{IJ}, and R_{iI} as,

$$r_{ij} = |\mathbf{r}_i - \mathbf{r}_j|\,, \quad R_{IJ} = |\mathbf{R}_I - \mathbf{R}_J|\,, \quad R_{iI} = |\mathbf{r}_i - \mathbf{R}_I|\,.$$

where $\mathbf{r}_i$ gives the position of electron i and $\mathbf{R}_I$ the position of nucleus I. In Eq. 2.14 (and throughout this chapter), we make use of atomic units: $\hbar = e = m_\mathrm{e} = 4\pi\epsilon_0 = 1$, where e is the elementary charge, m_e is the electron mass, and $4\pi\epsilon_0$ is permittivity.

In its full many-body form, the Schrödinger equation is analytically insoluble (except in a few particular cases). Therefore, certain approximations are required. Owing to a large disparity in the masses, the nuclear and electronic motions can be decoupled such that the electrons can be considered as moving in a field of fixed nuclear charge. Under this clamped-nuclei (Born-Oppenheimer) approximation, the total wavefunction is factorised into electronic and nuclear parts, $\Psi_\mathrm{BO} = \Psi_\mathrm{e}(\mathbf{r};\mathbf{R})\Psi_\mathrm{n}(\mathbf{R})$, in which the former displays only a parametric dependence on $\mathbf{R}$ and is obtained as an eigenfunction of the electronic Schrödinger equation,

$$\hat{H}_\mathrm{e}\Psi_\mathrm{e}(\mathbf{r};\mathbf{R}) = E_\mathrm{e}(\mathbf{R})\Psi_\mathrm{e}(\mathbf{r};\mathbf{R}), \tag{2.15}$$

where $\hat{H}_\mathrm{e}$ is the electronic Hamiltonian operator. Traditionally, Eq. (2.15) can be solved by decomposing Ψ_e into products of one-electron orbitals, ψ_i, where each orbital is composed of a linear combination of functions defined by the basis set

$$\psi_i = \sum_s \phi_s(\boldsymbol{r}) c_s^{(i)}, \tag{2.16}$$

where ϕ_s are the chosen basis and $c_s^{(i)}$ denote the coefficients.

Hartree-Fock and post-HF methods

Following this formalism, one can derive many of the seminal theories underpinning quantum chemistry. Hartree-Fock theory, one of the earliest attempts at approximating the wavefunction of a many-body system [79, 80], formulates $\boldsymbol{\Psi}$ as a single Slater determinant [81],

$$\boldsymbol{\Psi} = \frac{1}{\sqrt{N!}} |\chi_1, \chi_2, ..., \chi_N|, \tag{2.17}$$

where N gives the total number of electrons, and χ_n represent the one-electron spinorbitals. Whilst able to account for Pauli repulsion (analogous to switching two rows under the

matrix representation), this formalism is limited by its inability to describe the dynamic correlations between electrons. For such electron correlation, we need to extend our scheme to more complicated schemes. For example, in full configuration interaction (FCI), we incorporate multiple Slater determinants corresponding to excited (virtual) states of our particular system. By including these determinants, we can arrive at a result that is exact within the space spanned by the basis set, albeit at exorbitant computational cost. Other, more computationally accessible approximations include Möller-Plesset perturbation theory (MP) [82] and coupled-cluster (CC) methods [83]. We highlight the role of CCSD(T) [84] - which incorporates single, double, and perturbative triple excitations - as the 'gold standard' for performing computational quantum chemistry. Alongside obtaining new chemical insights [85–87], CCSD(T) is often used as a benchmark for conducting highly accurate quantum mechanical calculations [88, 89].

Whilst impressive in their accuracy, these correlated wavefunction methods still pose daunting calculation times for all but the simplest molecular systems, with MP4 and CCSD(T) scaling as $\mathcal{O}(N^7)$ for electron count N. Local coupled cluster methods (e.g., Domain-based Local Pair Natural Orbital (DLPNO)-CCSD(T) [90]), can reduce calculation times by 1–2 orders of magnitude, but these are still prohibitive costs. Treating extended molecular simulations over multiple time-steps, therefore, requires an alternative formulation of quantum chemistry.

Density functional theory

An alternative approach to quantum chemistry is realised in density functional theory (DFT). Owing to its favourable compromise between accuracy and computational efficiency, this theory provides the means of making accurate, quantum-level predictions for a fraction of the cost of correlated wavefunction methods. The theory itself was first presented by Hohenberg and Kohn in 1964 [91] and involves reformulating the Hamiltonian in terms of an electron density, ρ, such that the energy of the system is a functional of that density, $E[\rho(\mathbf{r})]$. For N electrons of position $\mathbf{r}_N$ and spin s_N, the electron density ρ is formally

given as

$$\rho(\mathbf{r}) = N \int ... \int |\Psi(\mathbf{r}_1, \mathbf{r}_2, ..., \mathbf{r}_N)|^2 \mathrm{d}s_1, \mathrm{d}\mathbf{r}_2, ..., \mathrm{d}\mathbf{r}_N. \tag{2.18}$$

According to the first two theorems of Hohenberg and Kohn, this density is uniquely defined by an external potential, V_{ext}, and the true ground-state density can be determined when ρ is variationally minimised. Using these principles, Kohn and Sham would go on to recast the system into a form that was solvable [92]. Specifically, they demonstrated that the electron density of an interacting system of electrons, ρ_0, was identical to that of a fictitious non-interacting system, ρ_{s}. Using Kohn-Sham orbitals, ϕ_i, the authors re-expressed the electron density as $\rho_0 = \sum_{i=1}^{\mathrm{occ}} |\phi_i(\mathbf{r})|^2$ and demonstrated that the ground-state energy could be re-written as

$$E_{\mathrm{KS}} = E[\rho] = T_{\mathrm{s}}[\rho] + V_{\mathrm{ext}}[\rho] + J[\rho] + E_{\mathrm{xc}}[\rho] \tag{2.19}$$

where $T_{\mathrm{s}}[\rho]$ gives the non-interacting kinetic energy,

$$T_{\mathrm{s}}[\rho] = -\frac{1}{2} \sum_{i}^{N} \langle \phi_i | \nabla^2 | \phi_i \rangle \tag{2.20}$$

$V_{\mathrm{ext}}[\rho]$ is the interaction of the density with the external potential, $\hat{V}_{\mathrm{ext}}$,

$$V_{\mathrm{ext}}[\rho] = \int \hat{V}_{\mathrm{ext}} \rho(\mathbf{r}) d\mathbf{r}, \tag{2.21}$$

and J and E_{xc} are the Coulombic repulsion and exchange-correlation energy, respectively. Of all the terms in equation (2.19), E_{xc} proves to be both the most important and the most controversial. E_{xc} arises as an artefact of our non-interacting framework and the classical treatment of electron-electron interactions. It is defined according to

$$E_{\mathrm{xc}}[\rho] = T[\rho] - T_{\mathrm{s}}[\rho] + V_{\mathrm{ee}}[\rho] - J[\rho], \tag{2.22}$$

where T is the kinetic energy of the interacting system, and V_{ee} is the actual electron interaction potential. In principle, DFT is rigorously exact; in practice, the form of E_{xc} is unknown, and so the energy of the system cannot be precisely defined.

Jacob's ladder

Developing new approximations to the form of E_{xc} constitutes an active area of research in computational chemistry, and there exist numerous possible functional forms. These forms are arranged as 'rungs' on a metaphorical ladder, with higher rungs equating to more extended/sophisticated formalisms. Often, this also entails higher accuracy, but it should be noted that this is not guaranteed, and performance will often depend upon the system being treated [93].

At the base of Jacob's ladder is the local density approximation (LDA) [92]. LDA represents the simplest approximation to E_{xc}, which is derived assuming a constant electron density and is a functional purely of the electron density ρ; this is shown in Eq. (2.23) where ϵ_{xc} is the exchange-correlation energy per particle. Obviously, the electron density is not uniform for real systems. Therefore, we can introduce a dependence on the density gradient $\nabla\rho(\mathbf{r})$ to give the generalised gradient approximations (GGAs), such as the PW91 and PBE functionals [94, 95], with the general form shown in Eq. (2.24). Meta-GGAs, such as SCAN and r2SCAN [96, 97], can be constructed through the inclusion of the kinetic energy density, $\tau(\mathbf{r}) = \frac{1}{2}\sum_{i=1}^{N} |\nabla\psi_i(\mathbf{r})|^2$. Taking this form and developing it further by including some fraction of the exact exchange energy, $(1-\alpha)E_{\text{x}}^0$, gives what are known as the hybrid functionals, shown in Eq. (2.25), which include well-known functionals such as PBE0 [98], B3LYP [99], and HSE [100]. By including exact exchange, we can help mitigate some of the effects arising from the self-interaction error (SIE) (a result of the mean-field approximation, in which an electron 'interacts with itself'). High rungs of the ladder include double hybrids, which incorporate an MP2-like perturbative term (e.g., B2PLYP [101], ωB97M(2) [102]) as well as the random phase approximation (RPA), which obtains non-local electron correlations through integration of the electron response [103, 104].

$$E_{\mathrm{xc}}^{\mathrm{LDA}} = \int \rho(\mathbf{r})\epsilon_{\mathrm{xc}}[\rho(\mathbf{r})]d\mathbf{r} \tag{2.23}$$

$$E_{\mathrm{xc}}^{\mathrm{GGA}} = \int \rho(\mathbf{r})\epsilon_{\mathrm{xc}}[\rho(\mathbf{r}), \nabla\rho(\mathbf{r})]d\mathbf{r} \tag{2.24}$$

$$E_{\mathrm{xc}}^{\mathrm{hybrid}} = \alpha E_{\mathrm{x}}^{\mathrm{GGA}} + (1-\alpha)E_{\mathrm{x}}^{0} + E_{\mathrm{c}}^{\mathrm{GGA}} \tag{2.25}$$

Dispersion forces

Owing to a good compromise between accuracy and efficiency, GGA functionals are often selected for performing AIMD simulations. However, they are not without drawbacks. As mentioned above, GGA functionals exhibit SIEs and thus often display an overdelocalisation of the electron density. Further, GGAs are effectively 'short-sighted' in nature; their dependence solely on the electron density and its gradient make them a semi-local theory. This proves problematic for systems displaying prominent long-range effects, e.g., noble gas dimers, inhomogeneous fluids, and molecular crystals [105–107].

To rectify this, we can introduce new formalisms to explicitly account for non local interactions. In one approach, we can explicitly include non-local corrections into the electronic structure calculations themselves, reformulating the exchange correlation functional to give:

$$E_{\mathrm{xc}} = E_{\mathrm{x}}^{\mathrm{GGA}} + E_{\mathrm{c}}^{\mathrm{LDA}} + E_{\mathrm{c}}^{\mathrm{nl}}, \tag{2.26}$$

where the non-local function takes the general form

$$E_{\mathrm{c}}^{\mathrm{nl}} = \int\int n(\mathbf{r})\phi(\mathbf{r},\mathbf{r'})n(\mathbf{r'})d\mathbf{r}d\mathbf{r'} \tag{2.27}$$

Here, $\phi(\mathbf{r},\mathbf{r'})$ represents an integration kernel that ensures the correct asymptotic $1/R^6$ dependence. Through the addition of this non-local correlation term, we can explicitly incorporate dispersion interactions determined from the electron density into our description. Examples of these functionals include vdW-DF [108], vdW-DF2 [109], rev-vdW-DF2 [110], and optB88-vdW [111].

An alternative route towards incorporating long-range effects involves augmenting the overall energy with a correction term,

$$E = E_{\mathrm{DFT}} + E_{\mathrm{disp}} \tag{2.28}$$

Here, E_{disp} represents a summation of pair-wise atomistic terms,

$$E_{\mathrm{disp}} = -\sum_{A<B}\left[s_6\,\frac{C_6^{AB}}{R_{AB}^6} f_{\mathrm{damp}}^{(6)}(R_{AB}) + s_8\,\frac{C_8^{AB}}{R_{AB}^8} f_{\mathrm{damp}}^{(8)}(R_{AB})\right] + \ ... \tag{2.29}$$

where R_{AB} gives the distance between species A and B, C_x^{AB} gives the appropriate dispersion coefficients acting between them (i.e., strength of the interaction), and f_{damp} is a function to prevent divergence at short range. The exact nature of these functions vary depending on the scheme used. In Grimme's D1 and D2 methods [112, 113], C_6^{AB} is predetermined from ionisation potentials and static polarisabilities [114]. In the D3 method [115], the value of C_6^{AB} and also C_8^{AB} changes according to the AB pairing and the hybridisation state of the species. In this way, we can incorporate geometric information into the determination of the dispersion correction. And finally, in the D4 method [116], both geometric and classically calculated charges inform the value of the dispersion correction. Beyond Grimme's correction, other schemes such as the Tkatchenko and Scheffler [117] as well as the exchange-hole dipole moment schemes [118] exist.

The work reported in this thesis has primarily made use of GGA functionals combined with Grimme's D3 corrections. This combination enables a good compromise between accuracy and efficiency, whilst still enabling treatment of long-range dispersion effects.

Practical DFT Calculations

The vast majority of calculations reported in this thesis were performed using the open-source CP2K software [119, 120]. This code is based on the Gaussian and Plane Waves (GPW) method [121], which reduces the computational overhead from calculating the Hartree component of the energy and from wavefunction orthogonalisation [119]. Under

this method, the electron density is described using two representations. In the first, the electron density is represented using localised Gaussian atomic orbitals,

$$n(\boldsymbol{r}) = \sum_{\mu\nu} P^{\mu\nu}\phi_\mu(\boldsymbol{r})\phi_\nu(\boldsymbol{r}) \tag{2.30}$$

where $P^{\mu\nu}$ gives the density matrix and $\phi_\mu(\boldsymbol{r})$ represents a contracted expansion of Gaussians. In the second, we utilise an auxiliary basis of plane waves to represent the density on a regular grid,

$$\tilde{n}(\boldsymbol{r}) = \frac{1}{\Omega}\sum_{\boldsymbol{G}} \tilde{n}(\boldsymbol{G}) \exp(i\boldsymbol{G}\cdot\boldsymbol{r}), \tag{2.31}$$

where Ω gives the cell dimensions and $\boldsymbol{G}$ gives the reciprocal lattice vectors. By transforming the basis to a plane-wave representation, we facilitate the Fast Fourier Transforms required to solve the Poisson equation and obtain the Hartree energy term. Computational efficiency is aided by the use of *pseudopotentials*, V^{PP}, which reproduce the effective influence of the core electron density interacting with the atomic nucleus. As such, we replace an all-electron problem with an effective valence-only problem. This is a reasonable approximation for core electrons, given that the most interesting chemistry is a result of the valence (Kohn-Sham) electrons. The GPW method, therefore, represents a computationally efficient route towards electronic structure predictions, thus enabling CP2K to treat extended, liquid-like and interfacial systems at minimal cost [119]. This efficiency underscores our choice in this methodology, though other codes such as VASP [122–125] (plane-wave orbitals with projector augmented-wave datasets) and FHI-aims (an all-electron, full-potential code) [126, 127] are available.

Having shown how to perform first-principles electronic structure calculations, we now demonstrate how to incorporate these into finite temperature dynamics.

Quantum forces, classical dynamics

In conventional AIMD, at each time t of a simulation, we use DFT to determine the ground-state potential energy surface of a system - these are known as 'on-the-fly' calculations. There exist three variations by which this is implemented in practical simulations: Ehrenfest molecular dynamics, Born-Oppenheimer molecular dynamics (BOMD) and Car-Parrinello molecular dynamics (CPMD) [128]. In Ehrenfest dynamics, the classical equations of motion are solved simultaneously with the time-dependent electronic Schrödinger equation, meaning that the electrons are treated strictly within a quantum framework (this is known as *intrinsic dynamics*). In BOMD, we make an approximation in restricting the wavefunction of the system to just the ground-state adiabatic form, Ψ_0, and solving the time-independent electronic Schrödinger equation for each δt at fixed nuclear coordinates. From these calculations, the Born-Oppenheimer potential energy surface is obtained, and the resulting BOMD equations of motion are written as

$$\begin{aligned} M_I\ddot{\mathbf{R}}_I(t) &= -\nabla_I \min\left\{ \langle\Psi_0|\hat{H}_e|\Psi_0\rangle \right\} \\ &= -\nabla_I \min\left\{E_{\mathrm{KS}}\right\}. \end{aligned} \tag{2.32}$$

where E_{KS} is the Kohn-Sham energy calculated in Eq. (2.19). In 1985, further approximations to this framework were made by R. Car and M. Parrinello by extending the classical Lagrangian of the system [22]. So as to avoid the costly iterations involved in solving for the BOMD energy, a fictitious time-dependence was introduced for the electronic orbitals, $\psi_i(t)$, such that they could be propagated using specialised orbital dynamics from minima to minima along the simulation trajectory [129]. The corresponding equations of motion are

$$\begin{aligned} M_I\ddot{\mathbf{R}}_I(t) &= -\frac{\delta}{\delta\mathbf{R}_I(t)}\left\{ \langle\Psi_0|\hat{H}_e|\Psi_0\rangle \right\} + \frac{\delta}{\delta\mathbf{R}_I(t)}\{\text{constraints}\} \\ &= -\nabla_I E_{\mathrm{KS}} \end{aligned} \tag{2.33}$$

$$\begin{aligned} \mu\ddot{\psi}_i(\mathbf{r},t) &= -\frac{\delta}{\delta\psi_i^*(\mathbf{r},t)}\left\{ \langle\Psi_0|\hat{H}_e|\Psi_0\rangle \right\} + \frac{\delta}{\delta\psi_i^*(\mathbf{r},t)}\{\text{constraints}\} \\ &= -\frac{\delta E_{\mathrm{KS}}}{\delta\psi_i^*(\mathbf{r},t)} + \sum_j \Lambda_{ij}\psi_j(\mathbf{r},t), \end{aligned} \tag{2.34}$$

where μ is a fictitious mass that dictates the orbital dynamics and Λ is a Lagrange multiplier matrix that ensures orthonormality in the orbitals. For the last several decades, on account of its reduced computational costs, CPMD has been the choice method for performing AIMD [130]; however, citing algorithmic improvements and hardware development, BOMD now forms the basis of most MD software packages.

Equations $(2.32 - 2.34)$ describe the salient features of AIMD that drive our reactive, quantum-level molecular simulations. CPMD and BOMD are powerful tools that, over the last four decades, have enabled a plethora of interesting and seminal studies. These include: obtaining a quantum-level description of liquid water [131]; studying phase transitions in substances such as HBr-I [132] and H_2S [133]; performing 'wet chemistry' *in silico*, looking at the formation of sulfuric acid [134] to studying the decomposition of HCl in water [135]; simulating reactions and conditions pre-dating life on Earth as a virtual replica of the Urey-Miller experiment [136]; and many other studies, for which the reader is directed to Ref. [128]. In this respect, AIMD has been invaluable for studying the reactive and dynamical properties of small/medium-sized systems; however, large molecular systems and long simulation times prove intractable to *ab initio* treatment owing to the costly nature of iteratively solving for E at each time step. As computing power increases and we move to larger and more intricate systems of molecules, the computational demands of AIMD present a barrier to future work in this area. We require an alternative framework for these new systems and studies. A solution could possibly be found in the form of machine learning.

2.3 Machine-learned interatomic potentials

Over the last couple of years, machine learning has transformed scientific investigation, with data-driven research now forming the 'fourth paradigm' of science alongside empirical, theoretical, and computational approaches [137]. In the field of molecular simulations, machine-learned interatomic potentials (MLIPs) have greatly expanded the capabilities of MD simulations, enabling quantum-level simulations for a fraction of the traditional

computational cost. With the recent explosion of machine learning, there now exists a myriad of different MLIPs, each with its own advantages and unique features. These include neural-network models such as Behler–Parrinello high-dimensional neural network potentials [138] and DeePMD-type models [139]; kernel-based regression models such as Gaussian approximation potentials (GAP) [140]; and equivariant graph neural networks such as MACE [141], NequIP [142], and Allegro [143]. The reader is directed to the following reviews for explicit detail on these variants [36–38, 144, 145].

All MLIP methods operate on the principle that we can take the atomic coordinates of a system and map them onto an underlying potential energy surface. In formulating these architectures, it is crucial that they adhere to the symmetries of the underlying potential energy surface. In general, all observables must obey the following constraint [38]:

$$\phi\{Q\sigma_i\} = Q\phi\{\sigma_i\}, \tag{2.35}$$

where σ_i give the atomic configuration, Q is some symmetry operation, and $\phi\{...\}$ gives the output of the MLIP (e.g., energy, forces, dipole moment) [38]. Equation 2.35 expresses the equivariance condition of MLIPs with respect to Q: transforming the input and then applying the MLIP should be equivalent to transforming just the MLIP output. In the case of scalar quantities such as the total energy, Eq. 2.35 trivially reduces to the invariant form. For example, if Q represents a rotation, then the total energy should be unaffected by the operation. This contrasts with vectors or higher-order tensorial properties, which should transform in an equivariant manner. Working within a three-dimensional Euclidean environment, we are principally concerned with translations, rotations, reflections (including inversion), and the permutation of identical atoms.

The work presented in this thesis makes use of two specific MLIP architectures: 'high-dimensional' or 'Behler-Parrinello' neural-network potentials (HDNNPs/BPNNPs), one of the first general-purpose models used across a range of different atomistic systems [138]; and MACE potentials, which following their inception in 2022, have quickly become the preferred method for condensed-phase modelling simulations [141]. In the following section,

we describe these two architectures and consider future directions in this ever-changing field.

High-dimensional neural network potentials

First proposed by Behler and Parrinello in 2007 [138], HD-NNPs exploit the locality of interatomic interactions and use a series of feed-forward neural networks to express the potential energy of a system as a sum of local contributions. A typical feed-forward architecture is shown in Fig. 2.1a. At the input level of each network, atomic coordinates are taken and encoded in a specific mathematical format (G) that is readable by the algorithm and that displays a threefold invariance with respect to translation, rotation, and the permutation of identical atoms. These transformed coordinates are connected to the output energy of the system through use of 'nodes', y, where each node in layer i is connected to all nodes in the previous layer $(i-1)$ via a series of weights $a^{i-1,i}$ and through use of activation functions f^i (e.g., the hyperbolic tangent) that 'activate' the $i-1$ nodes. The value y_j^i of node j is then calculated via

$$y_j^i = f_j^i\left(b_j^i + \sum_{k=1}^{n_{i-1}} a_{k,j}^{i-1,i} \cdot y_k^{i-1}\right) \tag{2.36}$$

where b is a bias term, and k runs over the $i-1$ nodes of the preceding layer. The model parameters (i.e., the weights and biasing terms for each layer) are learned from the reference data, usually by employing standard gradient-based optimisers to minimise a loss function of the form,

$$\chi = \frac{1}{N}\sum_{i=1}^{N}(y_i - \hat{y}_i)^2, \tag{2.37}$$

where y_i is the *ab initio* reference energy and $\hat{y}_i$ is the predicted model energy. For HD-NNPs, extended Kalman-filter–type optimisers are often employed to obtain the model weights [146]. Upon completion of the training, these parameters are fixed, and the potential can be used to generate the necessary PESs for driving NNP-MD simulations.

A crucial component of HD-NNPs lies in their scalability, which arises from use of multiple NNs, with each NN corresponding to a different local atomic environment. The

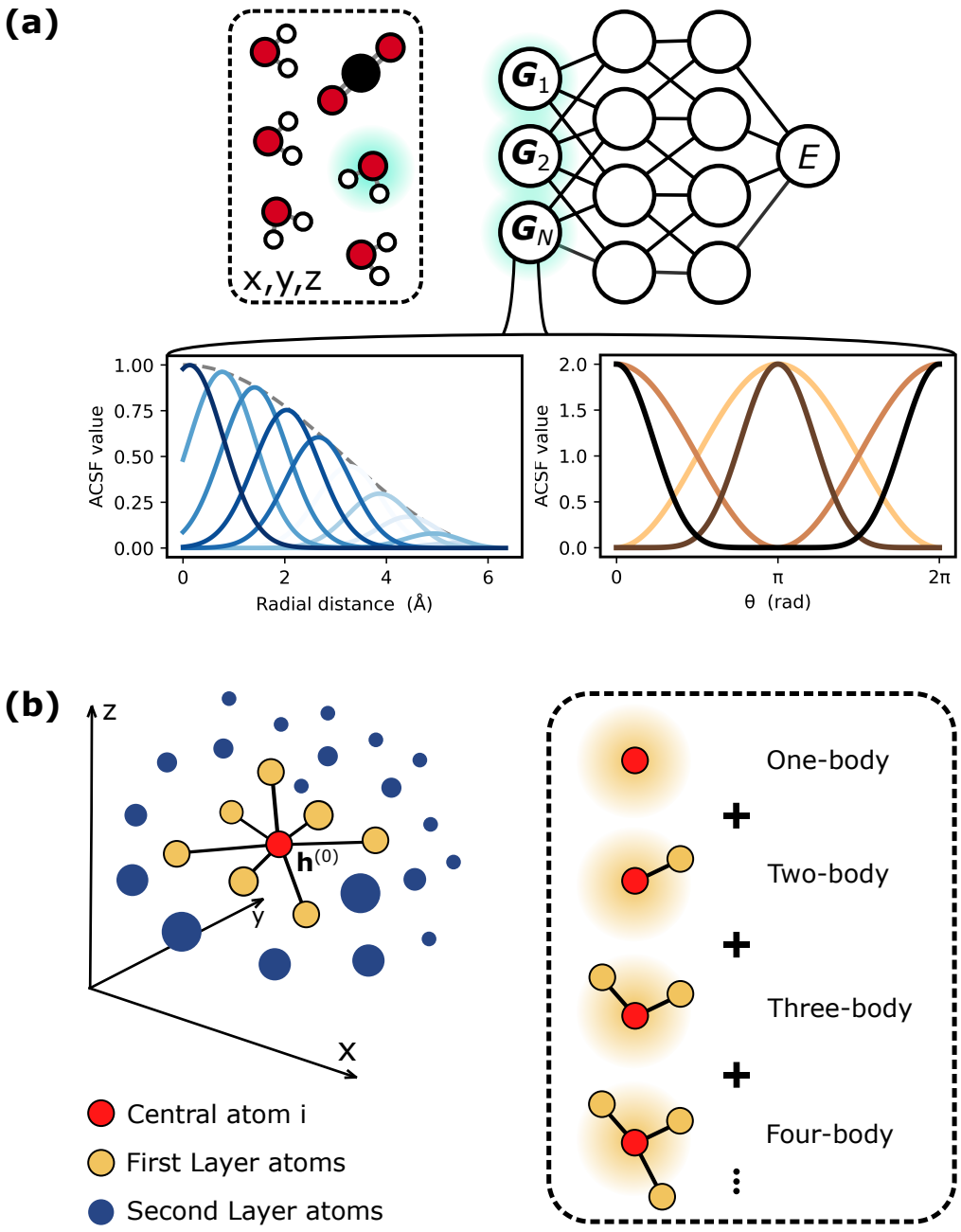

Fig. 2.1 Overview of machine-learning methods employed in this work. **(a)** Summary of the high-dimensional neural network potential (HD-NNP) architecture. Atomic coordinates are passed into a shallow, feed-forward neural network and mapped to a potential energy, E. The coordinates are encoded using atom-centered symmetry functions, $\boldsymbol{G}_N$, which are expressed using both a radial (left) and angular (right) basis. **(b)** Summary of the MACE message-passing architecture. Atoms (nodes) are embedded in a 3D graph, with edges (black lines) representing the connectivities between these atoms. A complete, high-body-order polynomial basis is constructed by summing the different body order terms (from the first-layer atoms) within a specific radius. Message passing allows us to propagate this information to encompass second layer atoms, thereby also extending the effective receptive field.

total potential energy can be calculated as a sum of the local contributions,

$$E_{\text{short}} = \sum_{k=1}^{N_{\text{elem}}} \sum_{i=1}^{N_{\text{atom}}^{k}} E_i^k \tag{2.38}$$

where k runs over the element type and i over the atoms. The local contribution, E_i^k, can be deduced through summation of interatomic interactions within a specified cutoff (usually on the order of 6-10 Å); in the absence of significant electrostatic or non-local contributions, this is a reasonable approximation for obtaining accurate PESs. Where each atom is assigned its own (element-specific) neural network, increasing the number of atoms in a simulation requires that we just increase the number of networks and account for the additional E_i^k values in the summation of (2.38). Therefore, neural networks trained on data of a particular system size can scale to simulate systems of varying composition and size.

Another important aspect of these HD-NNPs lies in their choice of chemical descriptor. HD-NNPs usually employ a systematic set of radial and angular functions known as atom-centred symmetry functions (ACSFs) [147]. For a central atom i, the radial contributions for each element-element pairing are usually calculated as a sum of Gaussians surrounding the centre,

$$G_{i,\mu}^{\text{rad}} = \sum_{j \neq i}^{N_{\text{atom}} \in R_{\text{c}}} \mathrm{e}^{-\nu_\mu (R_{ij} - R_{\text{s},\mu})^2} f_c(R_{ij}) \tag{2.39}$$

where R_{ij} gives the internuclear separation between central atom i and neighbour j, $f_c(R_{ij})$ is an arbitrary cutoff function dictating the length at which truncation occurs, and $R_{\text{s},\mu}$ and ν_μ are the Gaussian parameters, each combination of which constitutes a different radial symmetry function, μ. For $f_c(R_{ij})$, the cutoff distance R_{c} is chosen to be large enough to capture the semi-local environment of each atom but small enough to mitigate excessive computational costs; in practice, this often means setting $R_{\text{c}} \approx 6$ Å. For a chosen R_{c}, we then tailor R_{s} and ν values to ensure sufficient radial coverage of the local environment (see radial ACSF plot shown in Figure 2.1a). An additional angular

contribution can also be calculated according to

$$G_{i,\mu}^{\text{ang}} = 2^{1-\eta_\mu} \sum_{i,j,k} (1 + \lambda_\mu \cos\theta_{ijk})^{\eta_\mu} \mathrm{e}^{-\nu_\mu (R_{ij}^2 + R_{ik}^2 + R_{jk}^2)} \, f_c(R_{ij}) \, f_c(R_{ik}) \, f_c(R_{jk}) \tag{2.40}$$

where θ_{ijk} is the angle between atom i and neighbours j and k, R gives the internuclear separations, $f_c(R)$ the cutoff functions, and ν_μ, λ_μ, and η_μ control the shape of the symmetry function, each unique combination of which is denoted by μ. Similar to $G_{i,\mu}^{\text{rad}}$, the various angular functions are chosen to ensure our descriptor space sufficiently covers the spherical near-atom region (see angular ACSF plot shown in Figure 2.1a). Equations 2.39 and 2.40 are the most common forms of $G_{i,\mu}^{\text{rad}}$ and $G_{i,\mu}^{\text{ang}}$, and their combination yields a representation capable of distinguishing between differing local atomic environments. A drawback to ACSFs, however, lies in their poor scaling with the number of elements of a system. In Eq. 2.39, $G_{i,\mu}^{\text{rad}}$ is defined for each element pairing, whilst in Eq. 2.40, $G_{i,\mu}^{\text{ang}}$ is defined for each element triplet. Accordingly, the computational cost scales as $\mathcal{O}(S^2)$ and $\mathcal{O}(S^3)$ with number of elements S for the radial and angular functions, respectively. In practice, HD-NNPs can run relatively efficiently for systems where $S < 5$.

MACE potentials

For over a decade, HDNNPs (alongside GAP potentials [140]) proved to be the method of choice for performing MLIP-MD [36, 37]. Despite their efficacy, certain limitations in their architectures precluded the treatment of some of the more complex systems and processes. As discussed above, this was particularly true for systems containing several different species, with computational costs rising exorbitantly beyond 5 or so chemical elements. MACE potentials, an extension of the atomic cluster expansion formalism introduced in 2019 [148], represent the next step in the development and application of MLIPs. Since their introduction in 2022 [141, 149], MACE potentials (alongside similar codes such as NequIP [142] and GRACE [150]) have quickly replaced HDNNPs and GAP potentials as the paradigmatic atomistic machine learning potential. Like with HDNNPs, MACE potentials provide a nonlinear mapping between the atomic coordinates of a system and

the potential energy of the system. Under the MACE formalism, the system is embedded in a 3D graph/tensorial network, where the nodes are analogous to atoms, and the edges represent connectivities between these atoms. Each node or atom i possesses a 'hidden state', $\boldsymbol{h}_i^{(s)}$, which contains the embedded features of that atom (for $\boldsymbol{h}_i^{(0)}$, this is just an embedding of the chemical elements). These features are updated through 'message passing' iterations (s), in which information from neighbouring nodes is passed to that atom and vice versa. After a certain number of message passes, S, the updated node features are mapped onto atomic site energies, E_i, which are then summed to give the total system energy. These various features are explained in more detail below.

One of the key components of the MACE architecture is the complete high-body-order polynomial basis (based on the ACE formalism developed by R. Drautz [148]) used to represent semi-local chemical environments. Under this graph representation, atoms are represented by nodes in three-dimensional space. The features of node/atom i are represented by $h_{i,klm}^{(s)}$ and indexed according to the channel index k, the angular momentum l, and the magnetic index m. For the zeroth layer (initialisation), the chemical elements of a system are embedded according to,

$$h_{i,k00}^{(0)} = \sum_z W_{kz}\delta_{zz_i}, \tag{2.41}$$

where z_i is the atomic number at node i, k gives the channel index, and W_{kz} are the learnable parameters represented by a matrix of size $n_{\text{channels}} \times n_{\text{elements}}$.[4] To an approximation, we can consider δ_{zz_i} to be a one-hot vector encoding the chemical identity, e.g., H = [1,0,0,...], He=[0,1,0,...]. The indices '00' for $h_{i,k00}^{(0)}$ correspond to $l = m = 0$ for model initialisation, showing that we are dealing with invariant features for the zeroth layer.

At the start of each layer s, we perform an initial mixing of the channels for each combination of l and m,

$$\bar{h}_{i,klm}^{(s)} = \sum_{\tilde{k}}^{K} W_{k\tilde{k}l} h_{i,\tilde{k}lm}^{(s)}. \tag{2.42}$$

[4]For this section, all learnable parameters are represented by W, with each instance of W representing a different learnable parameter block.

where $\tilde{k}$ is a dummy variable used for summing over K channels. Following this, we combine the features of each of the neighbouring nodes with displacement vectors connecting them to the central atom i. The displacement vectors are obtained by first computing the Bessel functions, j_0^n, for each node pairing according to,

$$j_0^n(r_{ij}) = \sqrt{\frac{2}{r_{\text{cut}}}} \frac{\sin\left(n\pi \frac{r_{ij}}{r_{\text{cut}}}\right)}{r_{ij}} f_{\text{cut}}(r_{ij}) \tag{2.43}$$

where r_{ij} is the interatomic distance, r_{cut} if a specified cutoff distance, and $f_{\text{cut}}(r_{ij})$ is a smooth cutoff function that goes to zero at $r_{ij} = r_{\text{cut}}$. We construct these Bessel functions for wavenumbers n up to some small maximum, following which they are passed into a multi-layer perceptron (MLP, not to be confused with MLIPs) to obtain learned radial coefficients,

$$R_{k\eta_1 l_1 l_2 l_3}(r_{ij}) = \text{MLP}(\{j_0^n(r_{ij})\}_n). \tag{2.44}$$

There are many outputs for Eq. 2.44, each indexed by η_1, l_1, l_2, l_3. Here, l_d labels the different types of angular momenta,[5] while η_1 accounts for the multiplicity of different couplings. The large number of outputs function as separate degrees of freedom.

Using the radial coefficients defined in Eq. 2.44 and the node features defined in Eq. 2.42, we can form a one-particle basis through combination with spherical harmonics, Y, and Clebsch–Gordan coefficients C,

$$\phi^{(s)}_{ij,k\eta_1 l_3 m_3} = \sum_{l_1 l_2 m_1 m_2} C^{l_3 m_3}_{\eta_1 l_1 m_1 l_2 m_2} \, R^{(s)}_{k\eta_1 l_1 l_2 l_3}(r_{ij}) \, Y^{l_1}_{m_1}(\hat{\boldsymbol{r}}_{ij}) \, \overline{h}^{(s)}_{j,kl_2m_2} \tag{2.45}$$

This basis is labelled as being 'one-particle' as it depends only on a single neighbour, j, what that neighbour is, and where it lies relative to the central atom i. The set of spherical harmonics encodes angular information into the basis, whilst the Clebsch–Gordan coefficients ensure that the one-particle basis maintains rotational invariance/equivariance. $\phi^{(s)}$ constitutes the atom-neighbour building blocks from which the many-body ACE basis functions are constructed. We can sum $\phi^{(s)}$ over all atoms in the neighbourhood to yield

[5] $l_1 \rightarrow$ from spherical harmonics, $l_2 \rightarrow$ from node features, $l_3 \rightarrow$ resulting edge feature.

the atomic basis,

$$A^{(s)}_{i,kl_3m_3} = \sum_{\tilde{k},\eta_1} W^{(s)}_{k\tilde{k}\eta_1 l_3} \sum_{j\in N(i)} \phi^{(s)}_{ij,\tilde{k}\eta_1 l_3 m_3}, \tag{2.46}$$

where $A^{(s)}_{i,kl_3m_3}$ is permutationally invariant over the neighbourhood atoms. Similar to the ACE formalism [148], a product basis $\boldsymbol{A}^{(s),\nu}_i$ can be constructed by taking the tensor product of the atomic basis with itself ν times,

$$\boldsymbol{A}^{(s),\nu}_{i,k\boldsymbol{lm}} = \prod_{\xi=1}^{\nu} A^{(s)}_{i,kl_\xi m_\xi} \tag{2.47}$$

Here, ξ runs over the l_3 and m_3 variables seen in Eq. 2.46, while ν controls the maximum body order. The product basis $\boldsymbol{A}^{(s),\nu}_{i,k\boldsymbol{lm}}$ represents the key innovation of the ACE descriptor, allowing us to construct high-body-order features without explicitly summing over atom tuples [151]. A fully contracted and rotationally invariant/equivariant basis is constructed using the generalised Clebsch–Gordan coefficient,

$$\boldsymbol{B}^{(s),\nu}_{i,\eta_\nu kLM} = \sum_{\boldsymbol{lm}} C^{LM}_{\eta_\nu \boldsymbol{lm}} \boldsymbol{A}^{(s),\nu}_{i,k\boldsymbol{lm}}, \tag{2.48}$$

where η_ν enumerates the different ways of arriving at a particular symmetry, and L and M denote the total angular momentum after Clebsch–Gordan coupling. The angular momenta features are truncated at a maximum order $L_{\max}$,[6] which determines the trade-off between accuracy and cost for running a MACE model. Finally, we can construct a message m_i as a linear combination of different many-body features of the neighbours,

$$m^{(s)}_{i,kLM} = \sum_{\nu} \sum_{\eta_\nu} W^{(s),\nu}_{z_i\eta_\nu kL} \, \boldsymbol{B}^{(s),\nu}_{i,\eta_\nu kLM} \tag{2.49}$$

[6] $L_{\max} = 0$: invariant features only; $L_{\max} = 1$: include equivariant features (vectors); $L_{\max} = 2$: include rank-2 tensors.

These messages are added to the nodes features of the previous layer to obtain the updated features according to,

$$h_{i,kLM}^{(s+1)} = \sum_{\tilde{k}} W_{kL,\tilde{k}}^{(s)} m_{i\tilde{k}LM}^{(s)} \; + \; \sum_{\tilde{k}} W_{kz_iL,\tilde{k}}^{(s)} h_{i,\tilde{k}LM}^{(s)} \tag{2.50}$$

Taken together, these node features constitute the updated hidden state $\boldsymbol{h}_i^{(s)}$ of node i. In practice, we usually employ two rounds of message passing, $S = 2$. The energy can be read out from the rotationally invariant parts of the node features,

$$E_i = \sum_{s=1}^{S} R^{(s)}(\boldsymbol{h}_{i,00}^{(s)}) \tag{2.51}$$

where $R^{(s)}$ is a simple linear mapping for $s < S$ and a shallow neural network for $s = S$. In the usual manner, the atom-wise forces can then be obtained through differentiation of the potential energy

$$\boldsymbol{F} = -\nabla \sum_i E_i. \tag{2.52}$$

MACE potentials break from more traditional MLIP variants in combining a systematic and complete local representation with equivariant message passing. Further, embedding the chemical elements into the local descriptors (i.e., $\boldsymbol{h}_i^{(0)}$) mitigates scaling with respect to the element count, thereby enabling multi-element simulations more naturally than earlier descriptor-based methods. Testing of the MACE architecture has yielded impressive results in terms of the accuracy, efficiency, and generalisability [149]. Testament to the efficacy of these potentials is the number of research groups (including our own) who have now taken up MACE potentials as the preferred means of performing MLIP-MD. Many of the non-learnable parameters detailed in the above equations can be set by the user; for example, one can set the radial cutoff r_{cut} (often 5 or 6 Å), the number of embedding channels k (usually 64-128), the highest permitted order L_{max} (usually set to 1), and the total number of layers S. In addition, one can control and optimise the model training procedure. Gradient-descent-based optimisers, such as AMSGrad [152], can be used to

alter the model weights W so as to minimise the overall loss function,

$$\mathcal{L} = \frac{\lambda_E}{B}\sum_{b=1}^{B}\left(\frac{E_b - \hat{E}_b}{N_b}\right)^2 + \frac{\lambda_F}{3B}\sum_{b=1}^{B}\sum_{i_b,\alpha=1}^{N_b,3}\left(-\frac{\partial E_b}{\partial r_{i_b,\alpha}} - \hat{F}_{i_b,\alpha}\right)^2. \tag{2.53}$$

where, for configuration b of batch B, $\hat{E}_b$ and $\hat{F}_{i_b,\alpha}$ give the reference *ab initio* energies and forces, whilst E_b and $\partial E_b/\partial r_{i_b,\alpha}$ give the predicted energies and forces from MACE. The parameters λ_E and λ_F are often set by the user and are used to control the relative weight of energy to force loss. It has been shown that keeping $\lambda_E < \lambda_F$ for most of the training (roughly 60 %) before switching to a larger λ_E (with reduced learning rate) helps to minimise loss for both the energies and forces [149].

Current developments in MLIPs

Since the first use of MLIPs in 1995 [153], to the creation of HDNNPs in 2007 [138] and GAP potentials in 2010 [140], to the recent introduction of MACE potentials in 2022 [141], the field of machine learning aided atomistic simulations is undergoing constant change and development. Beyond further improvements to the base MLIP architecture, there currently exist two main branches of development for this technology: the incorporation of long-range effects into the model description; and the generalisation of potentials to treat vast swathes of chemical space - these are so-called 'foundation models'.

In the first of these endeavours, we note that many of the base MLIP descriptors are incapable of describing long-range effects. The use of some form of cutoff function, f_c, limits our description to no more than ~ 10 Å surrounding the central atom, meaning that electrostatics and non-local influences are missed from the configuration embedding. This can prove important for the treatment of charges as well as modelling inhomogeneous molecular environments [42, 154, 155]. A number of schemes have been developed to try to rectify this. Many of these are analogous to the dispersion correction schemes discussed earlier for DFT,

$$E = E_{\mathrm{SR}} + E_{\mathrm{LR}} \tag{2.54}$$

In third generation models, the short- and long-range contributions to the potential energy are calculated separately using distinct neural network models: E_{SR} is obtained from standard, short-range MLIPs, whilst the LR component is obtained from a model trained to reproduce atomic charges from the local environment. Ewald summation can then be used to obtain E_{LR}. Third generation models have been shown to work well for a number of systems [156, 157]; however, the short-sighted nature of both the SR and LR models precludes treatment of non-local effects (e.g., distant charge transfer processes beyond two local radii $2R_{\mathrm{c}} \sim$ 10-12 Å). Fourth generation models can further improve the model description through some charge equilibration scheme [158]. In this manner, both E_{SR} and E_{LR} now contain non-local charge information. Both third and fourth generation models have seen application in HD-NNP architecture, and efforts are currently underway to extend these schemes to MACE and other MPNN potentials.

Concerning the second avenue of MLIP development, we note that recent improvements in MLIP architectures have uncovered the possibility for creating generalisable 'foundation models'. These MLIPs - applicable across vast swathes of chemical compound space - open the door to 'out-of-the-box' quantum-level simulations, therefore replacing the need for either cumbersome *ab initio* simulations or inaccurate FF descriptions. Previous attempts at generating such potentials had been confined to specific regions of chemical space, e.g., the GAP20 potential generated for carbon-like structures [159]. However, nowadays, there exists a whole multitude of foundation models for materials modelling, e.g., MACE-MP-0 [160], MACEOFF [161], GNoME [162], and MatterSim [163]. Whilst there is still some way to go concerning the underlying model architectures and the composition and completeness of their training datasets,[7] these foundation models have shown excellent performance and generalisability beyond their training data, and it is the hope of this field that we can approach GGA-level accuracy within the next several years.

[7]Overall model performance and capabilities will depend on the size, quality, and composition of the training dataset. Does the dataset contain non-equilibrium structures, a prerequisite for probing chemical reactions? Does the dataset contain spin-polarised data, necessary for modelling radical species? The MACE-MP0 model, as an example, is trained on the MPtrj dataset, which consists of both out-of-equilibrium and spin-polarised structures.

2.4 Free energy calculations

Undoubtedly, the recent development of MLIP methods has greatly expanded both the length and temporal scales accessible to quantum-level atomistic simulations. Despite this, however, many processes, events, and measurements remain beyond the scope of conventional MD simulations. These 'rare events', which often require surmounting energy barriers many times greater than $k_{\mathrm{B}}T$, would require many millions or even billions of simulation time steps to observe under normal MD conditions. There exist a number of techniques - known as *enhanced sampling* methods - that can allow us to accelerate the sampling of less accessible regions of the potential energy surface. In this section, we describe the various enhanced sampling schemes employed in this work.

Metadynamics

As a chemist by training, I find the most fascinating parts of my work to be the study of chemical reactions. In this field, we often characterise such processes through the idea of (Gibbs/Helmholtz) free energy: reactants and products are located at minima in the free energy surface (FES), whilst separating these basins are barriers capped by transition state structures (saddle points in the FES). Depending on the size of the energy barriers, often we may only sample one small region of the FES without ever exploring some of the more varied and exotic regimes. To help with escaping free energy minima, we can augment the underlying potential energy surface to penalise the free energy basins and promote sampling of the more energetically unfavourable regions. In metadynamics, we do this by implementing a history-dependent potential term, V_{bias}, that 'fills' free energy holes in a subspace of the total system configuration space,

$$H = T + U + V_{\mathrm{bias}} \tag{2.55}$$

This subspace is defined by a low-dimensional set of *collective variables* (CVs), which capture the system's slow modes and closely approximate the reaction coordinate for the process of interest [164]. By filling minima in this CV space, we force the system to

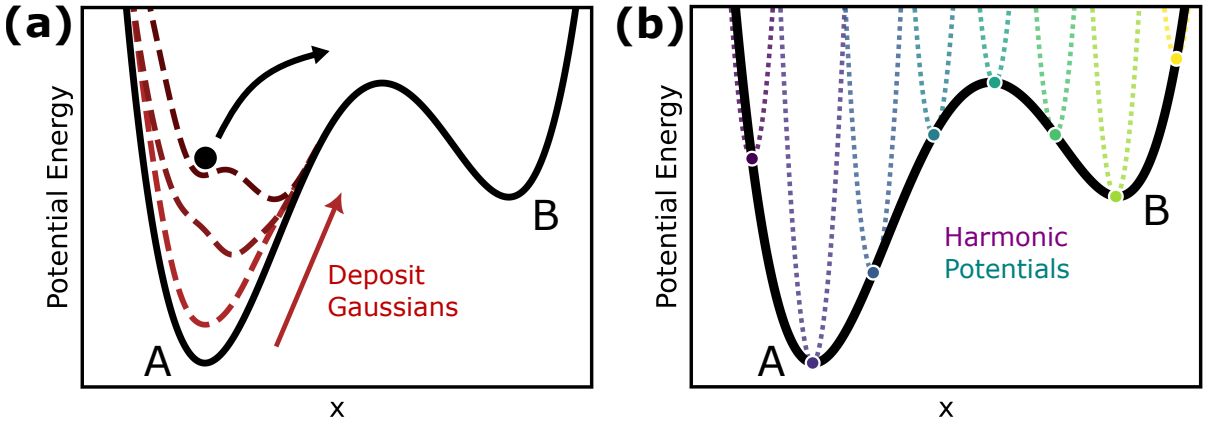

Fig. 2.2 Overview of the enhanced sampling methods employed in this work. **(a)** Using metadynamics to sample reactive processes. Plot shows an underlying potential energy surface (black) containing a reactant (A) and a product (B) basin plotted as a function of some reaction coordinate x. When performing metadynamics, Gaussians are periodically deposited in a history-dependent manner (i.e., at points in x space already visited by the system), gradually augmenting the potential energy surface (coloured surfaces) and promoting the transition to state B. In the limit of large timescales, the free energy surface can be recovered by inverting the bias potential formed by summing Gaussians. **(b)** Using umbrella integration to sample reactive processes. In this scheme, harmonic restraints are deposited along the coordinate connecting states A and B. At each point, we perform distinct MD simulations to gauge the variation in x. Using integration, we can then extract the underlying free energy of the system.

explore high-energy regions of the FES, thus accelerating our sampling of the approximate reaction coordinate.

Suppose we have a system with coordinates q and underlying potential energy surface $U(q)$. We can define a subset of q, such that a certain process may only be described by a small number of parameters, $\xi(q) = (\xi_1(q), \xi_2(q), ..., \xi_M(q))$.[8] In an unbiased simulation, one can extract the free energy as a function of $\xi(q)$ through the following relation:

$$A(\xi) = -k_{\mathrm{B}}T \lim_{t\to\infty} \ln N(\xi, t) \tag{2.56}$$

where T is the temperature, and $N(\xi, t) = \int_0^t \delta\Big(\xi - \xi(q(t'))\Big)\, dt'$ is a histogram of ξ obtained over simulation time t. To accelerate this process, we bias the dynamics of the system

[8]For the following section, we use ξ to represent the set of possible collective variables, acknowledging the fact that ξ can refer to either a single variable or a multidimensional CV space. The number and complexity of these CVs ultimately depends on the process we are studying and the questions we want to answer. For most purposes, M is limited to either one or two CVs such that we can visualise the free energy surfaces as either 2D or 3D plots.

by incorporating a history-dependent potential constructed from the regular depositing of Gaussian kernels in CV space. The idea here is that we promote sampling of the higher-energy regions of the free energy surface by gradually penalising the lower-energy basins. The form of V_{bias} is given by:

$$V_{\text{bias}}(\xi, t) = \sum_{k\tau<t} W(k\tau) \exp\left(-\sum_{i=1}^{M} \frac{[\xi_i - \xi_i(q(k\tau))]^2}{2\sigma_i^2}\right) \tag{2.57}$$

where τ is the rate of deposition of the Gaussians, k the number of Gaussians, σ gives the width, and W defines the height of the Gaussians. The appropriate values for each parameter can be determined by running unbiased MD simulations and analysing CV fluctuations and relaxation times. In the original implementation of metadynamics, the Gaussian height W is fixed at W_0 [165]. This often led to fluctuating estimates of the free energy, thus hampering efforts to determine the convergence (or not) of a simulation run. To help with this, a 'well-tempered' version was introduced in which W was altered during the course of a run [166],

$$W(k\tau) = W_0 \exp\left(\frac{-V_{\text{bias}}(\xi(q(k\tau)), k\tau)}{k_{\text{B}}\Delta T}\right) \tag{2.58}$$

where W_0 is the initial Gaussian height, and ΔT is the 'bias temperature' of the simulation. We can relate this temperature to the input parameter γ through $\Delta T = (\gamma - 1)T$. Known as the 'bias factor', γ represents the ratio between the CV temperature $(T + \Delta T)$ and the system temperature (T) and ultimately controls the rate of exploration of the potential energy surface; larger γ leads to faster barrier crossings and a more aggressive sampling of the free energy surface; smaller γ promotes more stable dynamics and is less sensitive to sub-optimal CVs. Using either ΔT or γ, we can obtain the free energy at ξ using the following relation

$$V_{\text{bias}}(\xi, t \to \infty) = -\frac{\Delta T}{T + \Delta T} A(\xi) + C = -(1 - \gamma)A(\xi) + C \tag{2.59}$$

In this way, in the limit of long timescales, metadynamics can be used to obtain the converged free energy as a function of the underlying collective variable(s), $A(\xi)$ [167].

In Chapter 3, we utilise this method for understanding the hydration reaction of CO_2 with water under various conditions. Naturally, this method assumes a reasonable choice of ξ such that states of interest are clearly separable within the ξ subspace. Further, the mathematical form of ξ should be continuous, such that we can obtain biasing forces according to

$$\frac{\partial V_{\text{bias}}}{\partial q_{j\alpha}} = \frac{\partial V_{\text{bias}}}{\partial \xi} \frac{\partial \xi}{\partial q_{j\alpha}}. \tag{2.60}$$

where $q_{j\alpha}$ gives the $\alpha \in \{x, y, z\}$ component of atom j. A commonly used collective variable is the coordination number (s_{AB}), which calculates the number of contacts that exist between two atoms groups, A and B. Coordination numbers are commonly defined as:

$$s_{AB} = \sum_{i \in A} \sum_{j \in B} C_{ij}, \tag{2.61}$$

where we can define C_{ij} to be,

$$C_{ij} = \frac{1 - \left(\dfrac{r_{\text{ij}} - d_0}{r_0} \right)^n}{1 - \left(\dfrac{r_{\text{ij}} - d_0}{r_0} \right)^m}. \tag{2.62}$$

Here, r_{ij} is the distance between atoms i and j (where $i \in A$ and $j \in B$), r_0 is a representative reference distance, and d_0, n, and m are parameters that control the offset and stiffness of s_{AB}. In practice, we can determine the most appropriate parameters for s_{AB} by simulating the stable (and metastable) states of a system under bias-free conditions. Parameters can be chosen to give physically meaningful coordination values (e.g., integer values for stable equilibrium states) and to ensure the reactants and products are clearly separable in s_{AB}. From these bias-free simulations, one may also determine the relevant metadynamics parameters to be used during enhanced sampling. Providing a suitable choice of these various parameters, well-tempered metadynamics offers a straightforward means of calculating equilibrium free energy differences, ΔA. This has been employed

towards the study of nucleation events [168, 169], phase transitions [170], and reactions under both gaseous and solvated conditions [171, 172]; the reader is directed to Ref. [173] for a review of these methods. Metadynamics can also be extended towards studying the kinetics of a physicochemical process [174, 175]. These schemes operate on the principle that, providing the rate of Gaussian deposition is slower than the time spent in a transition region, we can preserve the unbiased sequence of state-to-state transitions, thereby accessing unbiased rate information. This has been utilised towards modelling the rates and pathways of protein–ligand binding and unbinding [176].

Umbrella Sampling

Whilst practical and easy to use, metadynamics can sometimes suffer from inefficient FES exploration, visiting regions of CV space that ultimately hold little relevance to our simulations and to the questions we would like to answer. A more targeted enhanced sampling approach can be used instead: *umbrella sampling* [177]. Umbrella sampling is a stratified sampling approach whereby a system is simulated using biased 'windows' along a chosen collective variable ξ. In each window, a harmonic restraint is used to confine sampling to a particular region of CV space. From these simulations, we can obtain biased samples and their corresponding distributions, $P_i^{\mathrm{b}}(\xi)$, from which the free energy is calculated as a post-processing step.

To derive the salient umbrella equations, we first start with the bridge relation shown in Eq. 2.8. From this, one can show that the free energy difference between states A and B can be obtained via,

$$\Delta A_{\mathrm{A}\to\mathrm{B}} = \int_{\xi_{\mathrm{A}}}^{\xi_{\mathrm{B}}} \langle \frac{\partial U}{\partial \xi} \rangle d\xi' = \int_{\xi_{\mathrm{A}}}^{\xi_{\mathrm{B}}} \langle F_c \rangle d\xi' \tag{2.63}$$

where ξ gives the reaction coordinate, and F_c is a constraining force. In this way, we calculate the change in free energy $\Delta A_{\mathrm{A}\to\mathrm{B}}$ by integrating over the canonical average of F_c. In thermodynamic integration, F_c arises from fixed constraints imposed on the value of ξ [178]. In umbrella sampling, we instead *restrain* ξ at each window i using a quadratic

potential term,

$$w_i(\xi) = \frac{1}{2}\kappa(\xi - \xi_i)^2 \tag{2.64}$$

The unbiased free energy, A_i^{u}, is then obtained by considering the distribution of ξ according to,

$$A_i^{\mathrm{u}} = -\frac{1}{\beta}\ln P_i^{\mathrm{b}}(\xi) - w_i(\xi) + F_i \tag{2.65}$$

where $P_i^{\mathrm{b}}(\xi)$ gives the probability of ξ, and F_i appears as an unknown constant.

Eq. 2.65 shows how US can be used to calculate the free energy A_i^{u} of a window from knowledge of the biased probability distribution and the harmonic biasing potential. In practice, however, A_i^{u} is defined only up to an additive constant F_i, which motivates working instead with estimators that avoid explicit dependence on this unknown offset. For example, in *umbrella integration*, rather than evaluating A_i^{u} directly, one can instead estimate the mean force acting within each umbrella window, $\partial A^{\mathrm{u}}/\partial\xi$. Using the Gaussian approximation for $P_i^{\mathrm{b}}(\xi)$, we can rewrite Eq. 2.65 to give

$$\frac{\partial A_i^{\mathrm{u}}}{\partial\xi} = \frac{\partial A_i^{\mathrm{b}}}{\partial\xi} - \frac{\partial w_i}{\partial\xi} = -\frac{1}{\beta}\frac{\partial \ln P_i^{\mathrm{b}}(\xi)}{\partial\xi} - \frac{dw_i(\xi)}{d\xi} \approx \frac{\xi - \overline{\xi}_i^{\mathrm{b}}}{\beta(\sigma_i^{\mathrm{b}})^2} - \kappa(\xi - \xi_i) \tag{2.66}$$

where $\overline{\xi}_i^{\mathrm{b}}$ and $(\sigma_i^{\mathrm{b}})^2$ give the mean and variance of each umbrella window, respectively. The final potential of mean force acting over ξ can then be found by finding the weighted averages over a selected number of bins spanning the reaction coordinate,

$$\left.\frac{\partial A(\xi)}{\partial\xi}\right|_{\xi_{\mathrm{bin}}} = \sum_i^{\text{windows}} \alpha_i(\xi_{\mathrm{bin}})\left(\frac{\partial A_i^{\mathrm{u}}}{\partial\xi}\right)_{\xi_{\mathrm{bin}}} \tag{2.67}$$

where $\alpha_i(\xi_{\mathrm{bin}})$ gives the normalised weight of a particular ξ. From Eq. 2.67, it is then trivial to work out $A(\xi)$ through numerical integration.

Umbrella integration represents a cross between two forms of enhanced sampling: umbrella sampling to generate biased samples; and a thermodynamic-integration-style post-processing step to obtain free energies [177, 178]. Compared to umbrella sampling, umbrella integration benefits in being independent of the number of grid points (no

histogramming step required) as well as from the outputting of an error estimate on the calculated free energies [179]. In literature, umbrella sampling has been utilised towards studying ion conduction pathways in potassium ion channels [180] as well as proton accumulation at graphene interfaces [45], among other processes. In this thesis, we use umbrella integration to study the deprotonation of carbonic acid in Chapter 3 and CO_2 diffusion in Chapter 5.

As an alternative to umbrella integration, the unbiased free energy profile can also be reconstructed using reweighting-based estimators. These include methods such as the Weighted Histogram Analysis Method (WHAM) and Multistate Bennett Acceptance Ratio (MBAR) approach [181, 182]. In WHAM, data from multiple umbrella windows are combined to construct an unbiased probability distribution along ξ [181]. WHAM estimates this $P^{\mathrm{u}}(\xi)$ by combining the histograms from all umbrella windows with weights that depend on unknown free-energy offsets, which are solved self-consistently [183]. The self-consistent estimator for the unbiased probability is determined as such

$$P^u(\xi) = \frac{\sum_i^K h_i(\xi)}{\sum_j^K n_j \exp(\beta[F_j - w_j(\xi)])}, \tag{2.68}$$

where $h_i(\xi)$ is the count in bin ξ from window i, n_j is the total number of samples in window j, $w_j(\xi)$ is the umbrella bias for window j, and F_j is the corresponding free-energy offset given by

$$F_j = -\frac{1}{\beta} \ln \sum_{\xi} P^u(\xi) \exp(-\beta w_j(\xi)). \tag{2.69}$$

Solving these equations in a self-consistent manner, we can obtain the unbiased probability distribution and determine the free energy according to $A(\xi) = -k_{\mathrm{B}}T \ln P^u(\xi) + C$.

Similar to WHAM, MBAR uses statistical reweighting to provide an estimate of the free energy [182]. However, unlike WHAM, MBAR does not rely on binned histograms, but instead evaluates a reduced potential u_i for each thermodynamic state i. Here, u_i is given by

$$u_i(q) \equiv \beta_i[U_i(q) + p_i V(q) + \boldsymbol{\mu}_i^{\mathrm{T}} \boldsymbol{N}(q)] \tag{2.70}$$

where q denotes the configuration of the system within a certain configuration space, $V(q)$ give the volume of the space, and $\boldsymbol{N}(q)$ the number of molecules within each of M components of the system. For the thermodynamic state i, $U_i(q)$ gives the potential energy function, p_i the external pressure, and $\boldsymbol{\mu}_i$ the vector of chemical potentials of the M components. In the context of (NVT) umbrella sampling, each thermodynamic state corresponds to umbrella window i, and $u_i(q)$ reduces to the biased potential energy multiplied by the inverse temperature, $u_i(q) = \beta[U_0(q) + w_i(\xi(q))]$, where U_0 gives the unbiased potential. Using $u_i(q)$, an estimate of the dimensionless free energy f_i for window i can be obtained via

$$f_i = -\ln \sum_{n=1}^{N} \frac{\exp[-u_i(q_n)]}{\sum_{j=1}^{K} n_j \exp[f_j - u_j(q_n)]}, \tag{2.71}$$

where i and j run over the umbrella windows, n runs over the different configurations, and the dimensionless quantity f_i can be related to the free energy via $f_i = \beta_i A_i$ [184]. Solving for Eq. 2.71 self consistently, we can obtain the free energy different between states i and j by $\Delta f_{ij} = f_j - f_i = \beta(A_j - A_i)$.

Whilst not explicitly used in this thesis, WHAM and MBAR constitute two important post-processing tools for obtaining free energies from biased umbrella sampling runs. WHAM holds historical significance in providing a widely adopted systematic, self-consistent reconstruction procedure for PMFs. Nowadays, WHAM remains one of the standard post-processing strategies for umbrella sampling. MBAR holds significance in generalising Bennett's acceptance-ratio approach [185] to multiple thermodynamic states, enabling a binless multistate estimator that can be used across various enhanced sampling and free-energy workflows [186].

Chapter 3

Gas-Liquid Interface: Uncovering novel, surface-mediated reaction dynamics

> Look beneath the surface; let not the several quality of a thing nor its worth escape thee.
>
> *Marcus Aurelius*
> *Meditations*

In this first results chapter, we present work pertaining to the air-water interface. Under ambient conditions and concentrations, atomistic CO_2-H_2O systems consist of just a single CO_2 molecule in contact with liquid water. On paper, this might appear to be the simplest of the three aqueous interfaces, as we are only really dealing with a single condensed phase. However, as we shall see, the air-water interface presents a fascinating regime rich in chemistry and displaying several intriguing thermodynamic properties. The contents of this chapter are based on published work: 'CO_2 hydration at the air–water interface: A surface-mediated "in-and-out" mechanism' [187]. Files and data relating to this work can be found at `https://github.com/water-ice-group/interfacial_reactivity`.

3.1 Context

Over the past several decades, heightened CO_2 emissions have led to a substantial acidification of Earth's oceans. Since preindustrial times, oceans have seen a 30% increase in acidity [188], which has resulted in a myriad of adverse effects. These include the loss of marine biodiversity, the disruption of carbonate chemistry, and the unsettling of ecosystem stability, to name a few [1, 8, 189, 190].

Important to understanding the acidification process is a knowledge of the underlying chemistry. Ocean acidification is caused by the reaction between CO_2 and water to form carbonic acid (H_2CO_3) or bicarbonate (HCO_3^-). This occurs via the following equilibria,

$$CO_2 + 2H_2O \rightleftharpoons H_2CO_3 + H_2O \rightleftharpoons HCO_3^- + H_3O^+, \tag{3.1}$$

where bicarbonate and carbonic acid inter-convert via proton exchange with the surrounding solvent. Alongside ocean acidification, this process underpins a number of key processes including carbon sequestration, mineralisation, and the bicarbonate buffer system [191–193]. Realizing the implications of this process requires a detailed understanding of the $CO_2 + H_2O$ reaction at macroscopic and microscopic scales. Concerning the macroscopic properties, experimental work employing spectrophotometric stopped-flow measurements have revealed that, under ambient conditions and neutral pH, the $CO_2 + H_2O$ reaction is a thermodynamically unfavourable process in bulk solution [194]. The products of reaction, bicarbonate and carbonic acid, are destabilised by more than 6 kcal/mol relative to CO_2, and there exists a large free energy barrier separating the reactant and product states. Among the products, bicarbonate and carbonic acid interconvert via proton exchange with the surrounding water, with an associated pK_a of around 3.5 determined from infrared and fluorescence spectroscopy [195, 196].

In terms of the microscopic properties, much of our insight on the $CO_2 + H_2O$ reaction has come from computational work employing first-principles atomistic simulations [27, 171, 197–204]. Under partially solvated conditions, (e.g., in the gas-phase or in water clusters) the reaction proceeds in a concerted manner, with simultaneous C-O bond formation and

proton transfer events. In the limit of a single reacting water molecule (i.e., $nH_2O = 1$), this proton is donated by the attacking water (see Fig. 3.1a), and the overall process is characterized by a large free energy barrier, $\Delta F^{\ddagger} \sim 50$ kcal/mol at 300 K. Increasing the number of explicit waters present can help reduce this barrier, enabling a proton-relay mechanism characterized by a cyclic transition-state structure. High-level correlated wave function studies have found that increasing $nH_2O = 1$ to $nH_2O = 2$ effectively halves the activation energy for reaction, whilst the presence of $nH_2O = 3$ reduces the barrier to $\Delta F^{\ddagger} \sim 22$ kcal/mol [198]. Under these conditions, only carbonic acid forms as a viable product. However, by further increasing the number of explicit waters and moving towards fully solvated conditions, we also see the formation of bicarbonate ions, either through deprotonation of H_2CO_3 or as an intermediate in the step-wise conversion of CO_2 to H_2CO_3 (see Fig. 3.1a) [27]. *Ab initio* molecular dynamics (AIMD) studies have been invaluable for investigating these reactive pathways. Studies have shown how the degree of hydrophobicity/hydrophilicity impacts the surrounding solvation environment [199], how the choice of solvent alters the reaction energetics [202], and how pH can impact the outcome of reaction [203, 204].

Despite the valuable insights acquired from these studies, they focus on either gaseous or bulk-solution modelling. Crucially, a detailed understanding of the $CO_2 + H_2O$ reaction at the air-water interface is lacking. This omission is significant; Earth's oceans span a vast surface area on the order of 350 million km^2, upon which are adsorbed large quantities of atmospheric CO_2 (see Chapter 4). The contribution that this surface-adsorbed and near-surface CO_2 makes to the overall acidification process is currently unclear. Further, previous studies have identified that aqueous interfaces can display certain interesting properties and phenomena, including accelerated rates of reaction, altered product selectivities, and modified reaction mechanisms [205–209]. Whether any of these effects are present for interfacial CO_2 hydration also remains an open question.

To date, experimental and computational work have faced a number of challenges in modelling interfacial reactions and processes. Experimental work is hampered by the large volumetric ratio of bulk to interfacial environments, which makes the latter

difficult to probe spectroscopically. Some work has been undertaken to identify CO_2 and bicarbonate propensities for adsorption at the interface [210, 211], though such work is limited in the context of the hydration reaction and the various species involved. From a computational perspective, aqueous interfaces require both large length- and timescales to obtain converged results free from finite-size effects; this precludes the use of *ab initio* methods, which are the go-to for performing reactivity analysis. As a result, there are major gaps in our understanding of this reaction at the air-water interface.

A potential solution to this problem arises in the form of MLIPs. As discussed in Chapters 1 and 2, these models offer an *ab initio*-level of accuracy for a fraction of the computational cost [35–38, 212]. They have already been applied towards studying a variety of important reactions and processes at interfaces [39, 40, 213, 214]. Building on recent developments in the field of MLIPs, we aim to address the question of how exactly CO_2 reacts at the air-water interface. Specifically, how does this reaction proceed? Where at the interface does the reaction occur? And how does this process differ from the equivalent reactions in bulk and in the gas phase?

In this chapter, we develop and validate MACE models at various level of theory, for the study of the $CO_2 + H_2O$ reaction at the air-water interface. These models were trained on an extensive and representative collection of chemical structures, with subsequent validation of the models confirming the quality of their predictions. Importantly, this includes predictions at the beyond-DFT random phase approximation (RPA) level and benchmarks at the coupled-cluster level. Using MACE, we performed well-tempered metadynamics [166] targeting the reaction in the gas phase, in bulk solution, and at the air-water interface - specifically, within 10 Å of the air-water interface (see Fig. 3.1b). Our analysis uncovers an unconventional 'in-and-out' mechanism underpinning reaction at the air-water interface: CO_2 diffuses into the surface aqueous layer, reacts to form carbonic acid, and is subsequently expelled from solution. Characterization of this regime reveals that important solvation properties - specifically, the solute-solvent coordination number and hydrogen bond count - are bulk-like and uniform to within 1 Å of the instantaneous interface. The similarity between bulk and interfacial environments

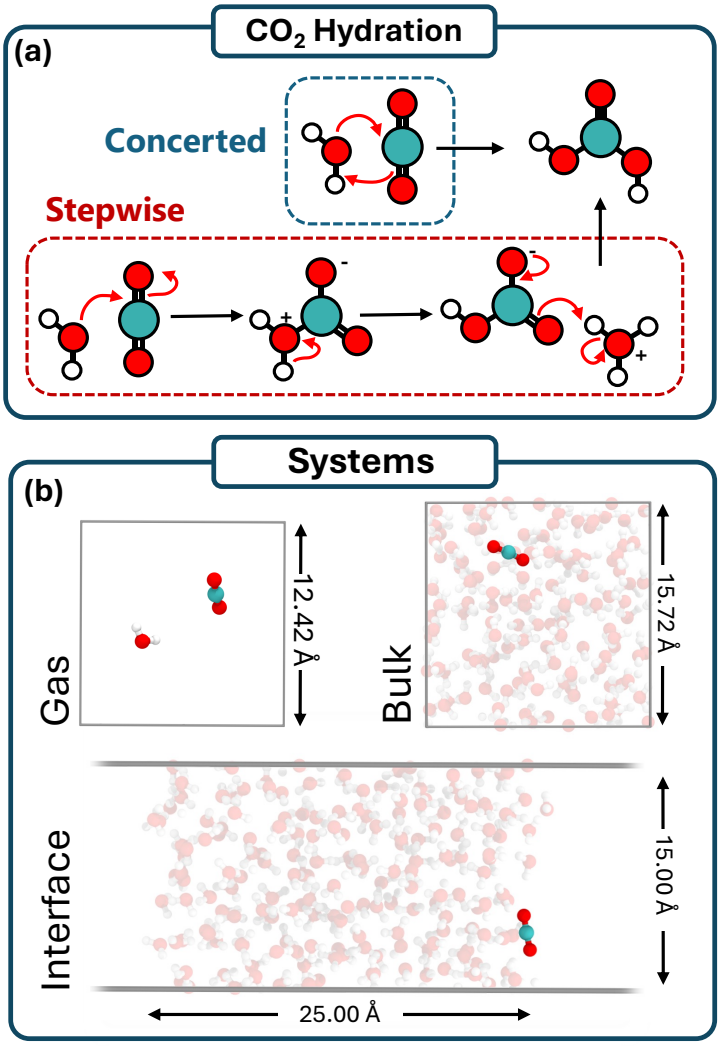

Fig. 3.1 Modelling the CO_2 + H_2O reaction through enhanced sampling molecular simulations. **(a)** Mechanisms detailing the reaction of CO_2 + H_2O to form carbonic acid (H_2CO_3) through both concerted and stepwise routes. The concerted route is shown for a single reacting water molecule, though additional H_2O molecules may participate to form a proton transfer chain. **(b)** System setups used to probe the CO_2 + H_2O reaction under gaseous, bulk, and interfacial environments.

engenders near-identical chemical reactions in terms of the free energies, ΔF, and free energy barriers, $\Delta F^{\ddagger}$. Our work highlights the correlation between the extent of reaction and the location of reacting substituents at the air-water interface. Further, it establishes the uniformity of solvation conditions for the near-interface aqueous regime. Together, these observations suggest that interfacial reactions can occur in very similar manner to their bulk counterparts, despite lower effective solvent densities. In the context of ocean

acidification, our results place a heightened importance on the role of surface-adsorbed CO_2 reactions and their contributions to the overall acidification process.

3.2 Methods

Our approach to this chapter's work can be separated into two main parts: first, the training and validation of a MACE model suitable for modelling the $CO_2 + H_2O$ reaction under differing solvation conditions; and second, the use of this model in performing well-tempered metadynamics simulations to extract free energies as well as structural and mechanistic data. Details on these procedures are provided below.

Training

Our training procedure follows well-established protocols developed for training MACE models [149]. These procedures have been tested against a range of published datasets and system types, including aqueous systems, medicinal compounds, organic chemicals, and functional materials. A diverse selection of structures was collated for training our model. Initially, structures were generated using *ab initio* molecular dynamics (AIMD). Subsequent iterations of our dataset were augmented with structures from MLIP-MD, which allowed for larger and more complex structure generation as well as structures from enhanced sampling and constrained MD runs. A variety of system types and compositions were incorporated into this training data, e.g., gaseous systems, periodic bulk and interfacial systems, pure water, pure CO_2, and systems of CO_2 in water. In total, this initial dataset comprised some 150,000 data points, including out-of-equilibrium and near-transition-state structures drawn from enhanced sampling simulations. Following the procedure outlined in Reference [215] (see Chapter 4), this dataset was optimized and its size reduced to $\sim$ 8000 representative structures. These structures are shown in Fig. A.2 as a projected two-dimensional subspace using the UMAP transformation (see Appendix A for more information) [216, 217].

Energies and atomistic forces were calculated for each structure at the DFT level of theory (spin unpolarised) using the QUICKSTEP method implemented in `CP2K` [119, 120]. For our main model, we employed the revPBE functional augmented by Grimme's D3 corrections (zero damping) [95, 115, 218]. revPBE-D3 benefits from a well-known error compensation: the neglect of nuclear quantum effects leads to overbinding, whilst revPBE-D3 is known to exhibit an underbinding effect. As a result, the use of revPBE-D3 for first-principles or machine-learned MD with classical nuclei often results in predictions consistent with those of experiment. This is true both for bulk and interfacial water, where revPBE-D3 has been shown to reproduce the structural, dynamical, and spectroscopic properties of liquid water [219–222]. Further, previous metadynamics work has shown that revPBE-D3 can reproduce certain free energies and reaction barriers pertaining to both the $CO_2 + H_2O$ hydration and the bicarbonate/carbonic acid equilibrium to within 1 kcal/mol of experimental measurement [202, 223]. Goedecker–Teter–Hutter (GTH) pseudopotentials were used for the treatment of the core electrons, whilst the TZV2P-GTH basis sets were used for treating the valence electron density. An auxiliary plane wave cutoff of 650 Ry was used. We benchmarked the predictions of this setup against those of DLPNO-CCSD(T)-F12 for simple nudged-elastic band calculations on the gas-phase reaction (see Fig. A.1 of Appendix A). We find that DFT and coupled-cluster calculations are consistent to within several kcal/mol for transition-state and product energies. Coupled-cluster calculations were performed using `ORCA` [224, 225]. Further details can be found in Appendix A.

With this optimised dataset, we trained a 2-layer MACE model (i.e., two rounds of message passing) with 128 equivariant messages and a maximal message equivariance of $L = 1$. A cutoff of 5 Å was employed, which translates to an effective receptive field of 10 Å after message passing ($r_{\text{eff}} = 2 \times r_{\text{c}} = 10$ Å). Whilst long-range effects, important for modelling liquid-vapour interfaces [42], are not explicitly included in our setup, we find that the large receptive field employed by our model is sufficient for recovering the interfacial properties of interest. Upon completion of the training, the model was validated against DFT energy and force predictions (RMSEs: 1.5 meV/atom and 28.8 meV/Å, respectively) as well as solvent and solute-solvent structural predictions. A bulk water density of 0.991

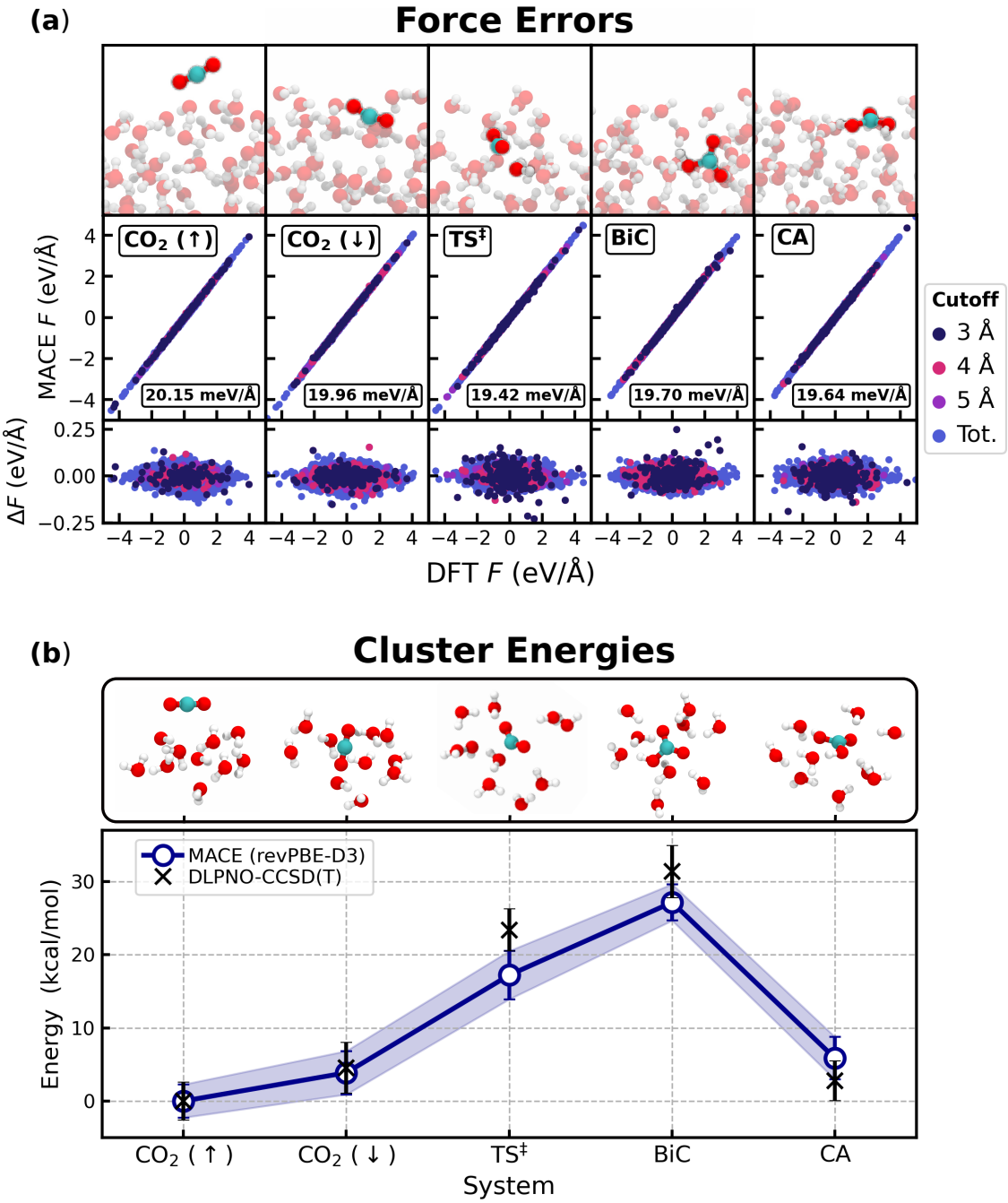

Fig. 3.2 Validating interfacial reactivity. **(a)** Comparison of our model's force predictions against those of revPBE-D3 for the five identified interfacial states. For each state, 10 representative structures are extracted from our dataset for analysis. Forces are calculated within differing radial cutoffs of the reactive carbon species and compared on an absolute scale (middle panel) and relative scale (ΔF, bottom panel). **(b)** A comparison of potential energies predicted by our MACE model and from CCSD(T). For each interfacial state, clusters containing the closest 9/10 waters to the central carbon molecule are extracted. DLPNO-CCSD(T) calculations are run using ORCA [224, 225] and using the def2/TZVPP basis set. The standard errors in the mean of the energies across each state are plotted as error bars on the figure.

$\pm$ 0.002 g/ml was attained by this model, consistent to within 3% of previous revPBE-D3 estimates obtained using CP2K [226] (see Table A.1) and also with the experimental value of 0.997 g/ml. An interfacial tension (IFT) of 83 $\pm$ 1 mN/m was obtained for the air-water interface, also in good agreement with previous computational estimates and only 10 % greater than the experimental value [34]. Whilst classical force fields can achieve IFT predictions closer to experiment, it should be noted that these models are usually molecule-specific and generally unable to treat reactive events. Our MACE (revPBE-D3) model gives reasonably accurate interfacial predictions whilst simultaneously enabling treatment of bond-making and bond-breaking events.

To further validate the efficacy of our model for treating the air-water interface, we tested the interfacial predictions of our model using targeted force error calculations and through the comparison of state energy predictions with coupled-cluster theory. The results of this comparison are shown in Fig. 3.2. In panel a, we plot the force predictions of our model against those of DFT for the various species encountered during the interfacial CO_2 hydration process. The errors in the prediction of F are consistently small across the various states and lower than the overall model error (28.8 meV/Å). Then, in panel b, we plot the energy predictions of our model against those of DLPNO-CCSD(T) for small cluster configurations extracted from the interfacial states. We find that, for these various states, our predicted energies agree with DLPNO-CCSD(T) values to within the combined uncertainties of both methods. Combining these two results, we can therefore have confidence in our MACE model for simulating the reactive and structural properties of the air-water interface. Further details, including information on the training and validation of additional BLYP-D3 and RPA models, can be found in Appendix A.

System Setup

Our work employed three system setups differing in size and composition. These are shown in Fig. 3.1b. The gaseous setup consisted of a single CO_2 molecule and a single H_2O molecule in a box of length 12.42 Å. The bulk system consisted of a single CO_2 molecule and 127 H_2O molecules in a 15.72 Å box, chosen to reproduce a bulk density of $\sim$ 1.00

g/ml. And finally, the interfacial system consisted of a single CO_2 molecule and 180 water molecules in a box of size 15 Å × 15 Å × 100 Å. Starting configurations for the interfacial setup were initialized such that the interface resided parallel to the xy plane. The resulting water slab has a length approaching 25 Å, which allows us to probe the interfacial region within 10 Å of each interface, recovering bulk-like water in the middle of the slab.

Metadynamics

Obtaining meaningful results from enhanced sampling simulations requires careful selection of the underlying collective variables (CVs). These can be selected by hand or, alternatively, generated through machine learning algorithms [164, 227, 228]. In this chapter, we made use of a C-O coordination number to track the principle attack of water on CO_2 alongside a protonation state CV to differentiate between bicarbonate and carbonic acid products.

In the case of the C-O coordination number, we made use of the same functional form across all three systems,

$$s_{\mathrm{CO}} = \sum_{\mathrm{i}\in\mathrm{O}} \frac{1-\left(\frac{r_{\mathrm{Ci}}}{r_0}\right)^n}{1-\left(\frac{r_{\mathrm{Ci}}}{r_0}\right)^m} \tag{3.2}$$

where r_{Ci} gives the distance between the central carbon and oxygen i, whilst r_0, n, m are parameters that control the shape of the function. For the gas-phase reaction, we used $r_0 = 2.0$ Å, $n = 6$, and $m = 12$. For the bulk and interfacial reactions, we imposed a stricter cutoff ($n = 12$, $m = 24$) to better differentiate between bound and unbound (solvent) oxygens. Under this representation, we find that $s_{\mathrm{CO}} = 2.0$ in the reactant state (2 oxygens bound to carbon, CO_2) and 3.0 in the product state (3 oxygens bound to carbon, HCO_3^-/H_2CO_3).

For the secondary collective variable, we made use of two distinct definitions for probing the product state identity. In the case of the gas-phase reaction, where the number of intact water molecules in the system can only ever be 1 or 0 (corresponding to the reactant

and product states, respectively), we can define the following collective variable,

$$C_{\mathrm{iH}}^{\mathrm{gas}} = \sum_{\mathrm{j}\in\mathrm{H}} \frac{1-\left(\frac{r_{\mathrm{ij}}}{r_0}\right)^6}{1-\left(\frac{r_{\mathrm{ij}}}{r_0}\right)^{12}} \tag{3.3}$$

$$s_{(\mathrm{OH})_{\mathrm{g}}} = \sum_{\mathrm{i}\in\mathrm{O}} 1 - \frac{1-\left(\frac{C_{\mathrm{iH}}^{\mathrm{gas}}}{C_{\mathrm{OH}}^{0}}\right)^6}{1-\left(\frac{C_{\mathrm{iH}}^{\mathrm{gas}}}{C_{\mathrm{OH}}^{0}}\right)^{12}} \tag{3.4}$$

where r_{ij} gives the pairwise oxygen-hydrogen distances, $r_0 = 1.5$ Å, and $C_{\mathrm{OH}}^{0} = 1.5$. This CV works by calculating the oxygen-hydrogen coordination number for each oxygen atom (Eq. 3.3) and determining how many of these are greater than 1.5 (Eq. 3.4). Very simply, $s_{(\mathrm{OH})_{\mathrm{g}}}$ counts the number of intact water molecules in the system, allowing us to distinguish between the reactant state ($s_{(\mathrm{OH})_{\mathrm{g}}} \sim 1$, CO_2 + H_2O) and the product state ($s_{(\mathrm{OH})_{\mathrm{g}}} \sim 0$, H_2CO_3). For visual consistency with the other free energy profiles, we plot $1 - s_{(\mathrm{OH})_{\mathrm{g}}}$ for the free energy profile.

Concerning the bulk and interfacial secondary collective variable, the situation is complicated by having numerous water molecules that can undergo reaction with CO_2. Determining the protonation state of the product therefore requires being able to distinguish between bound and unbound oxygens when counting the OH coordination numbers. We do this by introducing a radially dependent CV,

$$s_{(\mathrm{OH})_{\mathrm{aq}}} = \sum_{\mathrm{i}\in\mathrm{O}} \sigma_{\mathrm{i}} C_{\mathrm{iH}}^{\mathrm{sol}}, \tag{3.5}$$

where $C_{\mathrm{ij}}^{\mathrm{sol}}$ gives the coordination between the ith oxygen and the jth hydrogen,

$$C_{\mathrm{iH}}^{\mathrm{sol}} = \sum_{\mathrm{j}\in\mathrm{H}} \frac{1-\left(\frac{r_{\mathrm{ij}}}{r_0}\right)^{12}}{1-\left(\frac{r_{\mathrm{ij}}}{r_0}\right)^{24}}, \tag{3.6}$$

and σ_{i} is a switching function that acts to filter out coordination numbers calculated beyond a particular radius r_{C},

$$\sigma_{\mathrm{i}} = \frac{1 - \left(\frac{r_{\mathrm{Ci}}}{r_{\mathrm{C}}}\right)^{25}}{1 - \left(\frac{r_{\mathrm{Ci}}}{r_{\mathrm{C}}}\right)^{50}}. \tag{3.7}$$

Here, r_{ij} gives the distance between oxygen i and hydrogen j, r_{Ci} gives the distance between oxygen i and the central carbon atom, and r_0 and r_C are variables used to control the cutoffs of the defined functional forms ($r_0 = 1.25$, $r_C = 1.5$). In its presented form, $s_{(\mathrm{OH})_{\mathrm{aq}}}$ amounts to calculating all OH coordinations and only summing those that reside with ~ 1.5 Å of the central carbon atom of our reactive species.[1] Under this representation, $s_{(\mathrm{OH})_{\mathrm{aq}}} = 0$ in the reactant state and either 1.0 (HCO_3^-) or 2.0 (H_2CO_3) in the product state. Taken together, our collective variables (s_{CO}, $s_{(\mathrm{OH})_{\mathrm{g}}}$, $s_{(\mathrm{OH})_{\mathrm{aq}}}$) allow us to fully distinguish between reactant and product states in order to obtain a fully resolved free energy profile.

Well-tempered metadynamics was performed by coupling `LAMMPS` with the multiple-walker setup available in `PLUMED` [229–233]. In this setup, we initialise n replicas of a system with distinct starting configurations. We then perform n different metadynamics runs, with each simulation periodically depositing and reading from a central 'hills' file. In this way, we can use multiple system replicas to traverse and update the same energy surface, thereby expediting the convergence of our free energy profiles. We used three walkers to probe the gaseous reaction, whilst five walkers were used to look at the bulk and interfacial reactions. Starting configurations were extracted from restrained MD simulations where we gradually switched s_{CO} from 2 (CO_2) to 3 (H_2CO_3). These configurations were chosen to represent the various species observed in the $CO_2 + H_2O$ reaction and to maximize the initial free energy surface coverage and exploration. Simulations were performed under the NVT ensemble at 300 K, using the Nosé-Hoover thermostat with a time constant of 100 fs, chosen to minimise disturbance to the particle trajectories. A timestep of 1 fs was selected, and hydrogen atoms were switched for deuterium in order to improve numerical

[1] The form of $s_{(\mathrm{OH})_{\mathrm{aq}}}$ presented in equation 3.5 represents a summation of σ-weighted coordinations of each oxygen atom. Including a σ term in the denominator, we may also derive a σ-weighted mean coordination number according to $\bar{s}_{(\mathrm{OH})_{\mathrm{aq}}} = \sum_{\mathrm{i}\in\mathrm{O}} \sigma_{\mathrm{i}} C_{\mathrm{iH}}^{\mathrm{sol}} / \sum_{\mathrm{i}\in\mathrm{O}} \sigma_{\mathrm{i}}$.

stability.[2] Product free energies were monitored to gauge the profile convergence with time. For each system type, we achieve more than 10 barrier crossings and a cumulative simulation time of 50 ns across all walkers. Explicit details on the metadynamics setup, the free-energy convergence, and a discussion of near-transition-state predictions are presented in Appendix A.

It is important to note that, for the interfacial metadynamics runs, no restraints were applied to the position of the reacting species. This means that the reactive species were free to diffuse throughout the interfacial system and adopt their preferred solvation environment. This differs from previous studies, which have used harmonic potentials to constrain the z coordinate of the reacting species to a particular height relative to the interface. Our rationale for omitting such restraints lies in wanting to fully explore the positional dependence of molecules as a function of the extent of reaction.

3.3 Results

The interfacial reaction of CO_2 is bulk-like

To investigate the CO_2 + H_2O reaction, we generated a series of free energy profiles mapping the conversion of CO_2 to bicarbonate and carbonic acid. Profiles were generated for the gaseous, bulk, and interfacial reactions using the system setups shown in Fig. 3.1b. Using our MACE(revPBE-D3) model, we performed well-tempered metadynamics simulations for a cumulative time of 50 ns. The extent of reaction was monitored with the tuple, (s_{CO}, $s_{(\mathrm{OH})}$).

The free energy profiles obtained for the gaseous and bulk reactions are shown in Fig. 3.3. These reactions have been studied previously using correlated wavefunction and DFT modelling and thus serve as a good measure of the quality of our generated MACE potential [27, 198, 202]. Looking at the profiles, we note several important differences between the gaseous and bulk reactions. For the gas-phase profile, there are only two

[2]Whilst known to affect dynamical observables, changing the atomic mass will have limited effect on the calculated thermodynamic observables. For both hydrogen and deuterium, we sample the same underlying equilibrium free energy surface.

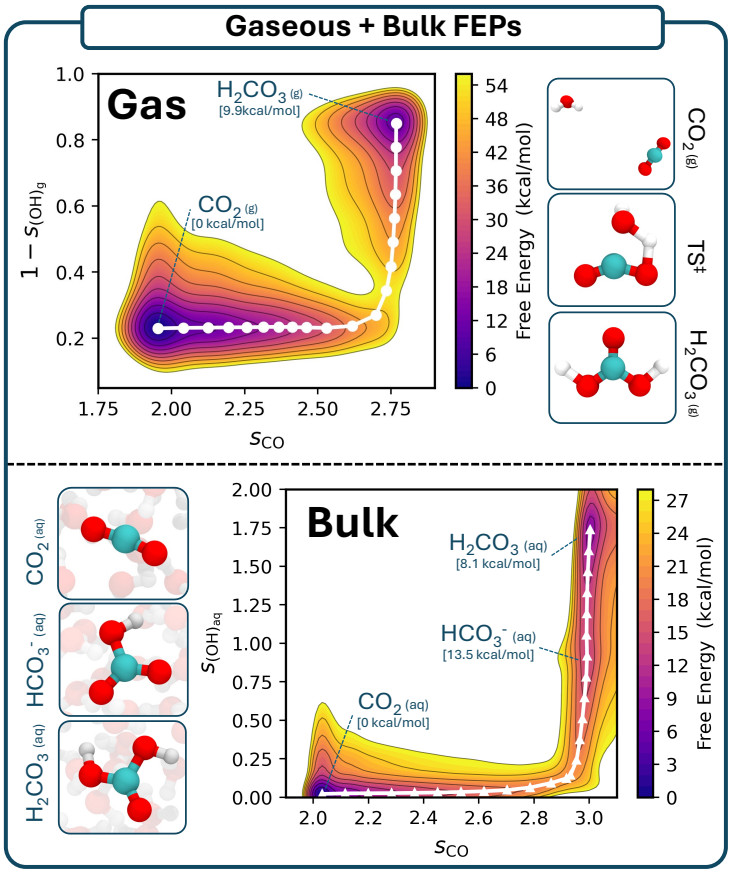

Fig. 3.3 Free energy profiles obtained from metadynamics simulations for the gaseous and bulk reactions. Free energies are plotted as a function of both the C-O coordination number (s_{CO}) as well as tailored protonation state collective variables for the gaseous ($s_{(OH)_g}$) and aqueous ($s_{(OH)_{aq}}$) phases. Representative snapshots of the various species encountered during simulations are shown alongside the profiles.

local minima: a reactant basin at (2.0, 0.2) denoting CO_2 and a product basin at (2.8, 0.8) denoting carbonic acid. Separating these minima is a large reaction barrier on the order of 50 kcal/mol. In contrast, the bulk reaction profile shows three distinct basins: a basin at (2.0, 0.0) denoting CO_2, a basin at (3.0, 1.0) corresponding to bicarbonate, and a basin at (3.0, 2.0) corresponding to carbonic acid. Separating the CO_2 and HCO_3^- basins is a reaction barrier on the order of $\Delta F^\ddagger \sim 20$ kcal/mol, whilst a smaller barrier of $\Delta F^\ddagger < 1$ kcal/mol connects H_2CO_3 to HCO_3^- (see Fig. A.11 for more information). From these observations, we can make two key inferences: the bulk reaction occurs with enhanced kinetic favourability compared to the gas-phase and bicarbonate can only form under solvated conditions.

These results are consistent with previous studies of the CO_2 + H_2O reaction. Our gas-phase predictions show excellent agreement with those of coupled cluster calculations [198], where we find that we can reproduce ΔF and $\Delta F^{\ddagger}$ to within a couple of kcal/mol. We have also benchmarked our DFT setup with respect to gas-phase coupled cluster calculations at the DLPNO-CCSD(T)-F12 level (see Fig. A.1 of Appendix A). The bulk-solution predictions of our model also show close agreement with those of previous DFT-based studies employing the BLYP and revPBE-D3 functionals [27, 202]. Looking at the H_2CO_3/HCO_3^- free energies, we derive a pK_a of 3.9 using $\Delta F = -RT\ln(K_a)$. This result compares favourably with experimental pK_a values of 3.45 and 3.49 obtained from spectroscopic measurement [195, 196]. The similarity between these various results attests to the quality of our generated potential for investigating the CO_2 + H_2O reaction under differing solvation conditions.

In Fig. 3.4a, we show the free energy profile obtained using the interfacial setup. Similar to the bulk reaction, we observe three different basins corresponding to CO_2, bicarbonate, and carbonic acid. We also observe free energies and reaction barriers that are remarkably similar to those of the bulk reaction, to within 1-2 kcal/mol. These similarities can be seen more clearly in Fig. 3.4b, where we plot the minimum free energy profiles (MFEPs) extracted from each profile. Looking at these MFEPs, we see almost identical modes of reaction for the bulk and interfacial regimes in terms of the free energies, reaction barriers, and the overall reaction pathways.[3] This may come somewhat as a surprise given the stark structural and compositional differences between the homogeneous bulk and the spatially anisotropic interface [41, 234]. Indeed, previous studies for other reactions have reported notable differences in the behaviour of processes occurring at an interface versus in bulk. Work by de la Puente et al. has shown how certain acids can become more or less acidic depending on their location at the air-water interface [40]. Buttersack et al. demonstrated that sulphur species can undergo stabilisation at the air-water interface, leading to unique dissociation behaviour relative to the bulk [235]. For the CO_2 hydration studied here, this

[3] Whilst not presented here, error bars on the MFEP points can be obtained through block averaging or through reweighting schemes (see Appendix A for discussion).

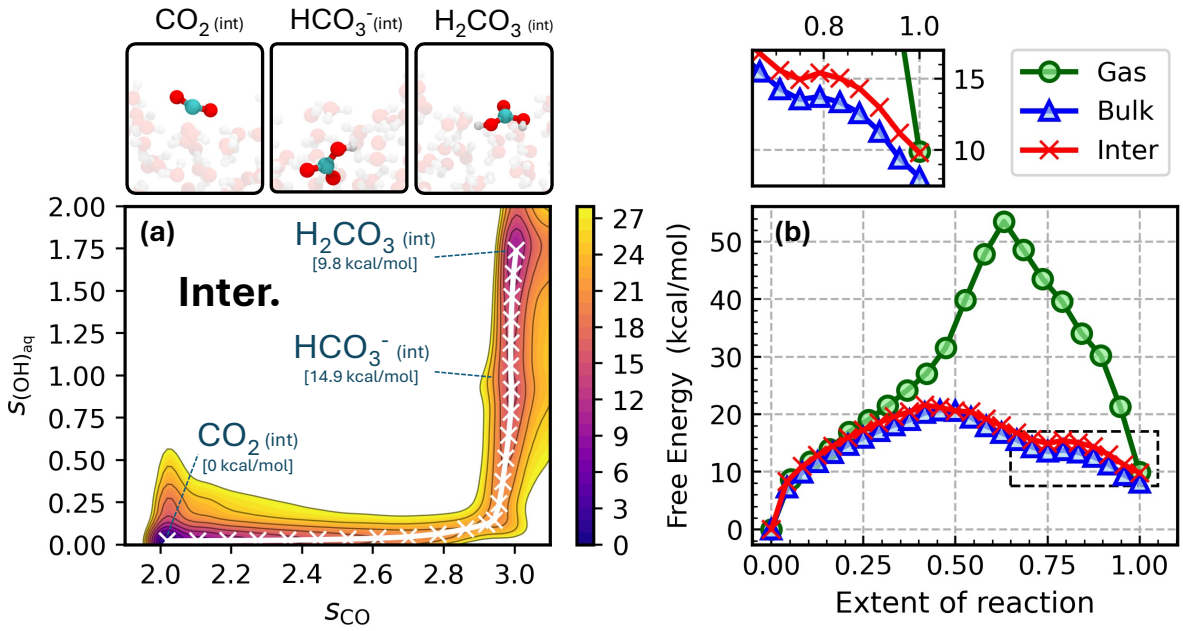

Fig. 3.4 Reaction free energies are almost identical for bulk and interfacial reactions. **(a)** Free energy profile obtained from metadynamics simulations for the interfacial reaction. Free energies are plotted as a function of both the C-O coordination number (s_{CO}) as well as an aqueous-phase protonation state collective variable ($s_{(OH)_{aq}}$). Representative snapshots of the various species encountered during the simulation are shown alongside the profile. **(b)** Minimum free energy profiles (MFEPs) obtained for the CO_2 + H_2O hydration reaction under gaseous, bulk, and interfacial regimes. MFEPs are plotted as free energies as a function of the extent of reaction, where 0 corresponds to the reactants (i.e., CO_2) and 1.0 corresponds to the products (i.e., carbonic acid). The additional figure situated above the main plot highlights the 'acidic' region of the graph, relating to the free energies of conversion between bicarbonate and carbonic acid.

is clearly not the case, with Fig. 3.4b suggesting an almost identical stabilisation of each of the species under both types of environment. Likely this results from both the difference in reaction type being treated as well as our simulation setup, in which we allow species to react freely with no restraints imposed on the position relative to the interface.

CO_2 reacts via surface-mediated 'in-and-out' Mechanism

Figure 3.4 demonstrates a likeness in the free energies of the bulk and interfacial CO_2 + H_2O reactions. Understanding this similarity requires a more detailed investigation of the mechanisms underpinning reaction at the air-water interface. In Fig. 3.5, we explore this mechanism in a statistical manner. Figure 3.5a shows a 2D histogram capturing the

joint frequency distribution of the C-O coordination number, s_{CO}, and the depth of the reacting species relative to the instantaneous air-water interface [236], d_{int}, across our multi-nanosecond simulation data. Frequency is encoded in the colour bar, whilst the averaged interfacial distance $\langle d_{int} \rangle$ at each s_{CO} is shown by the dashed line.

Looking at Fig. 3.5a, we observe a clear correlation between the carbon-oxygen coordination number s_{CO} and the distance to the instantaneous interface d_{int}. As s_{CO} increases from left to right - representative of converting from the reactants ($CO_2 + 2\,H_2O$) to the products ($H_2CO_3 + H_2O/HCO_3^- + H_3O^+$) - $\langle d_{int} \rangle$ gradually decreases, switching from a positive value (air-side) to a negative value (water-side) at $s_{CO} \sim 2.5$. A minimum in $\langle d_{int} \rangle$ is observed at $s_{CO} = 2.9$, which roughly coincides with the transition state of reaction. Beyond $s_{CO} = 2.9$, $\langle d_{int} \rangle$ starts to increase again and approach positive values.

Physically, these observations suggest an unconventional 'in-and-out' mechanism: CO_2 initially starts on top of the air-water interface; CO_2 then dives into the aqueous phase and reacts to form carbonic acid; finally, carbonic acid is expelled from solution. A thorough investigation of the metadynamics trajectories supports this proposed mechanism. In Fig. 3.5b, we plot a representative reactive event - extracted from our metadynamics simulations - in terms of the s_{CO} and d_{int} against simulation time. We observe that, prior to reaction, CO_2 resides on top of the air-water interface, with $d_{int} \geq 0$. Upon reaction - corresponding to an increase in s_{CO} from 2 to 3 - the molecule dives into the first layer with d_{int} falling to a minimum value of -2 Å. Following the formation of carbonic acid and the completion of the reaction, these products return towards the surface. At the end of this simulation segment, $d_{int} \sim -0.1$ Å which corresponds to H_2CO_3 residing near the top of the first molecular layer of water.

Looking at Fig. 3.5, we gain a number of valuable insights. First, CO_2 prefers to sit on top of the water-air interface, in accordance with previous studies [223]. Upon reaction, the surface-adsorbed CO_2 will partially dissolve in the molecular surface layer of water. In doing this, CO_2 moves from a solvent-deficient region to a solvent-rich one, thus stabilising the emerging charge found in the transition-state species. From this, we can infer that the $CO_2 + H_2O$ reaction is disfavoured on top of the air-water interface and that CO_2

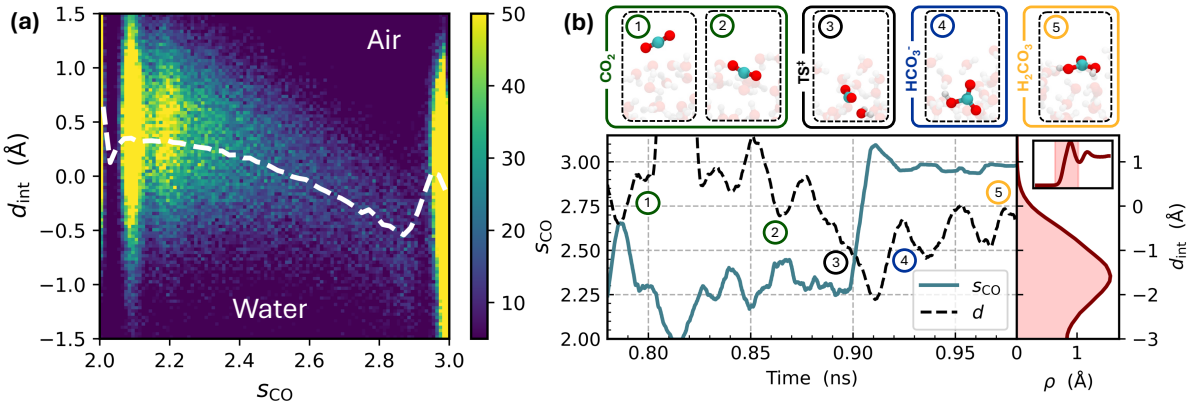

Fig. 3.5 CO_2 reacts with water via a surface-mediated 'in-and-out' mechanism. **(a)** A 2D histogram showing the joint frequency distribution of the C-O coordination number (s_{CO}) and the distance from the instantaneous interface (d_{int}), calculated using the Willard-Chandler formalism [236]. The averaged d_{int} value, obtained for each s_{CO} within the limits $-1.5 \leq d_{int} \leq +1.5$, is shown by the dashed curve. The frequency colourbar is capped at 50 to prevent over-saturation of the figure due to reactant and product states. **(b)** A representative reactive event, extracted from our metadynamics simulations, in which CO_2 reacts within the first molecular layer of the aqueous phase during reaction. This event is followed in terms of both s_{CO} and d_{int}, which are plotted as a function of the metadynamics walker time. Reaction occurs at around 0.9 ns. The density profile of water, plotted as d_{int} against density ρ, is shown for reference on the right-hand side of the figure. Representative snapshots showing some of the species encountered during simulation are shown along the top of the figure.

must be immersed within the first contact layer to facilitate reaction. This corresponds to a ~ 1 Å displacement of CO_2 into the aqueous phase. Whilst this may appear to be a relatively small displacement, clearly this is enough to switch the reaction mode from gaseous to bulk-like, thereby halving the barrier to reaction. That we can so profoundly change the nature of reaction over just a single ångström highlights the importance of solvation conditions and their influence on interfacial chemistry.

Overall, these insights suggest a correlation in the extent of reaction and the location of the reactive species at the interface. In the case of our proposed 'in-and-out' mechanism, in going from reactants to products, we observe d_{int} to initially decrease approaching the transition state, following which d_{int} starts to rise again. Accordingly, we can say that the depth of the species at the air-water interface can be determined by the extent of reaction, and vice versa.

Solvation conditions are uniform approaching the air-water interface

In Fig. 3.5, we uncover a reaction mechanism that involves a positional change of the reacting species relative to the air-water interface. We might expect such behaviour to be born of the varying adsorption affinities that the species in Eq. 3.1 show for the air-water interface. To further explore this idea, we plot a series of time-averaged profiles - extracted from our metadynamics simulations - for CO_2, bicarbonate, carbonic acid, and transition-state-like species (which we denote generically by $TS^{\ddagger}$). For each species, we analyse the density profiles, solute-solvent coordination numbers, and hydrogen-bond counts per molecule as a function of the distance from the instantaneous interface, d_{int}.

Looking first at the density profiles shown in Fig. 3.6a, we see that different species adsorb at different distances relative to the air-water interface. CO_2 resides mostly on top of the air-water interface (positive d_{int}), with a peak in the distribution occurring at d_{int} = 1.6 Å. Carbonic acid also resides mostly on top of the interface, albeit with a smaller d_{int} equal to 0.1 Å at the distribution peak. Looking at the underlying water profile, this suggests that carbonic acid is partially hydrated by the first water layer when located at its equilibrium position. In contrast to both CO_2 and carbonic acid, bicarbonate is able to freely move throughout the aqueous near-interface regime, with the equilibrium position residing at the second water layer, $d \sim -4.5$ Å. Finally, we observe that $TS^{\ddagger}$ structures can be located throughout the 10 Å regime. However, these species are found mostly in the topmost water layer, with $d \sim -1$ Å. This serves as the most likely site of reaction for our interfacial setup. Overall, our density profiles compare favourably with those obtained from unbiased MD simulations, which are shown in Fig. A.13 of Appendix A. The close agreement in adsorption locations and propensities show that we can recover the equilibrium spatial distributions of our reactive species from enhanced sampling MD. Moreover, this consistency demonstrates that each reactive state has undergone thorough sampling during our enhanced sampling runs, further supporting the convergence and quality of the interfacial results presented here.

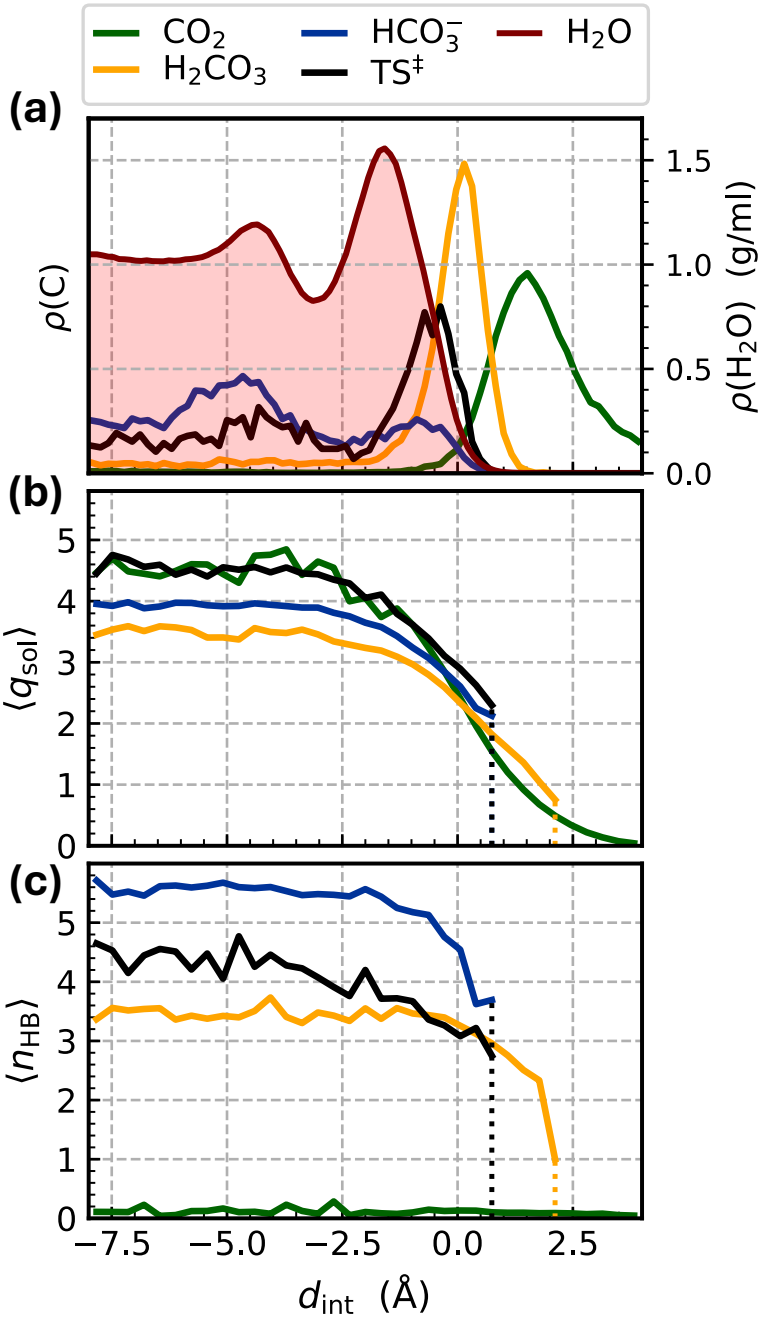

Fig. 3.6 Different carbon species reside at different distances from the instantaneous air-water interface. **(a)** Normalised densities of CO_2, carbonic acid, bicarbonate, and transition-state-like structures plotted as a function of the distance from the instantaneous interface, d_{int}. The background density profile for water is shown for reference in red. **(b)** The averaged solute-solvent coordination, $\langle q_{\text{sol}} \rangle$, plotted for each species as a function of d_{int}. q_{sol} is found by summing over all carbon-water coordinations, $n = (1-(r/r_{\text{C}})^p)/(1-(r/r_{\text{C}})^q)$, where r gives the individual carbon-water distances, $r_{\text{C}} = 3.5$ Å, $p = 12$ and $q = 24$. Accordingly, $q_{\text{sol}} = \Sigma n(r)$. **(c)** The averaged hydrogen-bond count, $\langle n_{\text{HB}} \rangle$, for each species plotted as a function of d_{int}. Hydrogen bond criteria: a donor-acceptor distance of less than 3.5 Å, and an O-H-O angle of greater than 150°.

The density profiles shown in Fig. 3.6a indicate the preferential locations of each of the species in Eq. 3.1 relative to the air-water interface. There are a number of factors controlling the exact shapes of these distributions, and there is extensive discussion in literature as to why ions and molecules will adsorb to different extents depending on their chemical nature [47, 237, 238]. A high-level analysis of the profiles in Fig. 3.6a reveals that neutral species (CO_2 and carbonic acid) reside on top of the interface (positive d_{int}) whilst charged and partially charged species (bicarbonate, and the zwitterionic $TS^{\ddagger}$) are located within the aqueous regime (negative d_{int}). Theoretical analysis has shown that the surface adsorption of neutral molecules is principally driven by enthalpic considerations [239]; the placement of hydrophobic CO_2 on top of the air-water interface preserves the hydrogen bonding network of the near-interface regime, thereby maximizing solvent-solvent interactions. Comparing the positions of CO_2 and carbonic acid, we observe that the latter molecule is more submerged within the topmost layer of water, a phenomenon attributed to the polarity of carbonic acid as well as its ability to partake in hydrogen bonding (see Fig. 3.6c). Concerning the 'in-water' behaviour of bicarbonate (and $TS^{\ddagger}$), the ionic nature of these species entails a large hydration enthalpy resulting from the stabilisation of a permanent negative charge. The ability of bicarbonate to diffuse throughout the near-interface regime puts it in league with other relatively large, polarisable anions such as I^- and Br^-, which have also been shown to display a propensity for the air-water interface [47, 240]. This contrasts with the behaviour of harder or more highly charged anions, which are usually repelled from the interface [47]. Our results suggest a clear tendency for bicarbonate to adsorb at the air-water interface [241]. This finding deviates from previous modelling using classical force-field MD [211], likely due to our use of a more accurate underlying theory - one that better captures the solute-solvent interactions occurring in this complex regime. Additional surface stabilisation of the interfacial reaction is due to the surface affinity of the hydronium ion H_3O^+, which is central to the bicarbonate-carbonic acid equilibrium. Fig. A.14 of Appendix A plots the density profile of H_3O^+ against distance from the instantaneous interface. Using $\Delta F = -RT \ln(\rho/\rho_0)$, we derive a free

energy of adsorption of − 1.3 kcal/mol of H_3O^+ at the air-water interface, which matches exactly the ΔF value determined from experiment [242].

Combining insights from Fig. 3.5 and Fig. 3.6, we deduce that reaction at the air-water interface predominantly occurs within the surface layer of water. At a high level, we can rationalize this propensity by considering the charge of our reacting species. However, the question remains why reactions are concentrated in this specific region at the interface. To address this, in Fig. 3.6b and Fig. 3.6c, averages of the solute-solvent coordination number, $\langle q_{\text{sol}} \rangle$, and the solute hydrogen-bond count, $\langle n_{\text{HB}} \rangle$, are plotted as a function of the distance from the interface. Looking at these properties, we observe that both are relatively uniform throughout the interfacial regime. For $\langle q_{\text{sol}} \rangle$, values are relatively constant up to $d_{\text{int}} = -2$ Å, whilst for $\langle n_{\text{HB}} \rangle$, values only start to reduce beyond -1 Å. Looking at $d_{\text{int}} \sim -1$ to -0.5 Å, which we have determined to be the most favourable location for reaction to occur, both $\langle q_{\text{sol}} \rangle$ and $\langle n_{\text{HB}} \rangle$ are comparable to their values in bulk (i.e., towards -8 Å) to within a couple of percent. This observation suggests that, despite lower effective solvent concentrations for this region, the surface layer of water provides bulk-like solvation conditions for reactive species. Therefore, reactions in this region can proceed with bulk-like free energies and reaction barriers in a way that minimizes disruption caused by hydrophobic CO_2 to the hydrogen-bonded solvent structure deeper in the aqueous phase.

'In-and-out' mechanism is consistent across differing levels of theory

In the preceding section, we suggested the existence of a new type of surface-mediated reaction, one characterised by a dynamic reaction site and with thermodynamic properties similar to those of the bulk reaction. Whilst compelling, it would be short-sighted of us to propose such a mechanism based on the results of just a single GGA functional. Therefore, work was undertaken to develop two additional MACE models, one trained at the BLYP-D3 level of theory and one at the RPA level, to validate the proposed mechanism. Further details on the training and testing of these models are provided in Appendix A.

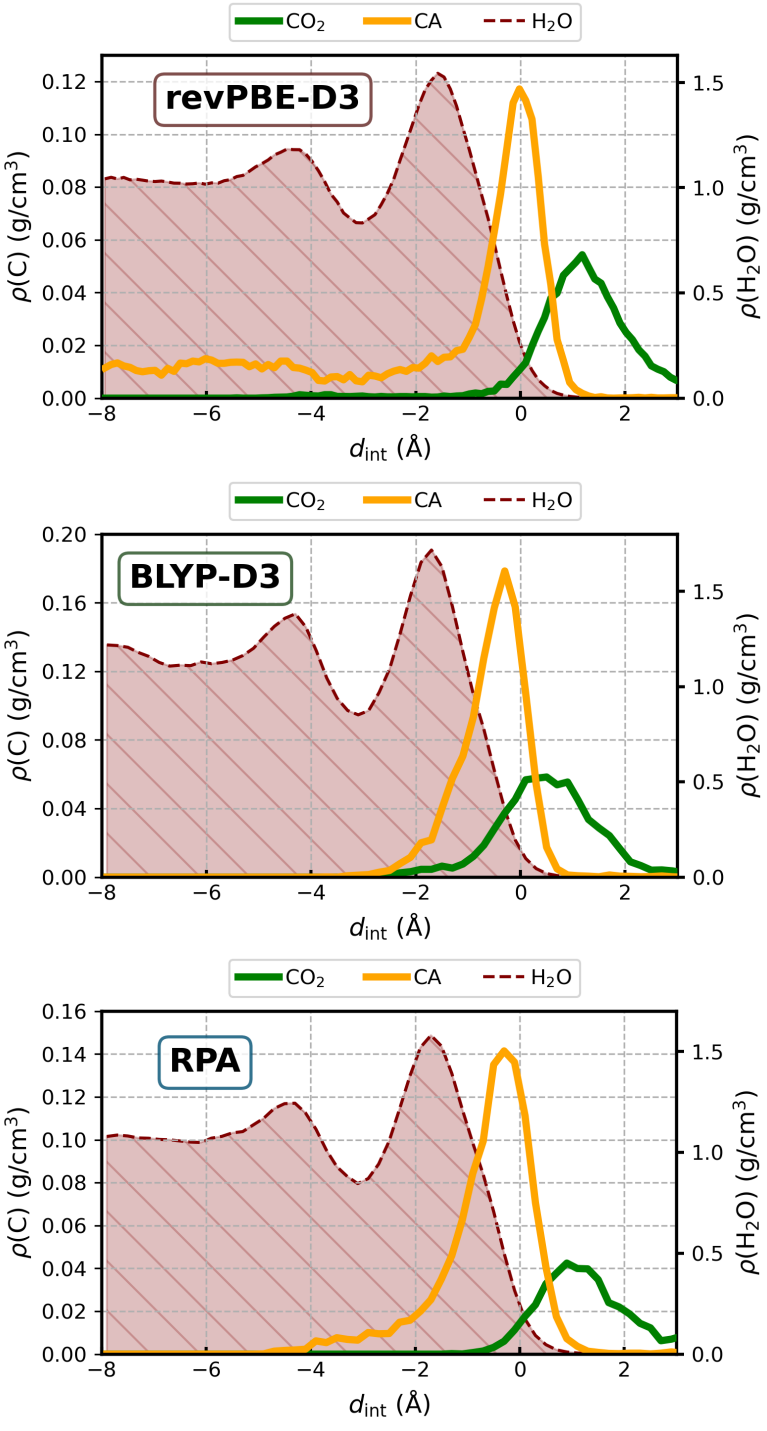

Fig. 3.7 Adsorption propensities of CO_2 and carbonic acid at the air-water interface. Profiles are shown for our main revPBE-D3 model as well as the BLYP-D3 and RPA models. In each panel, time-averaged densities are plotted as a function of distance from the instantaneous interface, with the carbon density given by the left axis and the water density given by the right axis.

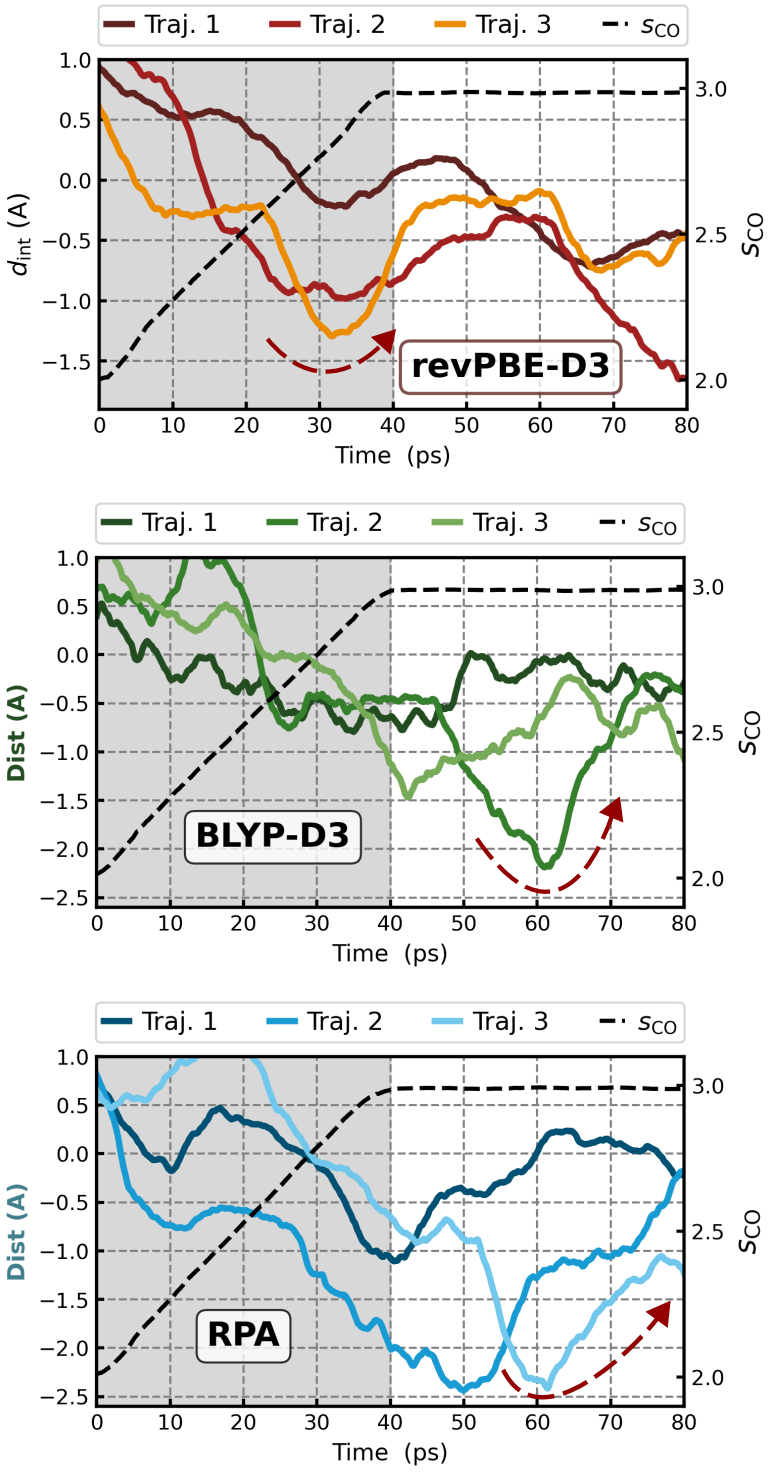

Fig. 3.8 The in-and-out mechanism observed using restrained MD. For each model (revPBE-D3, BLYP-D3, and RPA), three restrained MD runs are performed in which the C-O coordination number, s_{CO}, is gradually switched from 2.0 (CO_2) to 3.0 (carbonic acid). The resulting change in the distance of the reacting molecule to the instantaneous interface, d_{int}, is plotted against simulation time (coloured, solid lines - one for each trajectory). The shaded portion of the figure represents the period over which s_{CO} (dashed line) is switched from 2.0 to 3.0.

First, we obtained a series of density profiles for each model using free MD simulations. In each case, we extracted the water density, the CO_2 density, and the carbonic acid density. These profiles are shown in Fig. 3.7, where the carbon density (primary axis) and water density (secondary axis) are plotted as a function of the distance from the instantaneous interface. Looking at these profiles, we see very similar adsorption propensities for each model: CO_2 adsorbs on top of the interface at around 1 Å, whilst carbonic acid adsorbs at/just below the interface around the zero. Where CO_2 and carbonic acid represent the start- and endpoints of our interfacial reactions, these profiles are consistent with an in-an-out-style reaction mechanism, one in which the reactive species ultimately returns to the interface following reaction.

Having confirmed the interfacial adsorption propensities for CO_2 and carbonic acid, we could now more directly evaluate the reaction mechanism through restrained MD simulations at the air-water interface. In these simulations, we gradually switched the C-O coordination s_{CO} from 2.0 (CO_2) to 3.0 (carbonic acid, CA) over a 40 ps period, after which the restraint was fully switched off. For each model, three trajectories were initialized from different starting configurations and velocities (9 simulations in total), and the distance of the reacting species from the instantaneous interface, d_{int}, was monitored. The results of these simulations are shown in Fig. 3.8. In each panel, we plot d_{int} and s_{CO} (primary and secondary axes, respectively) as a function of simulation time. Across the 9 different trajectories, we observe similar trends in d_{int}: as s_{CO} is switched from 2.0 to 3.0, d_{int} decreases from an originally positive value to a negative value; following the removal of the restraint, d_{int} starts to increase again and tends towards the instantaneous interface. Whilst this behaviour is overall representative of an in-and-out mechanism, we caveat this by highlighting the statistical fluctuations in d_{int} with choice of system initialisation. Ideally, we would run many more replicas of this system for each level of theory, thereby allowing us to obtain an averaged $\langle d_{int} \rangle$ as a function of simulation time. However, that we can reproduce this in-and-out behaviour from a handful of simple restrained MD runs is reassuring and provides further, supplementary evidence for the existence of the in-and-out mechanism presented in Fig 3.5.

3.4 Summary and Outlook

In this chapter, we have shown that the CO_2 + H_2O hydration reaction proceeds via an 'In -and-Out' mechanism at the air-water interface. This mechanism is characterized by a change in the position of the reacting species at the interface, a phenomenon that reflects evolving solute-solvent interactions in converting from reactants to products. Similarities between the bulk and interfacial solvation environments promote similar modes of reactivity and near-identical free energy profiles for the bulk and interfacial processes. These similarities suggest that the CO_2 + H_2O reaction is equally as feasible at the interface as in bulk, therefore warranting greater attention for this region when considering the reactivity of complex, multi-component systems.

Importantly, the mechanistic insights reported here are consistent across the three models employed, from revPBE-D3 to RPA-based machine-learned potentials. By incorporating beyond-DFT RPA reference level, our MLIPs capture high-level electronic-structure accuracy while enabling statistically converged, multi-nanosecond sampling that would be out of scope for direct ab-initio molecular dynamics. These extended simulations are essential for resolving the 'in-and-out' mechanism of CO_2 hydration at the air–water interface. Despite their good description of interfacial properties, standard empirical force fields, being non-reactive, cannot be employed for such insight, underscoring the need for reactive MLIPs. The combination of high-accuracy reference data and enhanced sampling therefore establishes a new benchmark for exploring reactive events at interfaces and is readily transferable to other chemically complex systems.

In the context of ocean acidification, our results have revealed a viable path for carbonic acid formation at the air-water interface: surface-adsorbed CO_2 diffuses into the aqueous surface layer, reacts to form carbonic acid, and is then ejected out of solution. Given the notable concentrations of CO_2 adsorbed at the ocean's surface (see Chapter 4), our results suggest that H_2CO_3 and HCO_3^- formation will occur within a couple of Å of the ocean's surface. The experimental determination of H_2CO_3/HCO_3^- concentrations using sum-frequency generation techniques would be ideal to test this hypothesis. Computationally,

future work will explore the influence of ionic species, e.g., Na^+ and Cl^-, on the course of CO_2 hydration as well as potential clustering mechanisms for multiple carbon species [211]. A recent geoscience study has shown that subtle temperature fluctuations at the ocean surface promote enhanced CO_2 absorption, leading to a 7% increase in absorption rates compared to previous estimates [243]. Understanding this enhanced absorption, as well as the impacts on the ensuing acidification, will be important in helping to provide a more realistic picture of ocean acidification.

Beyond $CO_2 + H_2O$ systems, our work has important implications for more general chemistry at aqueous interfaces. Harnessing the accuracy and computational efficiency of MACE potentials, we have demonstrated that, for reactions involving some change in charge or polarity, there exists a correlation between the extent of reaction and molecular positioning at the aqueous interface. In simple terms, the depth of a reactive species relative to the air-water interface is determined by how far along the reactive process it is. The reactants, products, and transition state are all dynamic entities that adapt their positions in response to evolving solute-solvent interactions. Where previous studies considered only selected distances above or below an interface, our work considers the whole interfacial regime in evaluating reactivity. We hypothesize that, for most 'emerging-charge' reactions at the air-water interface, reaction occurs within the first molecular layer of water. This region offers a balance between charge stabilisation and minimizing disruption to the hydrogen-bonded solvent structure. We expect that these insights may have broader implications for other types of chemical reactions at interfaces, for example, in phase-transfer catalysis, where the location of the reactive site is central to chemical transformation [244].

In conclusion, the work presented in this chapter addresses the nature of $CO_2 + H_2O$ hydration at the air-water interface and represents a step forward in the way we approach interfacial reactivity. We have shown that solvation conditions are bulk-like for the near-interface regime and that reactive processes are accompanied by positional change at the air-water interface. Given the ubiquity of interfaces in nature, we anticipate that such insights will be of direct importance to the study of other processes in nature, for example,

'on-water' organic reactions, nanodroplet reactions, and phase-transfer catalysis. Our work makes the case for the inclusion of translational considerations in the treatment and representation of chemical reactions, which we expect to lead to a re-evaluation of important chemical processes and surface phenomena.

Chapter 4

Liquid-Liquid Interface: Modelling interfacial tensions and molecular build-up in pressurised CO_2-H_2O systems

> A line is a dot that went for a walk.
>
> *Paul Klee*

In the previous chapter, we uncovered new and interesting reaction phenomena occurring at aqueous interfaces under ambient conditions. Over the next few pages, we turn to more extreme, highly pressurised conditions relevant to geological environments and carbon storage applications. Under these conditions, CO_2 can exist in either gaseous or liquid form, thus opening the potential for interesting phase behaviour at the divide between CO_2 and water. The contents of this chapter are based on published work: 'The wetting of H_2O by CO_2' [223]. Files and data relating to this work can be found at `https://github.com/water-ice-group/co2-on-h2o`.

4.1 Context

The boundary between two immiscible fluids represents a unique and fascinating regime. The properties of this biphasic interface, noticeably different from those of bulk fluid, arise from its inhomogeneous composition and the anisotropic distribution of its constituent particles [245]. The resulting asymmetry in forces acting between these particles promotes a series of interesting phenomena, including molecular orientational alignment, density gradients and structuring, phase transfer effects, and variations in reactivity and dielectric properties [238, 245–247].

Arguably the most important biphasic interface is that of carbon dioxide and water, CO_2-H_2O. This interface exhibits a diverse range of properties, which stem from the distinct phases that CO_2 can form with subtle changes to temperature and pressure. For ambient temperatures, CO_2-H_2O exists as a gas-liquid interface for pressures p less than the critical pressure (P_C = 73.8 bar, T_C = 304.1 K) [248]. At higher pressures, CO_2-H_2O forms a liquid-liquid (or supercritical-liquid) system, suggesting that temperature or pressure can be used as a lever to modulate biphasic properties (see Fig. 4.1). Biphasic CO_2-H_2O finds use in a variety of real-world applications and phenomena, from compressible solvent design [249] to ocean acidification monitoring [250] to enhanced oil and gas recovery schemes [251]. They are also common to various carbon capture and storage (CCS) techniques, where anthropogenic CO_2 is captured at source and injected under pressure (usually in excess of 80 bar) into predominately aqueous subsurface storage sites, e.g., saline aquifers or disused coal seams [191]. In these storage sites, retention of the anthropogenic carbon is mediated by the interactions between injected CO_2 and *in situ* H_2O, meaning that both storage capacity and the duration are functions of the interfacial behaviour. Whether CO_2 is trapped as a liquid or in its supercritical state depends on the pressure and the temperature, which are determined by the depth of the storage site; in general, storing CO_2 more than 800 m below Earth's surface results in supercritical phase formation [252].

Realising these applications for biphasic CO_2-H_2O requires a detailed knowledge of its biphasic interface. This includes understanding both its microscopic properties (in terms

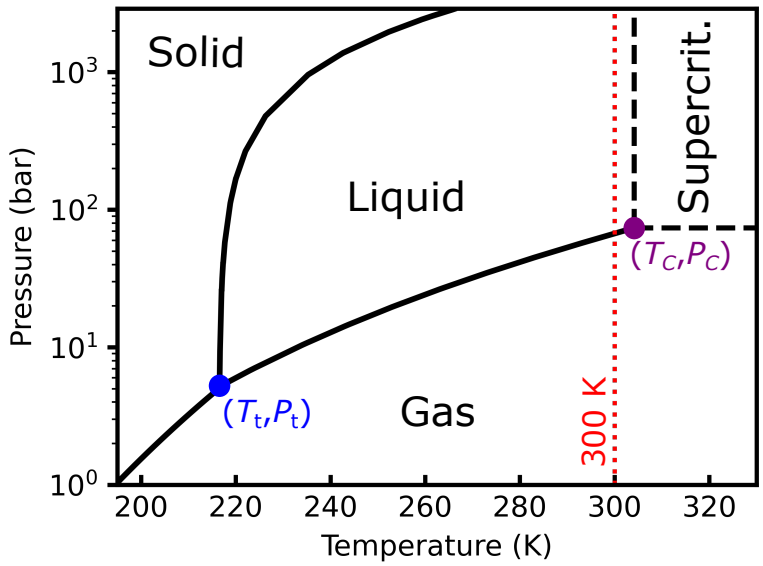

Fig. 4.1 Phase diagram of CO_2 for $T = 190 - 330$ K and pressures $P = 1 - 2900$ bar. Curves show the approximate boundaries between phases, with the triple and critical points highlighted on the figure. For $T = T_t = 217$ K and $P = P_t = 5.18$ bar [248], the solid, liquid, and gaseous phases coexist in equilibrium with one another. For $T > T_C = 304.1$ K and $P > P_C = 73.8$ bar [248], the boundary between liquid and gaseous phases disappears, and CO_2 becomes supercritical. The red vertical line denotes the temperature at which the simulations detailed in this chapter were performed.

of the structuring of molecules, their orientations, the nature of their bonding, etc.) as well as its macroscopic properties, such as phase densities and interfacial tensions (IFTs), γ. The IFT, in particular, is critical to understanding biphasic interfaces. This property encapsulates much of the macroscopic nature of the interfacial region and is used to gauge their relative miscibilities. In terms of CCS and CO_2-H_2O, γ is directly proportional to the sealing capillary pressure, which quantifies the volume of CO_2 that can be stored and thus is a good estimate of the efficacy of a chosen storage site [253, 254].

An extensive picture of both micro- and macroscopic properties of biphasic CO_2-H_2O has been built up over the last decades. In experimental literature, researchers have focused mostly on the measurement of γ under differing temperatures and pressures [255–265]. In general, γ is observed to decrease with either increasing pressure or increasing temperature, though the exact nature of this reduction is dependent upon which CO_2 phase is present (see later, Fig. 4.4). Measurements from experiment, however, are subject to significant variation depending on experimental setup (e.g., thermocouple placement, equilibration

times, density treatment) [253]. Therefore, experimental work is often supplemented by theoretical and computational estimates for γ. Statistical perturbation models, such as statistical associating fluid theory (SAFT), do a good job in reproducing experimental values but can sometimes lack sufficient microscopic insight on the origins of these results [266–268]. In contrast, force-field (FF)-MD simulations provide both estimates for γ and full atomistic detail on the behaviour of biphasic CO_2-H_2O. Although the exact description of the CO_2-H_2O interface is sensitive to the choice of the empirical parameters, FFs have provided several important trends and insights. These include: CO_2-H_2O interfaces are molecularly sharp; molecules form a layered structure within several angstrom of the interface; water's dipole orients parallel to the interface; and there exists a strong, lateral network of hydrogen bonds within the first contact layer of water [26, 253, 269–272].

Despite the valuable insight uncovered from these studies, a number of open questions remain surrounding biphasic CO_2-H_2O. For example, how exactly does γ behave in the vicinity of CO_2's critical point (P_C, T_C)? How do high pressures impact the value of γ? And what is the nature of interfacial CO_2 and H_2O molecules and how exactly do they interact with one another?

Building on previous work in the field, this chapter aims to provide a new perspective for characterizing the biphasic CO_2-H_2O interface. This work focuses on generating MLIPs, which we use to perform MD simulations with an *ab initio* level of accuracy. Unlike previously applied methods, our work breaks away from the empirical fitting to experimental or literature values and instead provides estimates from the ground up. As discussed in Chapter 2, MLIPs already have a proven history of success in simulating complex systems [35, 43, 50, 214, 273–275], and their use in simulating biphasic CO_2-H_2O would help address many of the open questions on this system. To date, however, an *ab initio* or MLIP description of biphasic fluid interfaces has remained elusive. Biphasic systems by definition require larger simulation boxes than bulk for direct *ab initio* simulations and for generating training data for MLIPs. At the same time, converging the properties of the bulk and interfacial regions requires long simulation time, beyond the reach of standard molecular dynamics.

In this chapter's work, we bring together *ab initio* accuracy and thorough sampling to accurately simulate large and complex mixtures. We utilize a number of distinct methodological features - specifically, MLIPs for fast and accurate *ab initio* total energy predictions, an active learning strategy to build compact and representative training sets, and replica exchange simulations for enhanced sampling of the interface. Our approach allows accurate and converged analysis of both macro- and microscopic properties of the biphasic CO_2-H_2O interface. Building on the extensive literature in this regime, we obtain room-temperature estimates of the interfacial tension as a function of pressure. These are found to be in good agreement with the available literature and help discern experimental reference data across the gas-liquid phase transition for CO_2. Improved predictions with respect to previous classical MD results, particularly for low pressure regions, are attributed to the greater accuracy of the underlying theory. Having obtained a correct description of the interfacial tension, we study the structural properties of the CO_2-H_2O interface to obtain key microscopic insights. Notable observations include the build-up of a liquid-like CO_2 layer for low pressures and a reduced structuring in the aqueous phase with increasing pressure. We anticipate the future application of our potential to studying other important state points for CO_2-H_2O as well as characterizing the dynamical system properties, e.g., in the form of diffusion coefficients and interfacial residence times. We believe that our approach will serve as a robust blueprint for investigating other complex biphasic interfaces.

4.2 Methods

Our approach to modelling the biphasic CO_2-H_2O interface comprises three established components: high-dimensional neural network potentials [138, 215, 276] (HD-NNPs) to act as our atomistic force generators; Query by Committee (QbC), an active learning technique for generating optimised structural datasets using a minimal number of training points [215]; and replica exchange molecular dynamics (REMD) to expedite the statistical convergence of interfacial properties over multiple thermodynamic state points. Combining these features allows us to apply accurate potential energy surfaces for simulating large,

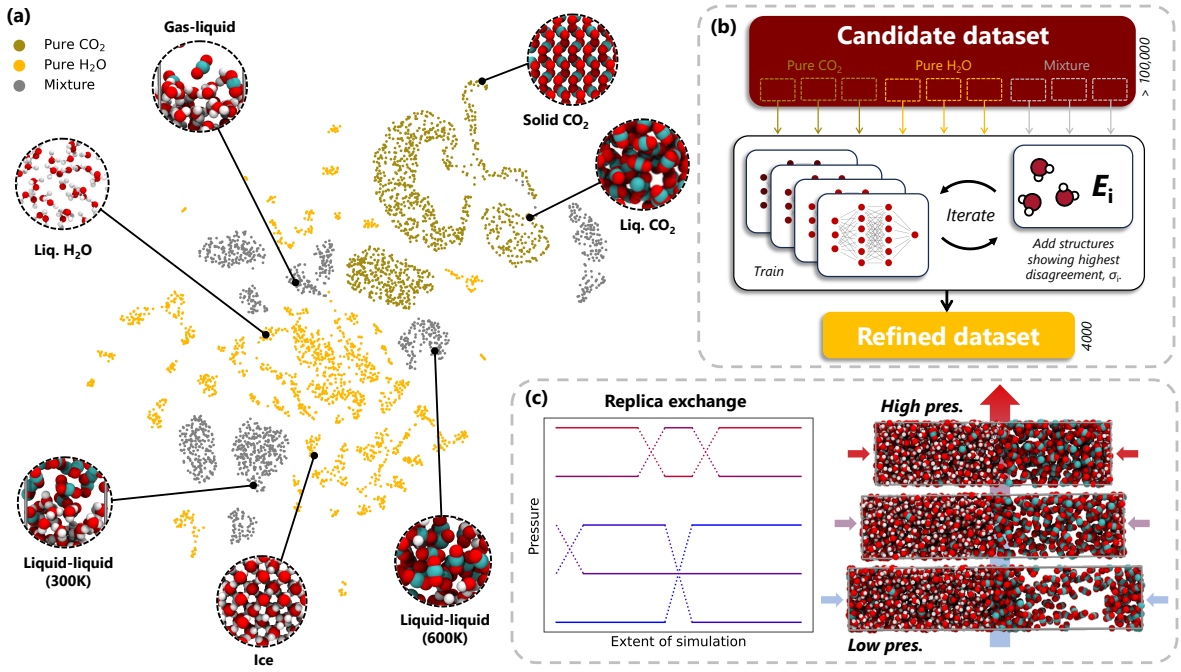

Fig. 4.2 Modelling biphasic fluid interfaces. **(a)** 2D projection of the structural data used to train our neural network potential. **(b)** Query-by-committee workflow for the creation of a compact, structurally diverse dataset for each constituent trajectory. **(c)** Application of the model using replica exchange molecular dynamics towards the determination of macroscopic and microscopic properties. System replicas are set up and run in parallel across 15 different pressures. Periodic configuration swaps between these replicas enable a faster exploration of configuration space and a more rapid convergence of equilibrium observables.

complex molecular systems over extended time periods. An overview of our approach is provided in Fig. 4.2.

Training

Our work follows the committee NNP development procedure outlined in Ref. [215]. We employ Behler-Parrinello HD-NNPs trained on DFT-level *ab initio* total energies and forces calculated with `CP2K` [120, 138]. Local atomic environments were described using atom-centred symmetry functions [215]. We employed the BLYP functional [277, 278] augmented by Grimme's D3 corrections [115]. This setup has been shown to closely reproduce the condensed-phase and structural properties of both pure CO_2 and pure H_2O [50, 279, 280]. Additionally, BLYP-D3 replicates the critical and vapor-liquid coexistence properties for CO_2, making it an appropriate selection for treating the various CO_2 phases

exhibited within our chosen pressure range [50, 280]. Goedecker-Teter-Hutter (GTH) pseudopotentials were used for treatment of the core electrons, TZV2P-GTH basis sets for the valence electron density, and a planewave cutoff of 1050 Ry was used.

Training of our NNPs was implemented using a QbC active learning strategy over multiple improvement cycles. In this approach, a candidate dataset is iteratively refined through the generation and repeated retraining of a 'committee' of NNP models. These models are initialised using different random seeds and trained on different initial subsets of the total candidate dataset. In our work, we trained 8 different models, or 'committee members', each seeded with 20 randomised structures extracted from the training dataset. Following this initial training round, the committee members then make predictions on the energies of a presented subset of structural configurations. Configurations presenting the largest error or disagreement between committee members are added to the training sets of each model. Each member is then retrained using the updated dataset - this constitutes one complete training cycle. Training is repeated over several improvement cycles until the overall model errors (evaluated through predictions on a validation dataset) converge. An overview of this active learning strategy is provided in Fig. 4.2b.

In our case, the candidate dataset was provided in the form of chemical structures labelled with revPBE-D3 energies and atomistic forces. Structures were generated using a mixture of flexible force field potentials (SPC/Fw [281] + Zhu [282], Lorentz-Berthelot combining rules) as well as preliminary NNPs across three active learning cycles. This gave a total of more than 100,000 structures. QbC - as implemented in the `AML` package [215] - was then used to trim and optimize this dataset, resulting in a refined dataset of some 4000 structures. Using this dataset, a final model was trained using the openly available N2P2 package [283].

This final, refined dataset is shown in Fig. 4.2a. A breadth of structures is included here - including gas-liquid, liquid-liquid, crystalline, and pure-phase structures - in order to maximize exploration of the relevant configuration space. A committee of NNPs was trained using `N2P2` (8 in total) [283], and the committee member displaying the lowest errors was selected as the final model. This final NNP was validated against the predictions

of *ab initio* MD in the form of energies and forces (test RMSEs: 3.31 meV/atom and 88.26 meV/Å, of similar performance to that reported in Ref. [284] for pure water) as well as structural predictions of pure-phase properties, which are detailed in Figs. B.1-B.3 of Appendix B. Long range tail corrections for the chosen NNP cutoff are expected to be on the order of 0.5-1 mN/m based on explicit classical model analysis [285], which is smaller than our usual statistical error obtained from block averaging. Due to these reasons, we have not applied any explicit tail correction to our data.

Simulation setup

System sizes and compositions were chosen to mitigate periodic error and finite-size effects, which have been shown in FF-MD to impact IFTs and other interfacial properties [286, 287]. Results from our system-size analysis in which we varied lateral (xy) dimensions and molecular compositions are shown in Fig. 4.3. This analysis was performed using a combination of water and CO_2 FFs (SPC/E + EPM2 [68, 288]) under the NP_zAT ensemble, with a fixed number of particles N, fixed lateral (xy) area $A = l_x \times l_y$, fixed temperature (300 K), and P_z set to the target pressure (i.e., variable l_z). Our choice of box size and composition reflects the smallest system for which γ converges to within 0.5 mN/m of the largest box limit. The final selected system consisted of 600 water molecules and 200 CO_2 molecules. Lateral dimensions xy were fixed at 20 Å, and periodic boundary conditions were applied along all three axes. Atomic configurations were initialized such that the CO_2-H_2O interface resided parallel to the xy plane.

Replica exchange simulations

To expedite the exploration of configuration space and the convergence of equilibrium properties, we performed REMD across 15 different systems replicas. Each replica i was simulated at a distinct pressure P_i, where $P_i \in [1, 500]$ bar. Every 1000 steps, configuration swaps between replicas i and j were proposed, each swap with an associated probability given by

$$p_{\text{acc}}(i \leftrightarrow j) = \min[1, \exp(-\beta\Delta)] \tag{4.1}$$

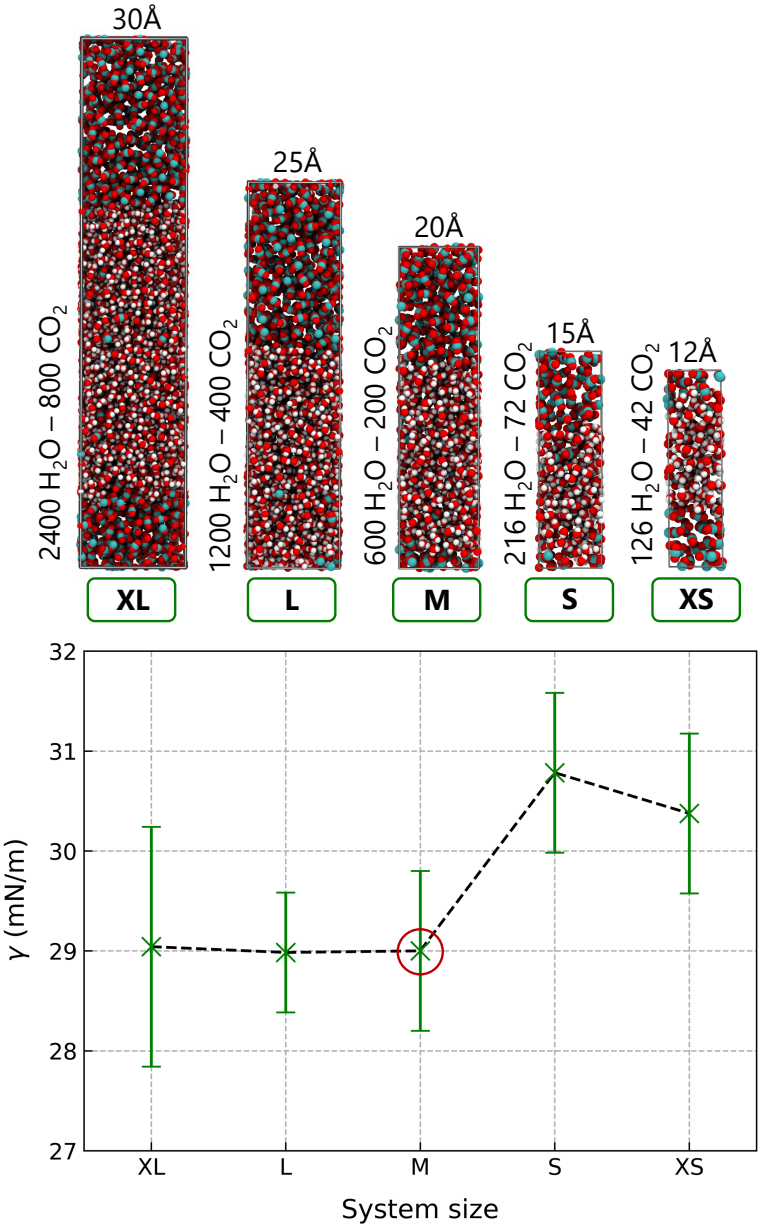

Fig. 4.3 The effect of system size on the convergence of interfacial tension. Plot shows the interfacial tension of biphasic CO_2-H_2O against system size for 300 K and 30 MPa. Simulations were performed using SPC/E + EPM2 for 120 ns. The setup selected for our production runs is highlighted by the red circle (M). Representative snapshots of each of these systems are shown along the top of the figure.

where β is the inverse temperature and $\Delta = (P_i - P_j)(V_j - V_i)$, where P and V give the replica pressure and volume, respectively [289]. In its presented form, Eq. 4.1 amounts to swapping the configurations between system replicas that are close in pressure and volume. A simplified schematic explaining REMD is shown in Fig. 4.2c. NNP-REMD was performed using the open-source `i-pi` package [290] with `LAMMPS` as the force generator

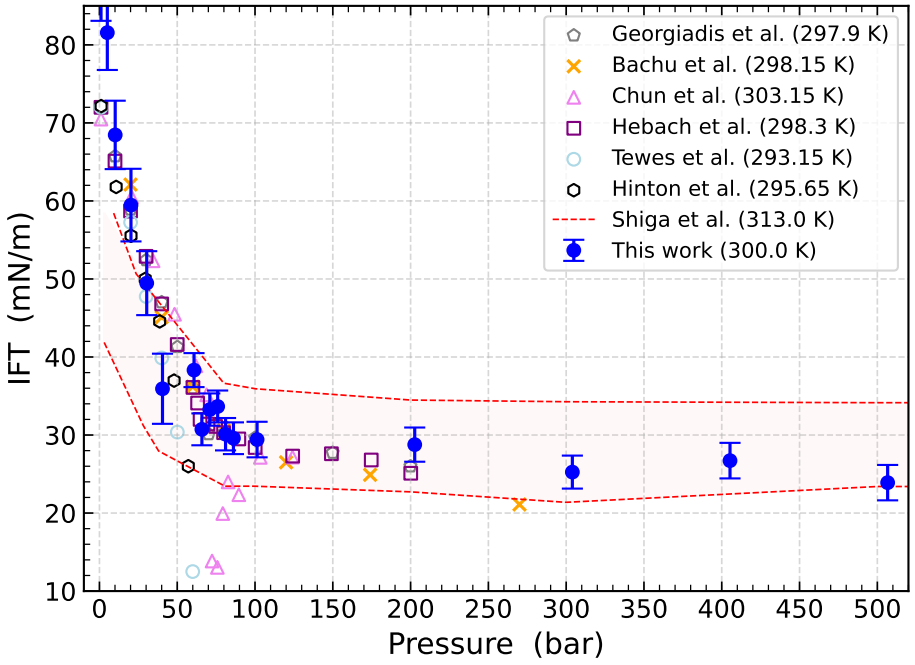

Fig. 4.4 Measuring the interfacial tension (γ) of CO_2-H_2O. Interfacial tension results for our neural network potential (blue, filled) measured at 300 K for pressures 1-500 bar. Error bars represent the 1σ uncertainty, estimated by integrating the autocorrelation function to a lag of 100 sampling intervals. Selected previous experimental results are shown as hollow markers. Computational results from Shiga et al. (FF molecular dynamics) [26] are encompassed within the shaded region and correspond to various combinations of H_2O (TIP4P/2005, SPC/E) and CO_2 (EPM2, PPL, TraPPE) FFs. The dashed red lines represent the maximum and minimum values of γ predicted by Shiga et al. at each pressure.

[229, 291] and substituting hydrogen for deuterium atoms. For each state point below 40 bar, simulations were run for 3 ns of simulation time, while above 40 bar simulations were run for 10 ns of simulation time corresponding to 3×10^6 and 10^7 steps, respectively. These were performed under the NP_zAT ensemble. Collectively, these simulations compile 150 ns of *ab initio*-quality data, forming a robust basis for our analysis. From our NNP-REMD data, we extracted macroscopic measurements (i.e., IFTs) as well as microscopic properties in the form of density profiles, molecular orientations, and radial distribution functions (RDFs). We have checked the sensitivity of our results on the choice of DFT functional by also training an NNP model to revPBE-D3. Resulting IFTs prove to be very similar overall, and these are shown in Fig. B.6 of Appendix B.

4.3 Results

IFT profile replicates experimental values

The interfacial tension is a key property for determining the miscibility of two phases. A number of previous experimental and computational studies have sought to characterize the IFT of CO_2-H_2O as a function of pressure. In Fig. 4.4, we plot the results of these studies at roughly room temperature alongside our own estimates obtained using the developed NNP. We compute γ using the statistical mechanical route of Kirkwood and Buff (KB) [292],

$$\gamma = \frac{L_z}{2}\left(P_{||} - P_{\perp}\right) \tag{4.2}$$

where L_z gives the z length of the simulation box, and $P_{||}$ and $P_{\perp}$ represent the normal and lateral pressure tensor components, respectively.

Inspection of Fig. 4.4 yields several observations. For low pressures ($p < 60\,\text{bar}$), our simulations predict a steep descent in γ with increasing pressure. This phenomenon is associated with the gradual accumulation of CO_2 at the water surface, a process which reduces the spatial anisotropy at the phase boundary and thus also the magnitude of γ (see later, Fig. 4.5). For intermediate pressures ($60 \leq p < 100\,\text{bar}$), our NNP results indicate an abrupt change in the behaviour of γ as we cross the critical pressure boundary (73.8 bar), going from gas-liquid to liquid-liquid. And finally for high pressures ($p \geq 100\,\text{bar}$), our model yields a slight reduction in γ with increasing pressure. The comparatively small gradient in γ for this regime is attributed to a saturation in the concentration of CO_2 close to the interface, such that changes to the pressure lead to minimal change in the near-surface environment. A minimum of 24 ± 2 mN/m is recorded at 500 bar.

Across Fig. 4.4, we observe close agreement between experimental and MLIP results, within the range of pressures for which experimental data is available. This is true for both low pressures ($p < 60\,\text{bar}$), where γ_{NNP} replicates the steep descent in gas-liquid IFTs, and high pressure ($p \geq 100\,\text{bar}$), where γ_{NNP} follows the gradual decline in liquid-liquid IFTs as reported by Hebach et al. [256] and Bachu et al. [259] A notable aspect of our

work is the extension of IFT predictions beyond the currently available experimental pressure range for $\sim$ 300 K. Moreover, γ_{NNP} values recorded for intermediate pressures (60 $\leq p <$ 100 bar) provide additional clarity on the nature of γ in the vicinity of CO_2's phase transition pressure p_{T} (73.8 bar). This region has previously been a point of contention, with experimental results differing by up to 20 mN/m for pressures close to p_{T}, as seen by the selection of results displayed in Fig. 4.4. Our results clearly support the presence of a break in the slope between gas-liquid and liquid-liquid regimes, as reported by a number of authors [256, 259, 260]. There is no evidence of the 'dip' or 'cusp' in γ near p_{T} as predicted by some experiments [255, 257]. Such observations are now thought to be artifacts of the experimental setup, e.g., differences in the thermocouple placement or due to the inherent uncertainty in near-phase-transition properties [253, 256].

Our results also qualitatively corroborate the results of previous FF simulations. These are encompassed within the shaded portion of Fig. 4.4, the limits of which represent the extent of γ predictions for varying combinations of FF models (e.g., SPC/E + EPM2, SPC/E + PPL, TIP4P/2005 + PPL, etc.) [26]. Whilst the exact value of γ is sensitive to the choice of models and parametrization, the overall range of FF predictions is in qualitative agreement with our NNP predictions, with a notable exception of the low pressure regime [26]. For these pressures, classical FFs systematically underpredict γ by 15-30 mN/m. We attribute the improved performance of our NNPs to the more accurate level of underlying theory compared to FFs, and the fact that our NNP is trained explicitly to replicate the *ab initio*-level interactions between CO_2 and H_2O. In comparison, bicomponent FFs are constructed using geometric/mathematical mixing rules, the choice of which is often *ad hoc* and can lead to substantial variation in the resulting thermodynamic properties [293–295]. This is exemplified by the large spread in γ values shown for FF-MD in Fig. 4.4.

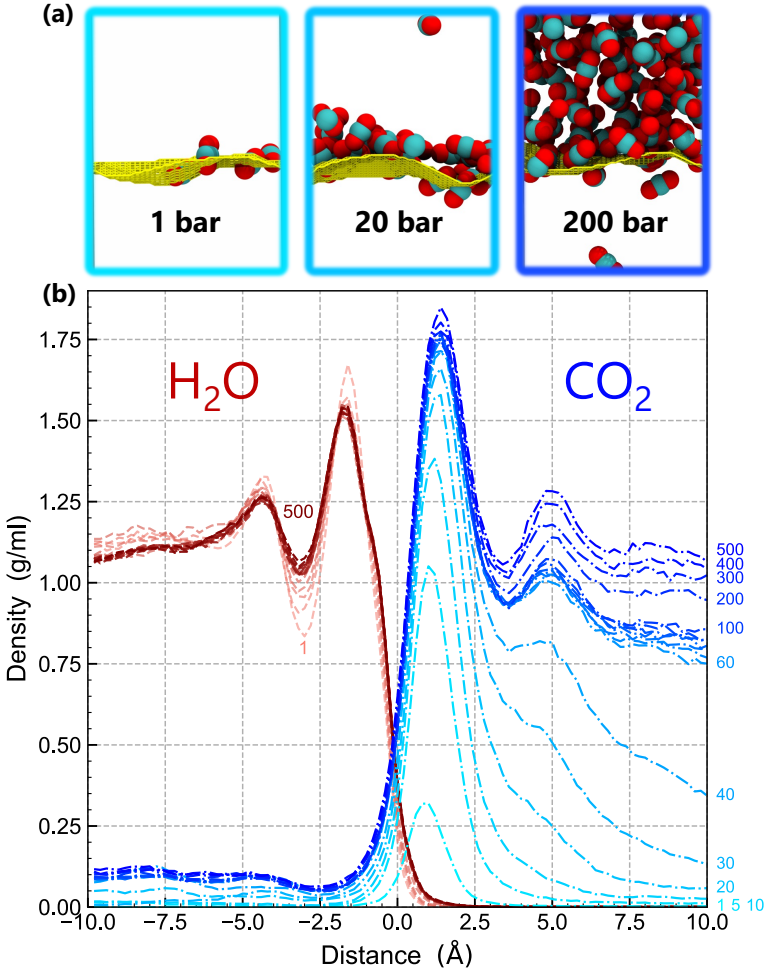

Fig. 4.5 Profiling the change in CO_2-H_2O from 1 to 500 bar. **(a)** Representative snapshots of the CO_2 phase and instantaneous interface (yellow mesh) for 1, 20, and 200 bar. H_2O has been omitted for visual clarity. **(b)** Density profiles are shown at different pressures for water (red) and CO_2 (blue) with distance from the instantaneous interface that separates them.

CO_2 forms a saturated monolayer at low pressure

To better understand the interfacial tension shown in Fig. 4.4, we plot a series of microscopic profiles detailing the variation in density ρ with distance d from the instantaneous interface. This interface is calculated at each timestep using the Willard-Chandler formalism [236], a coarse-grained approach that uses atom-centred Gaussians to identify instantaneous phase boundaries in a system (see Fig. B.7 for schematic). Under this formalism, the distance d is defined for each frame as the shortest distance between a molecule and the instantaneous surface. Resulting profiles are plotted in Fig. 4.5 for both H_2O (red) and CO_2 (blue). An inspection of Fig. 4.5 reveals a stark contrast in the phase behaviour of

water and CO_2. Focusing first on the water phase, we observe a layered structuring in ρ across all pressures, in close agreement with the behaviour of the air-water interface [275] (see Fig. 3.6 of Chapter 3). The shape of these profiles is relatively unvarying with changes to the pressure, though we do note an enhanced structuring of molecules for $p \leq 20\,\text{bar}$ approaching atmospheric pressure. In contrast to this behaviour, the CO_2 profile exhibits large changes in both magnitude and shape with changes to the pressure. For $p < 10\,\text{bar}$, density profiles register a sharp peak at roughly 1 Å with a density that tails off exponentially with distance from the interface. Physically, this represents a film of monolayer CO_2 adsorbed at the water surface and a gaseous CO_2 phase extending beyond to large distances. For $20 \leq p < 60\,\text{bar}$, a second peak is observed at 4 Å, suggesting the formation of a bilayer of CO_2 at the interface. Beyond 60 bar, the exponential decay in density is replaced by liquid-like layering that tends towards bulk density for large distances. For the sampled pressure range, the fraction of CO_2 located within the aqueous component increases with increasing pressure. This is a product of both greater CO_2 accumulation at the aqueous surface as well as a reduction in the interfacial sharpness at higher pressure. Calculated CO_2 solubilities are shown in Fig. B.5 of Appendix B and found to replicate the general trend in experimental results.

Relating these microscopic observations with the IFT profile of Fig. 4.4, it is clear that the variation in γ is a product of the physical changes in CO_2 with changing pressure. Unlike water, CO_2 is a nonpolar molecule that exhibits relatively weak intermolecular interactions. Its critical pressure P_C resides within our range of sampling, so we end up simulating two distinct phases of CO_2 as well as a phase transition region. In comparison, at 300 K, water is firmly within the liquid phase, and its high natural surface tension - a product of its extensive hydrogen bonding network - ensures preservation of its structural integrity and prevents extensive mixing with the CO_2 phase. The most significant change in the structuring of water occurs for low pressure ($p \leq 20$ bar). It is interesting to note that this change coincides with the emergence of the monolayer in CO_2. The combination of these observations possibly suggests that structuring of the aqueous phase is mediated

by the extent of monolayer coverage of the adsorbed phase and that subsequent adsorbed layers have minimal impact.

Our *ab initio*-level profiles share many similarities with previous force field modelling [269, 270]. This includes the formation of monolayer and bilayer CO_2 and the recovery of liquid-like properties at high pressure. Interestingly, however, the pressure at which our model predicts the emergence of a CO_2 monolayer (and therefore also the starting of a second CO_2 layer) is much lower compared to conventional FF predictions (e.g., those of SPC/E + EPM2). In our results, a fully saturated monolayer forms at 20 bar; in FFMD studies, this occurs at higher pressures (around 60 bar for SPC/E+EPM2), thereby suggesting a lower wettability for CO_2 [270]. These observations corroborate the *ab initio* work of Morishita et al.,[296] who have suggested that differences in the interfacial behaviour predicted by *ab initio*-level modelling and FF-MD stem from the weaker attractive CO_2-H_2O forces given by the latter. Similarly, we conclude that differences in the density profiles arise from the improved CO_2-H_2O descriptions provided by NNPs, which are trained to account for both polarization and charge transfer effects. On the other hand, the classical FFs used so far to study this interface are limited by the nature of their mixing rules and their rigid-body formulation, which we would not expect to fully represent the interfacial regime.

Monolayer shows liquid-like properties

Results from the microscopic profiling of biphasic CO_2-H_2O show the formation of a saturated CO_2 monolayer at low pressure. To better understand this phenomenon, we investigate the structural properties of CO_2 within 2.5 Å of the instantaneous interface, i.e., within the first contact layer. Fig. 4.6 plots both the 2D lateral distribution function (LDF) and angular distribution of these molecules. The LDF, $g(r)$ is calculated such that it accounts for the quasi-2D nature of this monolayer

$$g(r) = \frac{dn_{\mathrm{r}}}{dA \cdot \rho} = \frac{dn_{\mathrm{r}}}{2\pi r dr \cdot \rho} \tag{4.3}$$

where dn_r is the number of CO_2 molecules within an annulus of thickness dr, and ρ gives the local density. Our use of dA in the denominator (as opposed to the dV term used for RDFs) accounts for the mostly planar distribution of CO_2 molecules within 2.5 Å of the instantaneous interface (see Fig. B.8 for schematic). Inspection of Fig. 4.6a shows how the structuring of this layer quickly converges towards a bulk-like character. By 20 bar, we see a distribution that emulates that of bulk CO_2 and suggests a liquid-like nature for the first contact layer. This is true for pressures 20-500 bar.

In Fig. 4.6b, we show the distribution of angles between the instantaneous interface and the CO_2 orientation. Across all pressures, our results suggest a clear preference for CO_2 to lie flat at the water surface. This corroborates previous computational work, which suggest that interactions between water and CO_2 are maximized when the latter molecule lies parallel at the surface [269]. We note that the distribution is more pronounced at 90 degrees for $p < 20$ bar, where the adsorbed CO_2 is more exposed and has fewer molecules to interact with. The addition of more adsorbed molecules at the aqueous surface reduces the strength of water-CO_2 interactions, allowing for greater freedom in the latter molecule's orientational alignment with increasing pressure.

4.4 Summary and Outlook

Biphasic interfaces represent complex and dynamic regimes. In this chapter, we have highlighted an approach for analysing these regions in a way that combines *ab initio* accuracy with converged statistics and computational tractability. Our methodology allowed for nanosecond treatment of large CO_2-H_2O systems, which has yielded a converged IFT profile at an *ab initio* level of accuracy. Our results show good agreement with experimental literature for low- and high-pressure regimes, and microscopic insight into this behaviour has been provided. The reproduction of results in the vicinity of a phase transition (gas to liquid) is notable given the difficulty associated with treating this highly dynamic regime. We observe the formation of a saturated CO_2 monolayer at low pressure (20 bar) with structural properties akin to those of bulk CO_2. The emergence of this

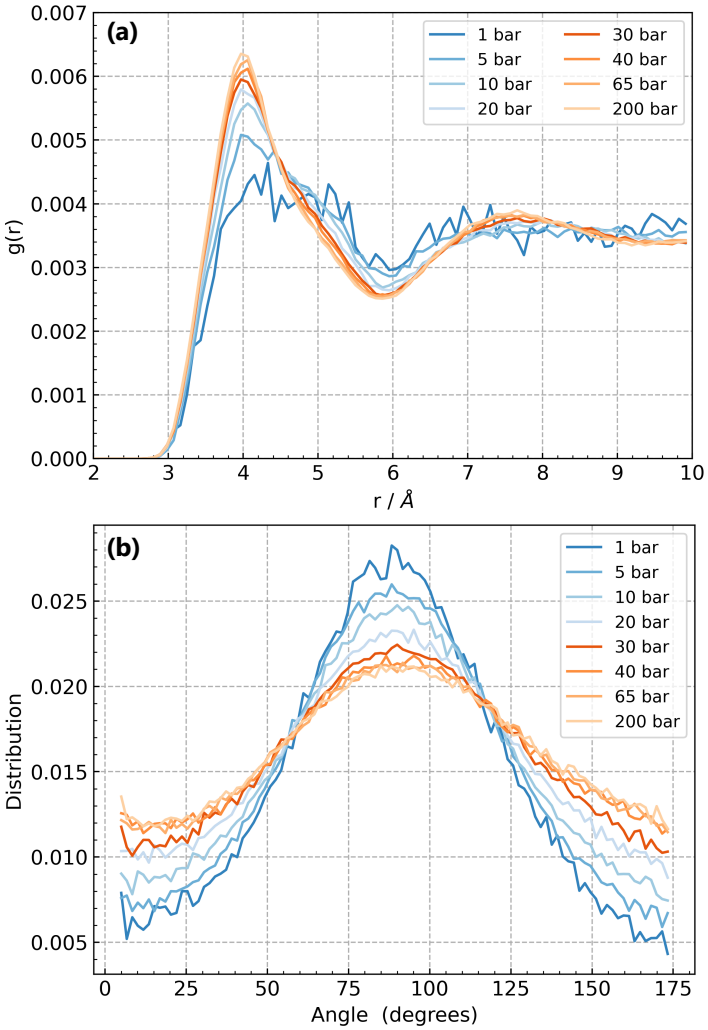

Fig. 4.6 Characterising CO_2 build-up. **(a)** Lateral distribution functions for CO_2 located within first layer. These are plotted for pressures up to 200 bar. **(b)** Angular distributions of CO_2 located within first layer. Angles (θ) are calculated between C-O vector, $\boldsymbol{v}_{\mathrm{CO}}$, and the surface-molecule vector, $\boldsymbol{v}_{\mathrm{surf}}$. The latter is defined as being the vector connecting the carbon of a CO_2 molecule and the point on the instantaneous surface closest to that molecule. θ is plotted for simulation pressures up to 200 bar. An isotropic distribution of angles (not shown) would be given by $\frac{1}{2}\sin\theta$ accounting for the azimuthal angle.

monolayer coincides with reduced structuring for near-interface water molecules, suggesting that interactions between the first contact layers of water and CO_2 are critical for aqueous phase structuring. We envisage that such insights will be important for realising CO_2-H_2O's many applications as well as shedding light on other significant biphasic systems, for example, in biological membranes [297] and for liquid-liquid interfaces facilitating nanoparticle assembly [298, 299].

In terms of carbon capture and sequestration, our NNP provides a robust tool for extending IFT measurements and providing benchmark figures for higher pressure regimes. In this way, coupled with additional geological measurements, one might use our model to provide estimates for a particular storage site of known temperature and pressure, thereby also providing an estimate of that site's suitability. Whilst we anticipate good generalisability for our NNP across different pressures and temperatures, we must caveat this by acknowledging the mostly gas-liquid and liquid-liquid composition of our current training dataset. Extending our work to high-temperature systems - where CO_2 is firmly in the supercritical regime - may require additional retraining or fine-tuning to ensure accurate model predictions. Compared with statistical perturbation models, our work has the advantage of providing additional microscopic insight to supplement predictions of γ. Future work could look to exploit this microscopic insight towards estimating other important storage parameters, for example, the contact angle between CO_2 and water. It would also be interesting to investigate ideas related to thermodiffusion in underground storage sites. Previous classical work has suggested that CO_2 aggregates in areas of low temperature,[300, 301] i.e., at the top of storage sites, as a result of the Soret effect. Investigating how these predictions change with NNP treatment would allow further comparison between classical and *ab initio*-level predictions as well as shed more light on this important phenomenon. A further degree of realism can also be added by incorporating Na^+ and Cl^- ions into our training data and simulations. In doing this, we would better replicate the saline conditions of underground storage reservoirs and thus enable more accurate predictions of a site's storage capacity.

Our work also unearths several differences between classical and *ab initio*-level modelling of the CO_2-H_2O interface. Comparing with previous classical results, we suggest that previous calculations of low-pressure CO_2 coverage in aqueous systems may be underestimated. This could have profound implications for our understanding of gaseous CO_2 exchange at the air-water interface. In Chapter 3, we showed how carbonic acid can form at the ocean surface with thermodynamics akin to those of the bulk hydration reaction. Combined with the elevated CO_2 surface coverages quantified in this chapter, we suggest a non-negligible surface contribution to the acidifying CO_2 hydration reaction, which further exacerbates current ocean pH levels and future trends. Extending our MACE model detailed in Chapter 3 to incorporate multiple CO_2 molecules, a natural next step would be to probe how pressure and local CO_2 concentration modulate the interfacial reaction and the effect this has on the resulting pH. Investigating the potential for cooperative CO_2 reactions would also shed further light on the impact of multi-CO_2 adsorption at the ocean surface.

In conclusion, we provide new insight on the nature of biphasic interfaces and demonstrate the significance of interactions occurring between molecules adsorbed in the first contact layer. We anticipate application of the combined set of techniques used here to other important biphasic systems. The immediate findings of this chapter concerning preferred CO_2 layering at H_2O are expected to be of direct relevance in geoscience, climate research, and material science.

Chapter 5

Solid-Liquid (I) Interface: Understanding the behaviour of CO_2 in nanoporous carbon

> I placed a jar in Tennessee... It took dominion everywhere.
>
> *Wallace Stevens*
> *Anecdote of the Jar*

Having understood CO_2-H_2O interfaces under ambient and pressurised conditions, we finally turn to the last phase of matter. For investigating solid-water interfaces, we focus on the graphene-water-CO_2 interface, which finds application across a range of CO_2 capture and energy applications. In this first Solid-Liquid Chapter, we detail results obtained from a collaborative theory-experiment project designed to understand and quantify the uptake of CO_2 in solvent-saturated nanoporous carbon environments. In the following Chapter (6), we then detail subsequent and ongoing work that looks to improve and extend our description of nanoporous environments. The contents of this chapter are based on published work: 'Unexpected oversolubility of CO_2 measured at electrode-electrolyte interfaces' [302]. Files and data relating to this work can be found at `https://github.com/water-ice-group/oversolubility`.

5.1 Context

The confinement of a material to nanometre scales forms the basis of numerous technological applications, from blue energy harvesting to water desalination to energy storage [53, 303–305]. In recent years, much effort has been directed towards developing new carbon capture technologies using carbon-based nanoporous devices. This includes direct and point source CO_2 capture schemes [306, 307] as well as methods to convert CO_2 to more useful products (e.g., CO) through electrochemical reduction [308, 309].

Central to the efficacy of these schemes is the solubility of CO_2 inside porous carbon. Simple chemical intuition would suggest we can model solubility using Henry's law in the limit of low pressure. However, over the last decade, a number of experimental studies have emerged reporting CO_2 solubilities that far exceed the levels expected for such nanometre-confined systems [310]. Indeed, in some instances, solubilities that are 1-2 orders of magnitude greater than bulk have been recorded [311]. This solubility enhancement (SE), termed 'oversolubility', can be simply defined as

$$\mathrm{SE} = \frac{b}{b_{\mathrm{bulk}}} \tag{5.1}$$

where b is the recorded molality of a dissolved gas, while b_{bulk} gives the molality of that species in bulk solution. With increases in SE, we expect greater CO_2 uptake and greater catalytic turnover numbers for carbon utilisation schemes [312, 313].

At the experimental level, we can measure SEs using quantitative spectroscopy. In this pursuit, NMR has proven to be a robust method for studying molecules and ions at electrode-electrolyte interfaces and inside porous carbon electrodes [53]. At the microscopic level, MD simulations can shine light on oversolubility effects and the behaviour of molecules residing in porous carbon materials. This has included modelling the uptake of gaseous CO_2, CH_4, and H_2 molecules [314–317] and studying their reactive in-pore properties [318]. From these various studies, we can categorise proposed oversolubility mechanisms into three distinct classes [319, 320]: 'adsorption' mechanisms, in which gas molecules preferentially adsorb at the pore-water interface, outcompeting adsorption from the solvent;

'absorption' mechanisms, in which gas molecules are included in high density layers between the in-pore solvent layers; and 'interface' mechanisms, where gas molecules adsorb on top of solvent layers located within partially solvated pore environments. Whilst previous work has offered some answers to the validity of each mechanism [320], there exist a number of inconsistencies between these studies, the methods employed, and the systems studied. Further, the relative contributions of key microscopic drivers (e.g., diffusion, solute-solvent interactions, solute-wall interactions) to the overall uptake process are currently unclear. Accordingly, there is a lack of consensus on which mechanism underpins CO_2 uptake in nanoporous materials.

In this chapter, by exploiting the benefits of MLIPs, we seek to provide clarity on the question of microscopic oversolubility for CO_2. Supporting the spectroscopic findings of experimentalists, we run a series of molecular dynamics simulations to explain the uptake of CO_2 molecules under nanoporous conditions. This includes free MD simulations to quantify microscopic in-pore structuring as well as enhanced sampling runs to obtain free energies of adsorption at the carbon-water interface. From our simulations, we find that CO_2 preferentially locates at the pore wall across a range of pore sizes and that CO_2 adsorption occurs mainly parallel to the pore wall. Calculation of interaction and adsorption energies reveal CO_2-graphene interactions are stronger than those of H_2O-graphene; free energy profiles confirm the preference of CO_2 for graphene adsorption versus dissolution in bulk. Together, these insights suggest an 'adsorption'-style mechanism underpinning CO_2 oversolubility in nanoporous carbon materials. Both the experimental and computational findings of this work highlight the importance of microscopic structuring and pore design for facilitating CO_2 uptake in electrochemical applications.

5.2 Methods

Training

Computational simulations were enabled through the use of MACE potentials [141]. These were trained on a representative selection of structures labelled with energies and forces

calculated at the DFT level. Structures were generated using a variety of methods, including *ab initio* MD, MACE-MD, enhanced sampling simulations, and constrained MD runs. The resulting dataset, optimised using the procedure outlined in Schran et al. [215], totalled some 9000 structures. A variety of systems were included: pure water, CO_2 in water, nanoconfined systems, and reactive CO_2 trajectories. Structures were labelled with DFT energies and forces calculated using the QUICKSTEP method of `CP2K` [119, 120]. The revPBE functional augmented by Grimme's D3 corrections [95, 115, 218] was chosen on account of its ability to reproduce the structural properties of bulk and interfacial water [219–222]. Goedecker–Teter–Hutter (GTH) pseudopotentials were selected for the treatment of core electrons, whilst the TZV2P-GTH (O and H) and DZVP-MOLOPT-SR-GTH (C) basis sets were chosen for valence electron density. We selected an auxiliary plane-wave cutoff of 1200 Ry.

Using this optimised dataset, a two-layer MACE model with 128 equivariant messages was generated. We selected a maximal message equivariance of L = 1 and a radial cutoff of $R_c = 5$ Å, equating to an effective receptive field of 10 Å after message passing. Validation of the model was performed to assess the accuracy of its force, energy, and structural predictions (Fig. C.1 and Fig. C.2). We report RMSEs of 1.2 meV/atom for the energies and 41.8 meV/Å for the forces. Radial distribution functions (RDFs) were generated for pure water and CO_2-water systems and compared with *ab initio*-MD and experimental RDFs. The results of this analysis, shown in Fig. C.2, demonstrate the accuracy of our model for reproducing the properties of bulk aqueous systems.

Production

Density profiles for H_2O, CO_2, and HCO_3^- were generated using unconstrained molecular dynamics simulations. We approximated the pore environment by using a nanoconfined aqueous system, with the flexible graphene sheets separated by 7 Å, 12 Å, and 15 Å. Details of the system setups are given in Table C.1 of Appendix C.

Molecular dynamics simulations were run using `LAMMPS` [229, 230]. Simulations were performed using the NVT ensemble at 300 K. The Nosé-Hoover thermostat was selected

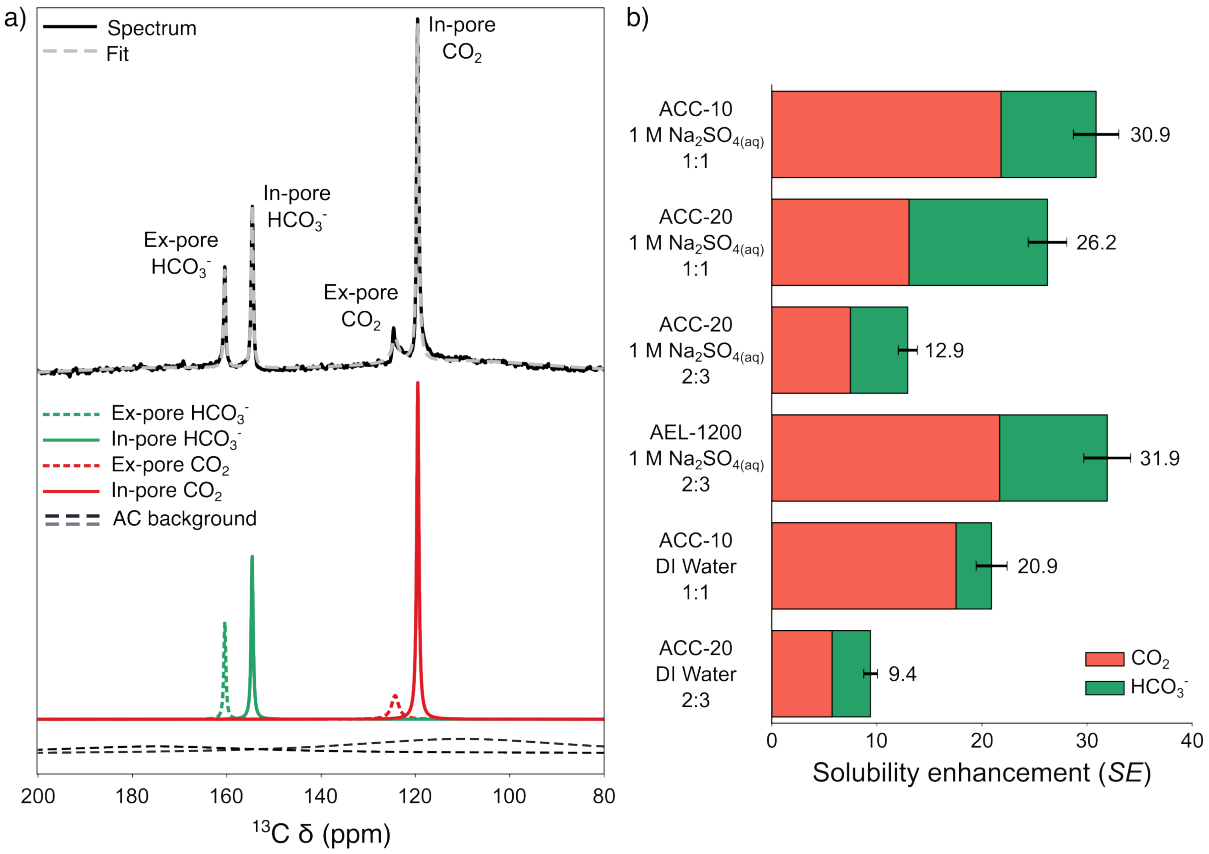

Fig. 5.1 Quantitative NMR results demonstrating oversolubility of CO_2 in porous carbons. Results were obtained by Zeke Coady as part of our collaborative experiment-theory paper [302]. **(a)** Typical NMR spectrum demonstrating the shift in signals expected for in-pore and ex-pore carbon. Spectra are shown for the raw and fitted (black and grey, respectively) signals as well as the deconvoluted peaks (green and red). **(b)** SE values reported for various carbon/solvent samples. Values are calculated relative to literature CO_2 solubility measurements. Reproduced from Ref. [302] with permission.

with a time constant of 100 fs. Deuterium masses were used for the hydrogen atoms along with a timestep of 1 fs.[1] Gaseous interaction energies were obtained from single-point VASP calculations of isolated graphene walls and gaseous CO_2/H_2O molecules. [122–125]. Aqueous adsorption energies were obtained using umbrella integration [321], where the free energy was calculated as a function of the distance of CO_2/H_2O to the graphene wall. For explicit details on these various measurements and calculations (densities, orientations, interaction and adsorption energies), we direct the reader to Appendix C.

[1]Switching H for D alters the dynamical timescales of our simulations but leaves the equilibrium properties relatively unperturbed (these depend on the underlying potential energy surface, rather than the atomic masses). Accordingly, this decision is justified for the study of equilibrium structural properties such as densities, orientations, adsorption free energies, etc.

5.3 Results

Spectroscopic results

To measure oversolubility effects in microporous carbons, a quantitative ^{13}C NMR setup was employed, the exact details of which can be found in Ref. [302]. Representative NMR results obtained in this project are shown in Fig. 5.1. In panel a, we show typical ^{13}C NMR spectra that highlight the shift in NMR signal that occurs for in-pore and ex-pore species. This shift arises from ring currents generated from the delocalised π electrons of aromatic carbon rings [322, 323], which act to shield in-pore species. In panel b, we report SE measurements obtained for a variety of nanoporous carbon-electrolyte systems. These include activated carbons of varying pore sizes (ACC-10 and ACC-20, the latter having the larger pores) as well as annealed carbon (AEL-1200) systems. From this work, we can report the following insights:

1. Oversolubility is observed across all types of microporous carbon systems.

2. Oversolubility is enhanced for smaller pore sizes. This can be seen in the larger SE values reported for ACC-10 over ACC-20 for CO_2.

3. The largest solubilities are obtained for simple carbons with minimal surface functionality. This can be seen in the results for the annealed AEL-1200 electrode, which reports the largest overall SE value.

Together, these insights suggest that CO_2 uptake in nanoporous carbons can be maximised by synthesising smaller, more graphenic domains with minimal defect contamination. The near thirty-fold enhancement in CO_2 solubility is unprecedented for these pore sizes and warrants further investigation at the microscopic scale [310, 320].

CO_2 adsorbs at the graphene-water interface

To better understand the mechanism underpinning CO_2 uptake, we carried out a series of atomistic simulations aimed at modelling idealized pore environments. These simulations were performed to provide an indirect assessment of oversolubility and to help interpret

some of the spectroscopic measurements discussed above. The objectives of this modelling were threefold: to understand the underlying mechanism for CO_2 oversolubility; to provide a quantitative rationale for observing this mechanism; and to elucidate the microscopic details driving the process.

To gauge the underlying mechanism for solute uptake in microporous carbon, we performed unbiased MD simulations modelling the behaviour of CO_2 and HCO_3^- in water-saturated pore environments. In each setup, we placed either a single CO_2 molecule or single HCO_3^- ion into an aqueous slab sandwiched between two graphene sheets. These sheets were initially positioned 7 Å, 12 Å, and 15 Å apart, corresponding to the system-relaxed separations that support layered water structures. Further, these separations enabled us to sample the relevant range of pore sizes seen in the ACC-10, ACC-20, and AEL-1200 carbons. The number of solvating waters for each system was chosen to give an in-pore CO_2:H_2O or HCO_3^-:H_2O mole fraction approaching that used for in-pore experimental measurements ($< 1.5\%$) (see Table C.2 for experiment-simulation compositions). Simulations were performed over several nanoseconds, allowing for fully converged statistics of the in-pore properties.

The resulting density profiles, shown separately for H_2O, CO_2, and HCO_3^-, are given in Fig. 5.2. These profiles reveal the important role of the pore-water interface. In all systems, the pore geometry results in the formation of layered water structures (pink) [318]. Analysis of the CO_2 and HCO_3^- profiles reveals that both species preferentially locate within the H_2O layers, albeit with distinct positional preferences. Across each pore width, CO_2 (black) exhibits a strong affinity for the water layer in contact with the pore wall. In contrast, HCO_3^- (purple) appears less constrained and is less likely to locate at the pore-water contact layer. This is particularly noticeable for larger pore widths. Although reactivity in these systems was possible, no exchange between CO_2 and HCO_3^- was observed over the studied timescales.

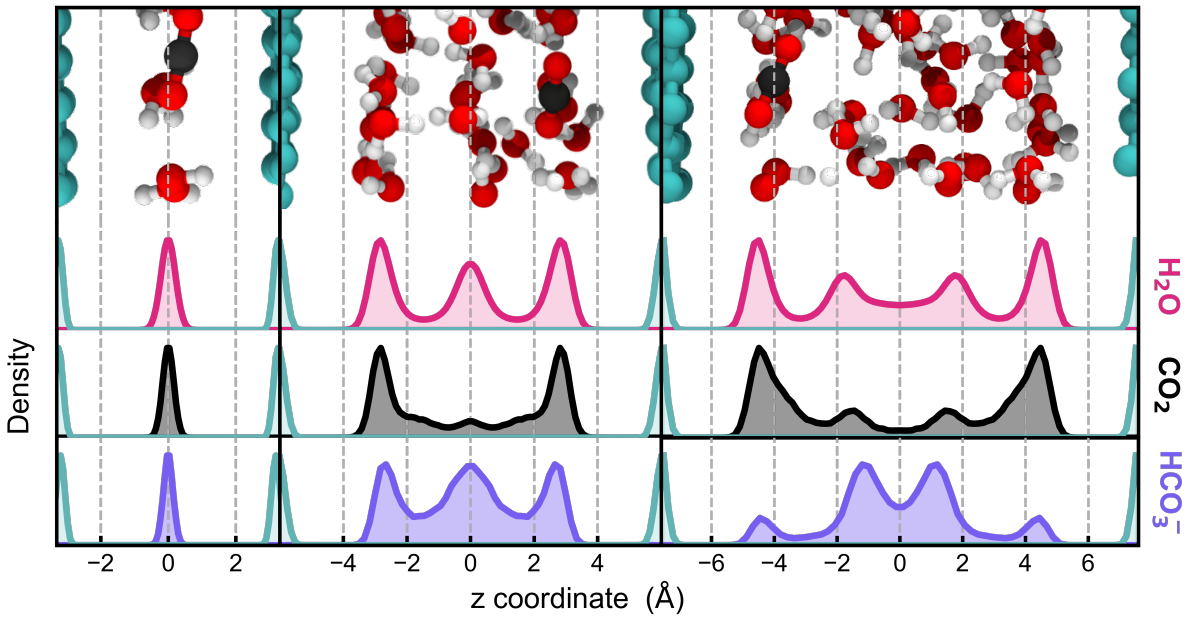

Fig. 5.2 Atomistic modelling suggests CO_2 uptake is driven by the adsorption mechanism. Density profiles are plotted for water (pink), CO_2 (black), and HCO_3^- (purple), as a function of the distance from the system centre of mass. Representative snapshots of the systems are shown above the density profiles.

Energy estimates show CO_2 adsorption to be stronger than H_2O adsorption

The profiles shown in Fig. 5.2 support an adsorption-like mechanism of oversolubility for CO_2. Uptake appears to be driven by a preferential adsorption of CO_2 at the pore walls, evidenced by the pronounced peaks in CO_2 density adjacent to the graphene distributions. To understand and quantify this behaviour, we measured the adsorption energies of CO_2 and H_2O under gaseous and pore-saturated conditions. In one approach, we computed single-molecule interaction energies of gaseous CO_2 and H_2O molecules interacting with isolated pore walls (Fig. 5.3a). In a complementary approach, enhanced sampling simulations of pore-saturated systems (30 Å width) were performed to obtain free energies as a function of the distance from the pore wall (Fig. 5.3b.) Together, these two analyses allowed us to gauge the relative affinities of CO_2 and H_2O for the pore wall both on a per-molecule basis and also accounting for solvation effects from water.

Both sets of results confirm the preferential adsorption of CO_2 over H_2O at the pore wall. In the gas phase, CO_2 adsorption is more favourable by 0.34 kcal/mol, whilst under pore-saturated conditions, CO_2's free energy of adsorption is 0.22 kcal/mol lower (more

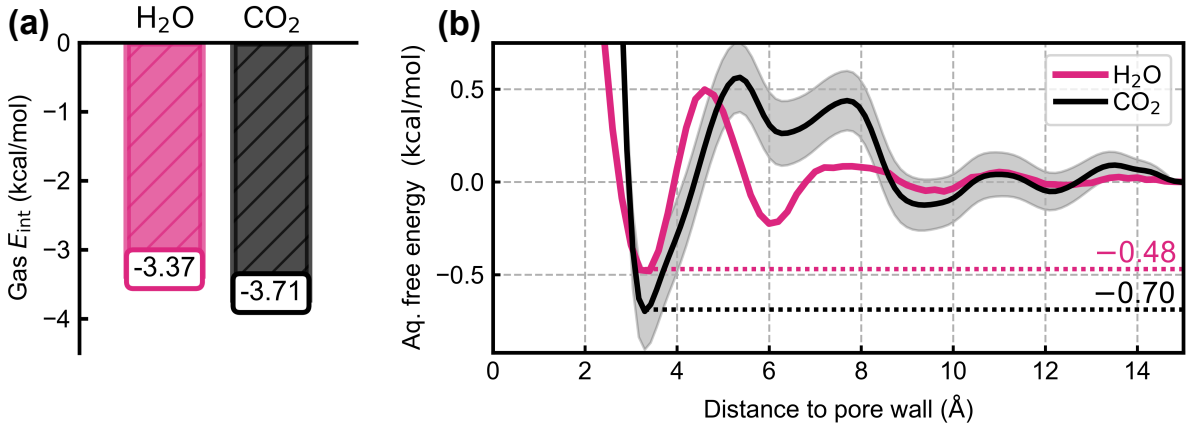

Fig. 5.3 Quantification of adsorption energies under gaseous and solvated conditions. a) Adsorption energies for isolated gaseous CO_2 and H_2O molecules interacting with a graphene-like pore wall. Energies were computed by Flavanio della Pia using VASP [122–125]. b) Free energy profiles of CO_2 and H_2O shown as a function of the distance from the pore wall under pore-saturated conditions (30 Å confinement).

stable) than that of H_2O. Likely, these enhanced stabilities arise from favourable dispersion interactions occurring between hydrophobic CO_2 and the basal graphene planes [272]. In addition, sequestering CO_2 at the pore-water interface minimizes disruption to the overall hydrogen bonding network, with water molecules located at the pore wall forming fewer hydrogen bonds on average compared to bulk water (see Fig. C.4). The free energy plot obtained for CO_2 is consistent with the density profiles shown in Fig. 5.2, with a free energy minimum located adjacent to carbon and an unstable regime (+1 kcal/mol) located 5-8 Å from the pore wall. We note that, for this large pore environment (30 Å, Fig. 5.3b), we recover bulk-like water towards the centre of the idealized pore slit (i.e., towards 15 Å). In this way, the analysis of Fig. 5.3b further evidences the preference of CO_2 to locate in pore environments versus in bulk solution. The favourability of the CO_2-pore wall interaction relative to the H_2O-pore wall interaction predicts that the adsorption mechanism of oversolubility will dominate [310, 320]. The unstable regime located 5-8 Å from the pore wall additionally indicates that the absorption mechanism is unfavourable.

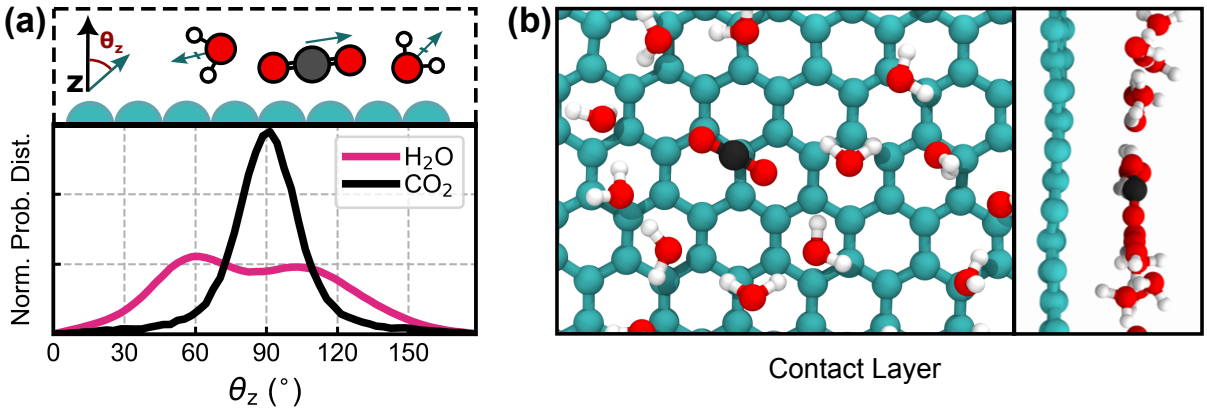

Fig. 5.4 Understanding how CO_2 adsorbs at the graphene-water interface a) Orientational distributions of the CO_2 bond vector and H_2O dipole vectors obtained for molecules at the pore-water contact layer. An isotropic distribution of angles would be given by $\frac{1}{2}\sin\theta_z$, accounting for the azimuthal angle. b) Visualization of the contact layer of the pore-water interface.

CO_2 adsorbs parallel to the pore wall

Having confirmed the preferential adsorption of CO_2 at the pore wall over H_2O, we then investigated the manner in which CO_2 is adsorbed. In Fig. 5.4a, orientational distributions for CO_2 and H_2O molecules residing at the contact layer of the pore-wall interface are shown. Orientations are measured by the angle between the z vector normal to the pore wall and either the C-O bond vector of CO_2 or the dipole vector of H_2O. Snapshots of the contact layer parallel and perpendicular to the z vector are shown in Fig. 5.4b.

Looking at Fig. 5.4a, we observe a peak in the distribution for CO_2 at 90°, suggesting that CO_2 adsorbs mainly parallel to the pore wall. In contrast, H_2O adsorbs across a broad distribution of orientations with a loose preference for two specific geometries: with dipoles pointing slightly towards the bulk (60°, most favoured); and with dipoles pointing slightly towards the pore walls (105°, less favoured). These observations are consistent with previous modelling of graphene-water interfaces [324]. The parallel adsorption of CO_2 likely enables more favourable interactions with the pore walls and facilitates the diffusion of CO_2 into narrow pore environments. Similar mechanisms have been observed to enhance CO_2 capture in dry activated carbon pores [325] and to enhance selectivity for CO_2 over H_2O in metal-organic framework pores [326]. In contrast, water's rough bimodal adsorption could present an obstacle to narrow-pore diffusion, precluding the uptake of

H_2O into more confined environments. This may help explain the stronger oversolubility effect observed for ACC-10 compared to ACC-20, given the smaller average pore size of the former.

Overall, the atomistic modelling of idealized slit pores suggests the following: the uptake of CO_2 in water-saturated microporous carbon is driven by the adsorption mechanism; this mechanism arises due to a preferential adsorption of CO_2 over H_2O at the pore-water interface; and CO_2 will adsorb parallel to the pore walls, potentially facilitating further uptake enhancements under narrow pore environments. Whilst the pore-slit model employed here may be relatively simple compared to the actual activated carbon pore environment [327], the higher SE observed in AEL-1200 compared to ACC-10 and ACC-20 supports the significance of simple, graphene-like domains for modelling this uptake effect.

5.4 Summary

In this chapter, we have taken steps to improve our understanding of how small molecules behave in nanoporous environments. Experimental results showed an oversolubility effect for CO_2 molecules confined to various nanoporous carbon electrodes. Atomistic modelling suggested this uptake to be a product of an adsorption-style mechanism in which CO_2-carbon interactions out-competed water-carbon interactions. The adsorption of CO_2 parallel to the surface likely facilitates uptake in smaller, more constrained pore environments, in line with experimental results. Together, these results suggest that the uptake of molecules in small materials can be controlled through the deliberate design of porous carbon electrodes, including tuning the pore size, functional group content, and graphene domain size.

Our results inform on the design of electrodes for implementing electrolytic carbon capture. For the uptake of small, nonpolar molecules, our combined experimental and computational insights suggest that we can maximise solubility by:

(i) Reducing the average pore size, and

(ii) Increasing the extent of graphitic domains.

The former maximises the number of contacts between CO_2 and the pore wall, while the latter strengthens the dispersion and quadrupole-π interactions between these species. These design principles are likely to be transferable to other small molecules, e.g., N_2, CH_4 and O_2, where dispersion and size effects dominate [310, 320]. In practice, we can realise small-pore, highly graphitised carbons either using carbide-derived carbons (with a tight control over the precursor carbide structure) [328] and/or zeolite-templated carbons [329], followed by high-temperature annealing to remove functionalisation whilst preserving the microporous structure.

Whilst we have presented a consistent mechanism for CO_2 oversolubility in nanoporous carbon, the role of the electrolyte (e.g., deionised water vs. Na_2SO_4) and pore size/topology warrants further study. We know from Fig. 5.1 that switching from Na_2SO_4 to pure water leaves CO_2 SE values unchanged but cuts the HCO_3^- solubility almost in half. Microscopically, it is currently unclear why this takes place. Extending our work to incorporate Na^+/SO_4^{2-} ions could help elucidate the mechanism driving ion uptake in electrolytic media [330] (e.g., ion-pair formation, pH effects).

Concerning the role of pore size and topology, future work could look to employ different types of nanoporous carbon model. In this chapter, we have utilised simple pore-slit models for simulating nanoporous carbon. These highly idealised geometric models constitute an efficient means of approximating porous carbon environments, enabling us to characterise solute-pore interactions in a clean and controlled manner [331–334]. However, such simple geometric models clearly have limitations. Pore-slit models represent a quasi-2D approximation to 3D networks and thus miss many distinctive geometric and topological effects, e.g., connectivity and percolation, tortuosity, curvature and roughness, and site heterogeneity. Whilst the idealised pore-slit model is appropriate for modelling CO_2 oversolubility effects (which are maximised in graphitic domains), it is clear that our current description of pore environments is not complete. Going forward, it might be prudent to look at more sophisticated pore-structure approximations. This could include simulating constructed atomistic models with prescribed motifs (e.g., including curvature

or controlled defect/functional-group placement) or even reconstructed synthesis-informed models generated directly from atomistic simulations mimicking experimental synthesis [327, 335]. Using these structural models, we could obtain additional metrics regarding CO_2 uptake in nanoporous carbon, for example, preferential adsorption locations within the 3D network, the influence of curvature and tortuosity on CO_2 uptake, and how heterogeneity can modify the physical and chemical properties of the porous material. Following on from this last point, in the following chapter (6), we utilise constructed geometric models to isolate and quantify the influence of specific defect motifs on solvated nanoporous systems.

Chapter 6

Solid-Liquid (II) Interface: Point defects in nanoporous carbons

> There is no excellent beauty that hath not some strangeness in the proportion.
>
> *Francis Bacon*
> *Essays - 'Of Beauty'*

In the first Solid-Liquid chapter, we detailed results on the physical adsorption of CO_2 molecules confined to carbon nanopores. In an attempt to improve our description of nanoporous environments, we now extend this model to look at defective graphene systems. We specifically focus on point defects (i.e., single vacancies, double vacancies, Stone-Wales defects) and their behaviour under solvent-saturated conditions. The results detailed in this chapter constitute ongoing work.

6.1 Context

The combination of spectroscopic measurement and computational modelling has proved invaluable for elucidating the nature of nanoporous carbons and in-pore molecular behaviour [336]. To date, most computational studies have utilised simple graphenic pore-slit

environments. In reality, nanoporous carbons are not uniform stacks of idealised graphene sheets. They are heterogeneous, highly disordered three-dimensional networks blending together a range of topologies and chemical functionalities. Spectroscopy has identified the existence of various structural motifs and inhomogeneities, from impurity atoms and functional groups to corrugated domains and edge-site terminations [337–342]. Together, these make for a complex functional material, the properties of which are determined by the local structuring and chemical composition.

The deliberate introduction of defects provides a means of modulating the electronic, magnetic, and mechanical properties of graphenic and graphitic materials. Pristine graphene is a zero-band-gap material [343], displays high thermal conductivity and tensile stress [344, 345], and exhibits a low basal-plane chemical reactivity [346, 347]. Defects - such as vacancies, edges, lattice corrugations and topological distortions - alter this baseline. For example, edge defects (which arise naturally from the termination of graphene sheets and nanoribbons) can induce band gaps and semiconducting behaviour in graphene sheets [348]. Similarly, introducing corrugation or curvature (as observed in carbon nanotubes) can help stimulate reactivity through mechanical strain effects [349, 350]. Heteroatom doping provides levers to tailor the charge distribution and catalytic properties [351].

Of the various types of graphene defects, atom vacancies are among the most common. These vacancies can arise during the synthesis process, or they can be artificially engineered through ionic or electron irradiation [352–354]. The single vacancy (SV) - created by the removal of just a single carbon - was first observed in graphene in 2004 [355]. Other point defects, including the theoretically predicted Stone-Wales defect [356], were later observed using transmission electron microscopy [357]. Nowadays, spectroscopic studies are able to regularly observe and characterise such defects [339, 358, 359].

At the atomistic scale, much of our insight into point defects comes from DFT calculations performed under gaseous conditions [360]. Once placed in a graphene sheet, these motifs have the potential to alter both the structural and electronic properties of the local environment. The SV, for example, is characterised by an enhancement in the local electron density. This enhancement arises from the creation of unbonded σ and π electrons

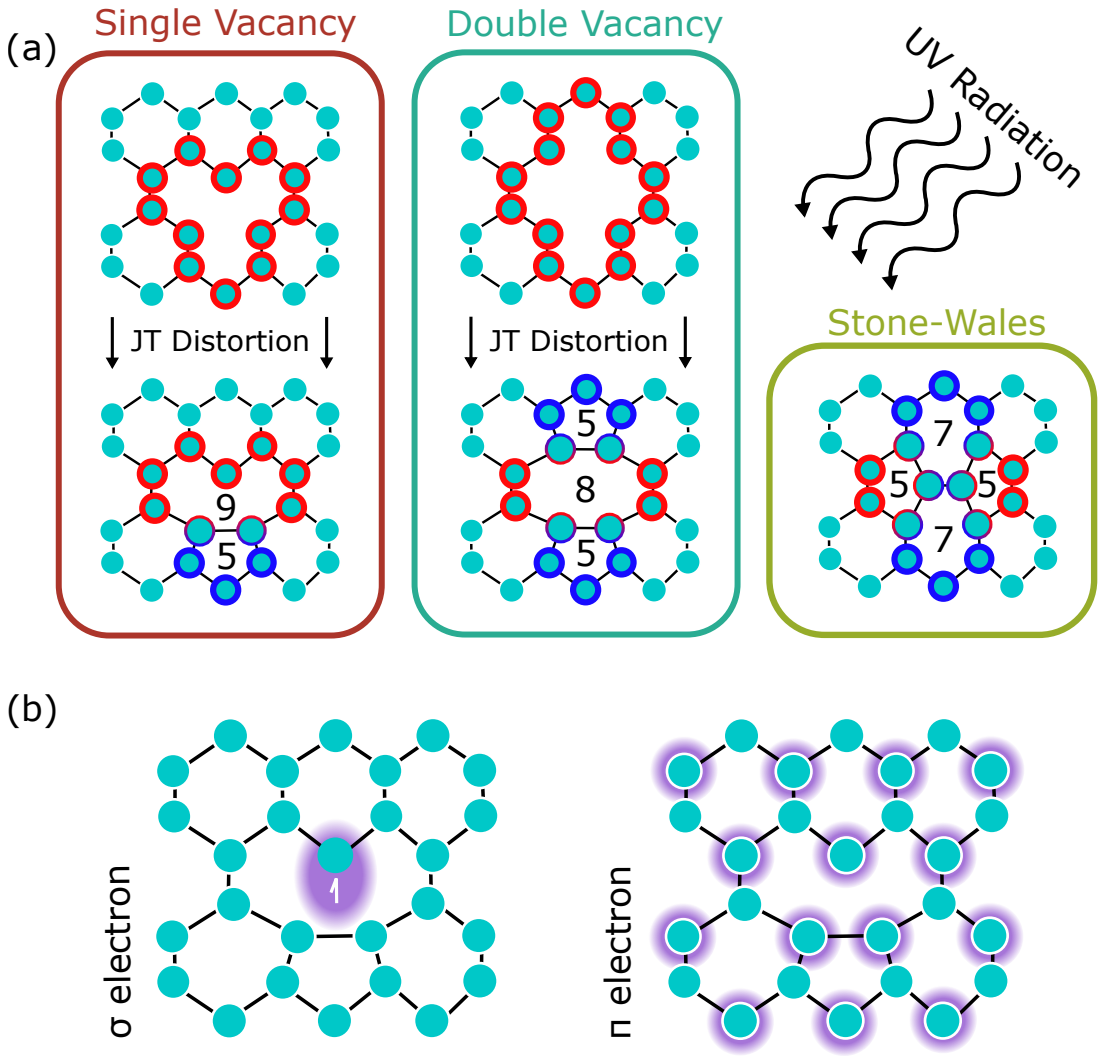

Fig. 6.1 Overview of point defects in graphene sheets. (a) Diagrams showing the single vacancy (SV), double vacancy (DV), and Stone-Wales defects formed following the irradiation of a graphene sheet. In the case of the SV and DV defects, we show structures both with and without Jahn-Teller distortion. (b) Schematic showing the predicted electron distribution of the two unbonded electrons found in SV systems.

upon the removal of an atom from the graphene plane. The σ electron becomes localised at one of the carbon sp^2 sites whilst the π electron is delocalised over the p orbitals of the A sub-lattice (see Fig. 6.1b). The extent of this delocalisation and the resulting magnetisation of the system are still a point of contention, but studies agree this lies in the range of $1 - 2\,\mu_B$ [361–364]. Overall, the SV serves as both a hydrophilic and highly reactive centre in an otherwise hydrophobic graphene plane. Indeed, this centre has been observed to quite readily strip protons from nearby molecules, with NEB studies showing that water can decompose to form a range of chemisorbed defect structures [365–367]. In

contrast, the DVs and SWs defects are chemically inert, though they can impose interesting local geometric constraints as well as participate in electron-mediated diffusion processes [368, 369].

The SV, DV, and SWs defects have received significant attention from gas-phase studies. However, a description of these point defects under solvated conditions is currently missing. FF modelling is precluded on the grounds that SVs are highly reactive species that trigger bond making and breaking events. *Ab initio* studies are frustrated by the difficulty associated with converging spin-polarised calculations, thus limiting studies to the picosecond range. To our knowledge, no previous study has attempted to fully characterise the physicochemical nature of solvent-saturated point defect systems. Seeking to address this, we identify two open questions surrounding point defect systems: how do point defects influence the structuring of surrounding aqueous media; and how are the relative defect stabilities affected by explicit solvation. In answering these questions, our work seeks to provide a more realistic description of nanoporous environments as well as inform on design choices in the synthesis of functionalised carbon materials.

In this section, we present preliminary results from our work looking at solvated point defects. Using a diverse training dataset labelled with spin-polarised DFT data, we train a MACE model to treat SV, DV, SWs defects under both gaseous and solvated conditions. Free MD simulations confirm the SV site to be both reactive and hydrophilic, leading to prominent H_2O adsorption (and even reaction) at 300 K. The DV and SWs defects, in contrast, exhibit no prominent adsorption. NEB calculations confirm the suitability of our model for treating reactive SV systems, with preliminary free energy results suggesting spontaneous H_2O dissociation under solvated conditions. Together, these results confirm the rich chemistry enabled by defect manufacturing in basal graphene planes. Future work in this project will look to obtain a more direct comparison between the relative defect stabilities of chemisorbed SV sites as well as electron distributions under bulk and gaseous conditions.

6.2 Methods

In this work, we train a two-layer MACE potential using structures labelled with DFT-level energies and forces. Structures were generated using a variety of methods, including through use of foundation MACE models (MP0)[160], through AIMD, and from preliminary NEB and umbrella integration runs. In total, some 6500 structures were generated, with configurations including defects under solvated, partially solvated, and gaseous conditions. For each configuration, single-point DFT calculations were performed using the QUICKSTEP functionality of `CP2K` [119, 120]. Calculations were performed using unrestricted Kohn-Sham theory, with an initial multiplicity of $M = 3$ set for spin-polarised structures and $M = 1$ for the spin-zero structures. For the SV calculations, an initial magnetisation of 0.6 μ_B was applied to the three radical carbon atoms surrounding the defect site. We chose the revPBE functional augmented by Grimme's D3 corrections [95, 115, 218] owing to good bulk and interfacial predictions for water [219–222]. Goedecker–Teter–Hutter (GTH) pseudopotentials were selected for the treatment of core electrons, whilst the TZV2P-GTH (O and H) and DZVP-MOLOPT-SR-GTH (C) basis sets were chosen for valence electron density. An auxiliary plane-wave cutoff of 1200 Ry was employed.

A two-layer MACE model was generated with 128 channels and a maximal message equivariance of $L = 1$. A radial cutoff of 5 Å was selected, which equates to an effective receptive field of 10 Å after message passing. The final model exhibited training RMSEs of 0.6 meV/atom and 31.6 meV/Å for the energies and forces, respectively. These compare with MAEs of 18 meV/atom and 39 meV/Å for the MACE-MP0 energies and forces, respectively [160].

Molecular dynamics simulations were run using `LAMMPS` [229, 230]. Simulations were performed using the *NPT* ensemble (Nosé-Hoover-style, anisotropic dimension control) at 300 K and 1 bar. Deuterium masses were used for the hydrogen atoms along with a timestep of 1 fs. For generating the potential energy profiles, NEB calculations were performed using ASE [370] with 20 system replicas. The reactant (image 0) and product (image 19) states were first geometry-optimised and the interconnecting states generated

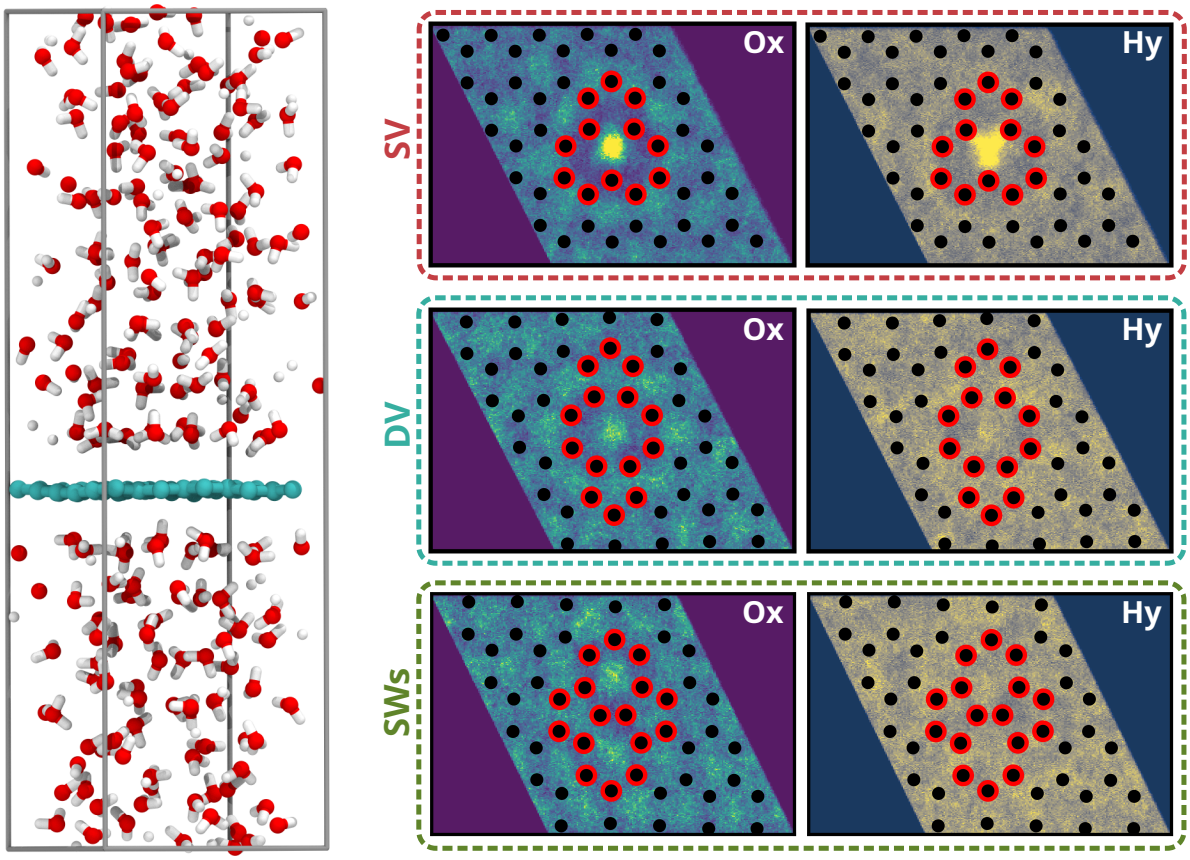

Fig. 6.2 SV acts as prominent adsorption site for water molecules. **(Left)** Snapshot of system used to probe contact layer. Setup includes $\sim$ 190 water molecules in contact with a sheet of $\sim$ 50 carbon atoms. **(Right)** 2D frequency histograms of water residing at the contact layer of the defect system (within 4 Å of sheet). Profiles are shown for oxygen (Ox) and hydrogen (Hy) atoms.

via IDPP interpolation [371]. The resulting images were optimised using the BFGS optimiser. The revPBE-D3 potential energy curves were generated from single-point DFT calculations on the MACE-generated images.

6.3 Results

SVs as hydrophilic centres

To gauge the influence of defect sites on the surrounding solvent, we performed free MD simulations modelling the interaction of a defective graphene sheet with water. Simulations were run over 0.5 ns using the NPT ensemble. A typical system setup is shown on the left-hand side of Fig. 6.2. From these simulations, we obtained 2D frequency histograms of

the contact layer positions of H_2O at the graphene-water interface. These were obtained for the SV, DV, and SWs defect, and the results are shown on the right-hand side of Fig. 6.2. Here, we show both the distribution of the oxygen atoms and hydrogen atoms. Higher density regions are represented by the brighter areas of the distributions.

Looking at Fig. 6.2, we can see that SV sites promote the strong adsorption of water molecules. Regions of high density are observed for both the oxygen and hydrogen distributions at the geometric centre of the SV. In the case of hydrogen, the directionality observed in the atom distribution (pointing towards the three radical carbons) suggests some form of hydrogen bond formation between the adsorbed waters and the radical carbons. In contrast, minimal adsorption effects are observed for the DV and SWs sites, which display a relatively uniform oxygen and hydrogen distribution across the two sites. In the case of the oxygen distributions, both the DV and SWs defects see slight enhancements at the vacancy centre and at the graphenic ring centres, similar to what is observed for pristine graphene sheets.

Intuitively, these observations make sense: the unquenched, localised electron in the SV acts to form strong intermolecular bonds with the polarised water molecules.[1] In this way, SVs act as hydrophilic centres in an otherwise hydrophobic basal graphene plane. Conversely, for the DV (which undergoes spin quenching with JT distortion) and SWs sites, there exist no unpaired electrons, and thus these systems act much the same as planar graphene surfaces. In line with previous DFT calculations, we can say that DV and SWs are chemically inert species (though they do engender out-of-plane distortions of the graphene sheet).

In Fig. 6.2, we show that SV sites promote the strong adsorption of water molecules at the graphene-water contact layer. To further explore these interactions, in Fig. 6.3, we analyse SV-water binding and the potential for hydrogen bond formation between water molecules and radical carbon atoms. At each frame t, we compute the minimum

[1] In some runs, we observe reaction between water and the SV. Only the results from the unreacted runs are shown here.

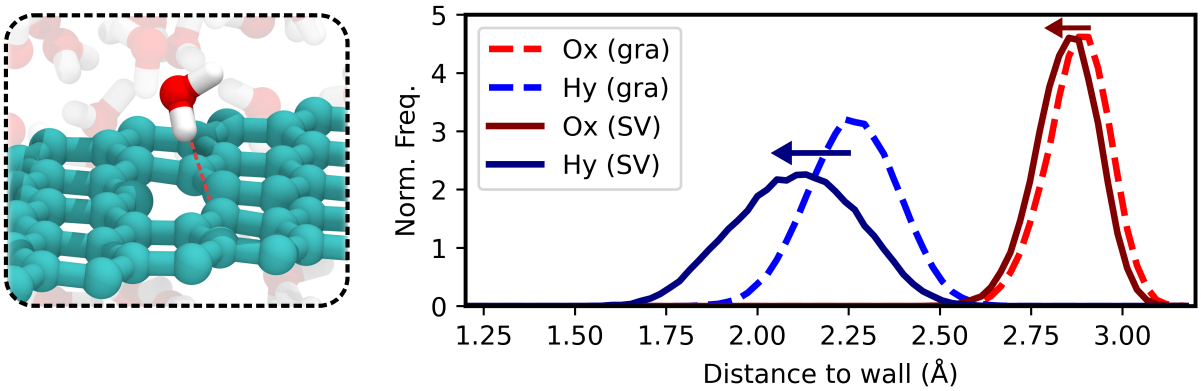

Fig. 6.3 Water adsorbs at the SV through hydrogen bonding. **(Left)** Snapshot of a water molecule adsorbing at the SV defect. **(Right)** Frequency histograms of the closest distance of approach for oxygen (blue) and hydrogen (red). Curves are obtained for both the SV (solid) and for pristine graphene (dashed), with arrows showing the shift in distribution upon the introduction of the defect.

water-graphene distance as

$$d_{\min}(t) = \min_{i \in \mathrm{C},\, j \in \mathrm{O_w}} \|\mathbf{r}_i(t) - \mathbf{r}_j(t)\|\,, \tag{6.1}$$

where $\mathbf{r}_i(t)$ and $\mathbf{r}_j(t)$ give the positions of carbon i and oxygen j at time t. In effect, Eq. 6.1 determines the distance between the free-standing graphene sheet and the water molecule situated closest to it. The distribution $p(d)$ was then obtained by histogramming $\{d_{\min}(t)\}_{t=1}^{N_{\mathrm{frames}}}$. We plot $p(d)$ for both the single vacancy sheet (dark, solid) and for the pristine graphene sheet (dashed, lighter).

Looking at Fig. 6.3, we see that the SV sites adsorb water molecules more closely than pristine graphene sheets. Both for oxygen and hydrogen, the peak in the minimum distances shifts to smaller values when a vacancy is present. This is a particularly noticeable effect for hydrogen (dark blue, solid), which shifts 0.3 Å closer to defective sheet than for the pristine case. The peaks in the SV distances - 2.1 Å for hydrogen and 2.8 Å - satisfy the typical conditions required for hydrogen bond formation. Accordingly, we can suggest that the origin of the SV's hydrophilic nature arises from the potential for hydrogen bonding between the unpaired electron of the defect site and the surface-adsorbed water. This insight is consistent with results from Chapter 5, where experimental and

computational results suggest the importance of defect-free, graphene-like domains for facilitating CO_2 uptake. That the introduction of defects reduces the oversolubility of hydrophobic CO_2 molecules likely stems from the preferential attraction these sites display for water molecules and other polar/ionic species.

It should be noted that, in some instances, this surface-adsorption becomes so strong that we observe reaction between the SV and water in which the latter is stripped of one of its protons. We further explore this idea of SV reactivity in the following section.

MLIPs for modelling reactive SV sites

Ultimately, we would like to understand how the stability and relative reactivity of vacancy sites change upon immersion in solvent. As a result of its unpaired electrons, SV defects are usually highly reactive and will readily undergo reaction with nearby molecules; previous DFT studies have investigated the reaction with O_2 [372], CO_2 [373], NH_3 [374], and butane [375], among other molecules [376]. In the case of water, the SV defect reacts to form various chemisorbed SV-H_2O species (see Fig. 6.4a) [365–367]. In Fig. 6.4a, we show some of these chemisorbed species. Upon approaching the defect, water is stripped of one of its hydrogen atoms by the bare defect, leading to the formation of a C-H bond and a hydroxy C-OH group. In this spin-polarised hydroxy species, we observe proton transfer between the OH group and the spin-polarised carbon atom, leading to the formation of a ketone-like species. The ketone group can then undergo conversion to form the (slightly) more stable pyran-like structure, either through stepwise chemical reactions or through a concerted process.

To gauge the efficacy of our MLIPs for treating these various processes and species, we first conducted a series of NEB calculations targeted at various chemisorbed states of the gaseous single-vacancy defect. The results of these NEB calculations are shown in Fig. 6.4b-d for each of the conversion steps detailed for H_2O chemisorption. These are compared with potential energies calculated using the reference DFT method (revPBE-D3) as well as previous DFT estimates from literature. Plots of the net Mulliken spin population M_s and the sum of the absolute Mulliken spins M_s^{abs} are include above each set of profiles.

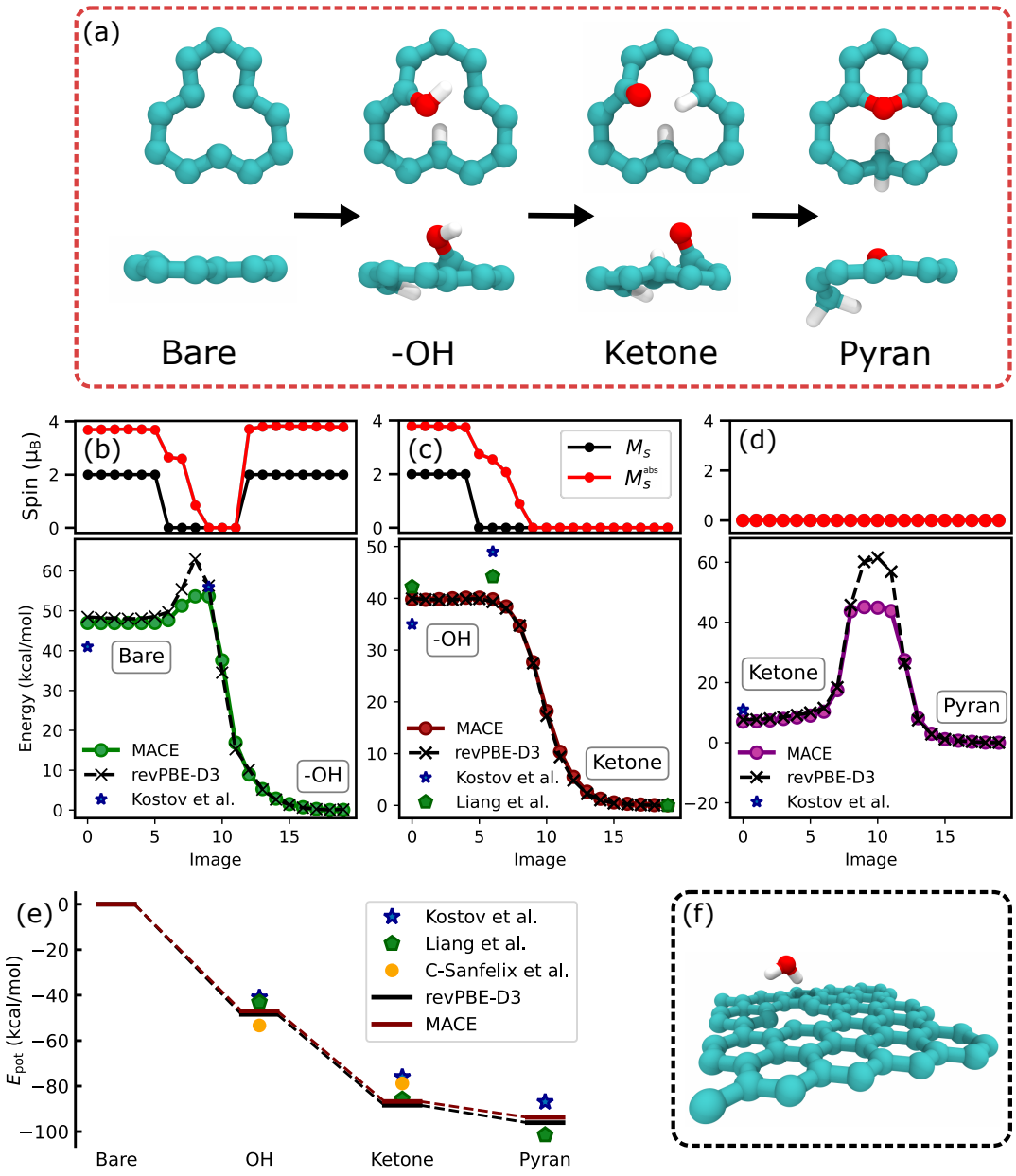

Fig. 6.4 MACE model reproduces gas-phase reaction energies with water. **(a)** Schematic showing the stepwise conversion of the bare SV to form a pyran-like defect. Only atoms outlining the defect are shown. **(b)** Nudged-elastic band (NEB) profile showing the conversion of the bare SV to form the hydroxy defect. Profiles are shown for the MACE model as well as the reference DFT method, revPBE-D3. Predictions are compared with those of previous studies [366, 367]. Above the profiles, we plot the Mulliken net spin populations (M_s) and the sum of absolute Mulliken spins (M_s^{abs}) obtained from our revPBE-D3 calculations for each frame. Similar profiles are shown for **(c)** the conversion of the hydroxy defect to the ketone defect and **(d)** for the conversion between the ketone and pyran defects. **(e)** Overall state energy profile connecting the bare defect to the pyran defect. Energies are compared to those obtained in previous DFT studies [365–367]. **(f)** Representative snapshot of the gaseous structures used to obtain the NEB profiles.

An overall state energy profile connecting the bare SV defect to the pyran-like structure is shown in panel e.

Looking at Fig. 6.4, we see a relatively good agreement between the predictions of our MACE model and those of revPBE-D3 and previous literature estimates [365–367]. At each stage of the reaction, the change in potential energy between the initial and final states is consistent to within a couple of kcal/mol of revPBE-D3 values. Moreover, the qualitative ordering in the stability of these defects appears accordant with predictions from previous studies (panel e). However, there are some inconsistencies in the barrier predictions of these various methods. Specifically, we note that our MACE model systematically underpredicts barriers in the conversion between these species. This is particularly evident in panel d where there is an almost 20 kcal/mol difference between the MACE and revPBE-D3 barrier for the ketone-to-pyran conversion. Additionally, in panel c, we note that our current system setup predicts an almost barrierless process for the hydroxy-to-ketone reaction, contrasting with previous DFT predictions. Likely, discrepancies between our results and those of previous work stem from the difficulty of accurately describing near-transition-state regions at the DFT level. As can be seen in the Mulliken spin profiles, these regions exhibit complex spin behaviour, with both non-magnetic ($M_s = M_s^{\text{abs}} = 0$) and antiferromagnetic ($M_s = 0, M_s^{\text{abs}} > 0$) configurations being observed across a single reactive process. Likely, the energetic proximity of distinct spin surfaces makes DFT barriers highly sensitive to small changes in the atomistic positions and details of SCF convergence. At the same time, it is probable that our current MACE model undersamples the out-of-equilibrium portion of the potential energy surface corresponding to near-transition-state structures. Therefore, additional training data targeting this regime (e.g., from umbrella sampling runs where we can restrict sampling to specific parts of the reaction coordinate) will be included in future models. At any rate, that the conversion between the hydroxy defect and the ketone defect is barrierless does not seem surprising. Under the starting configuration, we have an electropositive hydrogen atom geometrically constrained to the vicinity of an unpaired electron; it would not be unreasonable to suggest rapid attack of the carbon radical on the hydrogen atom here.

6.4 Summary

In an effort to extend and improve our description of nanoporous environments, this chapter has reported an initial characterisation of graphene point defects under fully solvated conditions. We find that the SVs act as a hydrophilic centre in an otherwise hydrophobic graphene plane, leading to prominent aqueous adsorption and, in some cases, even reactivity. The hydrophilicity of these sites arises from hydrogen-bond interactions between the spin-polarised defect site and the adsorbed water molecules. Furthermore, we demonstrate that these adsorbed waters can undergo decomposition to form various chemisorbed states. The predicted energies and relative stabilities are consistent with previous modelling using DFT methods. Our work highlights the potential of the defect engineering of SV sites as reactive centres for effecting controlled chemical transformation.

Together with the results presented in Chapter 5, these insights highlight the intricate properties of nanoporous carbon systems. These materials exhibit a wide spectrum of properties according to their structuring and composition; our work shows how we can tailor these towards specific applications. For example, we can facilitate small-molecule adsorption by engineering carbons with small pore domains and a high level of graphitisation. Conversely, if we want to promote ion or polar molecule uptake, we can synthesise carbons with high levels of structural or compositional heterogeneity in the form of defects, heteroatom doping, and lattice corrugation effects. Recent studies on supercapacitor energy-storage devices have explored this principle [53]. The authors showed that the overall capacitance of such devices is directly linked to the level of disorder in the carbon electrodes, which acts to promote localisation of the charge in the lattice plane. Extending our work to treat electrolytic solutions (e.g., NEt_4BF_4/ACN (1 M)) would provide valuable insights on ion behaviour and charge-storage mechanisms in disordered carbon. Likely, in contrast to what was observed with HCO_3^- under pristine graphene conditions (see Fig. 5.2), the defect sites will promote the adsorption and accumulation of ions at the carbon surface, thereby explaining the observed capacitance trends.

Beyond molecule uptake and adsorption, nanoporous carbon material could also function as 'nanoreactors' through the engineered placement of SV defects. We have demonstrated the inherent reactivity of these sites under gaseous and solvated conditions. By tailoring the location and concentration of these defects, it may be possible to create designer lattice frameworks capable of effecting targeted chemical synthesis with control over rates, pathways, and product conversions. Whilst the experimental realisation of such a framework remains challenging, defect engineering remains an active field of study [377], and the insights obtained from our MD simulations could help inform on future syntheses and applications.

Having understood the influence of point defects on the structuring of the surrounding media as well as their intrinsic reactivity, future work will look to fully address the influence of solvation on defect-mediated chemical reactions. Making use of umbrella integration, we intend to probe the various stages of reaction in converting from the bare defect to the pyran-type reconstructed state. Results will be analysed and compared for both gaseous and solvated conditions. We anticipate that explicit solvation will help facilitate certain reactive processes (e.g., the initial attack of water on the SV site) while also changing the relative energies of the chemisorbed states (e.g., stabilising the chemisorbed hydroxy state through hydrogen bonding with the surrounding aqueous media).

Once the base reactivity of SVs is determined, we then aim to understand the adsorption and reaction of CO_2 molecules at defective graphene. Previous work has shown that individual CO_2 molecules can react and decompose at SV sites to form pristine graphene plus O_2 [373, 378]. In this way, the SV + CO_2 reaction could provide a new mechanism for repairing holes in defective graphene sheets. Using MD simulations, it would be interesting to evaluate the feasibility of this scheme as a means of producing highly graphitic nanoporous carbon, e.g., by passing supercritical CO_2 through the porous structure.

Chapter 7

Conclusions

> The universe is made of stories, not of atoms.
>
> *Muriel Rukeyser*
> *The Speed of Darkness*

In a world beset by rising temperatures and an ever-changing climate, the solution to our problems lies at surfaces and interfaces. These regions provide the means to capture, store, convert, and utilise anthropogenic CO_2 [379, 380], enabling the production of useful synthetic and industrial compounds whilst simultaneously mitigating some of the harsher effects of climate change. As we have shown, aqueous interfaces incorporating CO_2 molecules display a plethora of interesting physicochemical properties and phenomena. Understanding these properties at the microscopic scale can help inform decisions made at the macroscopic scale, thereby influencing the design and implementation of future CCS strategies, e.g., selecting appropriate underground reservoirs for liquefied CO_2 injection or designing new nanoporous electrodes to help maximise CO_2 uptake in electrochemical systems.

This thesis represents the culmination of four years' worth of work aimed at improving our understanding of CO_2 molecules at aqueous interfaces. In Chapter 1, we identified four outstanding questions on the nature of CO_2-H_2O interfaces. From our work, we found that, for ambient conditions at the air-water interface, CO_2 reacts with water via

a novel 'in-and-out' mechanism. This process is characterised by a dynamic reaction site, one that adapts its position according to evolving solute-solvent interactions and which engenders bulk-like properties for an inherently interfacial process. For higher pressure simulations and multiple CO_2's, we found that we could extend interfacial tension measurements using a combination of MLIPs and replica exchange MD. We determined that, with increasing pressure, CO_2 accumulates in a layered fashion at the water surface, forming a CO_2 monolayer at $p < 20$ bar with properties akin to those of liquid CO_2. And finally, for solid carbon-water systems, we provided an atomistic rationale for the observed oversolubility of CO_2 molecules in nanoporous carbon under ambient conditions. Within these environments, CO_2 preferentially locates at the pore wall, a phenomenon associated with favourable CO_2-wall interactions that out-compete those between the solvent and the wall. Citing certain limitations of the pore-slit model, we then provided details of current work looking to improve and extend our current description of nanoporous carbon environments. From our preliminary work, we recognised single vacancies as hydrophilic centres in an otherwise hydrophobic basal plane, and highlighted the potential of SVs as reaction sites in otherwise inert graphene planes.

Alongside addressing these open questions, we highlight three key takeaways regarding CO_2 at aqueous interfaces: (i) CO_2 preferentially does not mix with H_2O at ambient temperature; (ii) the properties of CO_2-H_2O interfaces are determined by the local conditions and surrounding environment; (iii) and MLIP methodology has reached the necessary maturity to enable the routine modelling of complex, interfacial regimes.

The first of these insights might appear somewhat obvious. Water is a polar molecule that exhibits a strong molecular dipole (1.85 D [381] in gas phase, $\sim$ 2.9 D in bulk water [382]) and undergoes extensive hydrogen bonding with neighbouring molecules. In contrast, CO_2 is non-polar and mainly interacts with other species via quadrupole, dispersion or induced-dipole interactions [29, 383]. In our work, we have seen many manifestations of this lack of mixing between these molecules. At the air-water interface, we identify CO_2's preferential location as being out of solution, on top of the interface. Whilst dispersion and induced-dipole forces facilitate CO_2 adsorption at this interface, these interactions are not

sufficiently strong to break the lateral network of hydrogen bonds between interfacial waters [384]. Then, at the liquid-liquid interface, we see how, even under immense pressures, the CO_2 and water fractions retain their cohesive integrity. Only partial dissolution of CO_2 in H_2O is observed, whilst H_2O appears completely insoluble in the CO_2. And finally, at the graphene-water interface, we observe that CO_2 is confined to the edge of the pore-slit environments, preferring to adsorb at the graphene walls than undergo dissolution in the more bulk-like components of the solvent. Likely, the phenomena detailed here are relevant to other molecule-water systems (e.g., H_2, CH_4), and our insights are applicable to the design of novel molecular separation schemes [385, 386].

In terms of the second insight from this work, recognising the relative insolubility of CO_2 in water, we see that the most interesting properties and phenomena of these systems are found at interfaces [30]. These spatially anisotropic regimes are unique in providing distinct solvation or phase environments over distances of just a couple of Å. Citing the limitations of FFs and AIMD (see Chapter 2), these regions have until now received comparatively little attention compared to bulk solution. Targeting these interfacial regimes, in Chapter 3, we uncover a new surface-mediated reaction mechanism between CO_2 and water. This previously undetermined mechanism highlights the dynamic nature of reaction sites at aqueous interfaces, something that we believe to be a general phenomenon for other interfacial reactions and processes. This has likely implications for fields such as organic chemistry (e.g., for 'on-water reactions' which undergo acceleration at aqueous interfaces [387]) and nanochemistry (e.g., nanodroplets as a form of reactor for chemical synthesis [388]). At the liquid-liquid interface, we observe novel CO_2 accumulation at the water interface with increasing pressure, a phenomenon likely associated with cross-phase and dipole-induced CO_2-H_2O interactions (something that FF modelling usually misses). And at the graphene-water interface, we find that molecular adsorption and reaction propensities can be modulated by controlling the pore topology and functionalisation. Through the deliberate engineering of graphitic and defect-rich regimes, we can likely tailor similar adsorption/reaction processes for other molecules, e.g., for chemical synthesis or industrial manufacturing.

And finally, making note of the various insights obtained in this work, we remark that all of this was made possible by the advent and subsequent maturity of MLIP techniques. The complexity and size of these interfaces - from the air-water to the liquid-water to the solid-water - would have previously precluded any sort of *ab initio*-level modelling. Indeed, even the simplest unconstrained MD simulation would be impeded by large computational costs and issues with SCF convergence. However, by combining the power of established sampling techniques (e.g., umbrella integration, metadynamics, replica exchange) with the efficiency and accuracy of now-mature MLIP approaches, we have been able to acquire various properties and insights at a first-principles level. This includes equilibrium properties (e.g., densities, orientations), mechanical observables (e.g., interfacial tensions), and free energies (e.g., of reaction and diffusion). In Chapter 3, we even obtained beyond-DFT accuracy by training an MLIP on RPA reference data. Extending MLIPs towards post-DFT (CC) accuracy now constitutes an active and promising field of research in the atomistic modelling community [389, 390].

Concerning the next steps for this work, there is a lot to be done to extend and improve the projects detailed in this thesis. An overarching improvement would be to include ionic species in our modelling, thereby improving the realism of our models and aligning our work more with experimental conditions. In the case of the air-water and liquid-water projects, this would involve incorporating sodium and chloride ions to our training data. Likely, this will alter some of the thermodynamic properties, e.g., stabilising reaction intermediates as well as disrupting aqueous surface cohesion through sub-layer ion adsorption [204, 391, 392]. There is also the potential for Na^+ and Cl^- to catalyse the CO_2 hydration reaction, thereby exacerbating current acidification predictions. Future work could potentially investigate preventative measures against carbonic acid formation, e.g., using natural or biologically derived surfactants to suppress CO_2 exchange at the ocean surface [393, 394]. In the case of the solid-liquid interface, modelling the influence of the electrolyte (Na^+, SO_4^{2-}, HCO_3^-) on CO_2 uptake and in-pore behaviour would also be a worthwhile pursuit [306, 330]. In the more immediate future, however, work will be undertaken to fully characterise the nature of defects under solvent-saturated conditions,

discerning exactly how solvation changes the structural and reactive properties of these defect sites.

Looking at the field of molecular simulations as a whole, there is a lot to be excited for going forward. The continual development of MLIP architecture and methods is ever opening new avenues for scientific exploration [38]. Foundation models are becoming increasingly more accurate and generalisable [395] and will help facilitate many of the new projects undertaken as part of this work and beyond. With all these new various methods and models, I think it is important that we are able to step back and assess the current methodological landscape. In a field that seems to change by the week (indeed, the MLIP frameworks I used at the start of this PhD are not the same as the ones I am finishing with), it is important that we are able to stop and utilise the available techniques towards obtaining insights into new and interesting systems. Method development, for all its usefulness, is nothing without application. In my PhD, I have used this conviction to help uncover new fundamental insights into the nature of atoms and molecules.

In summary, in this thesis we have uncovered a new reaction mechanism relevant to air-water interfaces, reported novel CO_2 accumulation at pressurised liquid-liquid interfaces, and showed that CO_2 uptake in nanoporous environments is mediated by pore wall adsorption. Methodologically, we have shown that MLIPs coupled with established free energy methods deliver first-principles accuracy for complex interfacial systems. Whilst certain aspects of this can be improved in future work (e.g., beyond-GGA baselines, extended training domains, improved sampling techniques), the framework utilised is readily extendable to electrolytic environments and defect-rich carbon environments. The work presented in this thesis connects atomistic insights on the nature of CO_2 and water with practical strategies for carbon capture and utilisation technologies.

References

(1) Gattuso, J.-P. et al. Contrasting futures for ocean and society from different anthropogenic CO2 emissions scenarios. *Science.* **2015**, *349*, aac4722.

(2) Ballester, J.; Quijal-Zamorano, M.; Méndez Turrubiates, R. F.; Pegenaute, F.; Herrmann, F. R.; Robine, J. M.; Basagaña, X.; Tonne, C.; Antó, J. M.; Achebak, H. Heat-related mortality in Europe during the summer of 2022. *Nat. Med.* **2023**, *29*, 1857–1866.

(3) Zhang, W.; Zhou, T.; Wu, P. Anthropogenic amplification of precipitation variability over the past century. *Science.* **2024**, *385*, 427–432.

(4) Abatzoglou, J. T.; Williams, A. P. Impact of anthropogenic climate change on wildfire across western US forests. *Proc. Natl. Acad. Sci.* **2016**, *113*, 11770–11775.

(5) Hoegh-Guldberg, O. et al. Coral Reefs Under Rapid Climate Change and Ocean Acidification. *Science.* **2007**, *318*, 1737–1742.

(6) Petit, J. R. et al. Climate and atmospheric history of the past 420,000 years from the Vostok ice core, Antarctica. *Nature* **1999**, *399*, 429–436.

(7) IPCC Summary for Policymakers. In: Climate Change 2023: Synthesis Report, {https://www.ipcc.ch/report/ar6/syr/summary-for-policymakers/}, 2023.

(8) Orr, J. C. et al. Anthropogenic ocean acidification over the twenty-first century and its impact on calcifying organisms. *Nature* **2005**, *437*, 681–686.

(9) Doney, S. C.; Fabry, V. J.; Feely, R. A.; Kleypas, J. A. Ocean Acidification: The Other CO2 Problem. *Ann. Rev. Mar. Sci.* **2009**, *1*, 169–192.

(10) Gilfillan, S. M. V.; Lollar, B. S.; Holland, G.; Blagburn, D.; Stevens, S.; Schoell, M.; Cassidy, M.; Ding, Z.; Zhou, Z.; Lacrampe-Couloume, G.; Ballentine, C. J. Solubility trapping in formation water as dominant CO2 sink in natural gas fields. *Nature* **2009**, *458*, 614–618.

(11) Orr, F. M. Onshore Geologic Storage of CO2. *Science.* **2009**, *325*, 1656–1658.

(12) Binford, T. B.; Mapstone, G.; Temprano, I.; Forse, A. C. Enhancing the capacity of supercapacitive swing adsorption CO2 capture by tuning charging protocols. *Nanoscale* **2022**, *14*, 7980–7984.

(13) Seo, H.; Hatton, T. A. Electrochemical direct air capture of CO2 using neutral red as reversible redox-active material. *Nat. Commun.* **2023**, *14*, 313.

(14) Frenkel, D.; Smit, B. In *Underst. Mol. Simul.* Frenkel, D., Smit, B., Eds.; Academic Press: San Diego, 2002, pp 23–61.

(15) Frenkel, D.; Smit, B. In *Underst. Mol. Simul.* Frenkel, D., Smit, B., Eds.; Academic Press: San Diego, 2002, pp 63–107.

(16) Metropolis, N.; Rosenbluth, A. W.; Rosenbluth, M. N.; Teller, A. H.; Teller, E. Equation of State Calculations by Fast Computing Machines. *J. Chem. Phys.* **1953**, *21*, 1087–1092.

(17) Alder, B. J.; Wainwright, T. E. Phase Transition for a Hard Sphere System. *J. Chem. Phys.* **1957**, *27*, 1208–1209.

(18) Rahman, A. Correlations in the Motion of Atoms in Liquid Argon. *Phys. Rev.* **1964**, *136*, A405–A411.

(19) Abascal, J. L. F.; Vega, C. A general purpose model for the condensed phases of water: TIP4P/2005. *J. Chem. Phys.* **2005**, *123*, 234505.

(20) Shaw, D. E.; Maragakis, P.; Lindorff-Larsen, K.; Piana, S.; Dror, R. O.; Eastwood, M. P.; Bank, J. A.; Jumper, J. M.; Salmon, J. K.; Shan, Y.; Wriggers, W. Atomic-Level Characterization of the Structural Dynamics of Proteins. *Science.* **2010**, *330*, 341–346.

(21) Marrink, S. J.; Risselada, H. J.; Yefimov, S.; Tieleman, D. P.; de Vries, A. H. The MARTINI Force Field: Coarse Grained Model for Biomolecular Simulations. *J. Phys. Chem. B* **2007**, *111*, 7812–7824.

(22) Car, R.; Parrinello, M. Unified Approach for Molecular Dynamics and Density-Functional Theory. *Phys. Rev. Lett.* **1985**, *55*, 2471–2474.

(23) Hassanali, A.; Giberti, F.; Cuny, J.; Kühne, T. D.; Parrinello, M. Proton transfer through the water gossamer. *Proc. Natl. Acad. Sci.* **2013**, *110*, 13723–13728.

(24) Goldman, N.; Fried, L. E.; Kuo, I.-F. W.; Mundy, C. J. Bonding in the Superionic Phase of Water. *Phys. Rev. Lett.* **2005**, *94*, 217801.

(25) Jiao, D.; Rempe, S. B. CO2 solvation free energy using quasi-chemical theory. *J. Chem. Phys.* **2011**, *134*, 224506.

(26) Shiga, M.; Morishita, T.; Sorai, M. Interfacial tension of carbon dioxide - water under conditions of CO2 geological storage and enhanced geothermal systems: A molecular dynamics study on the effect of temperature. *Fuel* **2023**, *337*, 127219.

(27) Stirling, A.; Pápai, I. H2CO3 Forms via HCO3− in Water. *J. Phys. Chem. B* **2010**, *114*, 16854–16859.

(28) Prasetyo, N.; Hofer, T. S. Structure, Dynamics, and Hydration Free Energy of Carbon Dioxide in Aqueous Solution: A Quantum Mechanical/Molecular Mechanics Molecular Dynamics Thermodynamic Integration (QM/MM MD TI) Simulation Study. *J. Chem. Theory Comput.* **2018**, *14*, 6472–6483.

(29) Wheatley, R. J.; Harvey, A. H. Intermolecular potential energy surface and second virial coefficients for the water–CO2 dimera). *J. Chem. Phys.* **2011**, *134*, 134309.

(30) Björneholm, O.; Hansen, M. H.; Hodgson, A.; Liu, L.-M.; Limmer, D. T.; Michaelides, A.; Pedevilla, P.; Rossmeisl, J.; Shen, H.; Tocci, G.; Tyrode, E.; Walz, M.-M.; Werner, J.; Bluhm, H. Water at Interfaces. *Chem. Rev.* **2016**, *116*, 7698–7726.

(31) Tang, F.; Ohto, T.; Sun, S.; Rouxel, J. R.; Imoto, S.; Backus, E. H. G.; Mukamel, S.; Bonn, M.; Nagata, Y. Molecular Structure and Modeling of Water–Air and Ice–Air Interfaces Monitored by Sum-Frequency Generation. *Chem. Rev.* **2020**, *120*, 3633–3667.

(32) Shen, Y. R.; Ostroverkhov, V. Sum-Frequency Vibrational Spectroscopy on Water Interfaces: Polar Orientation of Water Molecules at Interfaces. *Chem. Rev.* **2006**, *106*, 1140–1154.

(33) Hua, W.; Verreault, D.; Adams, E. M.; Huang, Z.; Allen, H. C. Impact of Salt Purity on Interfacial Water Organization Revealed by Conventional and Heterodyne-Detected Vibrational Sum Frequency Generation Spectroscopy. *J. Phys. Chem. C* **2013**, *117*, 19577–19585.

(34) Nagata, Y.; Ohto, T.; Bonn, M.; Kühne, T. D. Surface tension of ab initio liquid water at the water-air interface. *J. Chem. Phys.* **2016**, *144*, 204705.

(35) Deringer, V. L.; Caro, M. A.; Csányi, G. Machine Learning Interatomic Potentials as Emerging Tools for Materials Science. *Adv. Mater.* **2019**, *31*, 1902765.

(36) Behler, J. Four Generations of High-Dimensional Neural Network Potentials. *Chem. Rev.* **2021**, *121*, 10037–10072.

(37) Deringer, V. L.; Bartók, A. P.; Bernstein, N.; Wilkins, D. M.; Ceriotti, M.; Csányi, G. Gaussian Process Regression for Materials and Molecules. *Chem. Rev.* **2021**, *121*, 10073–10141.

(38) Thiemann, F. L.; O'neill, N.; Kapil, V.; Michaelides, A.; Schran, C. Introduction to machine learning potentials for atomistic simulations. *J. Phys. Condens. Matter* **2024**, *37*, 73002.

(39) Galib, M.; Limmer, D. T. Reactive uptake of N2O5 by atmospheric aerosol is dominated by interfacial processes. *Science.* **2021**, *371*, 921–925.

(40) De la Puente, M.; David, R.; Gomez, A.; Laage, D. Acids at the Edge: Why Nitric and Formic Acid Dissociations at Air–Water Interfaces Depend on Depth and on Interface Specific Area. *J. Am. Chem. Soc.* **2022**, *144*, 10524–10529.

(41) Wohlfahrt, O.; Dellago, C.; Sega, M. Ab initio structure and thermodynamics of the RPBE-D3 water/vapor interface by neural-network molecular dynamics. *J. Chem. Phys.* **2020**, *153*, 144710.

(42) Niblett, S. P.; Galib, M.; Limmer, D. T. Learning intermolecular forces at liquid–vapor interfaces. *J. Chem. Phys.* **2021**, *155*, 164101.

(43) Kapil, V.; Schran, C.; Zen, A.; Chen, J.; Pickard, C. J.; Michaelides, A. The first-principles phase diagram of monolayer nanoconfined water. *Nature* **2022**, *609*, 512–516.

(44) Fong, K. D.; Sumić, B.; O'Neill, N.; Schran, C.; Grey, C. P.; Michaelides, A. The Interplay of Solvation and Polarization Effects on Ion Pairing in Nanoconfined Electrolytes. *Nano Lett.* **2024**, *24*, 5024–5030.

(45) Advincula, X. R.; Fong, K. D.; Michaelides, A.; Schran, C. Protons Accumulate at the Graphene–Water Interface. *ACS Nano* **2025**, *19*, 17728–17737.

(46) Tian, X.; Gardini, A. T.; Raucci, U.; Xiao, H.; Zhuo, Y.; Parrinello, M. Electrochemical Potential-Driven Water Dynamics Control CO2 Electroreduction at the Ag/H2O Interface. *ChemRxiv* **2025**.

(47) Jungwirth, P.; Tobias, D. J. Specific Ion Effects at the Air/Water Interface. *Chem. Rev.* **2006**, *106*, 1259–1281.

(48) Ringrose, P. S.; Furre, A.-K.; Gilfillan, S. M. V.; Krevor, S.; Landrø, M.; Leslie, R.; Meckel, T.; Nazarian, B.; Zahid, A. Storage of Carbon Dioxide in Saline Aquifers: Physicochemical Processes, Key Constraints, and Scale-Up Potential. *Annu. Rev. Chem. Biomol. Eng.* **2021**, *12*, 471–494.

(49) Nealson, K. Lakes of liquid CO2 in the deep sea. *Proc. Natl. Acad. Sci.* **2006**, *103*, 13903–13904.

(50) Mathur, R.; Muniz, M. C.; Yue, S.; Car, R.; Panagiotopoulos, A. Z. First-Principles-Based Machine Learning Models for Phase Behavior and Transport Properties of CO2. *J. Phys. Chem. B* **2023**, *127*, 4562–4569.

(51) Meunier, V.; Ania, C.; Bianco, A.; Chen, Y.; Choi, G. B.; Kim, Y. A.; Koratkar, N.; Liu, C.; Tascon, J. M. D.; Terrones, M. Carbon science perspective in 2022: Current research and future challenges. *Carbon N. Y.* **2022**, *195*, 272–291.

(52) Rahimi, M.; Khurram, A.; Hatton, T. A.; Gallant, B. Electrochemical carbon capture processes for mitigation of CO 2 emissions. *Chem. Soc. Rev.* **2022**, *51*, 8676–8695.

(53) Liu, X.; Lyu, D.; Merlet, C.; Leesmith, M. J. A.; Hua, X.; Xu, Z.; Grey, C. P.; Forse, A. C. Structural disorder determines capacitance in nanoporous carbons. *Science.* **2024**, *384*, 321–325.

(54) Fong, K. D.; Grey, C. P.; Michaelides, A. On the Physical Origins of Reduced Ionic Conductivity in Nanoconfined Electrolytes. *ACS Nano* **2025**, *19*, 13191–13201.

(55) Frenkel, D.; Smit, B. In *Underst. Mol. Simul.* Frenkel, D., Smit, B., Eds.; Academic Press: San Diego, 2002, pp 9–22.

(56) Huang, K., *Statistical mechanics*; John Wiley & Sons: 2008.

(57) Tuckerman, M. E., *Statistical Mechanics: Theory and Molecular Simulation*; Oxford University Press: 2023.

(58) Swope, W. C.; Andersen, H. C.; Berens, P. H.; Wilson, K. R. A computer simulation method for the calculation of equilibrium constants for the formation of physical clusters of molecules: Application to small water clusters. *J. Chem. Phys.* **1982**, *76*, 637–649.

(59) Verlet, L. Computer "Experiments" on Classical Fluids. I. Thermodynamical Properties of Lennard-Jones Molecules. *Phys. Rev.* **1967**, *159*, 98–103.

(60) Gear, C. W., *Numerical initial value problems in ordinary differential equations*; Prentice-Hall series in automatic computation; Prentice-Hall: Englewood Cliffs, N.J. ; London, 1971.

(61) Andersen, H. C. Molecular dynamics simulations at constant pressure and/or temperature. *J. Chem. Phys.* **1980**, *72*, 2384–2393.

(62) Bussi, G.; Donadio, D.; Parrinello, M. Canonical sampling through velocity rescaling. *J. Chem. Phys.* **2007**, *126*, 014101.

(63) Hoover, W. G. Canonical dynamics: Equilibrium phase-space distributions. *Phys. Rev. A* **1985**, *31*, 1695–1697.

(64) Parrinello, M.; Rahman, A. Polymorphic transitions in single crystals: A new molecular dynamics method. *J. Appl. Phys.* **1981**, *52*, 7182–7190.

(65) Martyna, G. J.; Tobias, D. J.; Klein, M. L. Constant pressure molecular dynamics algorithms. *J. Chem. Phys.* **1994**, *101*, 4177–4189.

(66) Martyna, G. J.; Tuckerman, M. E.; Tobias, D. J.; Klein, M. L. Explicit reversible integrators for extended systems dynamics. *Mol. Phys.* **1996**, *87*, 1117–1157.

(67) Jones, J. E. On the determination of molecular fields. —II. From the equation of state of a gas. *Proc. R. Soc. London. Ser. A, Contain. Pap. a Math. Phys. Character* **1924**, *106*, 463–477.

(68) Berendsen, H. J. C.; Grigera, J. R.; Straatsma, T. P. The missing term in effective pair potentials. *J. Phys. Chem.* **1987**, *91*, 6269–6271.

(69) Maier, J. A.; Martinez, C.; Kasavajhala, K.; Wickstrom, L.; Hauser, K. E.; Simmerling, C. ff14SB: Improving the Accuracy of Protein Side Chain and Backbone Parameters from ff99SB. *J. Chem. Theory Comput.* **2015**, *11*, 3696–3713.

(70) Van Duin, A. C. T.; Dasgupta, S.; Lorant, F.; Goddard, W. A. ReaxFF: A Reactive Force Field for Hydrocarbons. *J. Phys. Chem. A* **2001**, *105*, 9396–9409.

(71) Tuckerman, M. E. Ab initio molecular dynamics: basic concepts, current trends and novel applications. *J. Phys. Condens. Matter* **2002**, *14*, R1297.

(72) Markland, T. E.; Ceriotti, M. Nuclear quantum effects enter the mainstream. *Nat. Rev. Chem.* **2018**, *2*, 109.

(73) Feynman, R. P. Space-Time Approach to Non-Relativistic Quantum Mechanics. *Rev. Mod. Phys.* **1948**, *20*, 367–387.

(74) Feynman, R. P.; Mechanics, A. R. H. Q. Path integrals. *Lect. Notes Phys* **1979**, *106*, 64.

(75) Sarnthein, J.; Pasquarello, A.; Car, R. Origin of the High-Frequency Doublet in the Vibrational Spectrum of Vitreous SiO2. *Science.* **1997**, *275*, 1925–1927.

(76) Tuckerman, M.; Laasonen, K.; Sprik, M.; Parrinello, M. Ab initio molecular dynamics simulation of the solvation and transport of hydronium and hydroxyl ions in water. *J. Chem. Phys.* **1995**, *103*, 150–161.

(77) Fink, C. K.; Jenkins, S. J. First-principles molecular dynamics of the initial oxidation of Si[001] by ozone. *Phys. Rev. B* **2008**, *78*, 195407.

(78) Thake, H.; Jenkins, S. J. First-Principles Dynamics of the Surface Fluorination of Diamond. *Langmuir* **2025**, *41*, 16315–16327.

(79) Hartree, D. R. The Wave Mechanics of an Atom with a Non-Coulomb Central Field. Part I. Theory and Methods. *Math. Proc. Cambridge Philos. Soc.* **1928**, *24*, 89–110.

(80) Fock, V. Näherungsmethode zur Lösung des quantenmechanischen Mehrkörperproblems. *Zeitschrift für Phys.* **1930**, *61*, 126–148.

(81) Slater, J. C. Note on Hartree's Method. *Phys. Rev.* **1930**, *35*, 210–211.

(82) Møller, C.; Plesset, M. S. Note on an approximation treatment for many-electron systems. *Phys. Rev.* **1934**, *46*, 618–622.

(83) Čížek, J. On the Correlation Problem in Atomic and Molecular Systems. Calculation of Wavefunction Components in Ursell-Type Expansion Using Quantum-Field Theoretical Methods. *J. Chem. Phys.* **1966**, *45*, 4256–4266.

(84) Raghavachari, K.; Trucks, G. W.; Pople, J. A.; Head-Gordon, M. A fifth-order perturbation comparison of electron correlation theories. *Chem. Phys. Lett.* **1989**, *157*, 479–483.

(85) Sinnokrot, M. O.; Sherrill, C. D. Highly Accurate Coupled Cluster Potential Energy Curves for the Benzene Dimer: Sandwich, T-Shaped, and Parallel-Displaced Configurations. *J. Phys. Chem. A* **2004**, *108*, 10200–10207.

(86) Tsuzuki, S.; Mikami, M.; Yamada, S. Origin of Attraction, Magnitude, and Directionality of Interactions in Benzene Complexes with Pyridinium Cations. *J. Am. Chem. Soc.* **2007**, *129*, 8656–8662.

(87) Qin, J.; Liu, Y.; Li, J. Quantitative dynamics of paradigmatic SN2 reaction OH− + CH3F on accurate full-dimensional potential energy surface. *J. Chem. Phys.* **2022**, *157*, 124301.

(88) Tajti, A.; Szalay, P. G.; Császár, A. G.; Kállay, M.; Gauss, J.; Valeev, E. F.; Flowers, B. A.; Vázquez, J.; Stanton, J. F. HEAT: High accuracy extrapolated ab initio thermochemistry. *J. Chem. Phys.* **2004**, *121*, 11599–11613.

(89) Takatani, T.; Hohenstein, E. G.; Malagoli, M.; Marshall, M. S.; Sherrill, C. D. Basis set consistent revision of the S22 test set of noncovalent interaction energies. *J. Chem. Phys.* **2010**, *132*, 144104.

(90) Riplinger, C.; Sandhoefer, B.; Hansen, A.; Neese, F. Natural triple excitations in local coupled cluster calculations with pair natural orbitals. *J. Chem. Phys.* **2013**, *139*, 134101.

(91) Hohenberg, P.; Kohn, W. Inhomogeneous Electron Gas. *Phys. Rev.* **1964**, *136*, B864–B871.

(92) Kohn, W.; Sham, L. J. Self-Consistent Equations Including Exchange and Correlation Effects. *Phys. Rev.* **1965**, *140*, A1133–A1138.

(93) Santra, B.; Michaelides, A.; Scheffler, M. On the accuracy of density-functional theory exchange-correlation functionals for H bonds in small water clusters: Benchmarks approaching the complete basis set limit. *J. Chem. Phys.* **2007**, *127*, 184104.

(94) Burke, K.; Perdew, J. P.; Wang, Y. In *Electron. Density Funct. Theory Recent Prog. new Dir.* Springer: 1998, pp 81–111.

(95) Perdew, J. P.; Burke, K.; Ernzerhof, M. Generalized Gradient Approximation Made Simple. *Phys. Rev. Lett.* **1996**, *77*, 3865–3868.

(96) Sun, J.; Ruzsinszky, A.; Perdew, J. P. Strongly Constrained and Appropriately Normed Semilocal Density Functional. *Phys. Rev. Lett.* **2015**, *115*, 36402.

(97) Furness, J. W.; Kaplan, A. D.; Ning, J.; Perdew, J. P.; Sun, J. Accurate and Numerically Efficient r2SCAN Meta-Generalized Gradient Approximation. *J. Phys. Chem. Lett.* **2020**, *11*, 8208–8215.

(98) Adamo, C.; Barone, V. Toward reliable density functional methods without adjustable parameters: The PBE0 model. *J. Chem. Phys.* **1999**, *110*, 6158–6170.

(99) Becke, A. D. Density-functional thermochemistry. III. The role of exact exchange. *J. Chem. Phys.* **1993**, *98*, 5648–5652.

(100) Heyd, J.; Scuseria, G. E.; Ernzerhof, M. Hybrid functionals based on a screened Coulomb potential. *J. Chem. Phys.* **2003**, *118*, 8207–8215.

(101) Grimme, S. Semiempirical hybrid density functional with perturbative second-order correlation. *J. Chem. Phys.* **2006**, *124*, 34108.

(102) Mardirossian, N.; Head-Gordon, M. Survival of the most transferable at the top of Jacob's ladder: Defining and testing the ωB97M(2) double hybrid density functional. *J. Chem. Phys.* **2018**, *148*, 241736.

(103) Furche, F. Molecular tests of the random phase approximation to the exchange-correlation energy functional. *Phys. Rev. B* **2001**, *64*, 195120.

(104) Eshuis, H.; Bates, J. E.; Furche, F. Electron correlation methods based on the random phase approximation. *Theor. Chem. Acc.* **2012**, *131*, 1084.

(105) Van Mourik, T.; Wilson, A. K.; Dunning JR, T. H. Benchmark calculations with correlated molecular wavefunctions. XIII. Potential energy curves for He2, Ne2 and Ar2 using correlation consistent basis sets through augmented sextuple zeta. *Mol. Phys.* **1999**, *96*, 529–547.

(106) in 't Veld, P. J.; Ismail, A. E.; Grest, G. S. Application of Ewald summations to long-range dispersion forces. *J. Chem. Phys.* **2007**, *127*, 144711.

(107) Reilly, A. M.; Tkatchenko, A. Role of Dispersion Interactions in the Polymorphism and Entropic Stabilization of the Aspirin Crystal. *Phys. Rev. Lett.* **2014**, *113*, 55701.

(108) Dion, M.; Rydberg, H.; Schröder, E.; Langreth, D. C.; Lundqvist, B. I. Van der Waals Density Functional for General Geometries. *Phys. Rev. Lett.* **2004**, *92*, 246401.

(109) Lee, K.; Murray, É. D.; Kong, L.; Lundqvist, B. I.; Langreth, D. C. Higher-accuracy van der Waals density functional. *Phys. Rev. B* **2010**, *82*, 81101.

(110) Hamada, I. van der Waals density functional made accurate. *Phys. Rev. B* **2014**, *89*, 121103.

(111) Klimeš, J.; Bowler, D. R.; Michaelides, A. Chemical accuracy for the van der Waals density functional. *J. Phys. Condens. Matter* **2010**, *22*, 22201.

(112) Grimme, S. Accurate description of van der Waals complexes by density functional theory including empirical corrections. *J. Comput. Chem.* **2004**, *25*, 1463–1473.

(113) Grimme, S. Semiempirical GGA-type density functional constructed with a long-range dispersion correction. *J. Comput. Chem.* **2006**, *27*, 1787–1799.

(114) Guidez, E. B.; Gordon, M. S. Dispersion Correction Derived from First Principles for Density Functional Theory and Hartree–Fock Theory. *J. Phys. Chem. A* **2015**, *119*, 2161–2168.

(115) Grimme, S.; Antony, J.; Ehrlich, S.; Krieg, H. A consistent and accurate ab initio parametrization of density functional dispersion correction (DFT-D) for the 94 elements H-Pu. *J. Chem. Phys.* **2010**, *132*, 154104.

(116) Caldeweyher, E.; Ehlert, S.; Hansen, A.; Neugebauer, H.; Spicher, S.; Bannwarth, C.; Grimme, S. A generally applicable atomic-charge dependent London dispersion correction. *J. Chem. Phys.* **2019**, *150*, 154122.

(117) Tkatchenko, A.; Scheffler, M. Accurate Molecular Van Der Waals Interactions from Ground-State Electron Density and Free-Atom Reference Data. *Phys. Rev. Lett.* **2009**, *102*, 73005.

(118) Becke, A. D.; Johnson, E. R. Exchange-hole dipole moment and the dispersion interaction: High-order dispersion coefficients. *J. Chem. Phys.* **2006**, *124*, 14104.

(119) VandeVondele, J.; Krack, M.; Mohamed, F.; Parrinello, M.; Chassaing, T.; Hutter, J. Quickstep: Fast and accurate density functional calculations using a mixed Gaussian and plane waves approach. *Comput. Phys. Commun.* **2005**, *167*, 103–128.

(120) Kühne, T. D. et al. CP2K: An electronic structure and molecular dynamics software package - Quickstep: Efficient and accurate electronic structure calculations. *J. Chem. Phys.* **2020**, *152*, 194103.

(121) Lippert, G.; Hutter, J.; Parrinello, M. A hybrid Gaussian and plane wave density functional scheme. *Mol. Phys.* **1997**, *92*, 477–488.

(122) Kresse, G.; Hafner, J. Ab Initio Molecular Dynamics for Liquid Metals. *Physical Review B* **1993**, *47*, 558–561.

(123) Kresse, G.; Hafner, J. Ab Initio Molecular-Dynamics Simulation of the Liquid-Metal–Amorphous-Semiconductor Transition in Germanium. *Physical Review B* **1994**, *49*, 14251–14269.

(124) Kresse, G.; Furthmüller, J. Efficiency of Ab-Initio Total Energy Calculations for Metals and Semiconductors Using a Plane-Wave Basis Set. *Computational Materials Science* **1996**, *6*, 15–50.

(125) Kresse, G.; Furthmüller, J. Efficient Iterative Schemes for Ab Initio Total-Energy Calculations Using a Plane-Wave Basis Set. *Physical Review B* **1996**, *54*, 11169–11186.

(126) Blum, V.; Gehrke, R.; Hanke, F.; Havu, P.; Havu, V.; Ren, X.; Reuter, K.; Scheffler, M. Ab initio molecular simulations with numeric atom-centered orbitals. *Comput. Phys. Commun.* **2009**, *180*, 2175–2196.

(127) Ren, X.; Merz, F.; Jiang, H.; Yao, Y.; Rampp, M.; Lederer, H.; Blum, V.; Scheffler, M. All-electron periodic G0W0 implementation with numerical atomic orbital basis functions: Algorithm and benchmarks. *Phys. Rev. Mater.* **2021**, *5*, 13807.

(128) Marx, D.; Hutter, J., *Ab Initio Molecular Dynamics: Basic Theory and Advanced Methods*; Cambridge University Press: Cambridge, 2009.

(129) Iftimie, R.; Minary, P.; Tuckerman, M. E. Ab initio molecular dynamics: Concepts, recent developments, and future trends. *Proc. Natl. Acad. Sci.* **2005**, *102*, 6654–6659.

(130) Hutter, J. Car–Parrinello molecular dynamics. *WIREs Comput. Mol. Sci.* **2012**, *2*, 604–612.

(131) Laasonen, K.; Sprik, M.; Parrinello, M.; Car, R. "Ab initio" liquid water. *J. Chem. Phys.* **1993**, *99*, 9080–9089.

(132) Ikeda, T.; Sprik, M.; Terakura, K.; Parrinello, M. Pressure Effects on Hydrogen Bonding in the Disordered Phase of Solid HBr. *Phys. Rev. Lett.* **1998**, *81*, 4416–4419.

(133) Rousseau, R.; Boero, M.; Bernasconi, M.; Parrinello, M.; Terakura, K. Ab initio Simulation of Phase Transitions and Dissociation of H2S at High Pressure. *Phys. Rev. Lett.* **2000**, *85*, 1254–1257.

(134) Meijer, E. J.; Sprik, M. A Density Functional Study of the Addition of Water to SO3 in the Gas Phase and in Aqueous Solution. *J. Phys. Chem. A* **1998**, *102*, 2893–2898.

(135) Laasonen, K.; Klein, M. L. Ab Initio Molecular Dynamics Study of Hydrochloric Acid in Water. *J. Am. Chem. Soc.* **1994**, *116*, 11620–11621.

(136) Wang, L.-P.; Titov, A.; McGibbon, R.; Liu, F.; Pande, V. S.; Martínez, T. J. Discovering chemistry with an ab initio nanoreactor. *Nat. Chem.* **2014**, *6*, 1044–1048.

(137) Hey, T.; Tansley, S.; Tolle, K.; Gray, J., *The Fourth Paradigm: Data-Intensive Scientific Discovery*; Microsoft Research: 2009.

(138) Behler, J.; Parrinello, M. Generalized Neural-Network Representation of High-Dimensional Potential-Energy Surfaces. *Phys. Rev. Lett.* **2007**, *98*, 146401.

(139) Wang, H.; Zhang, L.; Han, J.; E, W. DeePMD-kit: A deep learning package for many-body potential energy representation and molecular dynamics. *Comput. Phys. Commun.* **2018**, *228*, 178–184.

(140) Bartók, A. P.; Payne, M. C.; Kondor, R.; Csányi, G. Gaussian Approximation Potentials: The Accuracy of Quantum Mechanics, without the Electrons. *Phys. Rev. Lett.* **2010**, *104*, 136403.

(141) Batatia, I.; Kovacs, D. P.; Simm, G.; Ortner, C.; Csányi, G. MACE: Higher order equivariant message passing neural networks for fast and accurate force fields. *Adv. Neural Inf. Process. Syst.* **2022**, *35*, 11423–11436.

(142) Batzner, S.; Musaelian, A.; Sun, L.; Geiger, M.; Mailoa, J. P.; Kornbluth, M.; Molinari, N.; Smidt, T. E.; Kozinsky, B. E(3)-equivariant graph neural networks for data-efficient and accurate interatomic potentials. *Nat. Commun.* **2022**, *13*, 2453.

(143) Musaelian, A.; Batzner, S.; Johansson, A.; Sun, L.; Owen, C. J.; Kornbluth, M.; Kozinsky, B. Learning local equivariant representations for large-scale atomistic dynamics. *Nat. Commun.* **2023**, *14*, 579.

(144) Mishin, Y. Machine-learning interatomic potentials for materials science. *Acta Mater.* **2021**, *214*, 116980.

(145) Friederich, P.; Häse, F.; Proppe, J.; Aspuru-Guzik, A. Machine-learned potentials for next-generation matter simulations. *Nat. Mater.* **2021**, *20*, 750–761.

(146) Kalman, R. E. A New Approach to Linear Filtering and Prediction Problems. *J. Basic Eng.* **1960**, *82*, 35–45.

(147) Behler, J. Atom-centered symmetry functions for constructing high-dimensional neural network potentials. *J. Chem. Phys.* **2011**, *134*, 74106.

(148) Drautz, R. Atomic cluster expansion for accurate and transferable interatomic potentials. *Phys. Rev. B* **2019**, *99*, 14104.

(149) Kovács, D. P.; Batatia, I.; Arany, E. S.; Csányi, G. Evaluation of the MACE force field architecture: From medicinal chemistry to materials science. *J. Chem. Phys.* **2023**, *159*, 44118.

(150) Bochkarev, A.; Lysogorskiy, Y.; Drautz, R. Graph Atomic Cluster Expansion for Semilocal Interactions beyond Equivariant Message Passing. *Phys. Rev. X* **2024**, *14*, 21036.

(151) Kovács, D. P.; van der Oord, C.; Kucera, J.; Allen, A. E. A.; Cole, D. J.; Ortner, C.; Csányi, G. Linear Atomic Cluster Expansion Force Fields for Organic Molecules: Beyond RMSE. *J. Chem. Theory Comput.* **2021**, *17*, 7696–7711.

(152) Reddi, S. J.; Kale, S.; Kumar, S. On the convergence of adam and beyond. *arXiv Prepr. arXiv1904.09237* **2019**.

(153) Blank, T. B.; Brown, S. D.; Calhoun, A. W.; Doren, D. J. Neural network models of potential energy surfaces. *J. Chem. Phys.* **1995**, *103*, 4129–4137.

(154) Cox, S. J. Dielectric response with short-ranged electrostatics. *Proc. Natl. Acad. Sci.* **2020**, *117*, 19746–19752.

(155) French, R. H. et al. Long range interactions in nanoscale science. *Rev. Mod. Phys.* **2010**, *82*, 1887–1944.

(156) Artrith, N.; Morawietz, T.; Behler, J. High-dimensional neural-network potentials for multicomponent systems: Applications to zinc oxide. *Phys. Rev. B* **2011**, *83*, 153101.

(157) Morawietz, T.; Sharma, V.; Behler, J. A neural network potential-energy surface for the water dimer based on environment-dependent atomic energies and charges. *J. Chem. Phys.* **2012**, *136*, 64103.

(158) Ko, T. W.; Finkler, J. A.; Goedecker, S.; Behler, J. A fourth-generation high-dimensional neural network potential with accurate electrostatics including non-local charge transfer. *Nat. Commun.* **2021**, *12*, 398.

(159) Rowe, P.; Deringer, V. L.; Gasparotto, P.; Csányi, G.; Michaelides, A. An accurate and transferable machine learning potential for carbon. *J. Chem. Phys.* **2020**, *153*, 34702.

(160) Batatia, I.; Benner, P.; Chiang, Y.; Elena, A. M.; Kovács, D. P.; Riebesell, J.; Advincula, X. R.; Asta, M.; Avaylon, M.; Baldwin, W. J. A foundation model for atomistic materials chemistry. *arXiv Prepr. arXiv2401.00096* **2023**.

(161) Kovács, D. P.; Moore, J. H.; Browning, N. J.; Batatia, I.; Horton, J. T.; Pu, Y.; Kapil, V.; Witt, W. C.; Magdău, I.-B.; Cole, D. J.; Csányi, G. MACE-OFF: Short-Range Transferable Machine Learning Force Fields for Organic Molecules. *J. Am. Chem. Soc.* **2025**, *147*, 17598–17611.

(162) Merchant, A.; Batzner, S.; Schoenholz, S. S.; Aykol, M.; Cheon, G.; Cubuk, E. D. Scaling deep learning for materials discovery. *Nature* **2023**, *624*, 80–85.

(163) Yang, H.; Hu, C.; Zhou, Y.; Liu, X.; Shi, Y.; Li, J.; Li, G.; Chen, Z.; Chen, S.; Zeni, C. Mattersim: A deep learning atomistic model across elements, temperatures and pressures. *arXiv Prepr. arXiv2405.04967* **2024**.

(164) Dietrich, F. M.; Advincula, X. R.; Gobbo, G.; Bellucci, M. A.; Salvalaglio, M. Machine Learning Nucleation Collective Variables with Graph Neural Networks. *J. Chem. Theory Comput.* **2024**, *20*, 1600–1611.

(165) Laio, A.; Parrinello, M. Escaping free-energy minima. *Proc. Natl. Acad. Sci.* **2002**, *99*, 12562–12566.

(166) Barducci, A.; Bussi, G.; Parrinello, M. Well-Tempered Metadynamics: A Smoothly Converging and Tunable Free-Energy Method. *Phys. Rev. Lett.* **2008**, *100*, 20603.

(167) Dama, J. F.; Parrinello, M.; Voth, G. A. Well-Tempered Metadynamics Converges Asymptotically. *Phys. Rev. Lett.* **2014**, *112*, 240602.

(168) Salvalaglio, M.; Perego, C.; Giberti, F.; Mazzotti, M.; Parrinello, M. Molecular-dynamics simulations of urea nucleation from aqueous solution. *Proc. Natl. Acad. Sci.* **2015**, *112*, E6–E14.

(169) Niu, H.; Yang, Y. I.; Parrinello, M. Temperature Dependence of Homogeneous Nucleation in Ice. *Phys. Rev. Lett.* **2019**, *122*, 245501.

(170) Sun, J.; Klug, D. D.; Martoňák, R.; Montoya, J. A.; Lee, M.-S.; Scandolo, S.; Tosatti, E. High-pressure polymeric phases of carbon dioxide. *Proc. Natl. Acad. Sci.* **2009**, *106*, 6077–6081.

(171) Kumar, P. P.; Kalinichev, A. G.; Kirkpatrick, R. J. Dissociation of carbonic acid: Gas phase energetics and mechanism from ab initio metadynamics simulations. *J. Chem. Phys.* **2007**, *126*, 204315.

(172) Gunaydin, H.; Houk, K. N. Molecular Dynamics Prediction of the Mechanism of Ester Hydrolysis in Water. *J. Am. Chem. Soc.* **2008**, *130*, 15232–15233.

(173) Barducci, A.; Bonomi, M.; Parrinello, M. Metadynamics. *WIREs Comput. Mol. Sci.* **2011**, *1*, 826–843.

(174) Tiwary, P.; Parrinello, M. From Metadynamics to Dynamics. *Phys. Rev. Lett.* **2013**, *111*, 230602.

(175) Salvalaglio, M.; Tiwary, P.; Parrinello, M. Assessing the Reliability of the Dynamics Reconstructed from Metadynamics. *J. Chem. Theory Comput.* **2014**, *10*, 1420–1425.

(176) Tiwary, P.; Limongelli, V.; Salvalaglio, M.; Parrinello, M. Kinetics of protein–ligand unbinding: Predicting pathways, rates, and rate-limiting steps. *Proc. Natl. Acad. Sci.* **2015**, *112*, E386–E391.

(177) Torrie, G. M.; Valleau, J. P. Nonphysical sampling distributions in Monte Carlo free-energy estimation: Umbrella sampling. *J. Comput. Phys.* **1977**, *23*, 187–199.

(178) Kirkwood, J. G. Statistical Mechanics of Fluid Mixtures. *J. Chem. Phys.* **1935**, *3*, 300–313.

(179) Kästner, J. Umbrella sampling. *WIREs Comput. Mol. Sci.* **2011**, *1*, 932–942.

(180) Fowler, P. W.; Abad, E.; Beckstein, O.; Sansom, M. S. P. Energetics of Multi-Ion Conduction Pathways in Potassium Ion Channels. *J. Chem. Theory Comput.* **2013**, *9*, 5176–5189.

(181) Kumar, S.; Rosenberg, J. M.; Bouzida, D.; Swendsen, R. H.; Kollman, P. A. THE weighted histogram analysis method for free-energy calculations on biomolecules. I. The method. *J. Comput. Chem.* **1992**, *13*, 1011–1021.

(182) Shirts, M. R.; Chodera, J. D. Statistically optimal analysis of samples from multiple equilibrium states. *J. Chem. Phys.* **2008**, *129*, 124105.

(183) Meng, Y.; Roux, B. Efficient Determination of Free Energy Landscapes in Multiple Dimensions from Biased Umbrella Sampling Simulations Using Linear Regression. *J. Chem. Theory Comput.* **2015**, *11*, 3523–3529.

(184) Shirts, M. R. Reweighting from the mixture distribution as a better way to describe the multistate Bennett acceptance ratio. *arXiv Prepr. arXiv1704.00891* **2017**.

(185) Bennett, C. H. Efficient estimation of free energy differences from Monte Carlo data. *J. Comput. Phys.* **1976**, *22*, 245–268.

(186) Matsunaga, Y.; Kamiya, M.; Oshima, H.; Jung, J.; Ito, S.; Sugita, Y. Use of multistate Bennett acceptance ratio method for free-energy calculations from enhanced sampling and free-energy perturbation. *Biophys. Rev.* **2022**, *14*, 1503–1512.

(187) Brookes, S. G. H.; Kapil, V.; Michaelides, A.; Schran, C. CO2 hydration at the air–water interface: A surface-mediated "in-and-out" mechanism. *Proc. Natl. Acad. Sci.* **2025**, *122*, e2502684122.

(188) Dupont, S.; Pörtner, H. Get ready for ocean acidification. *Nature* **2013**, *498*, 429.

(189) Kroeker, K. J.; Micheli, F.; Gambi, M. C. Ocean acidification causes ecosystem shifts via altered competitive interactions. *Nat. Clim. Chang.* **2013**, *3*, 156–159.

(190) Foster, T.; Falter, J. L.; McCulloch, M. T.; Clode, P. L. Ocean acidification causes structural deformities in juvenile coral skeletons. *Sci. Adv.* **2016**, *2*, e1501130.

(191) Leung, D. Y. C.; Caramanna, G.; Maroto-Valer, M. M. An overview of current status of carbon dioxide capture and storage technologies. *Renew. Sustain. Energy Rev.* **2014**, *39*, 426–443.

(192) Snæbjörnsdóttir, S. Ó.; Sigfússon, B.; Marieni, C.; Goldberg, D.; Gislason, S. R.; Oelkers, E. H. Carbon dioxide storage through mineral carbonation. *Nat. Rev. Earth & Environ.* **2020**, *1*, 90–102.

(193) Wang, X.; Zhang, F.; Li, L.; Zhang, H.; Deng, S. Carbon dioxide capture. *Adv. Chem. Eng.* **2021**, *58*, 297–348.

(194) Wang, X.; Conway, W.; Burns, R.; McCann, N.; Maeder, M. Comprehensive Study of the Hydration and Dehydration Reactions of Carbon Dioxide in Aqueous Solution. *J. Phys. Chem. A* **2010**, *114*, 1734–1740.

(195) Adamczyk, K.; Prémont-Schwarz, M.; Pines, D.; Pines, E.; Nibbering, E. T. J. Real-Time Observation of Carbonic Acid Formation in Aqueous Solution. *Science.* **2009**, *326*, 1690–1694.

(196) Pines, D.; Ditkovich, J.; Mukra, T.; Miller, Y.; Kiefer, P. M.; Daschakraborty, S.; Hynes, J. T.; Pines, E. How Acidic Is Carbonic Acid? *J. Phys. Chem. B* **2016**, *120*, 2440–2451.

(197) Leung, K.; Nielsen, I. M. B.; Kurtz, I. Ab Initio Molecular Dynamics Study of Carbon Dioxide and Bicarbonate Hydration and the Nucleophilic Attack of Hydroxide on CO2. *J. Phys. Chem. B* **2007**, *111*, 4453–4459.

(198) Nguyen, M. T.; Matus, M. H.; Jackson, V. E.; Ngan, V. T.; Rustad, J. R.; Dixon, D. A. Mechanism of the Hydration of Carbon Dioxide: Direct Participation of H2O versus Microsolvation. *J. Phys. Chem. A* **2008**, *112*, 10386–10398.

(199) Kumar, P. P.; Kalinichev, A. G.; Kirkpatrick, R. J. Hydrogen-Bonding Structure and Dynamics of Aqueous Carbonate Species from Car−Parrinello Molecular Dynamics Simulations. *J. Phys. Chem. B* **2009**, *113*, 794–802.

(200) England, A. H.; Duffin, A. M.; Schwartz, C. P.; Uejio, J. S.; Prendergast, D.; Saykally, R. J. On the hydration and hydrolysis of carbon dioxide. *Chem. Phys. Lett.* **2011**, *514*, 187–195.

(201) Wang, B.; Cao, Z. How water molecules modulate the hydration of CO2 in water solution: Insight from the cluster-continuum model calculations. *J. Comput. Chem.* **2013**, *34*, 372–378.

(202) Polino, D.; Grifoni, E.; Rousseau, R.; Parrinello, M.; Glezakou, V.-A. How Collective Phenomena Impact CO2 Reactivity and Speciation in Different Media. *J. Phys. Chem. A* **2020**, *124*, 3963–3975.

(203) Martirez, J. M. P.; Carter, E. A. Solvent Dynamics Are Critical to Understanding Carbon Dioxide Dissolution and Hydration in Water. *J. Am. Chem. Soc.* **2023**, *145*, 12561–12575.

(204) Bobell, B.; Boyn, J.-N.; Martirez, J. M. P.; Carter, E. A. Modeling bicarbonate formation in an alkaline solution with multi-level quantum mechanics/molecular dynamics simulations. *Mol. Phys.* **2024**, e2375370.

(205) Baer, M. D.; Tobias, D. J.; Mundy, C. J. Investigation of Interfacial and Bulk Dissociation of HBr, HCl, and HNO3 Using Density Functional Theory-Based Molecular Dynamics Simulations. *J. Phys. Chem. C* **2014**, *118*, 29412–29420.

(206) Lowe, B. M.; Skylaris, C.-K.; Green, N. G. Acid-base dissociation mechanisms and energetics at the silica–water interface: An activationless process. *J. Colloid Interface Sci.* **2015**, *451*, 231–244.

(207) Wei, Z.; Li, Y.; Cooks, R. G.; Yan, X. Accelerated Reaction Kinetics in Microdroplets: Overview and Recent Developments. *Annu. Rev. Phys. Chem.* **2020**, *71*, 31–51.

(208) Kusaka, R.; Nihonyanagi, S.; Tahara, T. The photochemical reaction of phenol becomes ultrafast at the air–water interface. *Nat. Chem.* **2021**, *13*, 306–311.

(209) Lee, K.; Cho, Y.; Kim, J. C.; Choi, C.; Kim, J.; Lee, J. K.; Li, S.; Kwak, S. K.; Choi, S. Q. Catalyst-free selective oxidation of C(sp3)-H bonds in toluene on water. *Nat. Commun.* **2024**, *15*, 6127.

(210) Tarbuck, T. L.; Richmond, G. L. Adsorption and Reaction of CO2 and SO2 at a Water Surface. *J. Am. Chem. Soc.* **2006**, *128*, 3256–3267.

(211) Devlin, S. W.; Jamnuch, S.; Xu, Q.; Chen, A. A.; Qian, J.; Pascal, T. A.; Saykally, R. J. Agglomeration Drives the Reversed Fractionation of Aqueous Carbonate and Bicarbonate at the Air–Water Interface. *J. Am. Chem. Soc.* **2023**, *145*, 22384–22393.

(212) Unke, O. T.; Chmiela, S.; Sauceda, H. E.; Gastegger, M.; Poltavsky, I.; Schütt, K. T.; Tkatchenko, A.; Müller, K.-R. Machine Learning Force Fields. *Chem. Rev.* **2021**, *121*, 10142–10186.

(213) Kapil, V.; Kovács, D. P.; Csányi, G.; Michaelides, A. First-principles spectroscopy of aqueous interfaces using machine-learned electronic and quantum nuclear effects. *Faraday Discuss.* **2024**, *249*, 50–68.

(214) Omranpour, A.; Montero De Hijes, P.; Behler, J.; Dellago, C. Perspective: Atomistic simulations of water and aqueous systems with machine learning potentials. *J. Chem. Phys.* **2024**, *160*, DOI: 10.1063/5.0201241.

(215) Schran, C.; Thiemann, F. L.; Rowe, P.; Müller, E. A.; Marsalek, O.; Michaelides, A. Machine learning potentials for complex aqueous systems made simple. *Proc. Natl. Acad. Sci.* **2021**, *118*, e2110077118.

(216) McInnes, L.; Healy, J.; Melville, J. Umap: Uniform manifold approximation and projection for dimension reduction. *arXiv Prepr. arXiv1802.03426* **2018**.

(217) Cheng, B.; Griffiths, R.-R.; Wengert, S.; Kunkel, C.; Stenczel, T.; Zhu, B.; Deringer, V. L.; Bernstein, N.; Margraf, J. T.; Reuter, K.; Csanyi, G. Mapping Materials and Molecules. *Acc. Chem. Res.* **2020**, *53*, 1981–1991.

(218) Zhang, Y.; Yang, W. Comment on "Generalized Gradient Approximation Made Simple". *Physical Review Letters* **1998**, *80*, 890–890.

(219) Bankura, A.; Karmakar, A.; Carnevale, V.; Chandra, A.; Klein, M. L. Structure, Dynamics, and Spectral Diffusion of Water from First-Principles Molecular Dynamics. *J. Phys. Chem. C* **2014**, *118*, 29401–29411.

(220) Soper, A. K. The radial distribution functions of water and ice from 220 to 673 K and at pressures up to 400 MPa. *Chem. Phys.* **2000**, *258*, 121–137.

(221) Skinner, L. B.; Huang, C.; Schlesinger, D.; Pettersson, L. G. M.; Nilsson, A.; Benmore, C. J. Benchmark oxygen-oxygen pair-distribution function of ambient water from x-ray diffraction measurements with a wide Q-range. *J. Chem. Phys.* **2013**, *138*, 74506.

(222) Ohto, T.; Dodia, M.; Xu, J.; Imoto, S.; Tang, F.; Zysk, F.; Kühne, T. D.; Shigeta, Y.; Bonn, M.; Wu, X.; Nagata, Y. Accessing the Accuracy of Density Functional Theory through Structure and Dynamics of the Water–Air Interface. *J. Phys. Chem. Lett.* **2019**, *10*, 4914–4919.

(223) Brookes, S. G. H.; Kapil, V.; Schran, C.; Michaelides, A. The wetting of H2O by CO2. *J. Chem. Phys.* **2024**, *161*, 84711.

(224) Neese, F. The ORCA program system. *WIRES Comput. Molec. Sci.* **2012**, *2*, 73–78.

(225) Neese, F. Software update: the ORCA program system, version 5.0. *WIRES Comput. Molec. Sci.* **2022**, *12*, e1606.

(226) Galib, M.; Duignan, T. T.; Misteli, Y.; Baer, M. D.; Schenter, G. K.; Hutter, J.; Mundy, C. J. Mass density fluctuations in quantum and classical descriptions of liquid water. *J. Chem. Phys.* **2017**, *146*, 244501.

(227) Rogal, J.; Schneider, E.; Tuckerman, M. E. Neural-Network-Based Path Collective Variables for Enhanced Sampling of Phase Transformations. *Phys. Rev. Lett.* **2019**, *123*, 245701.

(228) Bonati, L.; Piccini, G.; Parrinello, M. Deep learning the slow modes for rare events sampling. *Proc. Natl. Acad. Sci.* **2021**, *118*, e2113533118.

(229) Plimpton, S. Fast Parallel Algorithms for Short-Range Molecular Dynamics. *J. Comput. Phys.* **1995**, *117*, 1–19.

(230) Thompson, A. P.; Aktulga, H. M.; Berger, R.; Bolintineanu, D. S.; Brown, W. M.; Crozier, P. S.; in 't Veld, P. J.; Kohlmeyer, A.; Moore, S. G.; Nguyen, T. D.; Shan, R.; Stevens, M. J.; Tranchida, J.; Trott, C.; Plimpton, S. J. LAMMPS - a Flexible Simulation Tool for Particle-Based Materials Modeling at the Atomic, Meso, and Continuum Scales. *Computer Physics Communications* **2022**, *271*, 108171.

(231) Tribello, G. A.; Bonomi, M.; Branduardi, D.; Camilloni, C.; Bussi, G. PLUMED 2: New feathers for an old bird. *Comput. Phys. Commun.* **2014**, *185*, 604–613.

(232) Bonomi, M. et al. Promoting transparency and reproducibility in enhanced molecular simulations. *Nat. Methods* **2019**, *16*, 670–673.

(233) Tribello, G. A. et al. PLUMED Tutorials: A collaborative, community-driven learning ecosystem. *J. Chem. Phys.* **2025**, *162*, 92501.

(234) Bonn, M.; Nagata, Y.; Backus, E. H. G. Molecular Structure and Dynamics of Water at the Water–Air Interface Studied with Surface-Specific Vibrational Spectroscopy. *Angew. Chemie Int. Ed.* **2015**, *54*, 5560–5576.

(235) Buttersack, T. et al. Direct observation of the complex S(IV) equilibria at the liquid-vapor interface. *Nat. Commun.* **2024**, *15*, 8987.

(236) Willard, A. P.; Chandler, D. Instantaneous Liquid Interfaces. *J. Phys. Chem. B* **2010**, *114*, 1954–1958.

(237) Devlin, S. W.; Benjamin, I.; Saykally, R. J. On the mechanisms of ion adsorption to aqueous interfaces: air-water vs. oil-water. *Proc. Natl. Acad. Sci.* **2022**, *119*, e2210857119.

(238) Ruiz-Lopez, M. F.; Francisco, J. S.; Martins-Costa, M. T. C.; Anglada, J. M. Molecular reactions at aqueous interfaces. *Nat. Rev. Chem.* **2020**, *4*, 459–475.

(239) Hub, J. S.; Caleman, C.; van der Spoel, D. Organic molecules on the surface of water droplets – an energetic perspective. *Phys. Chem. Chem. Phys.* **2012**, *14*, 9537–9545.

(240) Petersen, P. B.; Saykally, R. J. On The Nature of Ions at the Liquid Water Surface. *Annu. Rev. Phys. Chem.* **2006**, *57*, 333–364.

(241) Yan, X.; Delgado, M.; Aubry, J.; Gribelin, O.; Stocco, A.; Boisson-Da Cruz, F.; Bernard, J.; Ganachaud, F. Central Role of Bicarbonate Anions in Charging Water/Hydrophobic Interfaces. *J. Phys. Chem. Lett.* **2018**, *9*, 96–103.

(242) Das, S.; Imoto, S.; Sun, S.; Nagata, Y.; Backus, E. H. G.; Bonn, M. Nature of Excess Hydrated Proton at the Water–Air Interface. *J. Am. Chem. Soc.* **2020**, *142*, 945–952.

(243) Ford, D. J.; Shutler, J. D.; Blanco-Sacristán, J.; Corrigan, S.; Bell, T. G.; Yang, M.; Kitidis, V.; Nightingale, P. D.; Brown, I.; Wimmer, W.; Woolf, D. K.; Casal, T.; Donlon, C.; Tilstone, G. H.; Ashton, I. Enhanced ocean CO2 uptake due to near-surface temperature gradients. *Nat. Geosci.* **2024**, *17*, 1135–1140.

(244) Ooi, T.; Maruoka, K. Recent Advances in Asymmetric Phase-Transfer Catalysis. *Angew. Chemie Int. Ed.* **2007**, *46*, 4222–4266.

(245) Llan Benjamin Mechanism and Dynamics of Ion Transfer Across a Liquid-Liquid Interface. *Science.* **1993**, *261*, 1558–1560.

(246) Shah, S. A.; Baldelli, S. Chemical Imaging of Surfaces with Sum Frequency Generation Vibrational Spectroscopy. *Acc. Chem. Res.* **2020**, *53*, 1139–1150.

(247) Gonella, G.; Backus, E. H. G.; Nagata, Y.; Bonthuis, D. J.; Loche, P.; Schlaich, A.; Netz, R. R.; Kühnle, A.; McCrum, I. T.; Koper, M. T. M.; Wolf, M.; Winter, B.; Meijer, G.; Campen, R. K.; Bonn, M. Water at charged interfaces. *Nat. Rev. Chem.* **2021**, *5*, 466–485.

(248) Span, R.; Wagner, W. A New Equation of State for Carbon Dioxide Covering the Fluid Region from the Triple-Point Temperature to 1100 K at Pressures up to 800 MPa. *J. Phys. Chem. Ref. Data* **1996**, *25*, 1509–1596.

(249) Medina-Gonzalez, Y.; Camy, S.; Condoret, J.-S. ScCO2/Green Solvents: Biphasic Promising Systems for Cleaner Chemicals Manufacturing. *ACS Sustain. Chem. Eng.* **2014**, *2*, 2623–2636.

(250) Hönisch, B.; Hemming, N. G. Surface ocean pH response to variations in pCO2 through two full glacial cycles. *Earth Planet. Sci. Lett.* **2005**, *236*, 305–314.

(251) Klewiah, I.; Berawala, D. S.; Alexander Walker, H. C.; Andersen, P. Ø.; Nadeau, P. H. Review of experimental sorption studies of CO2 and CH4 in shales. *J. Nat. Gas Sci. Eng.* **2020**, *73*, 103045.

(252) Van der Meer, L. G. H. The conditions limiting CO2 storage in aquifers. *Energy Convers. Manag.* **1993**, *34*, 959–966.

(253) Nielsen, L. C.; Bourg, I. C.; Sposito, G. Predicting CO2–water interfacial tension under pressure and temperature conditions of geologic CO2 storage. *Geochim. Cosmochim. Acta* **2012**, *81*, 28–38.

(254) Hosseinzadeh Dehaghani, Y.; Assareh, M.; Feyzi, F. Simultaneous Prediction of Equilibrium, Interfacial, and Transport Properties of CO2-Brine Systems Using Molecular Dynamics Simulation: Applications to CO2 Storage. *Ind. Eng. Chem. Res.* **2022**, *61*, 15390–15406.

(255) Chun, B.-S.; Wilkinson, G. T. Interfacial tension in high-pressure carbon dioxide mixtures. *Ind. Eng. Chem. Res.* **1995**, *34*, 4371–4377.

(256) Hebach, A.; Oberhof, A.; Dahmen, N.; Kögel, A.; Ederer, H.; Dinjus, E. Interfacial Tension at Elevated PressuresMeasurements and Correlations in the Water + Carbon Dioxide System. *J. Chem. Eng. Data* **2002**, *47*, 1540–1546.

(257) Tewes, F.; Boury, F. Thermodynamic and Dynamic Interfacial Properties of Binary Carbon Dioxide−Water Systems. *J. Phys. Chem. B* **2004**, *108*, 2405–2412.

(258) Chiquet, P.; Daridon, J.-L.; Broseta, D.; Thibeau, S. CO2/water interfacial tensions under pressure and temperature conditions of CO2 geological storage. *Energy Convers. Manag.* **2007**, *48*, 736–744.

(259) Bachu, S.; Bennion, D. B. Interfacial Tension between CO2, Freshwater, and Brine in the Range of Pressure from (2 to 27) MPa, Temperature from (20 to 125) °C, and Water Salinity from (0 to 334 000) mg · L−1. *J. Chem. Eng. Data* **2009**, *54*, 765–775.

(260) Georgiadis, A.; Maitland, G.; Trusler, J. P. M.; Bismarck, A. Interfacial Tension Measurements of the (H2O + CO2) System at Elevated Pressures and Temperatures. *J. Chem. Eng. Data* **2010**, *55*, 4168–4175.

(261) Aggelopoulos, C. A.; Robin, M.; Perfetti, E.; Vizika, O. CO2/CaCl2 solution interfacial tensions under CO2 geological storage conditions: Influence of cation valence on interfacial tension. *Adv. Water Resour.* **2010**, *33*, 691–697.

(262) Aggelopoulos, C. A.; Robin, M.; Vizika, O. Interfacial tension between CO2 and brine (NaCl+CaCl2) at elevated pressures and temperatures: The additive effect of different salts. *Adv. Water Resour.* **2011**, *34*, 505–511.

(263) Bikkina, P. K.; Shoham, O.; Uppaluri, R. Equilibrated Interfacial Tension Data of the CO2–Water System at High Pressures and Moderate Temperatures. *J. Chem. Eng. Data* **2011**, *56*, 3725–3733.

(264) Liu, Y.; Tang, J.; Wang, M.; Wang, Q.; Tong, J.; Zhao, J.; Song, Y. Measurement of Interfacial Tension of CO2 and NaCl Aqueous Solution over Wide Temperature, Pressure, and Salinity Ranges. *J. Chem. Eng. Data* **2017**, *62*, 1036–1046.

(265) Hinton, Z. R.; Alvarez, N. J. Surface tensions at elevated pressure depend strongly on bulk phase saturation. *J. Colloid Interface Sci.* **2021**, *594*, 681–689.

(266) Li, X.-S.; Liu, J.-M.; Fu, D. Investigation of Interfacial Tensions for Carbon Dioxide Aqueous Solutions by Perturbed-Chain Statistical Associating Fluid Theory Combined with Density-Gradient Theory. *Ind. Eng. Chem. Res.* **2008**, *47*, 8911–8917.

(267) Niño-Amézquita, G.; van Putten, D.; Enders, S. Phase equilibrium and interfacial properties of water+CO2 mixtures. *Fluid Phase Equilib.* **2012**, *332*, 40–47.

(268) Lafitte, T.; Mendiboure, B.; Piñeiro, M. M.; Bessières, D.; Miqueu, C. Interfacial Properties of Water/CO2: A Comprehensive Description through a Gradient Theory−SAFT-VR Mie Approach. *J. Phys. Chem. B* **2010**, *114*, 11110–11116.

(269) Da Rocha, S. R. P.; Johnston, K. P.; Westacott, R. E.; Rossky, P. J. Molecular Structure of the Water−Supercritical CO2 Interface. *J. Phys. Chem. B* **2001**, *105*, 12092–12104.

(270) Zhang, H.; Singer, S. J. Analysis of the Subcritical Carbon Dioxide−Water Interface. *J. Phys. Chem. A* **2011**, *115*, 6285–6296.

(271) Zhao, L.; Tao, L.; Lin, S. Molecular Dynamics Characterizations of the Supercritical CO2–Mediated Hexane–Brine Interface. *Ind. Eng. Chem. Res.* **2015**, *54*, 2489–2496.

(272) Li, W.; Nan, Y.; Zhang, Z.; You, Q.; Jin, Z. Hydrophilicity/hydrophobicity driven CO2 solubility in kaolinite nanopores in relation to carbon sequestration. *Chem. Eng. J.* **2020**, *398*, 125449.

(273) Unke, O. T.; Meuwly, M. PhysNet: A Neural Network for Predicting Energies, Forces, Dipole Moments, and Partial Charges. *J. Chem. Theory Comput.* **2019**, *15*, 3678–3693.

(274) Yang, M.; Bonati, L.; Polino, D.; Parrinello, M. Using metadynamics to build neural network potentials for reactive events: the case of urea decomposition in water. *Catal. Today* **2022**, *387*, 143–149.

(275) Litman, Y.; Lan, J.; Nagata, Y.; Wilkins, D. M. Fully First-Principles Surface Spectroscopy with Machine Learning. *J. Phys. Chem. Lett.* **2023**, *14*, 8175–8182.

(276) Schran, C.; Brezina, K.; Marsalek, O. Committee neural network potentials control generalization errors and enable active learning. *J. Chem. Phys.* **2020**, *153*, 104105.

(277) Becke, A. D. Density-functional exchange-energy approximation with correct asymptotic behavior. *Phys. Rev. A* **1988**, *38*, 3098–3100.

(278) Lee, C.; Yang, W.; Parr, R. G. Development of the Colle-Salvetti correlation-energy formula into a functional of the electron density. *Phys. Rev. B* **1988**, *37*, 785–789.

(279) Gillan, M. J.; Alfè, D.; Michaelides, A. Perspective: How good is DFT for water? *J. Chem. Phys.* **2016**, *144*, 130901.

(280) Goel, H.; Windom, Z. W.; Jackson, A. A.; Rai, N. Performance of density functionals for modeling vapor liquid equilibria of CO2 and SO2. *J. Comput. Chem.* **2018**, *39*, 397–406.

(281) Wu, Y.; Tepper, H. L.; Voth, G. A. Flexible simple point-charge water model with improved liquid-state properties. *J. Chem. Phys.* **2006**, *124*, 024503.

(282) Zhu, A.; Zhang, X.; Liu, Q.; Zhang, Q. A Fully Flexible Potential Model for Carbon Dioxide. *Chinese J. Chem. Eng.* **2009**, *17*, 268–272.

(283) Singraber, A.; Morawietz, T.; Behler, J.; Dellago, C. Parallel Multistream Training of High-Dimensional Neural Network Potentials. *J. Chem. Theory Comput.* **2019**, *15*, 3075–3092.

(284) Morawietz, T.; Singraber, A.; Dellago, C.; Behler, J. How van der Waals interactions determine the unique properties of water. *Proc. Natl. Acad. Sci.* **2016**, *113*, 8368–8373.

(285) Míguez, J. M.; Piñeiro, M. M.; Blas, F. J. Influence of the long-range corrections on the interfacial properties of molecular models using Monte Carlo simulation. *J. Chem. Phys.* **2013**, *138*, 34707.

(286) Janeček, J. Effect of the interfacial area on the equilibrium properties of Lennard-Jones fluid. *J. Chem. Phys.* **2009**, *131*, 124513.

(287) Longford, F. G. J.; Essex, J. W.; Skylaris, C.-K.; Frey, J. G. Unexpected finite size effects in interfacial systems: Why bigger is not always better—Increase in uncertainty of surface tension with bulk phase width. *J. Chem. Phys.* **2018**, *148*, 214704.

(288) Harris, J. G.; Yung, K. H. Carbon Dioxide's Liquid-Vapor Coexistence Curve And Critical Properties as Predicted by a Simple Molecular Model. *J. Phys. Chem.* **1995**, *99*, 12021–12024.

(289) Okabe, T.; Kawata, M.; Okamoto, Y.; Mikami, M. Replica-exchange Monte Carlo method for the isobaric–isothermal ensemble. *Chem. Phys. Lett.* **2001**, *335*, 435–439.

(290) Kapil, V. et al. i-PI 2.0: A universal force engine for advanced molecular simulations. *Comput. Phys. Commun.* **2019**, *236*, 214–223.

(291) Singraber, A.; Behler, J.; Dellago, C. Library-Based LAMMPS Implementation of High-Dimensional Neural Network Potentials. *J. Chem. Theory Comput.* **2019**, *15*, 1827–1840.

(292) Kirkwood, J. G.; Buff, F. P. The Statistical Mechanical Theory of Solutions. I. *J. Chem. Phys.* **1951**, *19*, 774–777.

(293) Delhommelle, J.; P, M. Inadequacy of the Lorentz-Berthelot combining rules for accurate predictions of equilibrium properties by molecular simulation. *Mol. Phys.* **2001**, *99*, 619–625.

(294) Boda, D.; Henderson, D. The effects of deviations from Lorentz–Berthelot rules on the properties of a simple mixture. *Mol. Phys.* **2008**, *106*, 2367–2370.

(295) Rouha, M.; Nezbeda, I. Non-Lorentz–Berthelot Lennard-Jones mixtures: A systematic study. *Fluid Phase Equilib.* **2009**, *277*, 42–48.

(296) Morishita, T.; Shiga, M. Ab Initio Characterization of the CO2–Water Interface Using Unsupervised Machine Learning for Dimensionality Reduction. *J. Phys. Chem. B* **2024**, *128*, 5781–5791.

(297) Pattni, B. S.; Chupin, V. V.; Torchilin, V. P. New Developments in Liposomal Drug Delivery. *Chem. Rev.* **2015**, *115*, 10938–10966.

(298) Dasgupta, S.; Auth, T.; Gompper, G. Nano-and microparticles at fluid and biological interfaces. *J. Phys. Condens. Matter* **2017**, *29*, 373003.

(299) Sokołowski, S.; Pizio, O. Density functional theory for the microscopic structure of nanoparticles at the liquid–liquid interface. *Phys. Chem. Chem. Phys.* **2019**, *21*, 3073–3082.

(300) Coelho, F. M.; Franco, L. F. M.; Firoozabadi, A. Thermodiffusion of CO2 in Water by Nonequilibrium Molecular Dynamics Simulations. *J. Phys. Chem. B* **2023**, *127*, 2749–2760.

(301) Coelho, F. M.; Franco, L. F. M.; Firoozabadi, A. Effect of Salinity on CO2 Thermodiffusion in Aqueous Mixtures by Molecular Dynamics Simulations. *ACS Sustain. Chem. Eng.* **2023**, *11*, 17086–17097.

(302) Coady, Z.; Brookes, S. G. H.; Shen, Z.; Rhodes, B. J.; Mapstone, G.; Xu, Z.; Yu, W.; Nishihara, H.; Schran, C.; Michaelides, A.; Forse, A. C. Unexpected Oversolubility of CO2 Measured at Electrode–Electrolyte Interfaces. *J. Am. Chem. Soc.* **2025**, *147*, 36310–36319.

(303) Liu, Y.-C.; Yeh, L.-H.; Zheng, M.-J.; Wu, K. C.-W. Highly selective and high-performance osmotic power generators in subnanochannel membranes enabled by metal-organic frameworks. *Sci. Adv.* **2025**, *7*, eabe9924.

(304) Tang, J.; Wang, Y.; Yang, H.; Zhang, Q.; Wang, C.; Li, L.; Zheng, Z.; Jin, Y.; Wang, H.; Gu, Y.; Zuo, T. All-natural 2D nanofluidics as highly-efficient osmotic energy generators. *Nat. Commun.* **2024**, *15*, 3649.

(305) Wang, Y.; Cao, Z.; Barati Farimani, A. Efficient water desalination with graphene nanopores obtained using artificial intelligence. *npj 2D Mater. Appl.* **2021**, *5*, 66.

(306) Li, H.; Zick, M. E.; Trisukhon, T.; Signorile, M.; Liu, X.; Eastmond, H.; Sharma, S.; Spreng, T. L.; Taylor, J.; Gittins, J. W.; Farrow, C.; Lim, S. A.; Crocellà, V.; Milner, P. J.; Forse, A. C. Capturing carbon dioxide from air with charged-sorbents. *Nature* **2024**, *630*, 654–659.

(307) UlHaq Khan, F.; Bilal, M.; Li, J.; Xu, X.; Landskron, K. Supercapacitive swing adsorption of CO2: advances and future prospects. *Trends Chem.* **2025**, *7*, 43–55.

(308) Ju, W.; Bagger, A.; Hao, G.-P.; Varela, A. S.; Sinev, I.; Bon, V.; Roldan Cuenya, B.; Kaskel, S.; Rossmeisl, J.; Strasser, P. Understanding activity and selectivity of metal-nitrogen-doped carbon catalysts for electrochemical reduction of CO2. *Nat. Commun.* **2017**, *8*, 944.

(309) Hursán, D.; Ábel, M.; Baán, K.; Fako, E.; Samu, G. F.; Nguyën, H. C.; López, N.; Atanassov, P.; Kónya, Z.; Sápi, A.; Janáky, C. CO2 Conversion on N-Doped Carbon Catalysts via Thermo- and Electrocatalysis: Role of C–NOx Moieties. *ACS Catal.* **2022**, *12*, 10127–10140.

(310) Coasne, B.; Farrusseng, D. Gas oversolubility in nanoconfined liquids: Review and perspectives for adsorbent design. *Microporous Mesoporous Mater.* **2019**, *288*, 109561.

(311) Liu, C.-C.; Chou, H.-J.; Lin, C.-Y.; Janmanchi, D.; Chung, P.-W.; Mou, C.-Y.; Yu, S. S.-F.; Chan, S. I. The oversolubility of methane gas in nano-confined water in nanoporous silica materials. *Microporous Mesoporous Mater.* **2020**, *293*, 109793.

(312) Zakharova, M. V.; Kleitz, F.; Fontaine, F.-G. Carbon Dioxide Oversolubility in Nanoconfined Liquids for the Synthesis of Cyclic Carbonates. *ChemCatChem* **2017**, *9*, 1886–1890.

(313) Boroun, S.; Sahraei, A. A.; Mokarizadeh, A. H.; Alamdari, H.; Fontaine, F.-G.; Larachi, F. Insights into the Solubility of Carbon Dioxide in Grafted Mesoporous Silica for the Catalytic Synthesis of Cyclic Carbonates by Nanoconfinement. *ACS Appl. Mater. Interfaces* **2021**, *13*, 27019–27028.

(314) Travis, K. P.; Gubbins, K. E. Transport Diffusion of Oxygen−Nitrogen Mixtures in Graphite Pores: A Nonequilibrium Molecular Dynamics (NEMD) Study. *Langmuir* **1999**, *15*, 6050–6059.

(315) Skoulidas, A. I.; Ackerman, D. M.; Johnson, J. K.; Sholl, D. S. Rapid Transport of Gases in Carbon Nanotubes. *Phys. Rev. Lett.* **2002**, *89*, 185901.

(316) Liu, H.; Dai, S.; Jiang, D.-e. Insights into CO2/N2 separation through nanoporous graphene from molecular dynamics. *Nanoscale* **2013**, *5*, 9984–9987.

(317) Yang, Y.; Narayanan Nair, A. K.; Sun, S. Adsorption and Diffusion of Carbon Dioxide, Methane, and Their Mixture in Carbon Nanotubes in the Presence of Water. *J. Phys. Chem. C* **2020**, *124*, 16478–16487.

(318) Stolte, N.; Hou, R.; Pan, D. Nanoconfinement facilitates reactions of carbon dioxide in supercritical water. *Nat. Commun.* **2022**, *13*, 5932.

(319) Ho, L. N.; Clauzier, S.; Schuurman, Y.; Farrusseng, D.; Coasne, B. Gas Uptake in Solvents Confined in Mesopores: Adsorption versus Enhanced Solubility. *J. Phys. Chem. Lett.* **2013**, *4*, 2274–2278.

(320) Ho, L. N.; Schuurman, Y.; Farrusseng, D.; Coasne, B. Solubility of Gases in Water Confined in Nanoporous Materials: ZSM-5, MCM-41, and MIL-100. *J. Phys. Chem. C* **2015**, *119*, 21547–21554.

(321) Kästner, J.; Thiel, W. Bridging the gap between thermodynamic integration and umbrella sampling provides a novel analysis method: "Umbrella integration". *J. Chem. Phys.* **2005**, *123*, 144104.

(322) Harris, R. K.; Thompson, T. V.; Norman, P. R.; Pottage, C. Phosphorus-31 NMR studies of adsorption onto activated carbon. *Carbon N. Y.* **1999**, *37*, 1425–1430.

(323) Forse, A. C.; Griffin, J. M.; Presser, V.; Gogotsi, Y.; Grey, C. P. Ring Current Effects: Factors Affecting the NMR Chemical Shift of Molecules Adsorbed on Porous Carbons. *J. Phys. Chem. C* **2014**, *118*, 7508–7514.

(324) Dufils, T.; Schran, C.; Chen, J.; K. Geim, A.; Fumagalli, L.; Michaelides, A. Origin of Dielectric Polarization Suppression in Confined Water from First Principles. *Chemical Science* **2024**, *15*, 516–527.

(325) Chen, L.; Watanabe, T.; Kanoh, H.; Hata, K.; Ohba, T. Cooperative CO2 Adsorption Promotes High CO2 Adsorption Density over Wide Optimal Nanopore Range. *Adsorption Science & Technology* **2018**, *36*, 625–639.

(326) Boyd, P. G. et al. Data-Driven Design of Metal–Organic Frameworks for Wet Flue Gas CO2 Capture. *Nature* **2019**, *576*, 253–256.

(327) De Tomas, C.; Suarez-Martinez, I.; Vallejos-Burgos, F.; López, M. J.; Kaneko, K.; Marks, N. A. Structural prediction of graphitization and porosity in carbide-derived carbons. *Carbon N. Y.* **2017**, *119*, 1–9.

(328) Yushin, G.; Dash, R.; Jagiello, J.; Fischer, J. E.; Gogotsi, Y. Carbide-Derived Carbons: Effect of Pore Size on Hydrogen Uptake and Heat of Adsorption. *Adv. Funct. Mater.* **2006**, *16*, 2288–2293.

(329) Nishihara, H.; Kyotani, T. Zeolite-templated carbons – three-dimensional microporous graphene frameworks. *Chem. Commun.* **2018**, *54*, 5648–5673.

(330) Lyu, D.; Märker, K.; Zhou, Y.; Zhao, E. W.; Gunnarsdóttir, A. B.; Niblett, S. P.; Forse, A. C.; Grey, C. P. Understanding Sorption of Aqueous Electrolytes in Porous Carbon by NMR Spectroscopy. *J. Am. Chem. Soc.* **2024**, *146*, 9897–9910.

(331) Biggs, M.; Agarwal, P. Mass diffusion of atomic fluids in random micropore spaces using equilibrium molecular dynamics. *Phys. Rev. A* **1992**, *46*, 3312–3318.

(332) Wongkoblap, A.; Do, D. D. Adsorption of Water in Finite Length Carbon Slit Pore: Comparison between Computer Simulation and Experiment. *J. Phys. Chem. B* **2007**, *111*, 13949–13956.

(333) Jagiello, J.; Olivier, J. P. Carbon slit pore model incorporating surface energetical heterogeneity and geometrical corrugation. *Adsorption* **2013**, *19*, 777–783.

(334) Jagiello, J.; Olivier, J. P. 2D-NLDFT adsorption models for carbon slit-shaped pores with surface energetical heterogeneity and geometrical corrugation. *Carbon N. Y.* **2013**, *55*, 70–80.

(335) Vallejos-Burgos, F.; de Tomas, C.; Corrente, N. J.; Urita, K.; Wang, S.; Urita, C.; Moriguchi, I.; Suarez-Martinez, I.; Marks, N.; Krohn, M. H.; Kukobat, R.; Neimark, A. V.; Gogotsi, Y.; Kaneko, K. 3D nanostructure prediction of porous carbons via gas adsorption. *Carbon N. Y.* **2023**, *215*, 118431.

(336) Zhu, Y.; Murali, S.; Stoller, M. D.; Ganesh, K. J.; Cai, W.; Ferreira, P. J.; Pirkle, A.; Wallace, R. M.; Cychosz, K. A.; Thommes, M.; Su, D.; Stach, E. A.; Ruoff, R. S. Carbon-Based Supercapacitors Produced by Activation of Graphene. *Science.* **2011**, *332*, 1537–1541.

(337) Vidano, R.; Fischbach, D. B. New Lines in the Raman Spectra of Carbons and Graphite. *J. Am. Ceram. Soc.* **1978**, *61*, 13–17.

(338) Casiraghi, C.; Hartschuh, A.; Qian, H.; Piscanec, S.; Georgi, C.; Fasoli, A.; Novoselov, K. S.; Basko, D. M.; Ferrari, A. C. Raman Spectroscopy of Graphene Edges. *Nano Lett.* **2009**, *9*, 1433–1441.

(339) Cançado, L. G.; Jorio, A.; Ferreira, E. H. M.; Stavale, F.; Achete, C. A.; Capaz, R. B.; Moutinho, M. V. O.; Lombardo, A.; Kulmala, T. S.; Ferrari, A. C. Quantifying Defects in Graphene via Raman Spectroscopy at Different Excitation Energies. *Nano Lett.* **2011**, *11*, 3190–3196.

(340) Eckmann, A.; Felten, A.; Mishchenko, A.; Britnell, L.; Krupke, R.; Novoselov, K. S.; Casiraghi, C. Probing the Nature of Defects in Graphene by Raman Spectroscopy. *Nano Lett.* **2012**, *12*, 3925–3930.

(341) Wang, Z.; Opembe, N.; Kobayashi, T.; Nelson, N. C.; Slowing, I. I.; Pruski, M. Quantitative atomic-scale structure characterization of ordered mesoporous carbon materials by solid state NMR. *Carbon N. Y.* **2018**, *131*, 102–110.

(342) Wisser, D.; Hartmann, M. 129Xe NMR on Porous Materials: Basic Principles and Recent Applications. *Adv. Mater. Interfaces* **2021**, *8*, 2001266.

(343) Novoselov, K. S.; Geim, A. K.; Morozov, S. V.; Jiang, D.; Zhang, Y.; Dubonos, S. V.; Grigorieva, I. V.; Firsov, A. A. Electric Field Effect in Atomically Thin Carbon Films. *Science.* **2004**, *306*, 666–669.

(344) Balandin, A. A.; Ghosh, S.; Bao, W.; Calizo, I.; Teweldebrhan, D.; Miao, F.; Lau, C. N. Superior Thermal Conductivity of Single-Layer Graphene. *Nano Lett.* **2008**, *8*, 902–907.

(345) Lee, C.; Wei, X.; Kysar, J. W.; Hone, J. Measurement of the Elastic Properties and Intrinsic Strength of Monolayer Graphene. *Science.* **2008**, *321*, 385–388.

(346) Eftekhari, A.; Garcia, H. The necessity of structural irregularities for the chemical applications of graphene. *Mater. Today Chem.* **2017**, *4*, 1–16.

(347) Yang, G.; Li, L.; Lee, W. B.; Ng, M. C. Structure of graphene and its disorders: a review. *Sci. Technol. Adv. Mater.* **2018**, *19*, 613–648.

(348) Son, Y.-W.; Cohen, M. L.; Louie, S. G. Energy Gaps in Graphene Nanoribbons. *Phys. Rev. Lett.* **2006**, *97*, 216803.

(349) Srivastava, D.; Brenner, D. W.; Schall, J. D.; Ausman, K. D.; Yu, M.; Ruoff, R. S. Predictions of Enhanced Chemical Reactivity at Regions of Local Conformational Strain on Carbon Nanotubes: Kinky Chemistry. *J. Phys. Chem. B* **1999**, *103*, 4330–4337.

(350) Park, S.; Srivastava, D.; Cho, K. Generalized Chemical Reactivity of Curved Surfaces: Carbon Nanotubes. *Nano Lett.* **2003**, *3*, 1273–1277.

(351) Wang, X.; Sun, G.; Routh, P.; Kim, D.-H.; Huang, W.; Chen, P. Heteroatom-doped graphene materials: syntheses, properties and applications. *Chem. Soc. Rev.* **2014**, *43*, 7067–7098.

(352) Vinogradov, N. A.; Schulte, K.; Ng, M. L.; Mikkelsen, A.; Lundgren, E.; Mårtensson, N.; Preobrajenski, A. B. Impact of Atomic Oxygen on the Structure of Graphene Formed on Ir(111) and Pt(111). *J. Phys. Chem. C* **2011**, *115*, 9568–9577.

(353) Krasheninnikov, A. V.; Nordlund, K. Ion and electron irradiation-induced effects in nanostructured materials. *J. Appl. Phys.* **2010**, *107*, 71301.

(354) Zhao, Z.; Chen, H.; Zhang, W.; Yi, S.; Chen, H.; Su, Z.; Niu, B.; Zhang, Y.; Long, D. Defect engineering in carbon materials for electrochemical energy storage and catalytic conversion. *Mater. Adv.* **2023**, *4*, 835–867.

(355) Hashimoto, A.; Suenaga, K.; Gloter, A.; Urita, K.; Iijima, S. Direct evidence for atomic defects in graphene layers. *Nature* **2004**, *430*, 870–873.

(356) Stone, A. J.; Wales, D. J. Theoretical studies of icosahedral C60 and some related species. *Chem. Phys. Lett.* **1986**, *128*, 501–503.

(357) Meyer, J. C.; Kisielowski, C.; Erni, R.; Rossell, M. D.; Crommie, M. F.; Zettl, A. Direct Imaging of Lattice Atoms and Topological Defects in Graphene Membranes. *Nano Lett.* **2008**, *8*, 3582–3586.

(358) Mao, J.; Jiang, Y.; Moldovan, D.; Li, G.; Watanabe, K.; Taniguchi, T.; Masir, M. R.; Peeters, F. M.; Andrei, E. Y. Realization of a tunable artificial atom at a supercritically charged vacancy in graphene. *Nat. Phys.* **2016**, *12*, 545–549.

(359) Zhang, Y.; Li, S.-Y.; Huang, H.; Li, W.-T.; Qiao, J.-B.; Wang, W.-X.; Yin, L.-J.; Bai, K.-K.; Duan, W.; He, L. Scanning Tunneling Microscopy of the π Magnetism of a Single Carbon Vacancy in Graphene. *Phys. Rev. Lett.* **2016**, *117*, 166801.

(360) Banhart, F.; Kotakoski, J.; Krasheninnikov, A. V. Structural Defects in Graphene. *ACS Nano* **2011**, *5*, 26–41.

(361) Yazyev, O. V.; Helm, L. Defect-induced magnetism in graphene. *Phys. Rev. B* **2007**, *75*, 125408.

(362) Palacios, J. J.; Ynduráin, F. Critical analysis of vacancy-induced magnetism in monolayer and bilayer graphene. *Phys. Rev. B* **2012**, *85*, 245443.

(363) Padmanabhan, H.; Nanda, B. R. K. Intertwined lattice deformation and magnetism in monovacancy graphene. *Phys. Rev. B* **2016**, *93*, 165403.

(364) Valencia, A. M.; Caldas, M. J. Single vacancy defect in graphene: Insights into its magnetic properties from theoretical modeling. *Phys. Rev. B* **2017**, *96*, 125431.

(365) Cabrera-Sanfelix, P.; Darling, G. R. Dissociative Adsorption of Water at Vacancy Defects in Graphite. *J. Phys. Chem. C* **2007**, *111*, 18258–18263.

(366) Kostov, M. K.; Santiso, E. E.; George, A. M.; Gubbins, K. E.; Nardelli, M. B. Dissociation of Water on Defective Carbon Substrates. *Phys. Rev. Lett.* **2005**, *95*, 136105.

(367) Liang, Z.; Li, K.; Wang, Z.; Bu, Y.; Zhang, J. Adsorption and reaction mechanisms of single and double H2O molecules on graphene surfaces with defects: a density functional theory study. *Phys. Chem. Chem. Phys.* **2021**, *23*, 19071–19082.

(368) Thiemann, F. L.; Scalliet, C.; Müller, E. A.; Michaelides, A. Defects induce phase transition from dynamic to static rippling in graphene. *Proc. Natl. Acad. Sci.* **2025**, *122*, e2416932122.

(369) Kotakoski, J.; Mangler, C.; Meyer, J. C. Imaging atomic-level random walk of a point defect in graphene. *Nat. Commun.* **2014**, *5*, 3991.

(370) Hjorth Larsen, A. et al. The atomic simulation environment—a Python library for working with atoms. *J. Phys. Condens. Matter* **2017**, *29*, 273002.

(371) Smidstrup, S.; Pedersen, A.; Stokbro, K.; Jónsson, H. Improved initial guess for minimum energy path calculations. *J. Chem. Phys.* **2014**, *140*, 214106.

(372) Carlsson, J. M.; Hanke, F.; Linic, S.; Scheffler, M. Two-Step Mechanism for Low-Temperature Oxidation of Vacancies in Graphene. *Phys. Rev. Lett.* **2009**, *102*, 166104.

(373) Cabrera-Sanfelix, P. Adsorption and Reactivity of CO2 on Defective Graphene Sheets. *J. Phys. Chem. A* **2009**, *113*, 493–498.

(374) Wang, B.; Tsetseris, L.; Pantelides, S. T. Introduction of nitrogen with controllable configuration into graphene via vacancies and edges. *J. Mater. Chem. A* **2013**, *1*, 14927–14934.

(375) Brooks, A.; Jenkins, S. J.; Wrabetz, S.; McGregor, J.; Sacchi, M. The dehydrogenation of butane on metal-free graphene. *J. Colloid Interface Sci.* **2022**, *619*, 377–387.

(376) Denis, P. A.; Iribarne, F. Comparative Study of Defect Reactivity in Graphene. *J. Phys. Chem. C* **2013**, *117*, 19048–19055.

(377) Krasheninnikov, A. V.; Banhart, F. Engineering of nanostructured carbon materials with electron or ion beams. *Nat. Mater.* **2007**, *6*, 723–733.

(378) Zhang, S.; Liang, Z.; Li, K.; Zhang, J.; Ren, S. A density functional theory study on the adsorption reaction mechanism of double CO2 on the surface of graphene defects. *J. Mol. Model.* **2022**, *28*, 118.

(379) Nitopi, S.; Bertheussen, E.; Scott, S. B.; Liu, X.; Engstfeld, A. K.; Horch, S.; Seger, B.; Stephens, I. E. L.; Chan, K.; Hahn, C.; Nørskov, J. K.; Jaramillo, T. F.; Chorkendorff, I. Progress and Perspectives of Electrochemical CO2 Reduction on Copper in Aqueous Electrolyte. *Chem. Rev.* **2019**, *119*, 7610–7672.

(380) Siegelman, R. L.; Kim, E. J.; Long, J. R. Porous materials for carbon dioxide separations. *Nat. Mater.* **2021**, *20*, 1060–1072.

(381) Clough, S. A.; Beers, Y.; Klein, G. P.; Rothman, L. S. Dipole moment of water from Stark measurements of H2O, HDO, and D2O. *J. Chem. Phys.* **1973**, *59*, 2254–2259.

(382) Gubskaya, A. V.; Kusalik, P. G. The total molecular dipole moment for liquid water. *J. Chem. Phys.* **2002**, *117*, 5290–5302.

(383) Buckingham, A. D.; Disch, R. L. The quadrupole moment of the carbon dioxide molecule. *Proc. R. Soc. London. Ser. A. Math. Phys. Sci.* **1997**, *273*, 275–289.

(384) Wang, R.; DelloStritto, M.; Klein, M. L.; Borguet, E.; Carnevale, V. Topological properties of interfacial hydrogen bond networks. *Phys. Rev. B* **2024**, *110*, 14105.

(385) Mazzola, P. G.; Lopes, A. M.; Hasmann, F. A.; Jozala, A. F.; Penna, T. C. V.; Magalhaes, P. O.; Rangel-Yagui, C. O.; Pessoa Jr, A. Liquid–liquid extraction of biomolecules: an overview and update of the main techniques. *J. Chem. Technol. Biotechnol.* **2008**, *83*, 143–157.

(386) Cotty, S. R.; Faniyan, A.; Elbert, J.; Su, X. Redox-mediated electrochemical liquid–liquid extraction for selective metal recovery. *Nat. Chem. Eng.* **2024**, *1*, 281–292.

(387) Butler, R. N.; Coyne, A. G. Organic synthesis reactions on-water at the organic–liquid water interface. *Org. Biomol. Chem.* **2016**, *14*, 9945–9960.

(388) Vannoy, K. J.; Edwards, M. Q.; Renault, C.; Dick, J. E. An Electrochemical Perspective on Reaction Acceleration in Microdroplets. *Annu. Rev. Anal. Chem.* **2024**, *17*, 149–171.

(389) Daru, J.; Forbert, H.; Behler, J.; Marx, D. Coupled Cluster Molecular Dynamics of Condensed Phase Systems Enabled by Machine Learning Potentials: Liquid Water Benchmark. *Phys. Rev. Lett.* **2022**, *129*, 226001.

(390) O'Neill, N.; Shi, B. X.; Baldwin, W. J.; Witt, W. C.; Csányi, G.; Gale, J. D.; Michaelides, A.; Schran, C. Towards Routine Condensed Phase Simulations with Delta-Learned Coupled Cluster Accuracy: Application to Liquid Water. *J. Chem. Theory Comput.* **2025**, *21*, 11710–11720.

(391) Hua, W.; Chen, X.; Allen, H. C. Phase-Sensitive Sum Frequency Revealing Accommodation of Bicarbonate Ions, and Charge Separation of Sodium and Carbonate Ions within the Air/Water Interface. *J. Phys. Chem. A* **2011**, *115*, 6233–6238.

(392) Litman, Y.; Chiang, K.-Y.; Seki, T.; Nagata, Y.; Bonn, M. Surface stratification determines the interfacial water structure of simple electrolyte solutions. *Nat. Chem.* **2024**, *16*, 644–650.

(393) Mustaffa, N. I. H.; Ribas-Ribas, M.; Banko-Kubis, H. M.; Wurl, O. Global reduction of in situ CO2 transfer velocity by natural surfactants in the sea-surface microlayer. *Proc. R. Soc. A Math. Phys. Eng. Sci.* **2020**, *476*, 20190763.

(394) Pereira, R.; Ashton, I.; Sabbaghzadeh, B.; Shutler, J. D.; Upstill-Goddard, R. C. Reduced air–sea CO2 exchange in the Atlantic Ocean due to biological surfactants. *Nat. Geosci.* **2018**, *11*, 492–496.

(395) Deng, B.; Zhong, P.; Jun, K.; Riebesell, J.; Han, K.; Bartel, C. J.; Ceder, G. CHGNet as a pretrained universal neural network potential for charge-informed atomistic modelling. *Nat. Mach. Intell.* **2023**, *5*, 1031–1041.

(396) Del Ben, M.; Schönherr, M.; Hutter, J.; VandeVondele, J. Bulk Liquid Water at Ambient Temperature and Pressure from MP2 Theory. *J. Phys. Chem. Lett.* **2013**, *4*, 3753–3759.

(397) Del Ben, M.; Hutter, J.; VandeVondele, J. Probing the structural and dynamical properties of liquid water with models including non-local electron correlation. *J. Chem. Phys.* **2015**, *143*, 054506.

(398) Duan, Z.; Sun, R. An improved model calculating CO2 solubility in pure water and aqueous NaCl solutions from 273 to 533 K and from 0 to 2000 bar. *Chem. Geol.* **2003**, *193*, 257–271.

(399) Kresse, G.; Joubert, D. From Ultrasoft Pseudopotentials to the Projector Augmented-Wave Method. *Physical Review B* **1999**, *59*, 1758–1775.

(400) Blöchl, P. E. Projector Augmented-Wave Method. *Physical Review B* **1994**, *50*, 17953–17979.

(401) Skinner, L. B.; Benmore, C. J.; Neuefeind, J. C.; Parise, J. B. The Structure of Water around the Compressibility Minimum. *The Journal of Chemical Physics* **2014**, *141*, 214507.

Appendix A

Supplementary Materials for Chapter 3

Here, we provide supplementary material relating to the contents of Chapter 3. Specifically, we give details of our model development, model validation, metadynamics simulations, additional structural analysis, and convergence monitoring. A repository containing the simulation data and files can be located at:
`https://github.com/water-ice-group/interfacial_reactivity`.

A.1 Model Development

Reference method validation

The following section contains details on our main (revPBE-D3) model and the validation tests used to assess its quality. In Fig. A.1, we compare the predictions of our chosen functional, revPBE-D3 - used to generate the training forces and energies - with those of DLPNO-CCSD(T)-F12 (def2-QZVPPD basis set). We obtained an optimized gas-phase reaction path using NEB simulations at the revPBE-D3 level of theory. Predicted energies were compared with DLPNO-CCSD(T)-F12 energies obtained using `ORCA` for the same structures [224, 225]. Overall, we find satisfactory agreement between the two methods for ΔF and $\Delta F^{\ddagger}$ to within 1.5 kcal/mol.

Model training and validation

In total, some 8000 structures - labelled with revPBE-D3 forces and energies - were used in the training of our MACE model. To aid with visualisation, these structures are transformed using the Uniform Manifold Approximation and Projection (UMAP) technique [216, 217] into the 2D projection shown in Fig. A.2. UMAP works by using local manifold approximations to construct topological representations of high-dimensional data. The layout is optimised by minimising the cross-entropy terms between these representations, leading to a clear separation of points in low-dimensional space [216]. Looking at the configurations in Fig. A.2, we see a range of different types of structures, including pure CO_2, pure H_2O, and combined CO_2/H_2O systems. The ability of our model to reproduce the underlying revPBE-D3 forces and energies for these structures is shown in Fig. A.3. Here, we plot MACE predictions on the forces against those of DFT for a random subset of test-set structures. Additionally, we compare MACE and DFT structural predictions for pure water, CO_2 in water, and carbonic acid in bulk water in Figs. A.4, A.5, and A.6, respectively. For both force/energy and structural predictions, we find a satisfactory agreement between the predictions of our model and those of reference revPBE-D3 calculations.

To test the interfacial predictions of our model, we extracted a compact subset of 50 structures corresponding to the five different molecular states found at the air-water interface: CO_2 on top of the interface ($CO_2(\uparrow)$); CO_2 within the air-water interface ($CO_2(\downarrow)$); the transition state ($TS^{\ddagger}$); bicarbonate (BiC); and carbonic acid (CA). For each state, the force predictions of our MACE model were compared with those of revPBE-D3 for increasingly large radial cutoffs about the central, reactive carbon molecule. Results of this analysis are displayed in Chapter 3 in Fig. 3.2a, where we can see consistently low errors across all five interfacial states. The more prominent force deviations seen for $TS^{\ddagger}$ and BiC likely stem from having fewer of these types of structures in our dataset; nonetheless, the overall errors are low relative to the total dataset error (28.8 meV/Å),

suggesting a good ability of our model to reproduce the reaction of CO_2 at the air-water interface.

To further assess the ability of our revPBE-D3 model to accurately describe interfacial chemistry, we decided to compare its energy predictions with those of coupled-cluster theory. Taking the 50-structure interfacial subset discussed above, we extracted carved-out clusters of the reactive carbon species and the closest 9 or 10 water molecules, keeping each cluster at 33 atoms in total. Single-point potential energies were calculated at the DLPNO-CCSD(T) (def2-TZVPPD basis set) level of theory using `ORCA` and then compared to our MACE predictions. The results of this analysis are shown in Fig. 3.2b, which plots the potential energy against the state identity. We see a close agreement between CCSD(T) and MACE energies, which agree to within the uncertainty of their error bars. Assuming that the most prominent contributions to the potential energy of interfacial states arise from local contributions, these results suggest we can be confident in our model's reactivity predictions for interfacial structures and processes.

To confirm the ambient nature of our model's 300 K simulations, we performed solid-liquid coexistence simulations. In this analysis, we ran NPT simulations using equilibrated ice-water biphasic systems. In Fig. A.7, we show how the fraction of ice structures gradually reduces with time before disappearing completely at around 550 ps. These observations confirm that our MACE model correctly predicts water to be the most stable phase under ambient conditions.

BLYP-D3 and RPA Models

The bulk and interfacial properties of condensed-phase systems are dependent upon the choice of underlying theory. Whilst our decision to train a MACE model on revPBE-D3 is grounded on its well-documented performance for aqueous systems [219–222], it is important that we can show that the main conclusions of this paper - the idea that certain interfacial reactions can proceed via an "in-and-out" mechanism - are robust with respect to differences in the underlying theory. Accordingly, we generated new MACE models

at two differing levels of theory to test the proposed mechanism. First, we developed a new DFT model at the **BLYP-D3** level. This was done by recalculating all force and energy labels of our 8000-structure dataset (with otherwise identical DFT parameters) and then training a new model from scratch (energy RMSE: 1.3 meV/atom; force RMSE: 67.8 meV/Å). In addition, we used transfer learning to obtain a MACE model at the **RPA** level. We implemented this training using a 700-structure subset of the main structural dataset consisting of 500 bulk structures (that is, CO_2, bicarbonate, carbonic acid, and transition-state-like species in bulk water) and 200 gaseous structures (energy RMSE: 1.2 meV/atom; force RMSE: 18.8 meV/Å). The structural predictions of these models - specifically, the bulk density ρ and the interfacial tension γ - are shown in Table A.1. Density estimates were obtained through NPT simulations at 300 K and 1 bar pressure; γ estimates were obtained using NVT simulations of 180-water molecule systems ($15 \times 15 \times 100$ Å). For γ, we used the Kirkwood-Buff approach for calculating interfacial tensions [292]. Good agreement is found between the predictions of our models and those of prior *ab initio* studies, with densities replicated to within 1 % and γ predictions consistent to within their error bars. The simulations used to support the findings of this work are shown in Fig. 3.7 and Fig. 3.8.

A.2 Metadynamics

Performing metadynamics simulations requires an appropriate selection of collective variables (CVs). For the $CO_2 + H_2O$ reaction, we use two main CVs: a coordination CV to probe the number of oxygens attached to carbon, allowing us to distinguish between CO_2 and the product species; and a protonation-state CV to count the number of hydrogen attached to carbon-bound oxygens. The nature of these CVs varies with system type and are defined in the main text.

Free energy convergence

For each metadynamics simulation, we obtain more than 50 ns worth of structural and thermodynamic data and observe 10 or more crossings in each instance. To check the free energy convergence, we plot ΔF values for the product(s) of reaction as a function of individual walker time. These are shown in Figs. A.8-A.10 for the gaseous, bulk, and interfacial reactions.

Whilst not undertaken here, further confidence in our metadynamics work could be obtained through the learning of committor functions for each reaction type. These functions quantify the probability that a system starting at some configuration reaches the product state B before returning to the reactant state A. For the true transition state $\xi_0^\ddagger$, $q(\xi)$ values will be centred around 0.5. Determining whether the transitions states from Figs. 3.3-3.4 align with $\xi_0^\ddagger$ would enable an assessment of the quality of our CVs - and therefore the final FEP - for predicting near-transition-state behaviour. Calculating error bars for our profiles, either through block averaging or through other free energy estimators, would further aid in this assessment.

A.3 Additional Analysis

Bicarbonate conversion

In Fig. 3.4, our minimum energy profiles for the bulk and interfacial reactions show a shallow minimum for the bicarbonate species. To confirm this part of the profile as an actual minimum, we perform additional analysis on the conversion between bicarbonate and carbonic acid. Umbrella sampling simulations were conducted to obtain the free energy profiles corresponding to the loss (gain) of a proton from carbonic acid (bicarbonate),

$$\mathrm{HCO_3^-} + \mathrm{H_3O^+} \rightleftharpoons \mathrm{H_2CO_3} + \mathrm{H_2O}, \tag{A.1}$$

under both bulk and interfacial conditions. Profiles are shown in Fig. A.11 as a function of a simplified aqueous protonation state $s_{(\mathrm{OH})_{\mathrm{aq}}}$ in which we specifically assign carbon-bound (Oc) and -unbound (Ow) waters. Under both bulk and interfacial conditions, there is a clear minimum in the free energy profiles around $s_{(\mathrm{OH})_{\mathrm{aq}}} = 1$, corresponding to bicarbonate. Differences between these profiles and those presented in Fig. 3.4 of the main text can be ascribed to differences in the methodology as well as the collective variable used.

Structural analysis

In Fig. 3.6, we present a series of profiles relating to the density, solvent interactions, and degree of hydrogen bonding for each of the main species involved in the CO_2 hydration reaction. To extract the relevant data for analysis, we specify specific cutoffs in CV space for each species around its equilibrium structure. These regions are shown Fig. A.12. Structures encountered during the metadynamics runs with $s_{(\mathrm{CO})}$ and $s_{(\mathrm{OH})}$ within these thresholds are extracted for profiling.

To understand how the density profiles of Fig. 3.6 compare with those from free MD simulations, we plot the latter for each species in Fig. A.13. These simulations were performed using the same system setups as used in the metadynamics runs. Simulations were performed under the NVT ensemble, with a total run time of 2.5 ns for each system. It is interesting to note the resemblance these profiles show with those extracted from the metadynamics runs. This is indicative of a convergence in the metadynamics runs and suggests that we are able to recover equilibrium positions from our enhanced sampling runs through the isolation of the equilibrium structures.

In addition to the species discussed above, in Fig. A.14 we also show the density profile obtained for the hydronium ion (H_3O^+) obtained from free MD. The setup for this simulation is similar to that discussed above; the only difference comes with the exchange of the main carbon molecule for an additional H^+. Similar to previous simulations, we find that the H_3O^+ ion adsorbs at the air-water interface. Using $\Delta F = -RT\ln(\rho/\rho_0)$, we find that this profile relates to an adsorption energy of -1.3 kcal/mol. This is in exact

agreement with previous measurements obtained from experimental SFG [242], attesting to the quality of this potential for treating ions at aqueous interfaces.

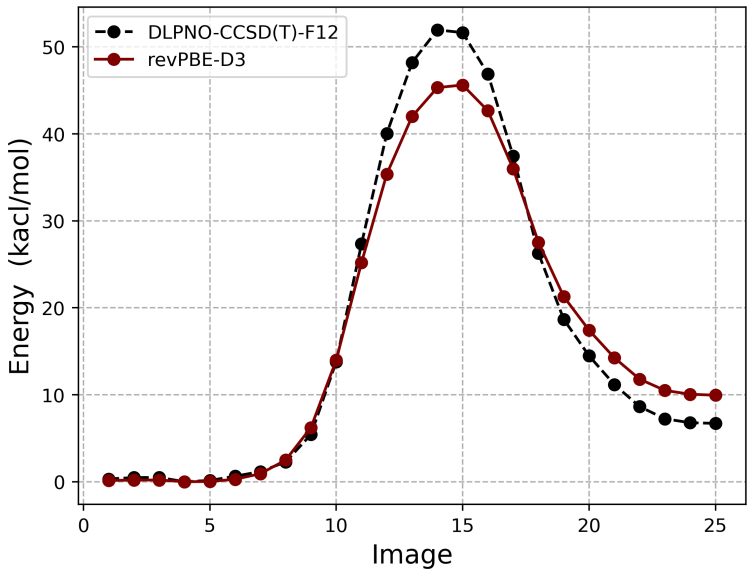

Fig. A.1 Potential energy curve obtained from nudged elastic band simulations of the gaseous CO_2 + H_2O reaction. System setups consist of a single CO_2 and a single H_2O molecule. Results are plotted for both revPBE-D3 and DLPNO-CCSD(T)-F12 (def2-QZVPPD basis set) levels of theory.

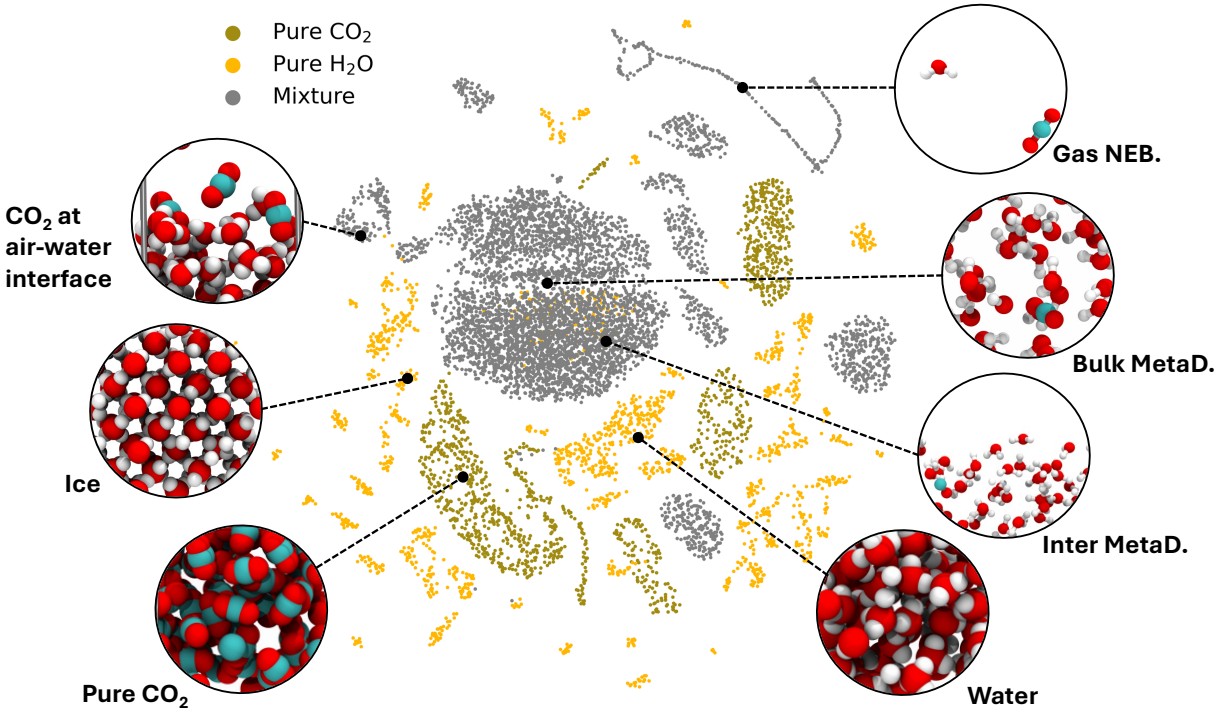

Fig. A.2 2D UMAP projection of the structural dataset used to train our MACE model, shown alongside snapshots of representative structures. A total of some 8000 structures were used for training. Structures were extracted from free MD simulations, from simulations employing some restraint on a distance or coordination CV, and from metadynamics runs. The most appropriate structures for training were identified using a 'Query-by-Committee' procedure, as described in Ref. [215].

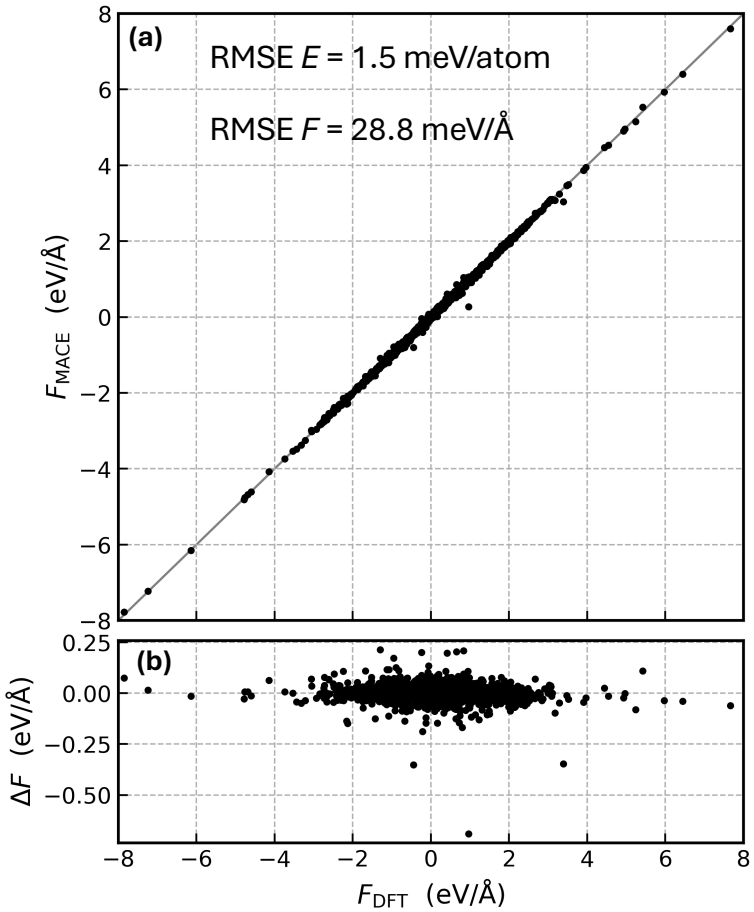

Fig. A.3 Comparing MACE and DFT force predictions. (**a**) Plot of the forces predicted by MACE against those of DFT. Forces are calculated for a random selection of 500 test structures. Total energy and force RMSEs are shown at the top of this figure. (**b**) Plot of the difference in MACE and DFT forces against the reference DFT forces.

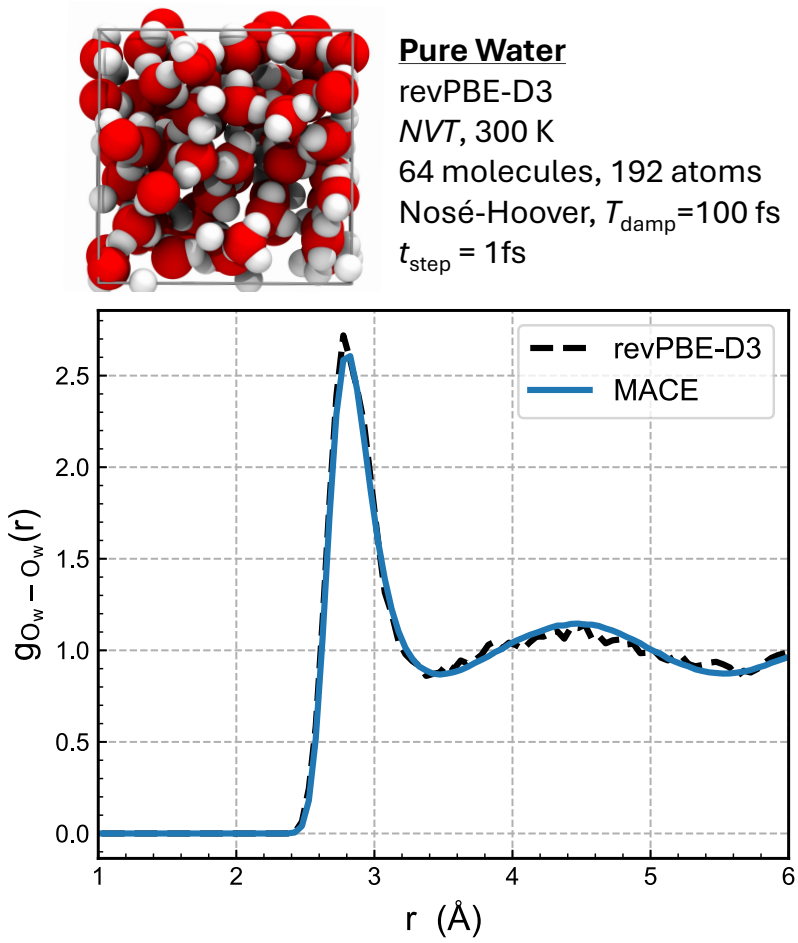

Fig. A.4 Radial distribution (g(r)) for Ow-Ow pairs obtained from *ab initio* MD and MACE-MD and plotted against distance r. AIMD simulations were run for 22 ps. MACE simulations were performed for 1 ns. System and simulation details are shown above.

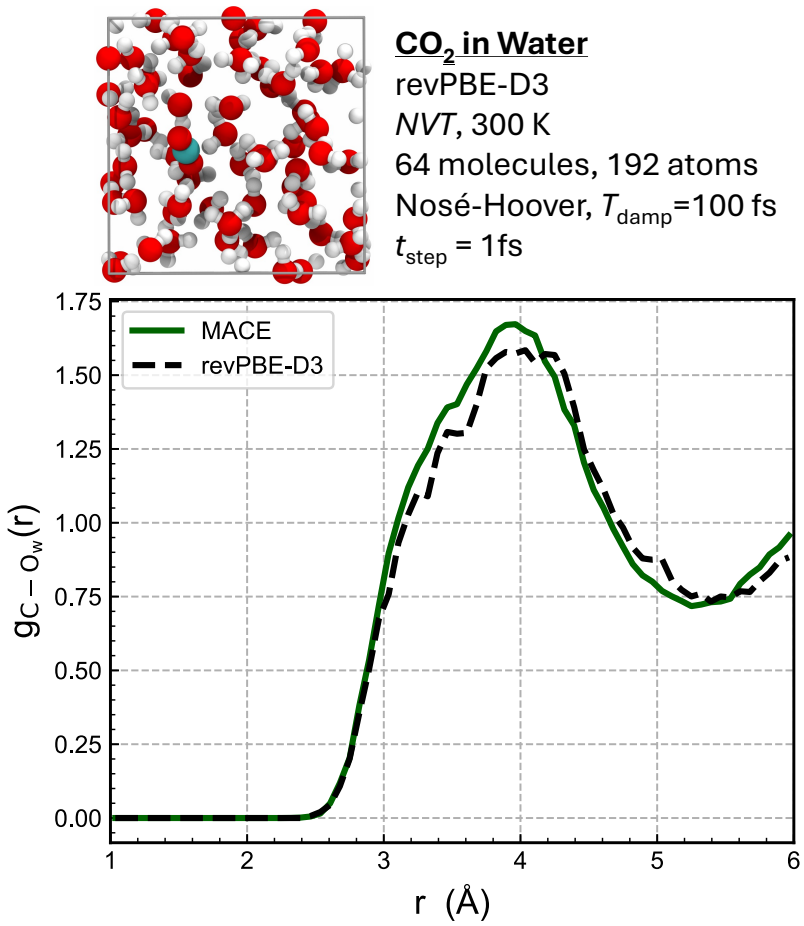

Fig. A.5 Radial distribution (g(r)) for C-Ow pairs (CO_2-water) obtained from *ab initio* MD and MACE-MD and plotted against distance r. AIMD simulations were run for 45 ps. MACE simulations were performed for 1 ns. System and simulation details are shown above.

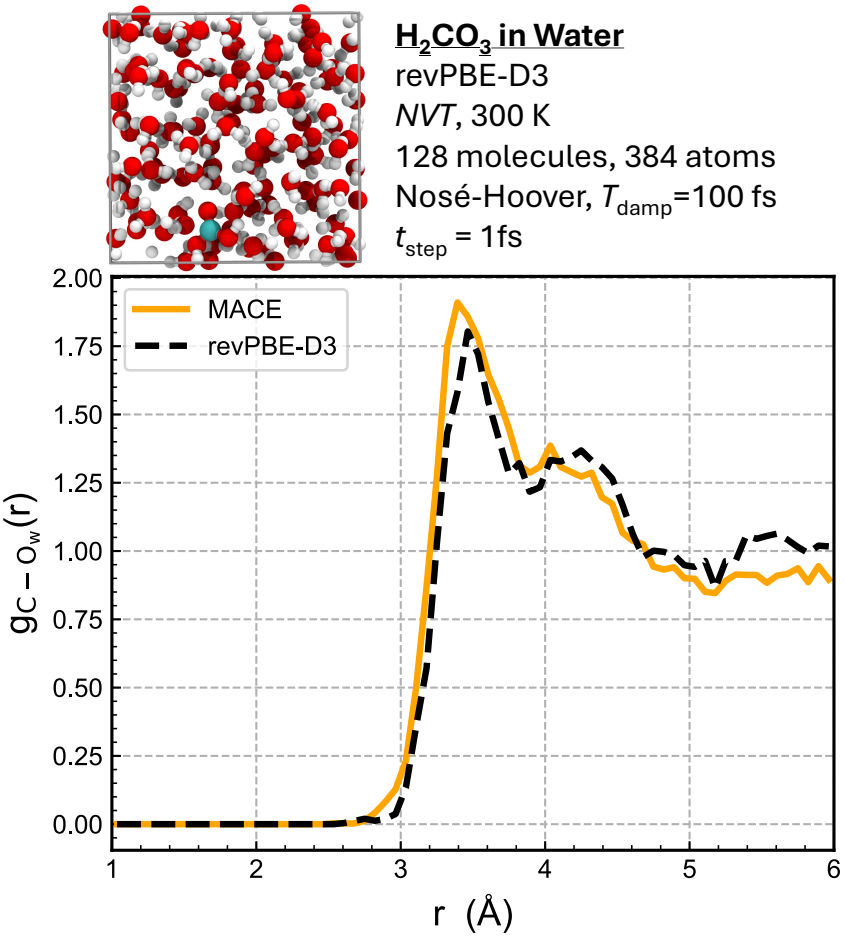

Fig. A.6 Radial distribution (g(r)) for C-Ow pairs (carbonic acid - water) obtained from *ab initio* MD and MACE-MD and plotted against distance r. AIMD simulations were run for 20 ps. MACE simulations were performed for 1 ns. System and simulation details are shown above.

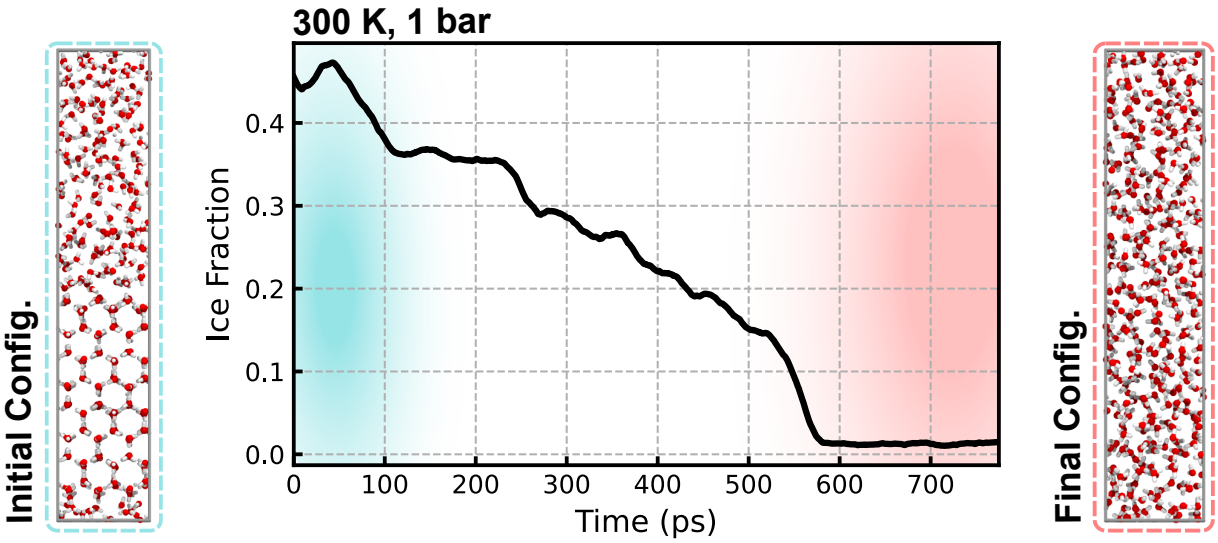

Fig. A.7 Solid-liquid coexistence analysis at 300 K and 1 bar. **(Left)** The biphasic setup used for this analysis. Ice and liquid water phases were constructed in a 1:1 ratio (192 molecule each). NPT simulations were performed over 1 ns, during which the locally averaged Steinhardt $\bar{q}_6$ order parameter (L=6, w_l) was monitored as a function of time. $\bar{q}_6$ values greater than 0.42 were ascribed to ice-like geometries; values less than 0.42 were ascribed to water-like geometries. **(Middle)** Plot of the fraction of ice-like environments at each stage of the simulation. The disappearance of the ice phase occurs at around 550 ps, coinciding with a sharp drop in $\bar{q}_6$. **(Right)** Snapshot of the final system configuration following the disappearance of the ice phase.

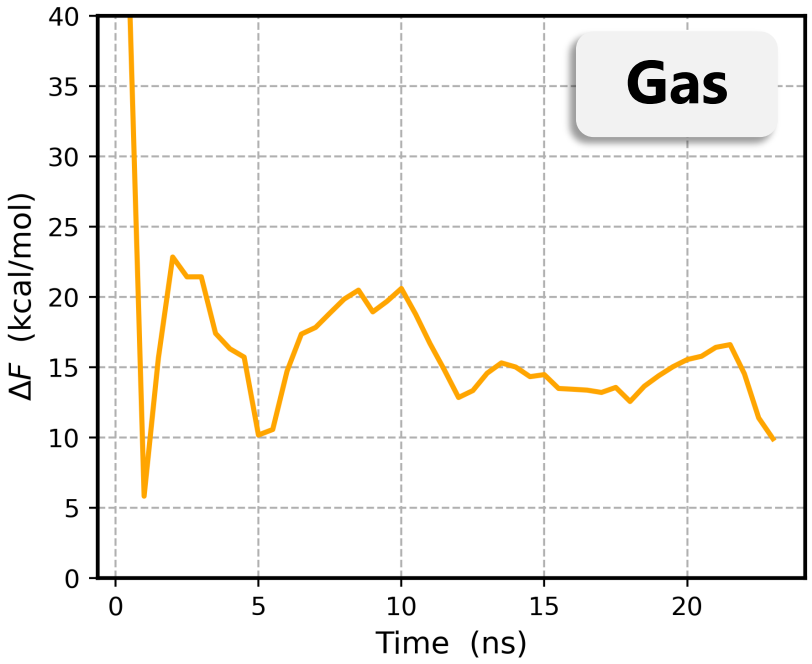

Fig. A.8 ΔF of carbonic acid (relative to CO_2) in the gas phase plotted as a function of the (individual) walker time. Cumulative walker time amounts to over 60 ns for the gas-phase reaction.

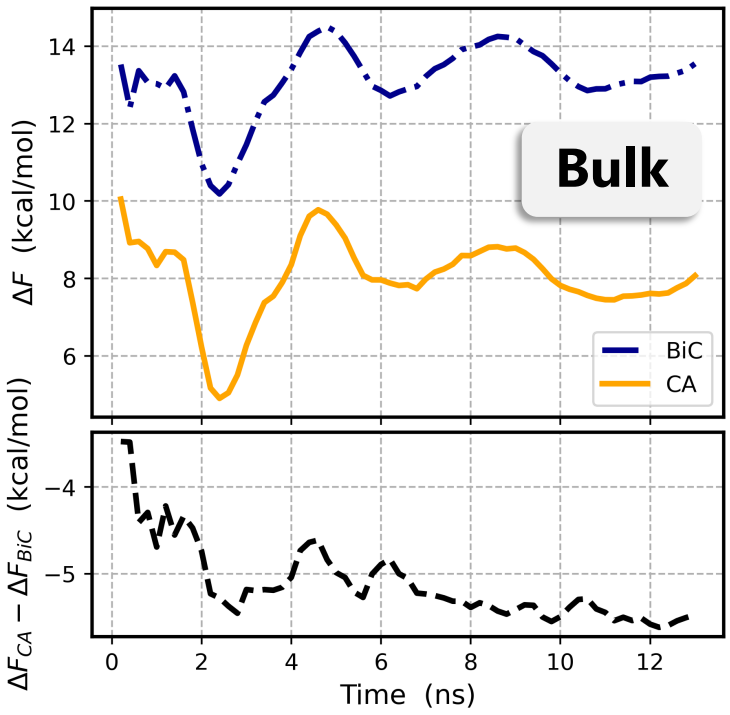

Fig. A.9 ΔF of carbonic acid and bicarbonate (relative to CO_2) in bulk plotted as a function of the (individual) walker time. The free energy difference between bicarbonate and carbonic acid are plotted below. Cumulative walker time amounts to over 50 ns for the bulk reaction.

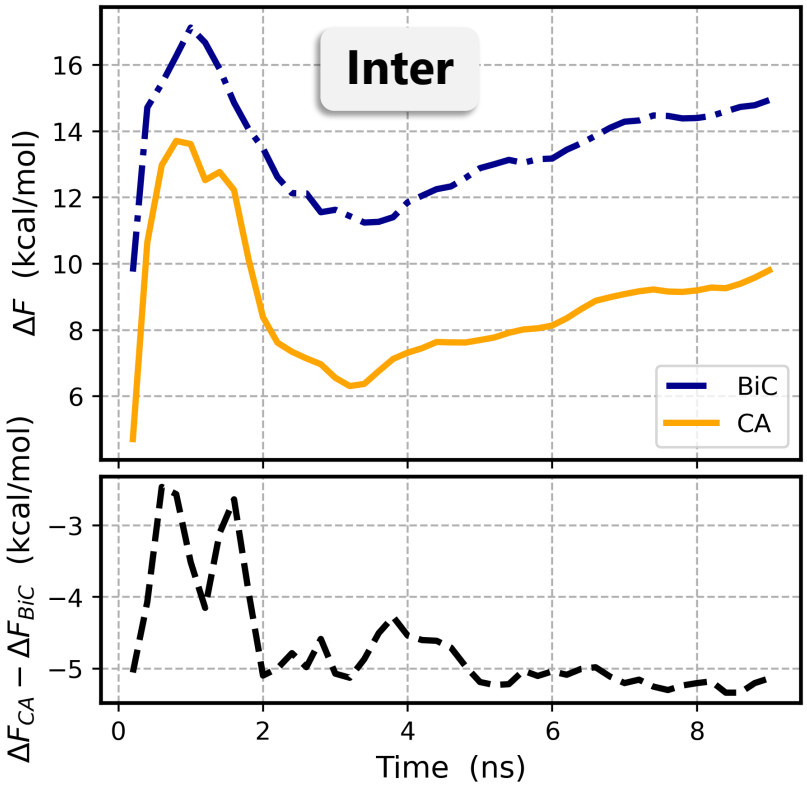

Fig. A.10 ΔF of carbonic acid and bicarbonate (relative to CO_2) at the interface plotted as a function of the (individual) walker time. Free energy differences between bicarbonate and carbonic acid are plotted below. Cumulative walker time amounts to over 50 ns for the interfacial reaction.

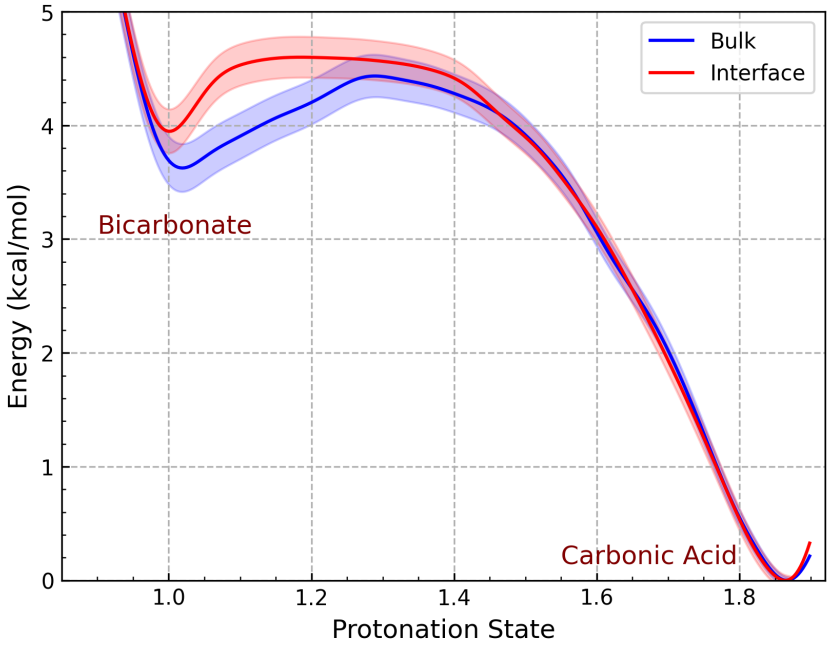

Fig. A.11 Free energy profiles tracking the deprotonation of carbonic acid (right-hand side) to form bicarbonate (left-hand side) in bulk and at the air-water interface. Free energies were obtained from umbrella sampling simulations and are plotted as a function of the protonation state of the carbon species. Errors obtained from this integration are plotted as shaded regions. Umbrella sampling simulations were run for 100 ps per umbrella under the NVT ensemble using the same bulk and interfacial system setups employed for metadynamics simulations.

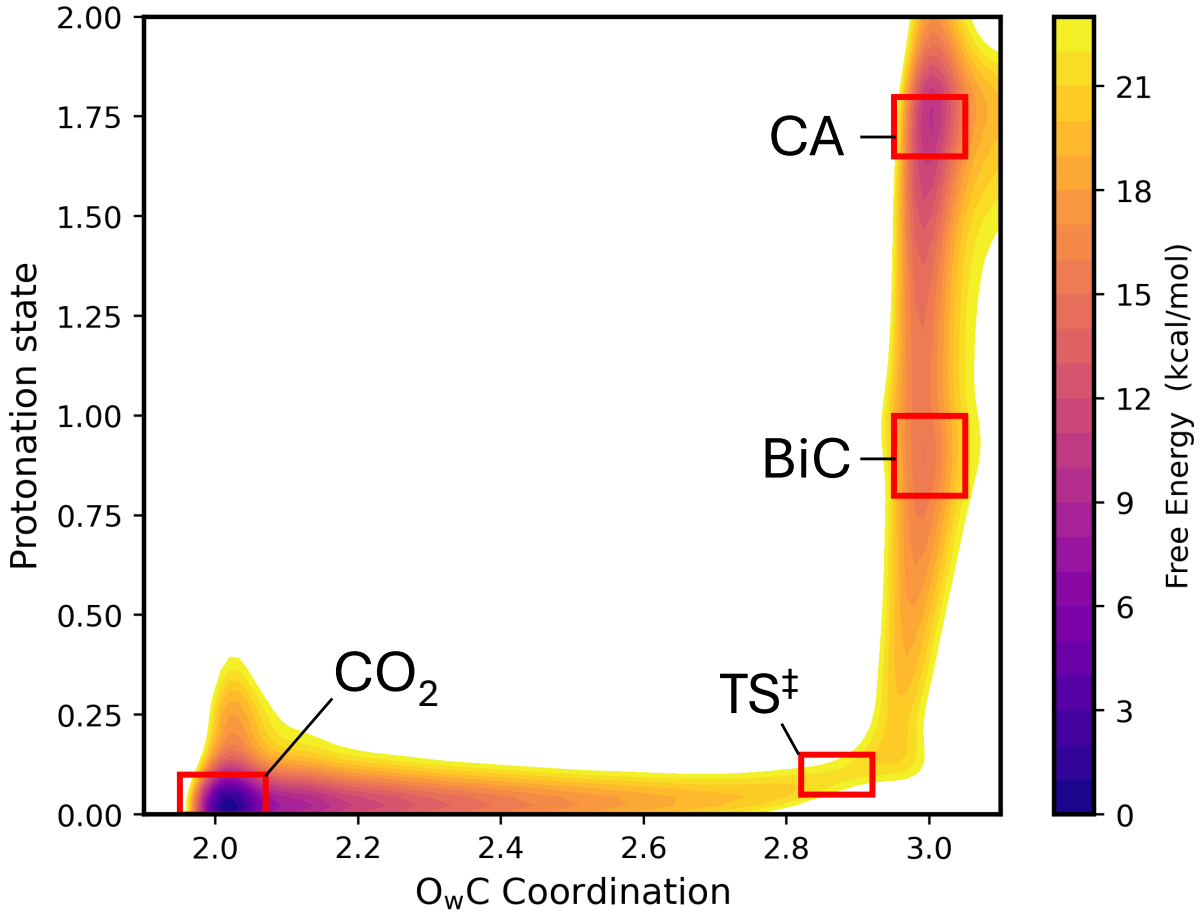

Fig. A.12 The interfacial free energy profile of reaction, labelled with the state boundaries used to isolate CO_2, bicarbonate, carbonic acid, and $TS^{\ddagger}$ structures for analysis.

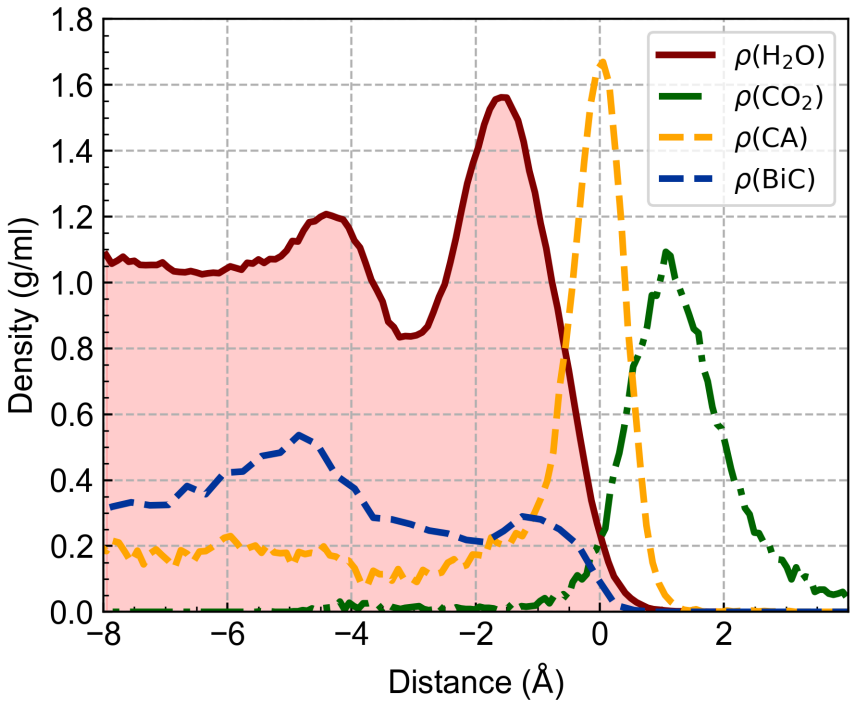

Fig. A.13 Density profiles obtained for CO_2, bicarbonate, and carbonic acid from free MD simulations. Simulations were performed under the NVT ensemble for a duration of 2.5 ns and using the same system setups as with our metadynamics interfacial run. Densities are plotted as a function of the distance from the instantaneous interface (water density given by y axis, carbon densities on arbitrary scale).

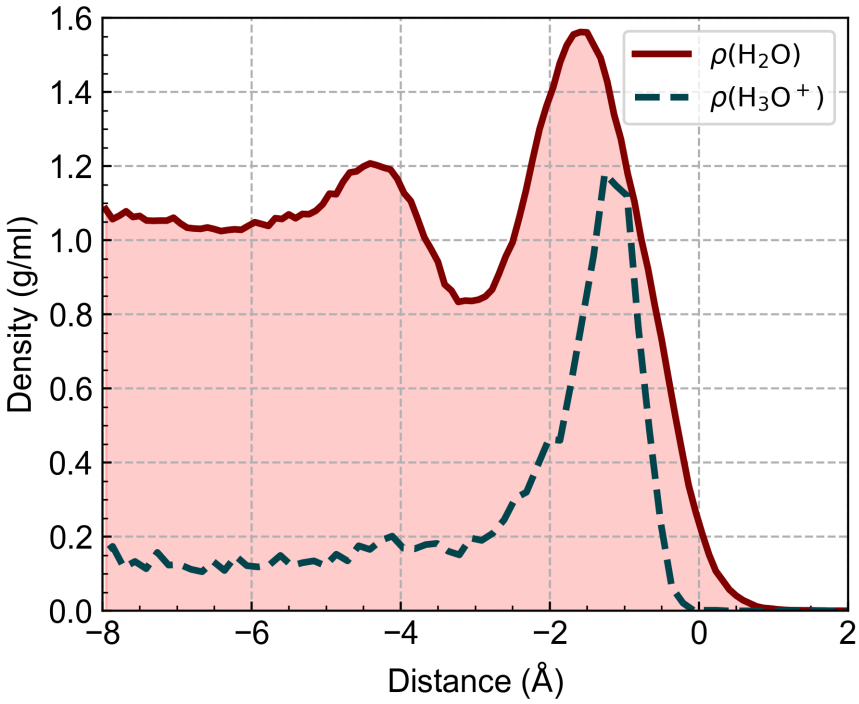

Fig. A.14 Density profile obtained for the hydronium ion from free MD simulations. Simulations were run under the NVT ensemble for 2.5 ns using the same interfacial setup as with the metadynamics runs. Densities are plotted as a function of the distance from the instantaneous interface (water density given by y axis, hydronium density on arbitrary scale). Using $\Delta F = -RT\ln(\rho/\rho_0)$, we determine a free energy of stabilization of − 1.3 kcal/mol for hydronium at the interface.

Table A.1 Key properties and predictions for the revPBE-D3, BLYP-D3, and RPA MACE models. For each model, the training errors - taken as the RMSE between the MACE-predicted forces and those from the reference method - are reported alongside the predicted density (ρ) and IFT (γ) values.

Reference Theory	**Train Er. (meV/Å)**	$\boldsymbol{\rho}$ **(g/ml)**	$\boldsymbol{\gamma}$ **(mN/m)**
revPBE-D3	28.8	0.991 ± 0.002	84 ± 1
Ref.[34, 226]		0.96 ± 0.03	83 ± 28
BLYP-D3	67.8	1.110 0.002	106 ± 4
Ref.[34, 396]		1.07 ± 0.02	92 ± 25
RPA	18.8	1.019 ± 0.002	81 ± 3
Ref.[397]		0.99 ± 0.02	/
Experiment	/	0.997	72.8

Appendix B

Supplementary Materials for Chapter 4

Here, we provide supplementary material relating to the contents of Chapter 4. This consists of model validation plots, supplementary analysis (densities and solubilities), a comparison of IFT potential across different models, and schematics showing how to calculate the Willard-Chandler interface and the lateral distribution function. A repository containing the simulation data and files can be found at:
`https://github.com/water-ice-group/co2-on-h2o`.

B.1 Model validation

20mm

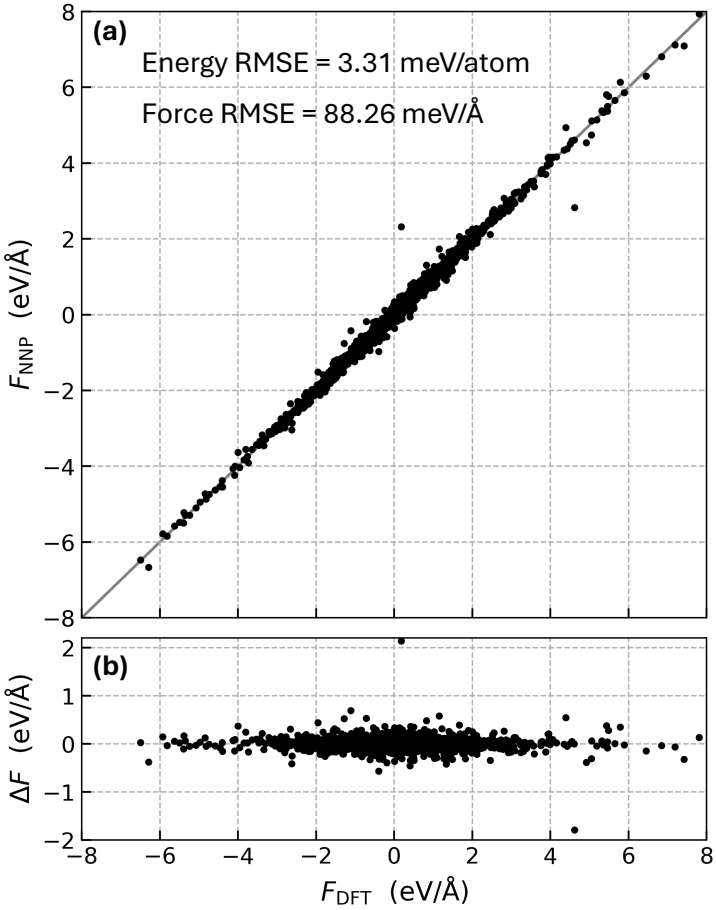

Fig. B.1 Comparing NNP and reference DFT force predictions. **(a)** Correlation plot showing NNP forces against DFT (BLYP-D3) forces for a test set of 400 structures. Forces were randomly sampled from this test set. The total test energy and forces RMSEs are displayed at the top of this plot. **(b)** Plot of the difference in predictions between NNP and DFT forces against the reference DFT forces.

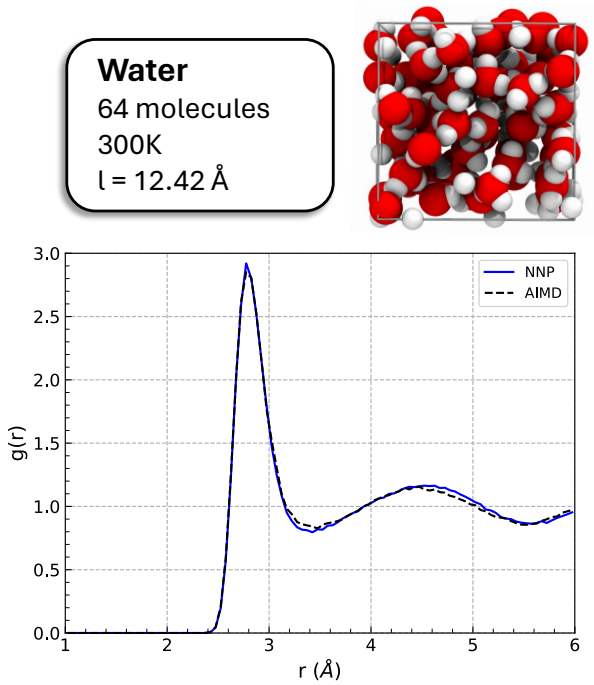

Fig. B.2 Radial distribution functions, $g(r)$, obtained for pure water at 300 K. Results are shown for both *ab initio* and NNP MD. Simulations were performed under the NVT ensemble, with fixed numbers of particles N (64 waters), fixed volume V ($l_x = l_y = l_z =$ 12.42 Å), and fixed temperature T (300 K). In total, 21 ps worth of *ab initio* data and 1 ns worth of NNP data were obtained for RDF calculations.

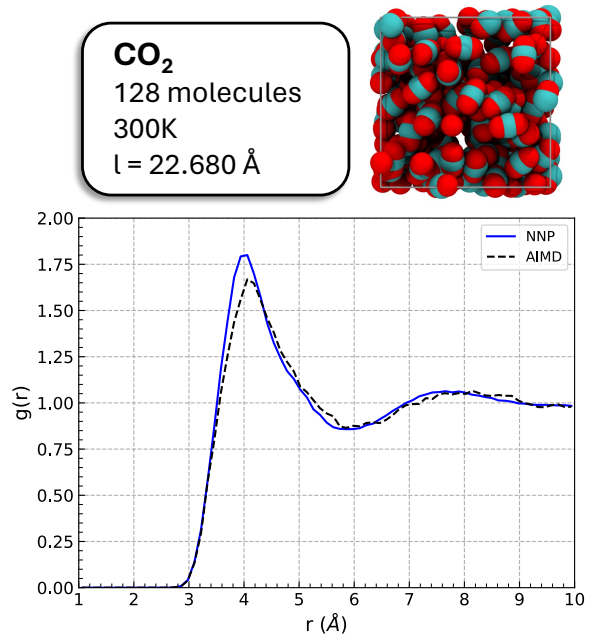

Fig. B.3 Radial distribution functions, $g(r)$, for pure CO_2 at 300 K. Results are shown for both *ab initio* and NNP MD. Simulations were performed under the NVT ensemble, with fixed numbers of particles N (128 CO_2s), fixed volume V ($l_x = l_y = l_z = 22.680$ Å), and fixed temperature T (300 K). In total, 6 ps worth of *ab initio* data and 1 ns worth of NNP data were obtained for RDF calculations.

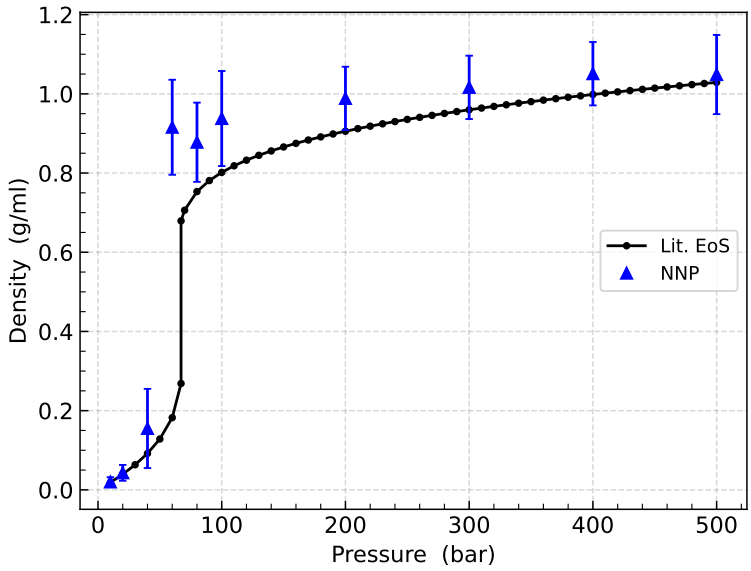

Fig. B.4 Densities predicted by NNP-MD for pure CO_2 across 10-500 bar at room temperature. Results are shown for NNP-MD alongside reference literature values obtained from an equation of state for CO_2 [248]. Simulations were performed under the NPT ensemble, with fixed numbers of particles N (128 CO_2s), fixed pressure P, and fixed temperature T (300 K). System size was allowed to vary isotropically with pressure (initial size, $l_x = l_y = l_z = 22.680$ Å). In total, 20 ns worth of NNP data was obtained for density calculations.

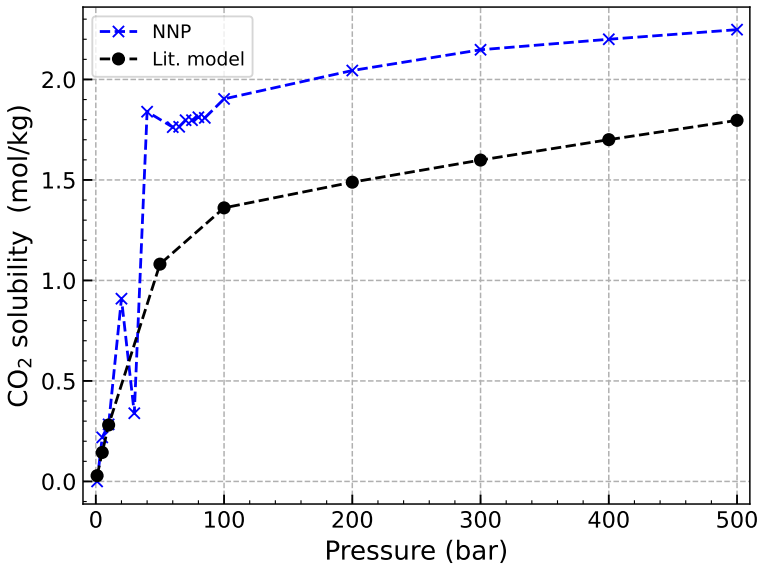

Fig. B.5 Solubility profiles of CO_2 in water. NNP-MD values are shown alongside reference literature values obtained from a thermodynamic CO_2 solubility model [398]. NNP solubilities are determined from the density plots of Fig. 3 in the main text. We consider only densities below -5 Å to obtain average bulk densities, which are subsequently converted to solubility values.

B.2 IFT Comparisons

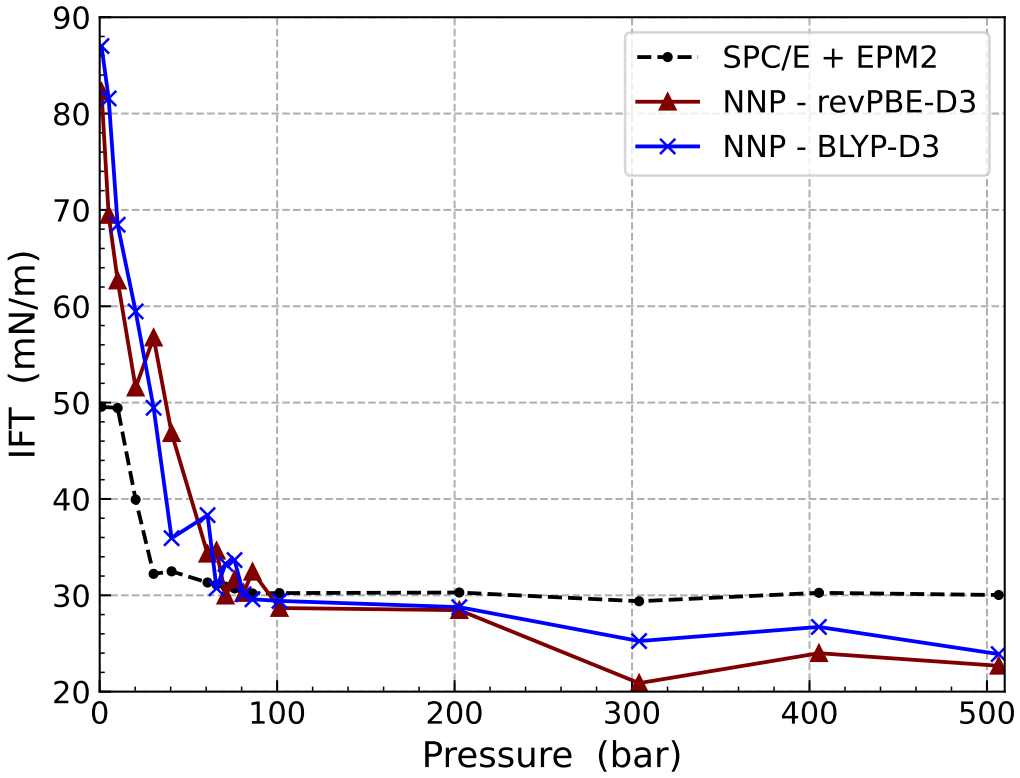

Fig. B.6 Comparing interfacial tension profiles for NNP and classical results. Interfacial tension profiles are shown for SPC/E + EPM2 (black), BLYP-D3 (blue) and revPBE-D3 (maroon, reduced dataset). Classical runs were performed for 25 ns using the same system setup as with NNP-MD but without requiring replica exchange.

B.3 Analysis Tools

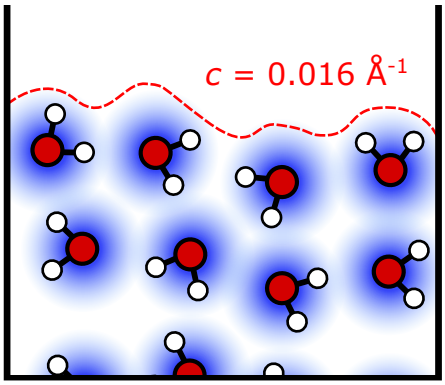

Fig. B.7 Schematic showing the identification of an instantaneous liquid interface using the Willard-Chandler approach [236]. At each molecular (water) site, we deposit Gaussians of fixed shape and height. We then construct a 3D grid in space and sum all Gaussians to construct a coarse-grained density field. The instantaneous interface is determined to be the point in space where the density field falls to half the critical density of water, i.e., 0.016 $Å^{-1}$. In this work, we use Gaussian parameters tailored to the distribution of water molecules; these can be adapted to cater to various other types of molecular systems.

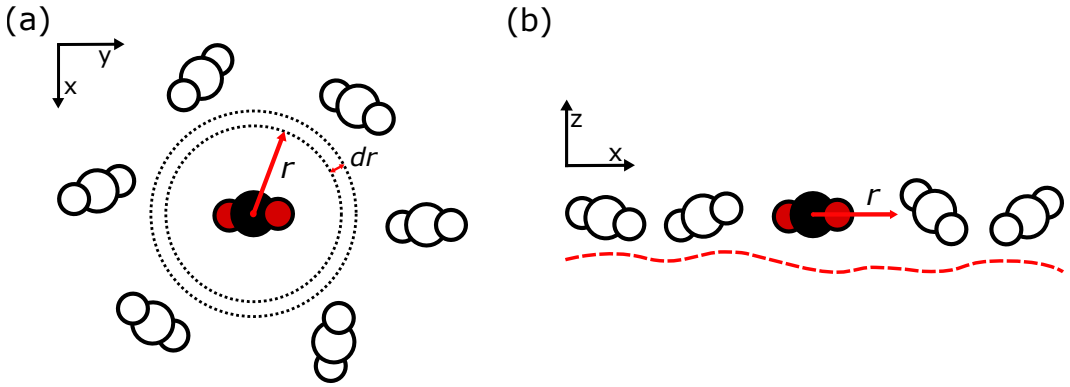

Fig. B.8 Schematic showing the lateral distribution function (LDF). The LDF is calculated according to $g(r) = \frac{dn_r}{dA \cdot \rho} = \frac{dn_r}{2\pi r dr \cdot \rho}$, where dn_r is the number of CO_2 molecules within an anulus of thickness dr, and ρ gives the local density. In practice, the LDF serves as the 2D analogue of the radial distribution function. Here, we switch the volume element, $dV = 4\pi r^2$, for the area element, $dA = 2\pi r$, to account for the fact that CO_2 molecules are mostly distributed in the plane of the monolayer at low pressure. Accordingly, we neglect non-planar contributions to the normalisation of our molecular distribution.

Appendix C

Supplementary Materials for Chapter 5

Here, we provide supplementary material relating to the contents of Chapter 5. Specifically, we give details of our model validation, free MD simulations, the calculation of interaction and adsorption energies, and additional structural analysis. A repository containing the simulation data and files can be located at:
`https://github.com/water-ice-group/oversolubility`.

Free MD simulations

In Fig. 5.2, we plot the densities of CO_2, H_2O, and HCO_3^- as a function of the distance of the species from the system centre. Convergence of the density profiles was monitored using block averaging, and each trajectory accumulated over several ns of simulation time. An additional profile obtained for 20 Å pore separation (see Table C.1, System 4) is shown in Fig. C.3.

In Fig. 5.4a of the main text, we detail orientational analyses of the molecules residing at the pore-water contact layer. For these analyses, we utilized structures extracted from the 12 Å pore trajectory (used in Fig. 5.2). Orientations were measured by the angle between the z axis and either the H_2O dipole vector or CO_2's bond vector. Only the

orientations of species adjacent to one pore wall were considered. Snapshots of this contact layer (omitting species beyond the first layer) are also shown in Fig. 5.4b.

Gaseous interaction energies

We report the interaction energies for gaseous CO_2 and H_2O interacting with an isolated graphene sheet (5×5 supercell, 20 Å vacuum) in Fig. 5.3a. Estimates of the interaction energy, E_{int}, were obtained from single-point DFT calculations of CO_2/H_2O located at different distances from the graphene plane. To calculate E_{int}, we used the following formula,

$$E_{\text{int}} = E[\text{Molec.} + \text{wall}] - E[\text{Molec.} - \text{wall}], \tag{C.1}$$

where E[Molec. + wall] gives the energy of the configuration in which CO_2/H_2O is adsorbed at the pore wall, and E[Molec. − wall] is the energy of the configuration where CO_2/H_2O is located 10 Å away (rigid translation). revPBE-D3 calculations were performed with VASP [122–125] using the projector-augmented plane wave method and hard pseudo-potentials [399, 400] (energy cutoff of 1000 eV). A 1×1×1 k-point grid was used to sample the Brillouin zone, providing converged energies to within 1 meV of a 4×4×1 grid.

Aqueous free energies of adsorption

In Fig. 5.3b, we report the free energies of both CO_2 and H_2O as a function of the distance from the pore wall under pore-saturated conditions. To generate these profiles, we utilized a 30 Å pore environment (System 5), the details of which can be found in Table C.1. The H_2O free energy curve was generated from a Boltzmann inversion of the underlying water density profile,

$$\Delta F = -RT \ln(\rho/\rho_0), \tag{C.2}$$

where T is the temperature, R is the gas constant, ρ is the density, and ρ_0 is the bulk density (CO_2 was removed from these runs to prevent artifacts in the profile). For CO_2, given the difficulty associated with obtaining converged statistics for a single molecule, free energies were obtained using the umbrella integration method [321]. The $\sim$ 15 Å

range of pore-CO_2 distances was divided into 50 separate windows. For each window, a harmonic restraint with force constant $k = 10$ kcal mol^{-1} Å^{-2} was applied. Each window was simulated for 400 ps. Errors of integrations are shown alongside free energies in the main plot. The H_2O and CO_2 free energies are aligned such that the energy zero is set at 15 Å (i.e., bulk) for both molecules.

	Pore Width	Cell Dimensions (Å)	n(CO_2/HCO_3^-)	n(H_2O)
System 1	7.0	12.35×12.834×31.0	1	14
System 2	12.0	17.29×17.112×35.0	1	81
System 3	15.0	17.29×17.112×40.0	1	115
System 4	20.0	17.29×17.112×35.0	1	157
System 5	30.0	12.35×12.834×55.0	1	140

Table C.1 System setups for the idealized pore environments used in this work. Systems highlighted in bold were used for obtaining the density profiles shown in Fig. 5.2. An additional free MD simulation was performed using System 4, the results of which can be found in Fig. C.3. System 5 was used for obtaining the aqueous free energy profiles shown in Fig. 5.3b of the main text.

System	Type	In-pore mole fraction of CO_2:water (%)
ACC-10/H_2O 1:1	Exp	1.5
ACC-20/H_2O 2:3	Exp	0.4
System 1 (7 Å)	Comp	6.6
System 2 (12 Å)	Comp	1.2
System 3 (15 Å)	Comp	0.9

Table C.2 Experimental and computational mole fractions of CO_2 in H_2O. These are presented for the experimental ACC-10/ACC-20 + deionized water setups as well as for the atomistic systems presented in Fig. 5.2. Mole fractions were computed by Zeke Coady.

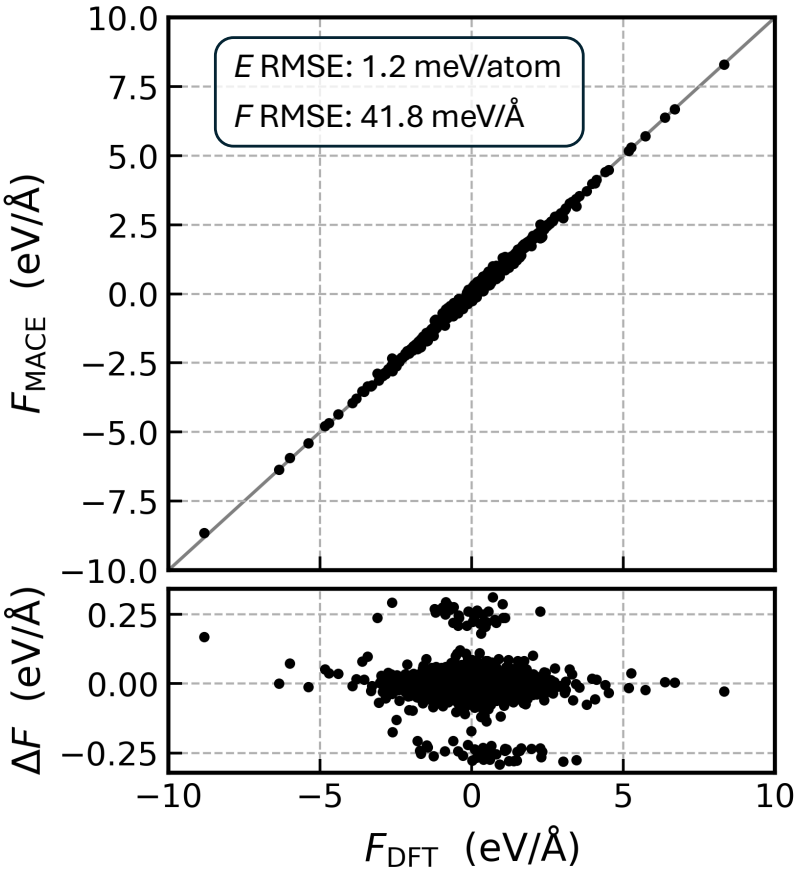

Fig. C.1 A comparison of MACE and DFT forces calculated for a subset of structures extracted from the main training dataset. (**Top**) Forces calculated using our MACE potential plotted against those of revPBE-D3. (**Bottom**) The difference in MACE and revPBE-D3 forces (ΔF) plotted against revPBE-D3 forces. Overall model RMSEs for the energies and forces are shown at the top of the plot.

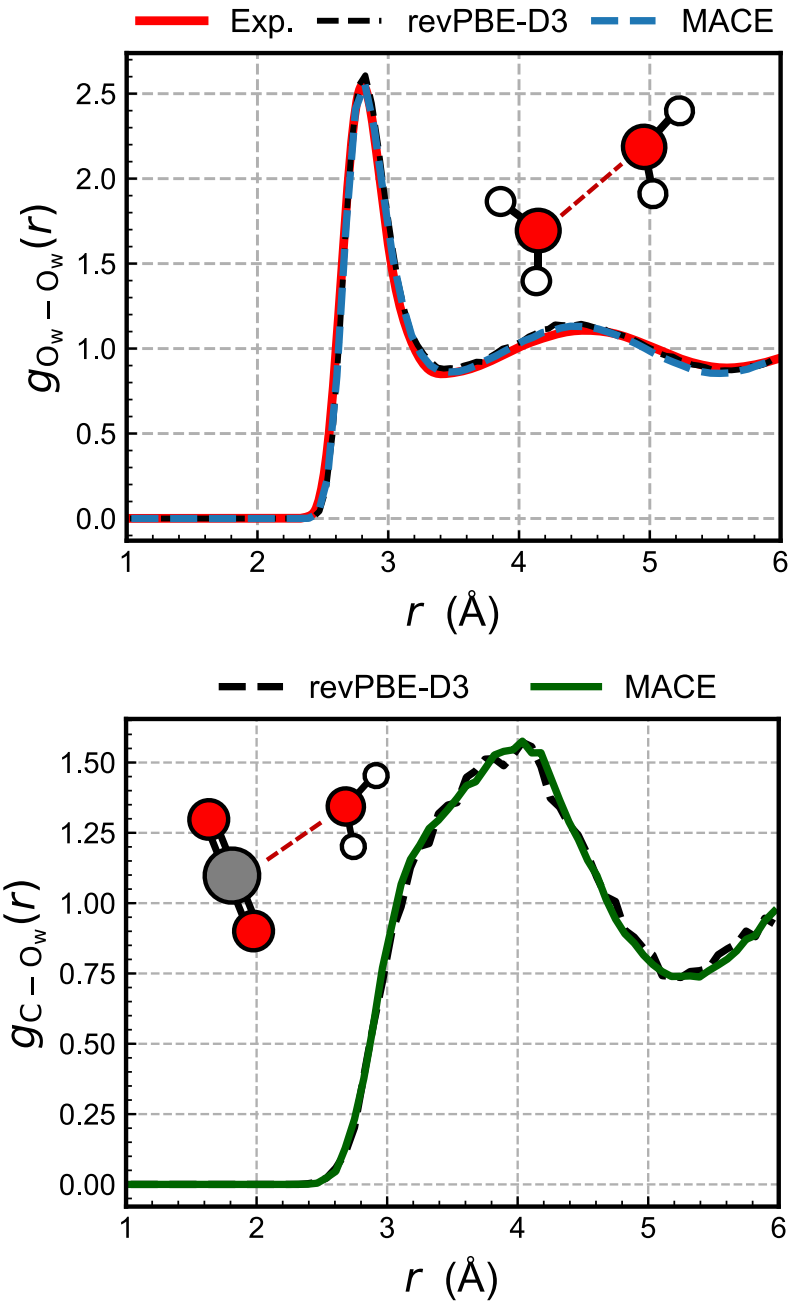

Fig. C.2 Radial distribution function (RDF) predictions of our MACE model compared with those of DFT (revPBE-D3). (**Top**) Ow-Ow RDFs obtained from MACE, revPBE-D3, and experiment. MACE RDFs were obtained using a 64-molecule water system with equal side lengths of 12.42 Å. MACE simulations were performed over 1 ns and the results compared to those of *ab initio*-MD obtained using identical system setups. Experimental results were taken from x-ray diffraction data [389, 401]. (**Bottom**) C-Ow RDFs compared for MACE and revPBE-D3. RDFs were obtained using a 63-molecule water system with a single CO_2 molecule and equal side lengths of 12.57 Å. MACE simulations were performed over 1 ns and the results compared to those of *ab initio*-MD obtained using identical system setups.

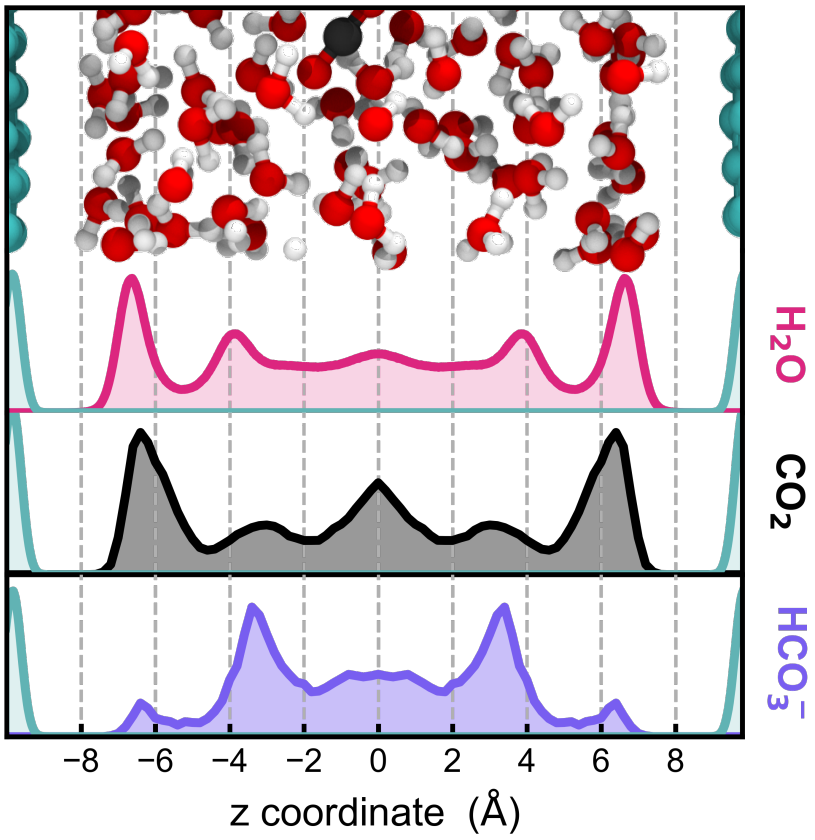

Fig. C.3 20 Å pore density profiles obtained for water (pink), CO_2 (black), and HCO_3^- (purple), plotted as a function of the distance from the system center of mass. Profiles are shown alongside a snapshot of the overall system.

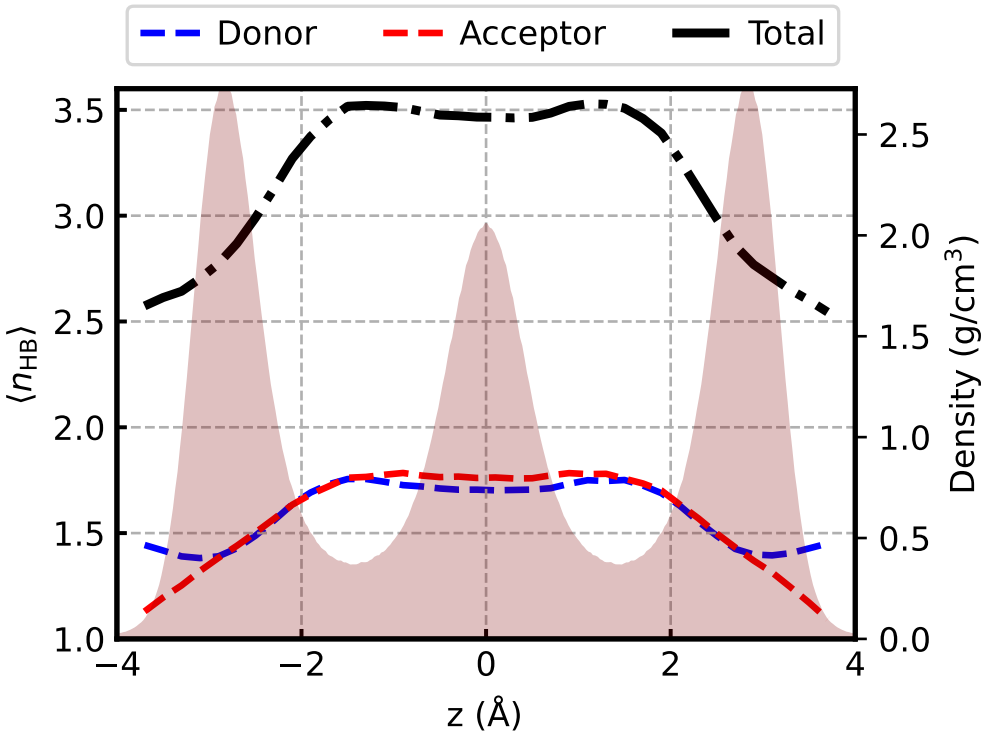

Fig. C.4 The nature of hydrogen bonding under pore-saturated conditions. The average hydrogen bond count, $\langle n_{\mathrm{HB}} \rangle$, is plotted as a function of the distance from the center of mass of the system (12 Å confinement). Hydrogen bonds are identified using a donor-acceptor distance of 3.5 Å and an O-H-O angle of 140°. The total hydrogen bond count (black) is decomposed into both donor (blue) and acceptor (red) contributions. The underlying water density (maroon) is plotted using the secondary axis.